NOVEL APPROACHES FOR QUANTIFYING SOURCE ZONE NATURAL ATTENUATION OF FOSSIL AND ALTERNATIVE FUELS

by

Natasha Julie Jane Sihota

A THESIS SUBMITTED IN PARTIAL FULFILLMENT OF

THE REQUIREMENTS FOR THE DEGREE OF

Doctor of Philosophy

in

The Faculty of Graduate and Postdoctoral Studies

(Geological Sciences)

THE UNIVERSITY OF BRITISH COLUMBIA
(Vancouver)

August 2014

Abstract

Natural attenuation represents an environmentally and economically sustainable means to manage contaminants *in situ*. To assess potential human and environmental risks associated with this strategy, there is a need to characterize the extent of contaminant containing source zones. Moreover, to obtain public and regulatory support, there is a need to demonstrate that mass losses are occurring. However, quantifying the extent and rate of natural attenuation under field conditions remain challenging. Here a novel approach for assessing and monitoring sites impacted by hydrocarbon and ethanol-blended fuels using surficial gas effluxes is developed. The approach is tested at several sites including those impacted by a crude oil pipeline rupture, ethanol-blended fuel train car derailments, and historic refinery operations. The approach was refined through inclusion of isotopic measurements, comparison to other approaches for monitoring microbial activity, and evaluation of seasonal dynamics and microbial communities. Process-based reactive transport modeling was used to integrate and interpret field data and develop and illustrate a more robust conceptual model of the processes occurring at the different field sites.

Results demonstrate that surficial gas effluxes are able to both delineate contaminant containing source zones, and distinguish between the rates of natural soil respiration and contaminant mineralization. In scenarios where methane oxidation goes to completion, carbon dioxide fluxes are sufficient for evaluating natural attenuation rates; when methane escapes oxidation, measurements of methane fluxes are also needed. Results also demonstrated that measurement of radiocarbon is particularly useful for determining the contribution of contaminant degradation to the measured efflux. Comparison of seasonal dynamics showed that both biological and physical parameters must be considered when quantifying average annual

contaminant degradation rates while comparison to other approaches for measuring microbial activity showed good correlations with gas effluxes. Comparison across the field sites investigated, showed degradation rates were relatively high at ethanol-blended fuel release sites. In-depth microbiological evaluation of microbial communities at one ethanol-blended fuel release site showed a substantial change in the microbial community associated with the release.

Overall, the novel methods provide a useful approach for assessing the extent and rate of natural attenuation at hydrocarbon contaminated field sites.

Preface

Research contributions

Chapter 2 is based on work conducted at a crude oil pipeline rupture near Bemidji, MN. I conducted fieldwork including CO_2 flux measurements, vadose zone gas sample collection, and analyses of vadose zone gas samples with support from Dr. Singurindgy. I wrote a paper draft, which Dr. Singurindgy commented on. Dr. Mayer and I both contributed to writing and editing the final manuscript. A version of chapter 2 was published as:

Sihota, N.J., O. Singurindgy, and K.U. Mayer. 2011. CO_2-Efflux Measurements for Evaluating Source Zone Natural Attenuation Rates in a Petroleum Hydrocarbon Contaminated Aquifer. Environmental Science & Technology 45: 482–488.

Chapter 3 is based on work conducted at a crude oil pipeline rupture near Bemidji, MN. I conducted CO_2 flux measurement and collected radiocarbon samples. I isolated carbon from samples on a vacuum line and analyzed samples for stable isotope analyses using Delta Finnegan Mass Spectrometer. I conducted modeling with guidance from Dr. Mayer. I wrote the manuscript with editorial guidance from Dr. Mayer. A version of chapter 3 was published as:

Sihota, N.J., and K.U. Mayer. 2012. Characterizing Vadose Zone Hydrocarbon Biodegradation Using Carbon Dioxide Effluxes, Isotopes, and Reactive Transport Modeling. Vadose Zone Journal 11.

Chapter 4 is based on work conducted at a crude oil pipeline rupture near Bemidji, MN. Paul Sihota and I conducted CO_2 flux measurements. I analyzed and interpreted CO_2 flux data, prepared figures and wrote text related to CO_2 flux results and interpretation.

A version of chapter 4 has been accepted for publication as:

Warren, E., Sihota, N.J., Hostettler, F., and B.A. Bekins. Comparison of Surficial CO_2 Efflux to other Measures of Subsurface Crude Oil Degradation, *Journal of Contaminant Hydrogeology*, DOI: 10.1016/j.jconhyd.2014.06.006

Chapter 5 is based on work conducted at a crude oil pipeline rupture near Bemidji, MN. I, Jared Trost, Andrew Berg and Brent Mason conducted fieldwork. I analyzed and interpreted the data jointly with Jared Trost. I conduced modeling and wrote the manuscript with editorial guidance from Dr. Mayer, which Jared Trost commented on.

A version of chapter 5 is in preparation for submission to a peer reviewed journal as:

Sihota, N.J., Trost, J., Bekins, B., Berg, A., Delin, G., B, Mason, B., Warren, E, and K.U. Mayer. Seasonal variability in vadose zone biodegradation at a crude oil pipeline rupture site. *In prep.*

Chapter 6 is based on work conducted at a former refinery site. I and Alysha Hakala conducted CO_2 flux measurements and collected samples for isotopic analyses. I isolated carbon from samples on a vacuum line. I analyzed the data and interpreted results. Ben McAlexander provided data for the meta-analyses and assisted with figure creation. I wrote the manuscript with editorial guidance from Dr. Mayer, which Dr. Lyverse and Ben McAlexander commented on.

A version of chapter 6 is under peer review as:

Sihota, N.J., McAlexander, B., Lyverse, M., and K.U. Mayer. CO_2 efflux and radiocarbon measurements for assessing SZNA at a large industrial site. *In review.*

Chapter 7 is based on work conducted at two denatured fuel grade ethanol release sites in southwestern MN. I conducted fieldwork with support from Joel Atwater. I analyzed the data, conducted modeling, and interpreted results with input from Dr. Mayer. Mark Toso provided

access to the field sites. I wrote the manuscript with editorial guidance from Dr. Mayer, which Mark Toso commented on.

A version of chapter 7 was published as:

Sihota, N.J., K.U. Mayer, M.A. Toso, and J.F. Atwater. 2013. Methane emissions and contaminant degradation rates at sites affected by accidental releases of denatured fuel-grade ethanol. Journal of Contaminant Hydrology 151: 1–15.

Chapter 8 is based on work conducted at a denatured fuel grade ethanol release site in southwestern MN. I conducted field and laboratory work, analyzed the data, and interpreted results with input from Dr. Hallam. Mark Toso provided access to the field site and coordinated the drilling. I wrote the manuscript along with Dr. Hallam, which Dr. Mayer commented on.

A version of chapter 8 has been submitted for submission to a peer reviewed journal as:

Sihota, N.J., Mayer, K.U., and S.J. Hallam. Catastrophic biofuel release activates syntrophic networks in the rare biosphere. *In submission.*

Chapter 9 is based on work conducted at two crude oil and denatured fuel grade ethanol release sites in MN. I conducted fieldwork with support from Paul Sihota and Joel Atwater. I analyzed the data, interpreted results and wrote the manuscript with input from Dr. Mayer. The USGS and Mark Toso provided access to the field sites.

A version of chapter 9 has been submitted for submission to a peer reviewed journal as:

Sihota, N.J., and K.U. Mayer. Comparison of source zone natural attenuation rates at crude oil and biofuel release sites. *In submission.*

Table of contents

Abstract ii

Preface iv

Table of contents vii

List of tables xi

List of figures xv

List of acronyms. xxv

Acknowledgements xxvii

Chapter 1: Introduction 1

- Motivation, literature review and issues to address 2
- Research goals and hypotheses 5
- Research overview 6

Chapter 2: CO_2-efflux measurements for evaluating source zone natural attenuation rates in a petroleum hydrocarbon contaminated aquifer 8

- Introduction 9
- Site history 12
- Methods 13
- Results and discussion 16

Chapter 3: Characterizing vadose zone hydrocarbon biodegradation using CO_2-effluxes, isotopes, and reactive transport modeling 29

Introduction 30

Methods 35

Results and discussion 39

Chapter 4: Comparison of surficial CO_2 efflux to other measures of subsurface crude oil degradation 69

Introduction 70

Methods 73

Results 77

Discussion 80

Conclusions 83

Chapter 5: Seasonal variability in vadose zone biodegradation at a crude oil pipeline rupture. 93

Introduction 94

Methods 96

Results and discussion 98

Conclusions 109

Chapter 6: CO_2 efflux and radiocarbon measurements for assessing SZNA at a large industrial site 126

Introduction 127

Methods 130

Results and discussion 134

Conclusions 143

Chapter 7: Methane emissions and contaminant degradation rates at sites affected by accidental releases of denatured fuel-grade ethanol 154

Introduction 155

Methods 157

Results.....165

Discussion 168

Conclusions 178

Chapter 8: Catastrophic biofuel release activates syntrophic networks in the rare biosphere 196

Introduction 197

Methods 199

Results.....202

Discussion 207

Chapter 9: Comparison of source zone natural attenuation rates at crude oil and biofuel release sites 212

Introduction 213

Methods 215

Results and discussion 219

Conclusions 226

Chapter 10: Summary and conclusions 235

Implications and applications.....240

Strengths and limitations 241

Future work 242

References 244

Appendix 1: Supporting information for chapter 2 281

Appendix 2: Supporting information for chapter 3 296

Appendix 3: Supporting information for chapter 4 303

Appendix 4: Supporting information for chapter 5 306

Appendix 5: Supporting information for chapter 6 310

Appendix 6: Supporting information for chapter 7 317

Appendix 7: Supporting information for chapter 8 321

List of tables

Table 2.1. CO_2-efflux measurements taken at the Bemidji field site with LI-COR LI8100 chambers. 24

Table 2.2. CO_2-efflux due to contaminant-related soil respiration (JCSR), corresponding biodegradation rates per unit surface area, and comparison of results to previous studies at the Bemidji crude oil spill sites and other sites..... 25

Table 3.1. Summary of soil parameters used in model simulation for well 9017. 56

Table 3.2. Reaction stoichiometries, rate constants, and isotopic ratios used in model simulation for well 9017. K_i^I: inhibition constant for species i; K_i^S: half-saturation constant; for species i; k_i: rate constant for species i. Reaction parameters' were selected based on Molins et al. (2010) and fitted through model calibration. 57

Table 3.3. Comparison of methods for estimation of SZNA rate. †assumes that the pMC of background CO_2 is 107%. ‡assumes well 531 can be excluded. 58

Table 3.4. Comparison of SZNA rate estimates for the Bemidji site from this and other studies.59

†assumes that the pMC of background CO_2 is 107%. ‡assumes well 531 can be excluded. 59

Table 4.1. Microbial concentrations (log_{10} copies/g), *n*-alkylcyclohexanes (nC total; sum of GCMS response), and CO_2 efflux (μmol m^{-2} s^{-1}) data used in correlation statistics. 84

Table 4.2. Pearson correlation statistics (r) between microbial concentrations (log_{10} copies/g), n-alkylcyclohexanes, and CO_2 efflux. (p value; number of samples). 85

Table 5.1. Results of average surficial CO_2 efflux measurements' and SZNA estimates obtained using the background correction method and comparison of seasonally-weighted values. 112

Table 5.2. Percent ancient carbon in vadose zone CO_2 samples collected from the shallow vadose zone (based on results of $^{14}CO_2$ measurements). 2009 values are taken from Sihota and Mayer (2012). 113

Table 6.1. Comparison of SZNA mass loss rates using the BGC and RCC methods. Fluxes are reported in μmol m^{-2} s^{-1}. * determined from radiocarbon measurements 145

Table 6.2. Comparison of SZNA mass loss rates reported in this study to mass loss rates obtained for other technologies and sites. TPH is reported as ($C_{10}H_{22}$). + point based area correction *shown in Figure 1. ^normalized to total site area. 146

Table 6.3. Comparison of site metadata and SZNA hotspots identified using the BGC method and the HR-BGC dataset. CO_2 flux threshold set as ~ 6.5 x background NSR. 147

Table 7.1. Parameters used in the reactive transport model. 181

Table 7.2. Real time CO_2 and CH_4 effluxes measured at Balaton and Cambria sites in 2012. [1]within the area defined as the source zone and CH_4 fluxes were detected. [2]assumed (geometric mean of replicate measurements). ND: non-detect. BG: background CO_2 efflux correction used. SE = Standard error, n = number of measurements. [3]based on an ebullition flux. 182

Table 7.3. Complete gas composition measured within the gas collection chambers at the Cambria site. [1]Ar contents are corrected based on Ar content in air. [2]sample contamination by air suspected. BD: below detection (< 15 ppm_v) 184

Table 7.4. Total carbon, CO_2 and CH_4 effluxes at Cambria and Balaton DFE spill sites in comparison to other contaminated and natural environments (values in brackets represent contaminant soil respiration i.e. corrected for natural soil respiration).NR: not reported.

Average CH_4 : CO_2 presented are calculated using the average of CH_4 : CO_2 obtained from individual measurements. 185

Table 9.1. Comparison of key attributes of the field sites. 228

Table 9.2. Comparison of gas efflux ranges, estimated extent of source zones, and inferred SZNA rates at the field sites. *delineated based on Sihota et al. (2011). **delineated based on those values ≥ twice the background value. ND: small influx detected, but below reporting threshold. 229

Table 10.1. Key strengths and limitations of the approaches developed in this dissertation. 241

Table A1.1: Simulated carbon balance along the North Pool Transect after T = 28 years (Analysis of mass balance data from Molins et al. (2010), calcite dissolution and speciation of aqueous carbonate species at equilibrium, biomass assumed at steady state. 282

Table A1.2. Evaluation of accuracy of the DCC method for estimation of contaminant mineralization rates in the source zone; also evaluated is the sensitivity of the accuracy to the magnitude of TSR in the 'affected' region (SEM = standard error on the mean value). 286

Table A1.3. Comparison of natural soil respiration (NSR) rates reported in the literature with background CO_2-efflux measurements obtained in present study 292

Table A1.4. CO_2 efflux calculations for wells 301 and 9017 using equations 1 and 2 in associated paper. 294

Table A2.1. Definition of abbreviations and acronyms. 297

Table A2.2 Diffusion Coefficients Used in Reactive Transport Modeling at Well 9017..... 300

Table 3.3. Reference gas viscosities used in reactive transport modeling at well 9017. 302

Table A3.1. Cross-reference names between sites in this paper and sites found on the Bemidji Site website (http://mn.water.usgs.gov/projects/bemidji/p/list.html) and x- and y-coordinates in UTMa, land surface elevationb, and water table elevationb for each site... 304

[a] NAD83 UTM Zone 15N [b] NAVD88 [c] June, 2011 304

Table A3.2. Elevations and microbial concentrations of samples taken from each site..... 305

Table A4.1. Seasonality in the extent of SZNA processes. *normalized to the extent of the oil body (2,790 m2) 307

Table A4.2. Summary of soil parameters used in model simulation. 308

Table A4.3. Reaction stoichiometries and rate constants used in model simulation. K_i^I: inhibition constant for species i; K_i^S: half-saturation constant; for species i; k_i: rate constant for species i. Reaction parameters' were selected based on Molins et al. (2010) and Sihota and Mayer (2012). All additional parameters are provided in (Sihota and Mayer, 2012).. 309

Table A5.1. Results of CO_2 flux measurements and calculated SZNA rates (μmol m^{-2} s^{-1}). P values are provided in brackets. * 312

Table A7.1. Depth distribution of Fisher diversity at the background and source zone locations. 325

Table A7.2. Metabolism represented in the intermediate and abundant community members at the SS using (16S rDNA frequency) : (16S DNA frequency), as represented in Figure 8.3. 326

Table A7.3. Network Properties. 327

Table A7.4. Comparison of modularity attributes for the SS rRNA:rDNA network. 328

Table A7.4. Comparison of modularity attributes for the SS rRNA:rDNA network. 329

List of figures

Figure 2.1. Conceptual model of processes affecting source zone natural attenuation and CO_2 migration at petroleum hydrocarbon contaminated sites. 26

Figure 2.2. Location of oil body, reaction zones, and vadose zone monitoring network along the North Pool transect, Bemidji crude oil spill site, MN. Monitoring well numbers are indicated above ground surface. 27

Figure 2.3. (A) Well locations and associated surficial CO_2-efflux (TSR = total soil respiration) along the North Pool Transect. (B) Corresponding vadose zone CO_2 concentration contours. 28

Figure 3.1. Conceptual model of contamination in the vadose zone at the Bemidji site. 60

Figure 3.2. Cross section of vadose zone gas composition (August, 2009) along the North pool transect at the Bemidji site. (a) O_2, (b) CH_4, (c) CO_2, (d) Ar, (e) N_2. 61

Figure 3.3. Cross section of vadose zone $\delta^{13}CO_2$ composition (August, 2009). 62

Figure 3.4. Cross section of pMC in vadose zone CO_2 along the North pool transect at the Bemidji site (August, 2009). Circled values show pMC measurements. 63

Figure 3.5. CO_2 effluxes above the North Pool transect at the Bemidji site (J_{CO2} = total measured surficial CO_2 efflux, J_{CSR}^{BGC} = CO_2 efflux related to contaminant degradation, J_{CO2} corrected for background soil respiration, J_{CSR}^{14C} = CO_2 efflux related to contaminant degradation, J_{CO2} corrected using radiocarbon data from shallow monitoring points. 64

Figure 3.6. Simulated and measured partial pressures at well 9017: a) CO_2, O_2, and CH_4 b) Ar and N_2. Grey shaded area delineates extent of low K layer. 65

Figure 3.7. Simulated reaction rates at well 9017: a) CO_2 production from soil respiration (NSR), aerobic and anaerobic CO_2 production (CSR), and anaerobic CH_4 production (CSR) b) CH_4 oxidation. Grey shaded area delineates extent of low K layer. 66

Figure 3.8. Simulated gas fluxes at well 9017: a) O_2, b) $^{12}CH_4$, c) $^{13}CH_4$, d) $^{12}CO_2$, e) $^{13}CO_2$ and F) $^{14}CO_2$. Grey shaded area delineates extent of low K layer. 67

Figure 3.9. Simulated and measured isotopic profiles at well 9017: a) $\delta\ ^{13}CH_4$ b) $\delta\ ^{13}CO_2$ and c) pMC. Grey shaded area delineates extent of low K layer. 68

Figure 4.1. Plan view of the Bemidji site showing surface topography, locations of the oil body (grey shading), pipelines (dark lines), wells and sample sites, and direction of groundwater flow (arrow). Site 1a is located 177 m upgradient from site 4. The coordinate system is NAD 1983 UTM Zone 15N. 86

Figure 4.2. Conceptual model of methane generation and oxidation in the unsaturated zone above the light non-aqueous phase liquid (LNAPL) (modified from Sihota et al., 2011). 87

Figure 4.3. Reactive gases, methane and oxygen, by volume in the unsaturated zone measured in September 2009 plotted against relative depth from land surface (0) to water table (1) at (a) well 9017G (near site 4) and (b) well 534G (near site 5). 88

Figure 4.4. CO_2 effluxes with standard deviations based on three measurements on June 14, 2011. Well 534G data was taken near site 5, 6.7 m away (Figure 4.1). 89

Figure 4.5. Microbial concentrations of aerobic methanotrophs at sites 2-4 as determined by qPCR using pmoA primers sets plotted against relative depth from land surface (0) to water table (1). 90

Figure 4.6. Maximum microbial concentrations of methanogens above the water table at sites 2-5 as determined by qPCR. Dashed line represents minimum detection limit. 91

Figure 4.7. Average n-alkylcyclohexane peak heights normalized to triC23 measured in two oily sediment samples taken just above and below the water table at each of the contaminated sites along with an archived sample of pre-spill Bemidji oil. 92

Figure 5.1. Conceptual overview of the vadose zone at the Bemidji site. Textured zone shows extent of an area of reduced hydraulic conductivity between ~ 428 and 430 m NAVD88. 'Affected' refers to wells affected by the residual oil (Sihota et al., 2011). 114

Figure 5.2. Seasonal variations in total surficial CO_2 efflux above the North Oil Pool. Locations of gas wells are identified on the upper x-axis. 114

Figure 5.3. Seasonal variations in fraction of CSR and estimates of SZNA using the background correction method above the North Oil Pool. A) total and natural CO_2 fluxes, B) measured and modeled contaminant soil respiration, and C) fraction of natural and contaminant related CO_2 flux. Error bars represent standard deviations on the measurements. 115

Figure 5.4. Soil temperature in the source zone [° C]. Circles represent measurement locations. 116

Figure 5.5. Seasonal variations in the extent of the surficial footprint of biodegradation above the North Oil Pool measured in 2011. Contour intervals show differences from background flux values in A) June 2011, B) October 2011, C) November 2011, D) December 2011, E) January 2012, and F) December 2012. 117

Figure 5.6. Composition of the vadose zone gases in the North Oil Pool in June 2011. Gas concentrations in % v/v for A) CH_4, B) O_2, C) CO_2, D) Ar, and E) N_2. 118

Figure 5.7. Seasonal variations in gas composition at the source zone well 9015G. Gas concentrations in % v/v for A) CH_4, B) O_2, and C) CO_2. 119

Figure 5.8. Seasonal variations in gas composition at the plume zone well 534G. Gas concentrations in % v/v for A) CH_4, B) O_2, and C) CO_2. 120

Figure 5.9. Seasonal changes in precipitation and soil water contents. A) daily precipitation and B) volumetric water content in the source zone..... 121

Figure 5.10. Field data supporting conceptual model of vadose zone processes at the Bemidji site. A) total and natural soil respiration, B) volumetric water content [cm^3 cm^{-3}], C) vadose zone CO_2 concentrations, and D) vadose zone temperatures. Grey box shows inset of volumetric water content measurement locations on vadose zone CO_2 concentrations. Hashed lines show periods where volumetric water content is underestimated based on frozen soil conditions..... 122

Figure 5.11. Scenario 1 simulation results. A) vadose zone O_2 concentration, B) vadose zone CH_4 concentration, and C) surficial CO_2 flux and vadose zone CO_2 concentration. Gas concentrations shown in % v/v. Grey rectangle shows extent of low permeability layer. . 123

Figure 5.12. Scenario 2 simulation results. A) vadose zone O_2 concentration, B) vadose zone CH_4 concentration, and C) surficial CO_2 flux and vadose zone CO_2 concentration. Gas concentrations shown in % v/v. Grey rectangle shows extent of low permeability layer. . 124

Figure 5.13. Scenario 3 simulation results. A) vadose zone O_2 concentration, B) vadose zone CH_4 concentration, and C) surficial CO_2 flux and vadose zone CO_2 concentration. Gas concentrations shown in % v/v. Grey rectangle shows extent of low permeability layer. . 125

Figure 6.1. Conceptual model of radiocarbon and CO_2 in a NAPL containing vadose zone. 148

Figure 6.2. Overview of the study site with sampling locations (Background: measurement locations used for BGC; SNZA: measurement locations used for SZNA rate estimates). Dashed line shows extent of 2013 smear zone excavation. Grey regions shows extent of

smear zone. Blue arrows show regional groundwater flow directions. Yellow line shows extent of barrier wall. Green and tan shapes show outlines of historical releases and site buildings, respectively. 149

Figure 6.3. Results of CO_2 flux measurements conducted for the HR-BGC dataset. A) Distribution of total CO_2 fluxes, B) Distribution of SZNA rates calculated using the BGC. Dashed lines show 'hotspot' regions of SZNA..... 150

Figure 6.4. Comparison of SZNA rates obtained for the HR-BGC dataset based on random data subsets. 151

Figure 6.5. Results of CO_2 flux measurements conducted for the MR-RCC dataset. A) Distribution of total CO_2 fluxes, B) Distribution of SZNA rates calculated using the BGC, C) Distribution of SZNA rates calculated using the RCC. 152

Figure 6.6. Comparison of SZNA rates obtained for the MR-RCC dataset obtained for the BGC and RCC fluxes. Error bars represent average standard error for the measurements. 153

Figure 7.1. Conceptual model of SZNA at sites impacted by EtOH blended fuel. 187

Figure 7.2. Plan view of Balaton site. Squares identify locations of monitoring wells, soil borings and vapour points used to delineate the ethanol and CH_4 containing zones (>1,000 ppb CH_4 contour shown (Spalding et al., 2011)). 188

Figure 7.3. Plan view of Cambria site. Squares identify locations of monitoring wells, soil borings and vapour points used to delineate the ethanol and CH_4 containing zones (>1,000 ppb CH_4 contour shown (Spalding et al., 2011)). Crosses identify locations of monitoring wells. Black circles identify locations of gas collection chambers..... 189

Figure 7.4. Distribution of measured gas effluxes [μmol m^{-2} s^{-1}] at the Balaton site. Small black circles denote measurement locations. Green squares denote measurement locations used to

define background conditions. a) CO_2, b) CH_4, and c) total carbon efflux, black dashed line denotes the extent of the delineated source zone. 190

Figure 7.5. Distribution of gas effluxes [μmol m^{-2} s^{-1}] calculated for the Cambria site. Small black circles denote measurement locations. Green squares denote measurement locations used to define background conditions. a) CO_2 and b) CH_4 and c) total carbon efflux, black dashed line denotes the extent of the delineated source zone. 191

Figure 7.6. Example of data used in estimation of gas fluxes at the Cambria site. a) diffusive regime and b) ebullitive regime. 192

Figure 7.7. Comparison of CH_4 content in reported by the CRDC in the field and CH_4 content determined by GC analysis of samples collected from the chamber headspace. Error bars for GC analyses represent 5% error, based on reproducibility of replicate standard material. 193

Figure 7.8. Simulated vadose zone gas profiles for Balaton scenario under quasi-steady state conditions, a) O_2, CH_4 and CO_2, b) CH_4 oxidation rate, c) Ar and N_2 193

Figure 7.9. Simulated vadose zone gas profiles for Cambria scenario under quasi-steady state conditions, a) O_2, CH_4 and CO_2, b) CH_4 oxidation rate, c) Ar and N_2. 194

Figure 7.10. Simulated vadose zone gas fluxes for Balaton scenario under quasi-steady state conditions, a) O_2, b) CH_4, and c) CO_2. 194

Figure 7.11. Simulated vadose zone gas fluxes for Cambria scenario under quasi-steady state conditions, a) O_2, b) CH_4, and c) CO_2. 195

Figure 8.1. Site layout. A) Distribution of DFE at the field site and locations of reference site (RS) and source site (SS) core collection. B) Depths of sample locations at the RS and SS and EtOH concentrations measured in core collected adjacent to the SS; colors show cluster zones. 209

Figure 8.2. Microbial community distribution at the SS. Distribution of A) rare, B) intermediate and C) abundant biosphere. Relationships between frequencies of 16S rRNA and 16S rDNA OTUs defined in the pyrosequence dataset at the SS. Euler circles show OTUs shared between the RS rDNA dataset and the fraction of the SS represented in associated scatterplots. Dashed lines represent 1:1 relationships..... 210

Figure 8.3. Active microbial community members at the SS. Distribution of taxa and traits mapped to the soil profile for the intermediate and abundant active microbial categories at the SS. Spark line shows EtOH concentration; filled triangle shows approx. location of the water table..... 210

Figure 8.4. Activity network. Network of active community members identified based on interactions between OTUs at the SS. Distribution of OTUs within A) soil zones, B) microbial community categories, C) phylogenetic mappings, and D) conceptual model of bioenergetic cycling and community interactions in perturbed ecosystems. Nodes are sized to closeness centrality. 211

Figure 9.1. Locations of the study sites. 230

Figure 9.2. Bemidji site. A) Key characteristics, B) total carbon losses and delineated source zone. Black circles show measurement locations. Boxes denote locations used in calculating background soil CO_2 effluxes. Dashed lines denote source zone area identified with surficial gas effluxes. 231

Figure 9.3. Cass Lake site. A) Key characteristics, B) total carbon losses and delineated source zone. Black circles show measurement locations. Boxes denote locations used in calculating background soil CO_2 effluxes. Dashed lines denote source zone area identified with surficial gas effluxes. 232

Figure 9.4. Balaton site. A) Key characteristics, B) total carbon losses and delineated source zone. Black circles show measurement locations. Boxes denote locations used in calculating background soil CO_2 effluxes. Dashed lines denote source zone area identified with surficial gas effluxes. White dashed lines indicate area where CH_4 effluxes were present at the time of measurement (modified from Sihota et al., 2013). 233

Figure 9.5. Cambria site. A) Key characteristics, B) total carbon losses and delineated source zone. Black circles show measurement locations. Boxes denote locations used in calculating background soil CO_2 effluxes. Dashed lines denote source zone area identified with surficial gas effluxes. White dashed lines indicate area where CH_4 effluxes were present at the time of measurement (modified from Sihota et al., 2013). 234

Figure A1.1. Observed CO2 efflux and precipitation near well 9017, August 19, 2009 288

Figure A1.2. Observed CO2 efflux and precipitation near well 601, August 15, 2009 289

Figure A1.3. Observed CO2 efflux and precipitation near well 601, August 16, 2009 289

Figure A1.4. Observed CO2 efflux and precipitation near well 310, August 18, 2009 290

Figure A1.5. Observed CO2 efflux and precipitation near well 534, August 13, 2009 291

Figure A1.6. Observed CO_2 efflux and precipitation near well 530, August 20, 2009 291

Figure A1.7. Observed vadose zone CH_4 concentration contours along the North Pool Transect. 295

Figure A1.8. Observed vadose zone O2-concentration contours along the North Pool Transect. 295

Figure A5.1. Distribution of parameter values used in correlation analyses. 313

Figure A5.2. Areas used in point-based SZNA mass loss calculations for the HR-BGC dataset (BGC method). Panels A and B show gridded areas for the complete and BGC data, respectively. 314

Figure A5.3. Areas used in point-based SZNA mass loss calculations for the MR-RCC dataset. Panels A, B and C show gridded areas for the complete, BGC, and RCC data, respectively. 315

Figure A5.4. Probability density of average SZNA rate over 10,000 iterations for the HR-BGC, MR-BGC, and MR-RCC. 316

Figure A6.1. Conceptual diagram of instrumentation used for real time measurement of CO_2 and CH_4 effluxes. 318

Figure A6.2. Comparison of CO_2 effluxes calculated using the IRGA and CRDS instruments under laboratory conditions. 318

Figure A6.3. Comparison of CO_2 effluxes calculated for the IRGA and CRDS instruments under field conditions. a) Balaton site. b) Cambria site. 319

Figure A6.4. Conceptual diagram of custom-designed gas collection chamber, used to evaluate the potential for accumulation of CH_4 and CO_2 in confined spaces. 320

Figure A7.1. Rarefaction curves for 16S rDNA and 16S rDNA OTUs defined in the pyrosequence dataset for the RS and SS. 331

Figure A7.2. Relationships between frequencies of 16S rRNA and 16S rDNA OTUs defined in the pyrosequence dataset at the SS. The points are paired 16S rRNA and rDNA frequencies for each OTUs. Colors represent OTUs in the VZ, CF, and SZ clusters, respectively. The dotted line is the 1:1 line. 332

Figure A7.3. Distribution and activity of microbial community composition at the RS and SS. A) Comparison of percentage of shared OTUs. B) Abundant and active community groupings at the RS (left-hand side) and SS (right-hand side). 333

Figure A7.4. Network of communities identified based on interactions between OTUs identified in the rDNA dataset at the SS. Distribution of OTUs within A) soil zones, B) microbial community categories, and C) phylogenetic mappings. Nodes are sized to rRNA:rDNA ratio with non-active OTUs assigned a size of 1. 334

Figure A7.5. Network of communities identified based on interactions between OTUs identified in the rRNA dataset at the SS. Distribution of OTUs within A) soil zones, B) microbial community categories, and C) phylogenetic mappings. Nodes are sized to rRNA counts. 335

List of acronyms.

Acronym	Definition
ATM	Atmosphere
BGC	Background correction
BLAST	Basic Local Alignment Tool
BTEX	Benzene, ethyl benzene, toluene, xylene
cDNA	Complementary DNA
CGM	Concentration gradient method (based on Fick's law)
CRDS	Cavity ring down spectroscopy
CSR	Contaminant-related soil respiration. Defined here as contaminant mineralization (Sihota et al., 2011)
CZ	Capillary zone
D_0	Free air diffusion coefficient [$m^2 s^{-1}$]
DCC	Dynamic closed chamber
DCM	Dichloromethane
D_{eff}	Effective diffusion coefficient [$m^2 s^{-1}$]
DFE	Denatured fuel-grade ethanol
EtOH	Ethanol
F_{CSR}	Fraction of contaminant soil respiration
F_{NSR}	Fraction of natural soil respiration
F_{TSR}	Fraction of total soil respiration
GC	Gas chromatograph
GCMS	Gas chromatography mass spectrometry
HR-BGC	High resolution – background corrected
IRGA	Infra red gas analyzer
J	Flux
J_{CSR}^{BGC}	Estimated CO_2 efflux attributable to contaminant degradation using background correction [$\mu mol\ m^{-2}\ s^{-1}$]
J_{CSR}^{14C}	Estimated CO_2 efflux attributable to contaminant degradation using 14C correction [$\mu mol\ m^{-2}\ s^{-1}$]
J_{CSR}^{CGM}	Effluxes using the concentration gradient method [$\mu mol\ m^{-2}\ s^{-1}$]
K	Permeability
LEL	Lower explosive limit
LIF	Laser-induced fluorescence
LNAPL	Light non-aqueous phase liquids
MASL	Meters above sea level
MBGS	Meters below ground surface
MLGMW	Multilevel gas monitoring well
MN	Minnesota
MNA	Monitored natural attenuation
MPCA	Minnesota Pollution Control Agency

MPN	Most probably number
MR-BGC	Medium resolution – background corrected
MR-RCC	Medium resolution – radiocarbon corrected
NA	Natural attenuation
NAPL	Non-aqueous phase liquid
NOSAMS	National Ocean Sciences Accelerator Mass Spectrometry
NSR	Natural soil respiration
OTU	Operational taxonomic units
PHC	Petroleum hydrocarbon compounds
pMC	Percent modern carbon
Q_{10}	Temperature coefficient is a measure of the rate of change of a biological or chemical system as a consequence of increasing the temperature by 10 °C
QIIME	Quantitative Insights Into Microbial Ecology
qPCR	Quantitative real-time polymerase chain reaction
R_{10}	Rate coefficient at 10 °C
RCC	Radiocarbon correction
rDNA	Ribosomal genes
rRNA	Ribosomal RNA
RS	Reference site
Sg	Soil gas saturation
SS	Source site
Soils	For the purposes of this work, soils are referred to as the sediment below the organic horizon
SVI	Soil vapor intrusion
SZ	Source zone
SZNA	Source zone natural attenuation, i.e. Attenuation processes taking place in regions of the vadose zone and capillary fringe that contain LNAPL
TCD	Thermal conductivity detector
TDR	Time-domain reflectometry
TEA	Terminal electron acceptor
TPH	Total petroleum hydrocarbon
TSR	Total soil respiration
USGS	United States Geological Survey
v/v %	Percent by volume
VFA	Volatile fatty acid
VPDB	Vienna pee dee belemnite
VZ	Vadose zone
WHOI	Woods Hole Oceanographic Institute

Acknowledgements

Firstly, I owe particular thanks to Dr. K.U. Mayer for his unending patience, guidance and encouragement. Secondly, I sincerely thank both Karen Lillos and Paul Sihota for the their support. I would also like to thank Joel Atwater and Judah Chen, whose assistance ensured the smooth operations of both field and laboratory experiments. At the US Geological Survey, I would like to offer my sincere thanks to the researchers involved in the Bemidji project, particularly Jared Trost, Andrew Berg, John Greene, Mindy Erickson, Barbara Bekins, Geoff Delin, Brent Mason, Isabelle Cozarelli, and Jeanne Jaeschke. At the Minnesota Pollution Control Agency, I would like to thank Mark Toso, Adam Sekely, and Tom Higgins. At Chevron, I would like to thank Tim Buscheck and Mark Lyverse. At TriHydro, I would like to thank Paul Michalski, Alysha Hakala and Ben McAlexander. At UBC, I would like thank Dr. R. Beckie and Dr. A. Black for serving on my supervisory committee and Dr. S. Hallam and Dr. K. Chan for welcoming me into their research groups and for their ongoing support and encouragement.

Funding for this work was provided through support from Chevron, the Natural Sciences and Engineering Research Council (NSERC) of Canada through a Discovery Grant (DG), a Discovery Accelerator Supplement (DAS) Award, and a Research Tools and Instrument (RTI) Grant, and a Strategic Project Grant (SPG) held by DR. Mayer and a PGS-D scholarship held by N. Sihota. Additional funding for instrumentation was provided through the Leaders Opportunity Fund (LOF) of the Canada Foundation for Innovation (CFI), through a grant awarded to DR. Mayer Support for I. was also provided through a Four Year Fellowship awarded by UBC.

Chapter 1: Introduction

Motivation, literature review and issues to address

Since the middle of the 19th Century, our unparalleled economic expansion has led to the widespread extraction, refining, and transport of hydrocarbon resources. The recognition of environmental contamination, as a consequence of accidental hydrocarbon releases and historical disposal practices, has highlighted the issue of how to best assess, manage, and remediate contaminated sites. Indeed, despite decades of research, these questions remain challenging due particularly to complex interactions amongst release characteristics (e.g., local geology, microbiology, climate, and contaminant composition). Moreover, as a consequence of the shift towards biofuels, increased transport of neat ethanol (EtOH) and EtOH-hydrocarbon blends has enhanced the reality of large-scale EtOH-blended fuel releases. The question then arises as to the extent to which emerging fuel blends present unique challenges for release site investigation and management.

Naturally occurring microbial consortia can, in most cases, metabolize contaminants *in-situ* to produce benign end-products such as CO_2 (Lundegard and Johnson, 2006). Indeed, source zone natural attenuation (SZNA) has become an academically and publicly acceptable management option (Mulligan and Yong, 2004; ITRC, 2009)). However, to justify the application of SZNA, a quantitative understanding of the spatial extent and rate of biodegradation is important for constraining estimates of source zone longevity and informing best management practices (Johnson et al., 2006; Lundegard and Johnson, 2006).

The spatial extent of biodegradation is often determined through a combination of physical, chemical, and isotopic characterization of contaminants and metabolites, as well as the distribution and composition of microbial communities mediating contaminant transformation processes (Conrad et al., 1997; Bekins et al., 1999; Amos et al., 2012). Under field conditions,

data for evaluating SZNA can be collected using direct push technologies (Dietrich and Leven, 2006), such as laser-induced fluorescence (Kram et al., 2001); geophysical techniques (Halihan et al., 2005); soil vapor surveys (Lundegard and Johnson, 2006); soil borings and soil sample collection (Nielsen, 2005); and installation of groundwater monitoring wells followed by groundwater sample collection (Bockelmann et al., 2003). However, while these approaches provide valuable data on subsurface contamination, the associated costs can preclude high-resolution temporal or spatial sampling, presenting additional challenges for characterizing subsurface contamination – especially at large sites with heterogeneous source distributions (e.g., former refineries) or for highly mobile contaminants (e.g., EtOH-blended fuels).

To understand the potential for applying SZNA as a management option, the rate and spatial extent of biodegradation must be understood. SZNA rates are often measured under laboratory conditions, using respiration tests (e.g., correlating CO_2 generation to contaminant mass loss (Hinchee and Ong, 1992) and isotopic fractionation (Mancini et al., 2003), or *in-situ* through installation of vadose and saturated zone monitoring wells followed by sampling and analyses of electron acceptors and reaction end products (e.g., O_2 and CO_2, respectively (Lundegard and Johnson, 2006)). However, similar to methods for spatial characterization, measurement of biodegradation rates can be expensive and time consuming.

While there are limitations associated with evaluating SZNA at sites impacted by traditional fuel blends (i.e., gasoline and crude oil), characterization of SZNA under scenarios of EtOH-blended fuel release pose even more significant challenges, as degradation processes may be initially inhibited (Spalding et al., 2010) due to the toxicity of highly concentrated EtOH to microbial populations (Nelson et al., 2010). However, due to EtOH's highly labile nature (when present at concentrations below the toxicity threshold (Powers et al., 2001; Gomez and Alvarez,

2010)) it can be expected to undergo very rapid degradation – potentially leading to persistent anaerobic conditions and CH_4 releases at the ground surface.

At a crude oil contaminated aquifer near Bemidji, MN, Molins et al. (2010) demonstrated that the majority of the gas produced from contaminant destruction reported to the ground surface as CO_2. This work revealed the potential for using surficial CO_2 flux measurements as a measure of the depth- and terminal electron acceptor integrated rate of SZNA. However, at sites where degradation rates are high and/or conditions favor advective transport, CH_4 fluxes, in addition to CO_2 fluxes, must be measured to provide a depth- and terminal electron acceptor integrated measure of SZNA. Indeed, CH_4 emissions have previously been measured in natural and anthropogenically impacted environments, including bogs and wetlands (Baird et al., 2004; Guimbaud et al., 2011), and landfills (Mosher et al., 1999; Lohila et al., 2007). However, the use of CH_4 flux measurements for evaluating SZNA at fuel spill sites has not previously been tested.

In addition to characterizing the composition of the gas emissions for quantifying SZNA rates, there is a need to understand how the magnitude of these emissions vary over time, particularly with respect to seasonal variations in environmental parameters. It is well understood, for example, that natural soil respiration exhibits seasonal variations (Hanson et al., 2000), suggesting that contaminant respiration may also vary on a seasonal basis. Indeed, the factors that affect the seasonal cycles in natural systems (particularly soil moisture and temperature (Hawley and Altizer, 2011; Conant et al., 2011; Suseela et al., 2012) are also known to impact contaminant respiration (Brakstad, 2008; Bagi et al., 2014) further suggesting the importance of research into the seasonality of SZNA rates.

Mechanistically, the use of surficial flux measurements for evaluating the spatial and temporal distributions of SZNA is attractive as chamber methods for conducting gas flux

measurements have been well-tested and documented in the literature (Jassal et al., 2012). Moreover, the approach is relatively straightforward, rapid, and cost effective in comparison to many of the traditional means for evaluating SZNA, many of which require specially trained staff and complex instrumentation. However, to provide confidence in the utility of surficial flux measurements for resolving SZNA rates under field conditions, several questions must be addressed. The research described in this work addresses these questions by means of eight research hypotheses, as outlined below. A more complete review of relevant literature associated with each hypothesis is provided in the respective research chapter.

Research goals and hypotheses

The overarching goal of the research conducted in this dissertation is to develop a straightforward, flexible, and cost-effective toolbox for rapid evaluation of SZNA under field conditions. At the outset this was phrased as the research question:

Can the measurement of surficial gas fluxes be used as an integrated representation of SZNA processes at sites impacted by hydrocarbons releases?

To achieve the overarching goal and address this research question, research proceeded by investigating each of the following eight hypotheses:

1. Based on the CO_2 generated from contaminant respiration, the extent and rate of source zone natural attenuation can be delineated using measurements of CO_2 fluxes at the ground surface;
2. Based on the differences in the age between carbon in recent contact with the atmosphere and carbon held in hydrocarbon compounds, radioisotopic (^{14}C) measurements can provide a constraint on the magnitude of natural soil respiration;

3. Based on the agreement between mass loss estimates obtained from CO_2 fluxes and other measures of contaminant mass loss, CO_2 flux measurements will compare reasonably well to other methods for measurement of microbial activity;
4. Based on the sensitivity of microbial respiration to changes in climatic variables (i.e., temperature and moisture availability), seasonal variations in SZNA processes will occur;
5. Based on the ability of CO_2 flux and radiocarbon measurements to delineate the extent and rate of SZNA, a combination of low-cost approaches can be used to assess SZNA processes at large complex sites with heterogeneous contamination distributions (e.g., former refineries);
6. Based on the labile nature of EtOH-blended fuels, substantial CO_2 and possibly also CH_4 emissions will occur at EtOH-blended fuel release sites;
7. Based on EtOH's toxicity to microbial populations, the underlying characteristics of the microbial communities will change following catastrophic EtOH exposure;
8. Based on variations between environmental conditions and fuel compounds, differences will exist between the composition and rate of gas emissions at particular sites.

These hypotheses are addressed sequentially in the research chapters described below.

Research overview

In **chapter 2** I described the development of a novel and straightforward method for evaluating the extent and rate of SZNA using CO_2 fluxes at the ground surface under field conditions. This chapter documents a 'proof of concept' study at the highly investigated Bemidji crude oil spill research site. In **chapter 3**, I expand upon the work documented in **chapter 2** and further investigate the suitability of the method through inclusion of radiocarbon data and reactive transport simulations. In **chapter 4**, I contributed to a comparison of methods for investigating

microbial activity at the Bemidji site through collaboration with USGS researchers, further testing the validity of the method developed in **chapter 2**. In **chapter 5**, I evaluated seasonal effects on SZNA processes likely to affect measurement of SZNA rates and discuss the implications for estimating average annual mass loss rates using the surficial CO_2 flux method. In **chapter 6**, I investigated the utility of the method developed in **chapters 2 and 3** for site investigation at a large-scale former refinery. In this study, CO_2 flux measurements were paired with radiocarbon measurements, enabling a thorough assessment of the tradeoffs between a radiocarbon and background correction for natural soil respiration at a site with heterogeneous contamination. In **chapter 7**, I extend the approach developed in **chapter 2** through integration of a laser based CH_4 analyzer for concurrent measurement of CO_2 and CH_4 fluxes. The augmented system was used to investigate surficial gas fluxes at two denatured fuel-grade ethanol release sites. In **chapter 8**, I investigate the microbial communities mediating the emissions of CO_2 and CH_4 fluxes measured at the Cambria site described in **chapter 7**. In **chapter 9**, I compared and contrasted four of the field sites investigated in the research described in preceding chapters.

Together, these eight chapters aim at providing an in-depth understanding of requirements for a straightforward, flexible, and cost-effective toolbox for rapid evaluation of SZNA under field conditions. Overall, results reveal a suite of approaches suitable for rapid and inexpensive investigation of SZNA for a variety of hydrocarbon-based contaminants and site conditions, and document some of the limitations and considerations for applying combinations of the tools.

Chapter 2: CO_2-efflux measurements for evaluating source zone natural attenuation rates in a petroleum hydrocarbon contaminated aquifer

Introduction

Light non-aqueous phase liquids (LNAPL's), specifically petroleum hydrocarbons, frequently contaminate the vadose zone, yet their distribution is difficult to assess and often remains largely unknown due to sediment heterogeneity and uncertainties regarding the spill history. Challenges with site characterization are compounded by a variety of processes that affect the behavior of hydrocarbon compounds including volatilization, adsorption, and microbially-mediated degradation (Nadim et al., 2000). These characteristics complicate source zone delineation and contaminant remediation (Nadim et al., 2000; Molins et al., 2010). In addition, many traditional remedial methods (e.g. soil vapor extraction) are disruptive, costly, and often ineffective (Nadim et al., 2000).

Monitored Natural Attenuation (MNA) of source zones and contaminant plumes has generated interest due to its relatively low cost and minimization of environmental disturbance (Krupka and Martin, 2001). Demonstration of the occurrence and rate of attenuation is critical in gaining regulatory support (Krupka and Martin, 2001). However, quantification of MNA rates, particularly biodegradation, has remained problematical (Anderson et al., 1998; Molins et al., 2010). A quantitative understanding of these rates can better inform estimates of contaminant destruction and source zone longevity, facilitating identification of best management practices. In the laboratory, respiration tests correlating CO_2 evolution rates to contaminant degradation are common practice (el-Din Sharabi and Bartha, 1993; Schoefs et al., 2004; Kim et al., 2005) and are often supported by isotopic techniques (e.g. el-Din Sharabi and Bartha, 1993; Caldwell et al., 1998). Field methods to determine source zone natural attenuation (SZNA) rates require installation of monitoring and possibly injection wells and involve calculation of soil gas effluxes constrained by measured moisture contents and CO_2 or O_2 concentration gradients

(Revesz et al., 1995; Lundegard and Johnson, 2006; Molins et al., 2010) or vadose zone push-pull tests (Urmann et al., 2005).

Figure 1 depicts a conceptualization of physical and chemical processes affecting the vadose zone carbon balance at hydrocarbon-contaminated sites. Contaminant degradation is influenced by the availability of terminal electron acceptors (TEAs) including O_2, NO_3^-, Mn-oxides, Fe-oxides, and SO_4^{2-}). Biodegradation reactions consume TEAs and result in contaminant decomposition and production of CO_2 (**Figure 2.1**). Hydrocarbon-contaminated source zones often become highly reducing - even in the vadose zone - leading to methanogenic conditions with production of CH_4 in addition to CO_2 (Amos et al., 2005). Due to their low solubility, CO_2 and in particular CH_4 tend to partition into the gas phase and migrate towards the surface by diffusive and advective gas transport (Molins et al., 2010). At sites where atmospheric O_2 ingress results in CH_4 oxidation, carbon loss across the ground surface is dominated by the efflux of CO_2 and CH_4 emissions are insignificant (Czepiel et al., 1996; Molins et al., 2010). Mass transfer of CO_2 to the saturated zone with groundwater recharge and exchange with carbonate minerals may also affect the carbon balance. However, mass balance results from reactive transport modeling of SZNA (all supporting information is provided in **Appendix (A) 1**; **Table A2.1**) indicate that these processes amount to less than 2% of the total carbon turnover. Carbon sequestration by biomass, in contrast, may cause incomplete contaminant mineralization and may affect the carbon balance in a more pronounced manner (Schoefs et al., 2004).

These observations suggest that the CO_2-efflux attributable to contaminant-related soil respiration (CSR) provides a direct measure of contaminant mineralization; actual contaminant biodegradation rates may be higher - if CH_4-efflux and carbon sequestration by biomass are

significant. As a result, CO_2-efflux at the ground surface may serve as a conservative estimate for the depth-integrated contaminant biodegradation rate.

Determination of CSR via CO_2-efflux measurements at hydrocarbon-contaminated sites is complicated by natural soil respiration (NSR), including contributions from plant roots and microbes present in the surficial soil zone (e.g. (Rochette and Eriksen-Hamel, 2008)) (**Figure 2.1**). Dynamic closed chamber (DCC) measurements will capture total soil respiration (TSR) and separation of CSR and NSR processes is required to use CO_2-efflux measurements as a proxy for contaminant degradation rates. This separation may be obtained, if background NSR can be quantified reliably and is significantly lower than TSR in the contaminated region.

Dynamic closed chamber methods have previously been used to precisely and accurately measure soil CO_2-efflux in the fields of ecosystem carbon cycling (Trumbore et al., 1999) and plant respiration (Black et al., 1996) and are able to capture spatial and temporal variability of soil respiration rates (Black et al., 1996; Law et al., 2001; Davidson et al., 2002; Rochette and Eriksen-Hamel, 2008). Kabwe et al. (2002, 2005) applied the DCC method to quantify CO_2-effluxes from a waste rock pile. Similar methods have been used to determine CH_4 and CO_2-effluxes from landfill covers (Czepiel et al., 1996). Application of DCCs to evaluate CO_2-efflux at contaminated sites appears attractive due to availability of reliable and well-tested instruments (Norman et al., 1997); existing knowledge on NSR as a function of soil type, climate and vegetation - measured with the same equipment (Davidson et al., 2002); and the non-invasive nature of the measurement. However, application of this technology to assess the overall depth-integrated rate of biodegradation at hydrocarbon-contaminated sites has not previously been documented.

Our study aims to evaluate the feasibility of using the DCC method as a non-invasive tool for both areal delineation of vadose zone LNAPL contamination and assessment of depth-integrated biodegradation rates at hydrocarbon contaminated sites. Specifically, the objectives of this study include determining if the DCC method provides a practical means to: (1) distinguish between NSR and CSR; (2) delineate the extent of hydrocarbon source zones and regions of active contaminant degradation; and (3) to quantify the depth-integrated rate of hydrocarbon mineralization in contaminated vadose zone sediments.

Site history

The study was conducted at a field site near Bemidji, MN (latitude 47°34'23", longitude 95°05'33"), maintained by the United States Geological Survey (USGS). In 1979, the rupture of an underground pipeline spilled 1,670 m^3 of crude oil over a 6,500 m^2 area of a glacial outwash aquifer. Remediation efforts removed approximately 75% of the oil; about 418 m^3 of the oil accumulated in the vadose zone, and formed three distinct oil bodies. This study focuses on the North Pool, which originally contained between 80,000 and 160,000 L of oil (Chaplin et al., 2002). The oil is held at residual saturation from approximately 1 m below land surface to the water table (6-9 m below ground) where it forms a pool (Dillard et al., 1997). **Figure 2.2** shows a cross-section of the North Pool, and outlines the location of the LNAPL and the geochemical zones that have developed in the aquifer. Previous investigations have demonstrated that a methanogenic region has evolved in the vadose zone, surrounded by a halo of aerobic contaminant degradation and CH_4 oxidation (Amos et al., 2005). The site is characterized by a sandy soil with a thin surfce horizon. Comprehensive site overviews can be found in Dillard et al (1997), Bekins et al. (1999), Chaplin et al. (2002), Amos et al. (2005), and Molins et al. (2010).

Methods

Surficial CO_2-efflux measurements: Real time surficial CO_2-efflux measurements were performed from August 9th-21st, 2009 along the transect shown in **Figure 2.2**. DCC measurements were conducted with both survey and long-term chambers (LICOR Inc., Lincoln, NE, USA; LI 8100-103 and LI 8100-104, respectively). To minimize the contribution of root respiration and maximize sensitivity to CSR, 10cm of topsoil was removed at each location. Subsequently, polyvinyl chloride (PVC) collars (20 cm ID) were inserted so that 4 cm remained above ground surface. All collars were located within a 1m radius of an existing vadose zone multilevel gas monitoring well (MLGMW) (**Figure 2.2**). After collar insertion, approximately 72 hours elapsed prior to initial data collection to allow re-stabilization of the CO_2-efflux (Law et al., 2001). To confirm that the CH_4-efflux is negligible at the site, gas samples were also collected by capping the collars and using a gas-tight syringe to remove a sample from a septum secured into the cap; samples were analyzed via gas chromatography (method described below).

The spatial distribution of the CO_2-efflux along the transect was established by conducting survey DCC measurements near all MLGMWs (**Figure 2.2**). Measurements were also taken at background locations upgradient of the oil spill, directly above the NAPL-containing source zone (as delineated by detailed core analyses (Dillard et al., 1997)); and downgradient of the most contaminated region (**Figure 2.2**). DCC measurements were performed in triplicate over several days at each location. To minimize CO_2 buildup and alteration of concentration gradients, measurement periods were limited to 1.5 minutes (Healy et al., 1996; Davidson et al., 2002). Temporal variability was evaluated at select locations using continuous chamber measurements (over 2-8 hours); locations were selected based on the highest

soil CO_2-effluxes noted during survey sampling (wells 9017 and 601). Continuous measurements were also conducted near background well 310 and downgradient wells 534 and 530 to evaluate temporal variations outside the source area.

For data analysis, sampling locations were placed into two groups: 'affected' and 'unaffected', according to both proximity to residual LNAPL and magnitude of CO_2-efflux deviation from background values (**Figure 2.2**). 'Affected' wells are located where LNAPL remains suspended in the vadose zone, roughly 25 m upgradient and downgradient from the center of the oil body (**Figure 2.2**). 'Affected' wells include: 9017, 9016, 301, 9015, 9014, and 601 (**Figure 2.2**). 'Unaffected' wells include background wells 310, 603 and 604 upgradient of the oil body and the downgradient wells 534, 9103, 533, 9101, 532, 518, 531 and 530.

CO_2-effluxes are reported in the common units of μmol m^{-2} s^{-1} and as g of total petroleum hydrocarbons (TPH) per square meter per day [g TPH m^{-2} day^{-1}]. Following Lundegard and Johnson (2006), TPH was represented by the n-alkane $C_{10}H_{22}$.

Vadose zone gas concentration measurements: To complement CO_2-efflux measurements, gas samples were collected from pre-existing MLGMWs constructed of 6.4 mm OD stainless steel tubing with 10 cm screens (Chaplin et al., 2002; Amos et al., 2005). A total of 17 MLGMWs were sampled; each with 8 sample ports (Hult and Grabbe, 1985). Samples were extracted using a peristaltic pump (GeoPump, Geotech Environmental Equipment Inc. Denver, Co., USA) operated at a flow-rate of 0.5 L min^{-1}; 3 line-volumes of soil gas were purged prior to sample collection via 10cc gas tight syringes (Hamilton Co. Nevada, USA). Compositional analysis of all samples was carried out in the field immediately after collection using a Varian CP-4900 dual channel gas chromatograph, equipped with TCD detectors, a Molsieve 5A PLOT column to

separate Ar, O_2, and N_2 and a PoraPLOT U column to separate CH_4 and CO_2; operating temperatures were 110°C and 50°C, respectively. Helium was the carrier gas (at 50 psi) and calibration and periodic verification was performed with air and 2 calibration gases (Scotty; 9.99% CH_4; 15% CO_2, 5.04% O_2 and 6.49% CO, respectively, balanced with N_2).

Indirect determination of CO_2-effluxes: At selected locations, CO_2-efflux (*J*) was also estimated based on the concentration gradient method (CGM) (Lundegard and Johnson, 2006) using Fick's first law, neglecting advection and reactions:

$$J_{CGM} = D_{eff} \frac{C_s - C_a}{\Delta z} \qquad [1]$$

Here, C_s [mol m^{-3}] is the subsurface concentration; C_a [mol m^{-3}] is the atmospheric concentration; and Δz defines the soil monitoring point depth in relation to ground surface. The CO_2 concentration gradient was estimated from atmospheric concentrations (using the 2008 global annual mean of 385 ppm (NOAA/ESR)) and concentrations from MLGMW (**Figure 2.3**) ports located near the anaerobic/aerobic interface (**Figure 2.2**); chosen to ensure that CO_2 from CH_4-oxidation is captured by J_{CGM}.

Effective diffusion coefficients (D_{eff}) are estimated based on Millington and Quirk, (1961), as a function of porosity (ϕ) and soil gas saturations (S_g).

$$D_{eff} = D_0 S_g^{10/3} \phi^{4/3} \qquad [2]$$

Porosity was assumed constant ($\phi = 0.38$) constrained by soil core analysis (Dillard et al., 1997). The free diffusion coefficient for CO_2 in air (D_0) was defined as 1.64 x 10^{-5} m^2 s^{-1} (Luo and Zhou, 2006) for T = 15 °C, representative for summer soil temperatures in the upper soil

horizons. Where available, water and oil saturations from Bemidji core samples (Chaplin et al., 2002) were used to estimate S_g and calculate D_{eff}.

Results and discussion

Distinction between natural and contaminant-related CO_2-efflux: Maximum CO_2-effluxes of 7.1 and 6.3 μmol m^{-2} s^{-1} were found above the oil body near wells 9017 and 9014, respectively. CO_2-effluxes at the remaining locations directly above the oil body were also significantly higher than at 'unaffected' locations. Smallest effluxes (2.6 and 2.8 μmol m^{-2} s^{-1}) were found at wells 531 and 532, respectively. These values are lower than the efflux measured near background well 310 and other wells distant from the oil body (530 and 603). This suggests that CO_2-effluxes above the groundwater plume and upgradient of the oil spill (**Figure 2.2**) do not show discernable differences from background values. These locations are classified as 'unaffected' from CSR and it is concluded that the corresponding effluxes are NSR-dominated. Locations with substantially elevated CO_2-effluxes are classified as 'affected' and include contributions of CSR (J_{CSR}) and NSR (J_{NSR}). Based on these groupings, first order estimates of the average CO_2-efflux can be obtained for each region, yielding an efflux of 5.9 μmol m^{-2} s^{-1} in the direct vicinity of the oil body ('affected area) and 6.3 μmol m^{-2} s^{-1} in the 'unaffected' region (**Table 2.1**). At well 530, CO_2-efflux is atypical for background locations; however, this may be explained by the proximity to trees (~1-2 m), while remaining measurement points are located on grassland.

Standard deviations for each measurement group are substantially smaller than the differences between CO_2-effluxes at 'affected' and 'unaffected' sampling locations (**Table 2.1**). Additional statistical analysis confirmed both that differences between 'unaffected' and 'affected' locations are significant and that no significant differences exist between upgradient

wells (310, 603, and 604) and downgradient wells (534, 9103, 533, 9101, 532, 518, 531 and 530) in the 'unaffected' region (**Table A1.2, A1**). These results indicate that the magnitude of CSR at the Bemidji site is approximately 80% of NSR, which is sufficiently large to provide a statistically distinguishable efflux signal (**Table A1.2, A1**).

Comparison of results from survey and averaged long-term measurements at the same location show that CO_2-effluxes obtained from the two methods differ slightly (**Table 2.1**). These differences are due to the influence of environmental factors (e.g.: barometric pressure fluctuations and rainfall), which the survey method fails to capture (Savage and Davidson, 2003). However, two sample t-tests performed on the long-term data collected for both regions again yield significant differences between 'affected' and 'unaffected' areas. The complete data set of the continuous measurements is provided in the SI (**Figures A1.1- A1.6**).

A comparison between background effluxes obtained at Bemidji and NSR rates reported in the literature indicate that the measured background values are within the high range expected for this vegetation and soil type (1.0-2.7 μmol m^{-2} s^{-1}, **Table A1.3, A1**). The relatively high values at the Bemidji site can be explained because measurements were performed in August and were restricted to day-time analysis, while NSR rates retrieved from literature were collected over time periods from 18 days to several years.

Figure 2.3 also reveals that the CO_2-efflux cannot be directly correlated to the subsurface CO_2 gradient. This observation highlights that the CO_2-efflux and soil gas gradients are strongly affected by soil texture, water content, and oil content which control S_g and gas phase tortuosity. For example, the gradient is steepest near wells 9015 and 301; however, the largest CO_2-effluxes are associated with wells 9014 and 9017. This is likely due to higher oil and water saturations near wells 9015 and 301, which increases resistance to CO_2 transport.

Delineation of contaminant source zone: Our results demonstrate that CSR and NSR are clearly distinguishable at the Bemidji site and that the region of most significant vadose zone degradation can be identified. There exists a favorable correlation between increased CO_2-effluxes and elevated vadose zone CO_2 concentrations ($P < 0.01$) and a clear relation to regions containing crude oil (as determined by core analysis (Chaplin et al., 2002)) (**Figure 2.3**). Locations where CO_2 concentrations within the vadose zone profile are greater than 15% correspond to sites nearest to the center of the oil body, and also show elevated CO_2-effluxes. Notably, surficial effluxes are not elevated along the entire extent of the floating oil, likely due to horizontal gas migration and more limited biodegradation. This implies that the method is most sensitive to identifying biodegrading NAPL present at shallow to intermediate depths within the vadose zone, conditions often encountered at LNAPL spill sites. In general, depth to water table and the distribution of LNAPL within the vadose zone will likely affect the strength of the signal that can be identified at the ground surface.

Quantification of CO_2-efflux and contaminant mineralization rates: Considering that there are significant and systematic differences between TSR above the oil body ($J_{TSR,}$, 'affected' area) and the upgradient and downgradient regions (J_{NSR}, 'unaffected' area), the efflux related to CSR (J_{CSR}) can be estimated based on the difference between effluxes in the two regions:

$$J_{CSR} = J_{TSR} - J_{NSR} \qquad [3]$$

The average estimated efflux related to CSR is 2.6 μmol m^{-2} s^{-1} (6.3 g TPH m^{-2} day^{-1}). The 95% confidence interval on CSR spans from 1.96 - 6.23 μmol m^{-2} s^{-1} (Table S2, SI) suggesting that the contaminant-related CO_2-efflux was determined with an accuracy of +/- 25% (i.e. 2.59 +/-

0.64 μmol m^{-2} s^{-1}) for this confidence interval. Depth-averaged contaminant mineralization rates can be calculated from surficial CO_2-effluxes assuming an average vadose zone thickness of 7 m (**Figure 2.2**). This results in a depth-averaged SZNA rate of 0.5 g TPH m^{-3} sediment day^{-1}. The average values for J_{CSR} and the SZNA rate were determined using survey measurements only to avoid introducing a bias from the limited number and targeted selection of continuous sampling locations (**Table 2.1**).

Dynamic closed chamber measurements can be compared to calculated effluxes based on the CGM (**Table 2.2**) using CO_2 concentrations measured in 2009 (**Figure 2.3**). As corresponding moisture contents and oil saturations are not available, the parameters required to evaluate D_{eff} were estimated using data from Dillard et al. (2002). Concentration gradient method CO_2-efflux calculations are restricted to wells 301 and 9016, because saturation data are only available at these locations. At well 301, CO_2-efflux is calculated as 6.0 μmol m^{-2} s^{-1} (6.6 g TPH m^{-2} day^{-1}, Table S4, SI). For well 9016, no moisture contents are available for the top 2 m of the vadose zone due to limited core recovery. At this location, CO_2-effluxes are evaluated for a representative S_g ranging from 0.6-0.8 yielding effluxes between 0.9-2.9 μmol m^{-2} s^{-1} (1.1-6.6 g TPH m^{-2} day^{-1}) (**Table A1.4, A1**). Revesz et al. (1995), also applied the CGM to estimate efflux and biodegradation rates at well 301 using an estimated S_g, resulting in an efflux of 6.2 μmol m^{-2} s^{-1} (6.8 g TPH m^{-2} day^{-1}), which coincides well with our more recent result. Furthermore, SZNA rates at other sites determined via the CGM (e.g. Guadalupe (Lundegard and Johnson, 2006)) are of similar magnitude and range from 0.2-2.2 μmol m^{-2} s^{-1} (0.3-2.7 g TPH m^{-2} day^{-1}).

CO_2-effluxes obtained using the CGM are likely dominated by CSR, as indicated by high subsurface CO_2 concentrations which do not occur at background locations (**Figure 2.3**); direct comparison to J_{CSR} is, therefore, appropriate. CO_2-effluxes calculated using the CGM compare

reasonably well with J_{CSR} calculated for wells 301 and 9016 (2.4 and 2.3 μmol m^{-2} s^{-1}, respectively) and the average CSR-associated efflux (2.6 μmol m^{-2} s^{-1}). Calculated CO_2-effluxes can also be compared to those obtained from modeling SZNA at the Bemidji site (Chaplin et al., 2002; Molins et al., 2010). Simulated effluxes range from 1.3-6.6 μmol m^{-2} s^{-1} (1.6-4.4 g TPH m^{-2} day^{-1}). Lower effluxes calculated by Chaplin et al. (2002) in 1985 were obtained for conditions still dominated by volatilization. Overall, comparison to other methods employed at the Bemidji site and other sites indicates that the magnitude of the CO_2-efflux associated with CSR obtained using the DCC method provides a reasonable estimate for SZNA rates per unit area.

Implications for assessing hydrocarbon degradation in the vadose zone: The fact that CO_2-effluxes measured with the DCC method compare favorably both with other measurements at the well-studied Bemidji site and at other field sites, suggest that this method can be effectively used to delineate locations and quantify depth-integrated rates of contaminant mineralization. At sites with limited subsurface information, the method may be appropriate as a reconnaissance tool to identify contamination "hot spots" and to guide additional site characterization efforts. The key requirement is that CO_2-effluxes due to CSR are significantly larger than NSR rates (at least by 25%). Although it remains difficult to determine SZNA rates with high accuracy, the DCC method provides a useful measure of SZNA rates at the Bemidji site. Statistical analyses suggest that CSR could also be positively distinguished from NSR for lower than observed CSR (to ≥ 25% of NSR; **Table A1.2, A1**). The method seems particularly well suited to delineate the LNAPL-containing source zone and is most sensitive to oil suspended in the vadose zone at shallow to intermediate depths. At the fringes of the source zone, where oil is only present as a floating pool on the water table, a distinguishable signal could not be identified.

Equation 3 directly quantifies depth-integrated contaminant mineralization rates and should provide a conservative estimate of contaminant biodegradation rates. The contribution of the CH_4-effluxes and the sequestration of carbon in biomass must be considered in estimating SZNA rates based on CO_2-efflux measurements. At the Bemidji site, the contribution of CH_4 to the total carbon efflux is insignificant. Analysis of vadose zone gas samples from the MLGMWs confirm that CH_4 is oxidized prior to reaching the ground surface (**Figures S7 and S8, SI**). In addition, CH_4 concentrations in samples collected from the capped collars were consistently below detection limits (<10 ppm).

Carbon sequestration by microorganisms may lead to underestimation of depth-integrated SZNA rates. Previous studies suggest that carbon uptake by biomass can be significant (e.g. (Schoefs et al., 2004)); however, others demonstrated that biomass growth is limited under nutrient-depleted conditions (Cherry and Thompson, 1997; Höhener et al., 2006) and that contaminant mineralization commonly reaches values greater than 90% (Edwards et al., 1992; Caldwell et al., 1998) in particular in the presence of a well-established microbial consortium (Semple et al., 2006). Both conditions are present at the Bemidji site (Anderson et al., 1998; Bekins et al., 1999).

Based on these considerations, it can be concluded that the contaminant biodegradation rate at the Bemidji site is estimated adequately by the proposed CO_2-efflux method. This statement holds particularly true because field methods to accurately (e.g. with an error of < 10%) determine SZNA rates over large sediment volumes are not available. Whether this is also the case at other hydrocarbon contaminated sites will have to be determined on a site-specific basis.

Our results confirm the findings reported in Davidson et al. (2002) and suggest that combining survey with continuous DCC measurements can provide a more complete representation of the processes affecting the CO_2-efflux, which may vary substantially in time and space (Kabwe et al., 2005). At the Bemidji site, the duration of the continuous measurements could not be extended; however, future work at other sites will include continuous measurements thereby allowing the investigation of diurnal and seasonal variations associated with atmospheric pressure and temperature effects, as well as water table fluctuations.

This study agrees with the findings of Kabwe et al. (2002) in highlighting difficulties associated with the CGM. As noted above, S_g is an important parameter for evaluating the CO_2-efflux using the CGM, as an increase in S_g leads to increased D_{eff} (e.g. Millington and Quirk, (1961)). However, required information on porosity and soil moisture is often not readily available. If the CGM were used, core collection and detailed analysis for porosity and fluid contents, or installation of instrumentation to measure moisture contents would be required to better constrain efflux calculations. As noted above, these variations likely explain apparent inconsistencies between measured CO_2-effluxes and the steepness of subsurface CO_2 gradients in **Figure 2.6.** In addition, efflux determinations based on the CGM assume no reactions along the diffusion path, not accounting for addition of CO_2 from contaminant degradation or carbon uptake by biomass. Although D_{eff} can be measured directly (Johnson et al., 1998), invasive methods are required. As a result, direct measurement of CO_2-effluxes provides an attractive alternative and may be useful to complement geophysical and/or subsurface-based techniques to identify contaminant source zones and quantify degradation rates. As demonstrated in this study, the measurements of CO_2-effluxes using the DCC method enables real-time determination of CSR at a large number of locations and also provides a technique suitable for transient analysis.

In addition, the method provides an integrated measurement of subsurface processes, and is, therefore, less prone to effects of heterogeneities, which strongly affect point measurements (e.g. CO_2 concentrations and moisture contents).

The method will be further evaluated at the Bemidji site and at other contaminated sites to assess effects of climate, vegetation type, soil conditions, contaminant character, and depth to water table. In addition, we will determine whether stable and radioisotope signatures in CO_2 (suggested by Conrad et al. (1997)) are useful in determining the fraction of CO_2-efflux attributable to CSR.

Tables

Table 2.1. CO_2-efflux measurements taken at the Bemidji field site with LI-COR LI8100 chambers.[1]

		Survey measurements		**Long-term measurements**	
	Well number	Average Efflux [µmol $m^{-2}sec^{-1}$]	Standard Deviation	Average Efflux [µmol $m^{-2}sec^{-1}$]	Standard Deviation
Unaffected - Upgradient (NSR)	**310**	6.25	0.6	2.27	0.4
	603	6.16	0.3		
	604	6.42	0.2		
Affected (TSR)	**9017**	7.12	0.1	7.16	0.7
	9016	5.50	0.6		
	9015	5.21	1.9		
	301	5.65	0.9		
	9014	6.32	0.8		
	601	5.52	0.1	5.73	0.7

[1] Contaminated-related soil respiration rates (CSR) are calculated based on natural soil respiration rates (NSR) measured at background locations and total soil respiration rates (TSR) measured above the LNAPL-contaminated region. All surficial vegetation and soil was removed prior to conducting the measurements, with the exception of the short-term measurements near well 534. Standard deviations for survey measurements are calculated based on three replicates, standard deviations for continuous measurements are calculated based on all data points collected at the specific location.

		Survey measurements		Long-term measurements	
	Well number	Average Efflux [µmol $m^{-2}sec^{-1}$]	Standard Deviation	Average Efflux [µmol $m^{-2}sec^{-1}$]	Standard Deviation
Unaffacted - Downgradient (NSR)	**534**	6.09	0.3	6.00	0.3
	9013	2.88	0.1		
	533	6.82	0.5		
	9101	6.48	0.4		
	532	2.77	0.2		
	518	6.28	0.1		
	531	2.63	0.4		
	530	4.45	0.02	6.42	0.2
Average (NSR)		3.29	0.5		
Average (TSR)		5.89	0.7		
CSR = TSR-NSR		2.59			

Table 2.2. CO_2-efflux due to contaminant-related soil respiration (JCSR), corresponding biodegradation rates per unit surface area, and comparison of results to previous studies at the Bemidji crude oil spill sites and other sites.

	Contaminant-related soil respiration efflux (J_{CSR}) (µmol m^{-2} s^{-1})	**Contaminant degradation rate (g TPH m^{-2} day^{-1})**	**Reference**
CO_2-efflux (Chambers)	2.6	6.3	Present Study
[1]Gradient method (CO_2)	0.9-6.0	1.1-6.6	
Modeled data	1985: 0.12-0.14	1985: 0.14-0.16	Chaplin et al. (2002)
	1997: 1.27-1.50	1997: 1.6-1.9	
Modeled data	6.6	4.4	Molins et al. (2010)
[1]Gradient method (CO_2)	6.2	6.8	Revesz et al. (1995)
Gradient method (O_2)	0.2-2.2	0.3-2.7	Lundegard and Johnson (2006)

[1]calculated for well 301 in center of oil body

Figures

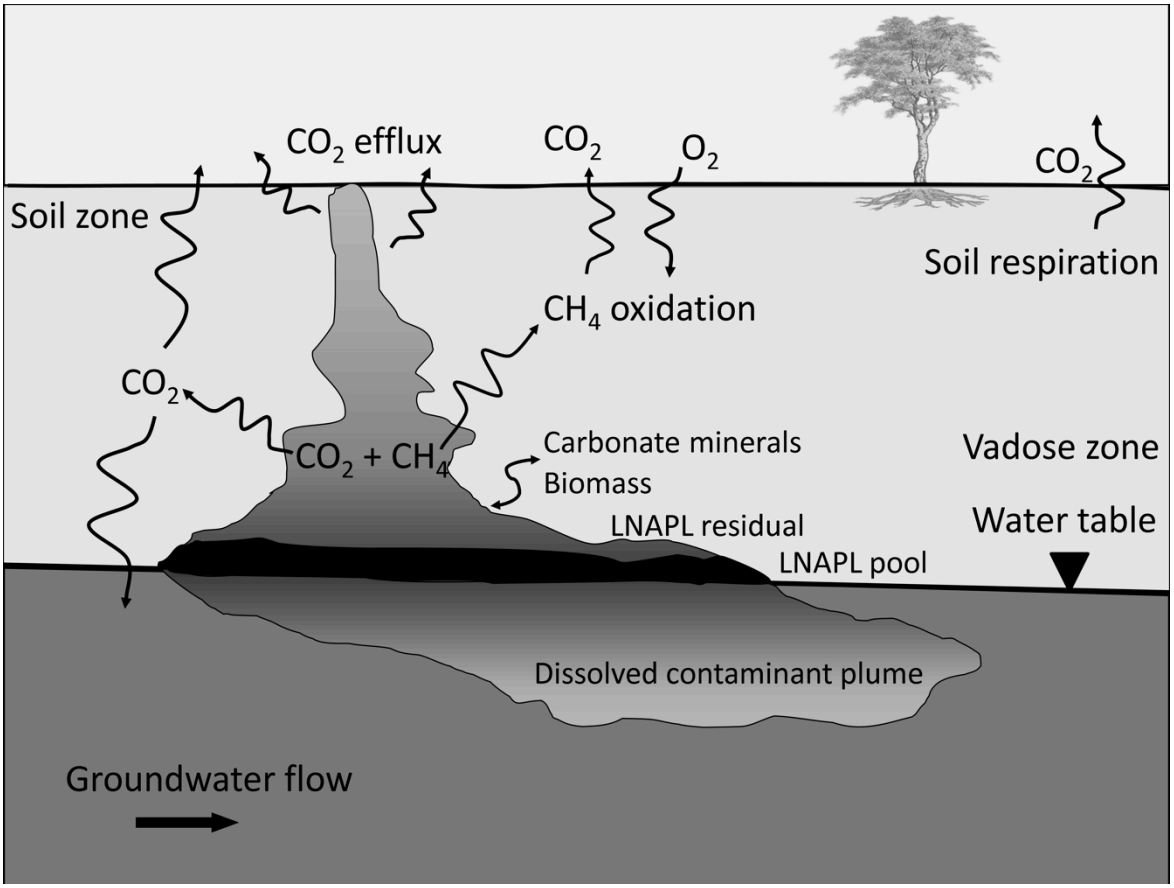

Figure 2.1. Conceptual model of processes affecting source zone natural attenuation and CO_2 migration at petroleum hydrocarbon contaminated sites.

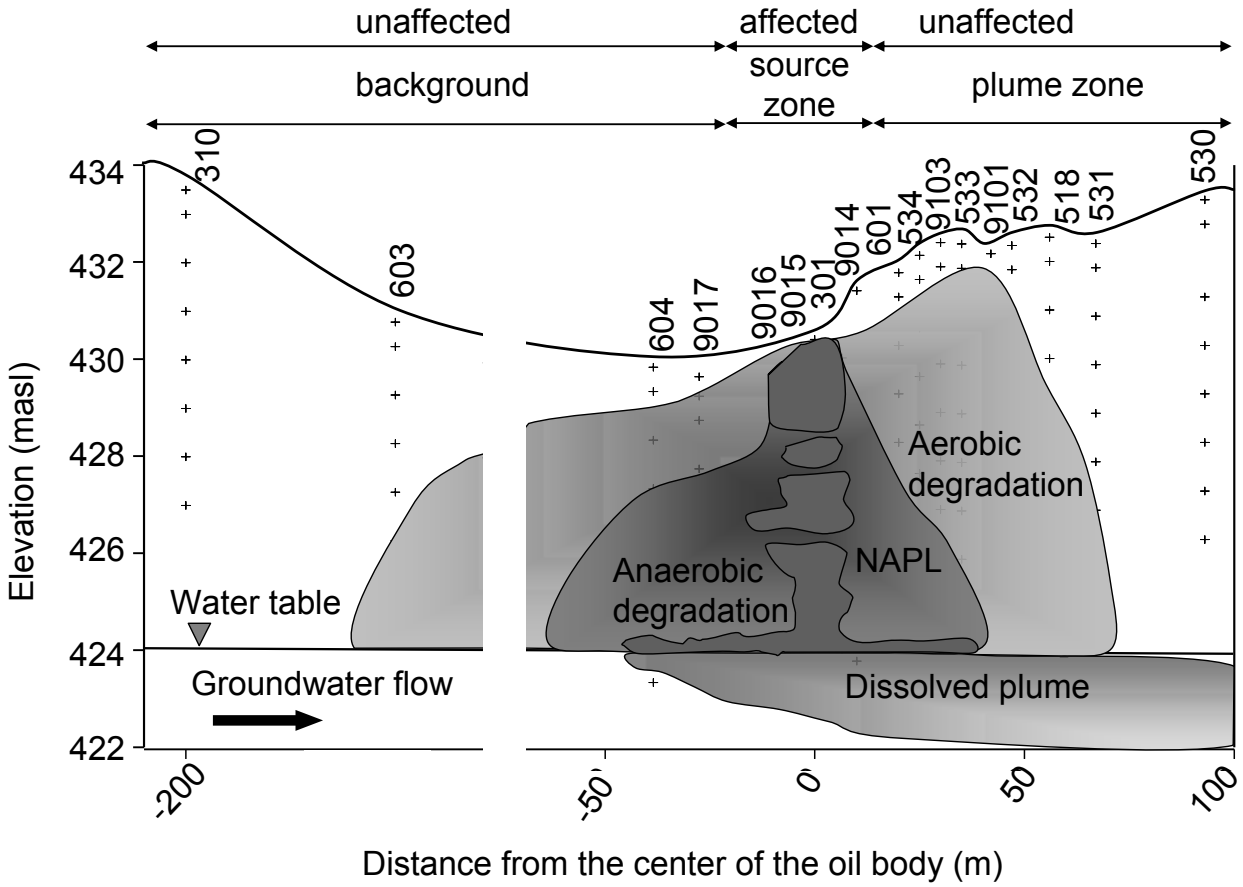

Figure 2.2. Location of oil body, reaction zones, and vadose zone monitoring network along the North Pool transect, Bemidji crude oil spill site, MN. Monitoring well numbers are indicated above ground surface.

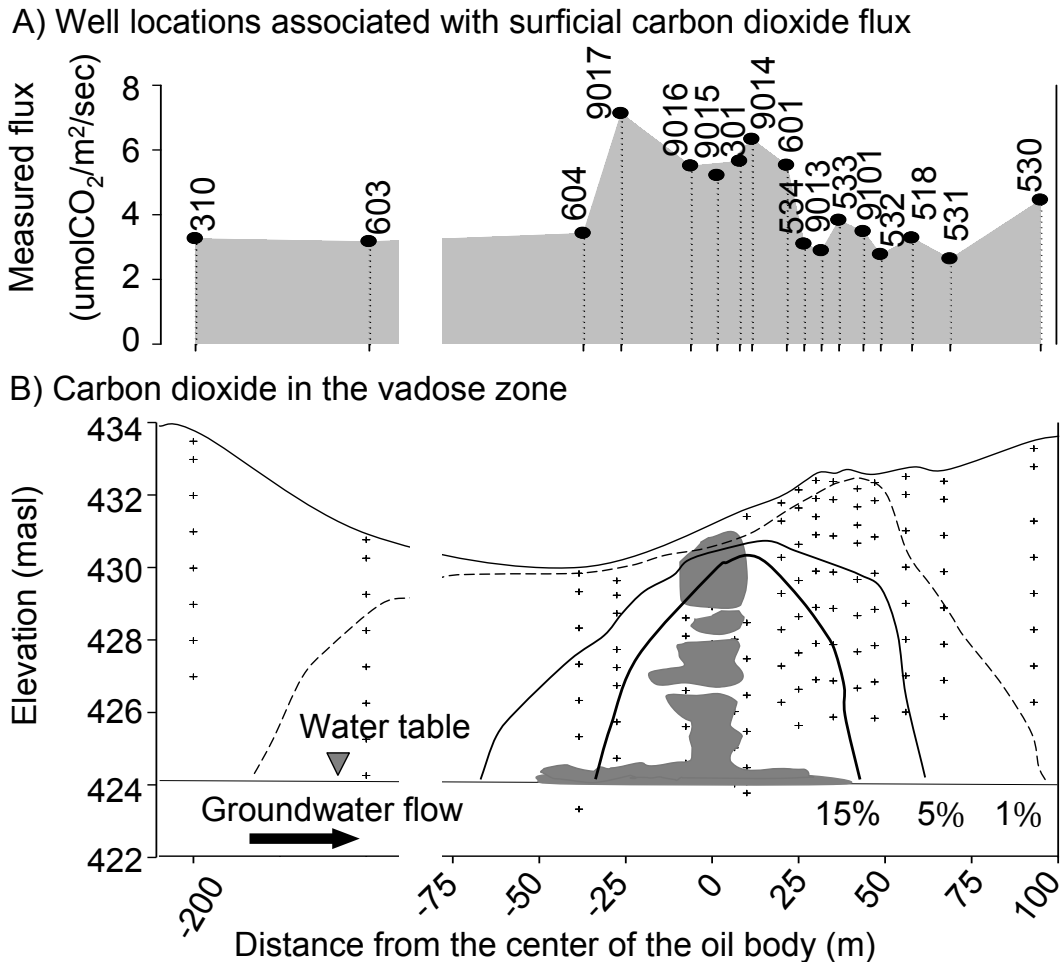

Figure 2.3. (A) Well locations and associated surficial CO_2-efflux (TSR = total soil respiration) along the North Pool Transect. (B) Corresponding vadose zone CO_2 concentration contours.

Chapter 3: Characterizing vadose zone hydrocarbon biodegradation using CO_2-effluxes, isotopes, and reactive transport modeling

Introduction

Petroleum hydrocarbon compounds (PHCs) frequently contaminate the environment as a result of their accidental release or improper disposal. In light of the persistence of PHC source zones (potentially hundreds of years) and toxicity of many PHCs (e.g. benzene), it is important to understand their environmental fate. As the majority of contamination events occur at or near land surface (e.g. surficial spills; pipeline ruptures; leaking underground storage tanks) attenuation processes are often mediated through the vadose zone. Under some conditions, remediation by natural attenuation (NA; microbially-mediated conversion of environmental contaminants into benign end-products (e.g. CO_2)) may be an appropriate management option. NA has become increasingly accepted by industry and regulators (Mulligan and Yong, 2004; Rittmann et al., 2004; Sondermann and Knorpp, 2004). This acceptance, however, may rest on the ability to demonstrate both the occurrence and rate of NA processes.

Several techniques have been developed to evaluate source zone natural attenuation (SZNA), i.e. attenuation processes taking place in regions of the vadose zone and capillary fringe that contain light non-aqueous phase liquids (LNAPLs). These methods include respirometry (Hinchee and Ong, 1992); non-reactive dissolved gas concentration analysis (Revesz et al., 1995); evaluation of microbial populations (Bekins et al., 1999); vadose zone biogenic gas analysis (Lundegard and Johnson, 2006); and isotopic techniques (Conrad et al., 1999; Aelion et al., 2010). Due to site and contaminant complexities, combining several of these techniques may be required (Kirtland et al., 2005). Recently, Sihota et al. (2011) used the measurement of CO_2 effluxes at the ground surface (using a dynamic closed chamber and infrared gas analyzer (LI-COR Inc, Lincoln, NE)) to demonstrate the occurrence and rate of SZNA at a crude oil contaminated aquifer. This method shows promise, and is attractive due to its non-invasive

nature, simplicity, and speed. However to determine the accuracy of the method, it must be evaluated whether CO_2 generated from PHC degradation can be quantitatively separated from other CO_2 sources within the aquifer. Specifically, it is required that the contaminant-derived soil respiration (CSR) can be distinguished from the natural soil respiration (NSR; resulting from degradation of detrital carbon and plant root respiration). To achieve this separation, Sihota et al. (2011) employed a background correction (hereafter the 'background correction method'), whereby the average value of NSR (measured in an area unaffected by PHCs) was subtracted from the total soil respiration measured in the area affected by PHCs. Although a substantial increase in CO_2 efflux was observed above the source zone (Sihota et al., 2011), variability of CO_2 efflux due to NSR is difficult to account for, and the fraction of the CO_2 efflux attributable to CSR is subject to some uncertainty.

Figure 3.1 summarizes the conceptual model for SZNA in petroleum hydrocarbon contaminated source zones. Dissolution and volatilization of hydrocarbon compounds leads to the spreading of the contaminants in the vadose zone. Ingress of atmospheric oxygen causes the aerobic degradation of hydrocarbon compounds, resulting in the production of CO_2. Depending on soil conditions and nature of the contamination, it is possible that O_2 becomes depleted and that anaerobic contaminant degradation occurs, leading to the production of CH_4. In turn, CH_4 will tend to migrate away from the source region and, in many cases, is oxidized by atmospheric O_2 in a halo that surrounds the LNAPL body. Due to its limited solubility, CO_2 gas generated by oil degradation and CH_4 oxidation will tend to migrate toward the ground surface. These processes occur concurrently with naturally occurring root and microbial soil respiration processes in the organic layer, which also produce and release CO_2. To evaluate contaminant

fate, tools capable of quantifying CO_2 sources and sinks and evaluating production and transport processes are needed.

Stable and radioisotopic methods are often used to identify and quantify NA processes (Aelion, 2010). Stable isotopic signatures can provide powerful insight into the relative importance of different reaction mechanisms and pathways (e.g. enzyme systems and electron acceptors), while radioisotopes enable identification of source materials (Conrad et al., 1999). Stable isotopic ratios represent the abundance of the rare isotope with respect to the abundant isotope (e.g. $^{13}C/^{12}C$). For the carbon in CO_2 this is represented as $N^{13}C/N^{12}C$, where $N^{13}C$ and $N^{12}C$ represent the amount of ^{13}C and ^{12}C, respectively (Coplen, 2011). Due to slight analytical variations, it is common to compare isotopic ratios measured in an unknown sample to those in a standard material; this results in the delta notation:

$$\delta^{13}C = \frac{N(^{13}C)_{CO2}/N(^{12}C)_{CO2} - N(^{13}C)_{std}/N(^{12}C)_{std}}{N(^{13}C)_{std}/N(^{12}C)_{std}} \qquad [1]$$

where $\delta^{13}C$ is the difference between the isotopic ratio of the sample and that of the internationally accepted standard material, $N(^{13}C)_{CO2}/$ $N(^{13}C)_{CO2}$ is the isotopic ratio of the unknown CO_2 sample and $N(^{13}C)_{std}/N(^{12}C)_{std}$ is the isotopic ratio of the internationally accepted standard material. A positive $\delta^{13}C$ value indicates that the unknown is more enriched in the amount of the ^{13}C isotope than the standard. A negative $\delta^{13}C$ value indicates that the unknown is depleted in the amount of the ^{13}C isotope, relative to that of the standard.

In contaminant hydrogeology, changes in $\delta^{13}C$ in CO_2 have been used to evaluate dominant NA processes (e.g. methanogenesis) and reaction pathways (e.g. acetate fermentation) (e.g. Suchomel et al., 1990; Aggarwal and Hinchee, 1991; Revesz et al., 1995; Conrad et al., 1997; Conrad et al., 1999). At PHC contaminated sites, stable isotopic analysis takes advantage of the

source composition of PHCs, which are enriched in the more abundant isotope (~ –28 ‰) relative to other aquifer components (e.g. carbonate minerals, $\delta^{13}C$ ~ 0 to –5 ‰, Aelion, 2010) and preferential microbial metabolism of the lighter isotope (due to lower energy costs associated with breaking intra-molecular bonds (Kendall and Caldwell, 1998)). Interpretation of stable isotopic data is, however, often complicated by the influences of multiple reaction pathways (Aelion, 2010). In some cases, analysis of stable isotopic concentrations alone may prove insufficient to quantitatively evaluate NA rates and distinguish NA processes from other controls on the isotopic ratio (i.e. dilution, adsorption and biodegradation of natural organic matter (Aelion, 2010).

Carbon's radioisotope (^{14}C) can be used to identify carbon sources, and distinguish CO_2 produced from CSR from that attributable to NSR (Conrad et al., 1997; Aelion, 2010). The use of ^{14}C as a CSR tracer relies on the relatively short half-life of this species (~5,730 ± 40 years) (Aelion, 2010) in relation to the age of PHCs. Consequently, CO_2 derived from PHC oxidation contains no modern carbon. In contrast, living organisms continually exchange ^{14}C with the atmosphere resulting in a circum-atmospheric signature (~114% modern carbon (pMC)) in living or recently living tissue (Aelion, 2010). Modern carbon is defined using a 1950 baseline to reflect atmospheric conditions prior to weapons' testing, which resulted in an approximate doubling of the ^{14}C content in the atmosphere between 1955-1964 (Trumbore, 2000). Consequently, pMC values of CO_2 often exceed 100 % in the natural environment (Trumbore, 2000). This is most frequent when soil carbon cycling is dominated by respiration of material deposited close to 1955-1964 (Trumbore, 2000). The contrast in ^{14}C content of modern and PHC sources can, therefore, be exploited to quantify CSR, assuming CSR and NSR are the dominant CO_2 production processes. In some cases, carbonate mineral dissolution-precipitation may also

affect the distribution of ^{14}C in CO_2, however, Molins et al. (2010) showed that thermodynamic constraints strongly limit the contribution of carbonate mineral dissolution to soil gas CO_2 at hydrocarbon contaminated sites, implying that this process has only a negligible effect on CO_2 radiocarbon signature.

In a two-end member system, Rayleigh fractionation can be used to describe changes in the isotopic signature (Van Breukelen and Prommer, 2008). However, in systems where multiple reaction pathways and transport processes cause confounding isotopic fractionation, Rayleigh fractionation may be insufficient to describe observed isotopic changes (Van Breukelen and Prommer, 2008). In these cases reactive transport modeling provides a powerful tool for identifying the influence of physical processes (i.e. advection and diffusion) and separating the effects of different biologically-mediated reaction pathways (Mahieu et al., 2008; Van Breukelen and Prommer, 2008). Gibson et al. (2011), for example, used reactive transport modeling to distinguish the effects of sulfate reduction in a permeable reactive barrier on sulphur isotopes. Similarly, Mahieu et al. (2008) used this approach to examine changes in $\delta^{13}C$ resulting from CH_4 oxidation in landfill cover soils. While Birkham et al. (2003) combined stable isotopic measurements with reactive transport modeling in an unsaturated waste rock pile, to our knowledge an integrated reactive transport modeling analysis of SZNA at hydrocarbon-contaminated sites constrained by pore gas composition, and CO_2 efflux, and isotopic data has not previously been conducted.

The goal of this contribution is to assess CO_2 efflux measurements to evaluate the depth- and terminal electron acceptor-integrated rates of SZNA. Specific objectives include determining the feasibility of 1) identifying dominant reactions involving CO_2 by correlating $\delta^{13}C$ in CO_2 with partial pressures of atmospheric gases in the region of SZNA; 2) combining the

use of vadose zone ^{14}C and surficially measured CO_2 efflux to evaluate the contributions of CSR and NSR to CO_2 efflux; 3) applying a reactive transport model to integrate concentration, CO_2 efflux, and isotopic measurements to further constrain SZNA processes; and 4) to evaluate the accuracy of the background correction to estimate the contribution of CSR.

Methods

Study location and site history: The study site is located in a shallow sand and gravel glacial outwash aquifer near Bemidji, MN. In 1979 a crude oil pipeline rupture resulted in the loss of ~1.7 million L of crude oil to the subsurface. Following remediation efforts ~ 400,000 L of oil remained in the subsurface (Hult and Grabbe, 1988), forming three floating oil bodies (the North, Middle and the South Pools); the focus of this investigation is on the North Pool. Comprehensive site overviews may be found in Hult and Grabbe (1988), Baedecker et al. (1993) and Bekins et al. (2001). The regional climate is characterized as continental with an average monthly precipitation of 28 mm and temperature of 18.7 °C in the summer (June-August) (NOAA Climate Normals). At the North Pool, average vadose zone thickness ranges between 6-9 m (Amos et al., 2005).

Data collection: To assess the controls on contaminant degradation and the fate of gases in the vadose zone, pore gas samples were collected for analysis of $\delta^{13}C$ in CO_2; ^{14}C in CO_2; and vadose zone pore gas composition (in August, 2009). In addition CO_2 efflux was measured using CO_2 flux chambers (Sihota et al., 2011). Pore gas samples for gas composition and isotopic analysis were collected from a transect of 17 vadose zone multilevel gas wells which run along the main axis of the North Pool. This transect is oriented perpendicular to the pipeline, and

parallel to the direction of groundwater flow. Wells are constructed of 6.2 mm I.D. stainless steel tubing, finished with 10 cm long, 6.4 mm O.D. stainless steel screens; construction details can be found in Hult and Grabbe (1988). On average, eight ports are available in each well, the first port being ~ 0.5 m below ground surface (mbgs); subsequent ports are spaced at ~ 1 m vertical intervals.

Gas samples were brought to the surface from each port using a peristaltic pump (Geotech Environmental Equipment, Inc.) set at a flow rate of 1.5 L min^{-1}; at least 3 line volumes were purged from each port prior to sample collection and ports were sampled in alternating order to avoid over-purging and cross-contamination. Samples for pore gas analysis were collected from each port in 10 mL gas-tight syringes (Hamilton). CO_2 efflux was measured adjacent to each well using a dynamic closed chamber and infra-red gas analyzer system (LI-COR Biosciences, Lincoln, NE).

Samples for isotopic analysis in CO_2 were collected to pre-evacuated 100 cc glass vials which had been sealed with butyl stoppers. Samples for $\delta^{13}C$ were collected from each port. Due to the cost of analysis only select samples were collected for ^{14}C analysis. These were chosen to provide high resolution data in the direct vicinity of the oil body and to evaluate the sensitivity of the surficial CO_2 efflux measurements to low CSR rates (far downgradient of the center of the oil).

Data analysis methods: Following the method by Amos et al. (2005), gas compositional analysis was performed in the field using a Varian CP-4900 gas chromatograph, equipped with thermal conductivity detectors and a Molsieve 5A PLOT column to separate Ar, O_2, and N_2 and a PoraPLOT U column to separate CH_4 and CO_2 (Sihota et al., 2011).

CO_2 effluxes were determined by fitting a linear regression line (using best-fit R^2) to the rise in CO_2 content within the chamber headspace over the measurement period (1.5 min), after removing early time data, while mixing was established in the chamber. All data processing was conducted using software provided by the manufacturer (LI-COR Biosciences, Lincoln, NE) (Sihota et al., 2011, for details).

Stable isotopic analysis was performed at the Pacific Centre for Isotopic and Geochemical Research (Department of Earth and Ocean Sciences, University of British Columbia) using a light stable isotope ratio mass spectrometer (Thermo Finnigan DeltaPlusXL). Following Coplen (2011) results are reported in delta notation ($\delta^{13}C$; Eq. 1). Reference material used for the carbon system was the Vienna equivalent for Belemnite from the Pee Dee formation (VPDB; 1.1237 x 10^{-2} (Kendall and Caldwell, 1998)).

Analysis of ^{14}C content in CO_2 was conducted at the Australian National University (Canberra) and the National Ocean Science Accelerator Mass Spectrometry (NOSAMS) Facility at Woods Hole Oceanographic Institution (WHOI, MA). Detailed methodologies for preparation of isotopic materials may be found in the Supporting Information provided in **Appendix 2**. Using the delta notation (Eq. [1]) results of ^{14}C analysis are converted to percent modern carbon (pMC):

$$pMC = \left(\frac{\delta^{14}C}{1000} + 1\right) * 100 \qquad [2]$$

where pMC is the percent of modern carbon (modern carbon is defined as 95% of the ^{14}C concentration (AD 1950) of NBS Oxalic Acid I (SRM 4990B) (Olsson, 1970) and $\delta^{14}C$ is ratio of $^{14}C/^{12}C$ 1.176 ± 0.010 x 10^{-12} (Karlen et. al., 1968).

Reactive transport modeling: Reactive transport modeling was conducted with MIN3P-DUSTY (Molins and Mayer, 2007). This code accounts for geochemical reactions in the vadose zone, multicomponent solute transport, as well as advective-diffusive multicomponent gas transport. Gas diffusion is described using the Dusty Gas Model (Mason and Malinauskas, 1983) with species-dependent diffusion coefficients; the tortuosity factor is described with the Millington (1959) formulation. The code has previously been applied to simulate biodegradation in the source zone at the Bemidji site (Molins and Mayer, 2007; Molins et al., 2010). For the present study, the model has been extended to include stable and radiocarbon isotopes in CO_2 and CH_4, and was constrained by measured effluxes and pore gas composition.

Evaluation of difference in transport behaviour between isotopologues – molecular species that differ only in isotopic composition (IUPAC, 2011) – was considered through inclusion of isotopologue-specific gas viscosities and reference binary diffusion coefficients. Isotopologue-specific reference gas viscosities η^o [Pa s] were calculated for vapor temperatures of 265.15 K (8 ºC) to represent the steady-state temperature in the lower vadose zone at the Bemidji site (Ean Warren, pers. comm.). This was done following Yoonm and Thodos (1970), recommended by Perry's Chemical Engineers' Handbook (2007):

$$\eta^o = \frac{46.1T_r^{0.618} - 20.4\exp(-0.449T_r) + 19.4\exp(-4.058T_r) + 1}{2.173424 \cdot 10^{11}(T_c)^{-1/6}(M)^{-1}(P_c)^{-2/3}} \qquad [3]$$

where T_r is the reduced temperature (the temperature of consideration – here 265.15 K – divided by the critical temperature (T_c [K]), M is the molar mass [mol g^{-1}] and P_c is the critical pressure [Pa].

According to the mass dependence of the diffusion coefficient, isotopologues will diffuse at different rates. Assuming standard diffusion coefficients to be calculated for the most

abundant isotopologue (e.g. $^{12}CO_2$), binary diffusion coefficients for rare isotopologues were calculated following Mahieu et al. (2008):

$$\frac{D_{ij}}{D_{ij'}} = \sqrt{\frac{M_{j'}}{M_j} \cdot \frac{M_i + M_j}{M_{i'} + M_{j'}}} \qquad [4]$$

where D_{ij} represents the binary diffusion coefficient of the reference pair (e.g. N_2 and $^{12}CO_2$) and $D_{ij'}$ represents the adjusted diffusion coefficient considering the isotopologue of interest (e.g. N_2 and $^{13}CO_2$). M_j is the mass of the reference isotopologue and $M_{j'}$ is the mass of the isotopologue of interest. Isotopologues considered include: $^{14}CO_2$, $^{13}CO_2$, $^{12}CO_2$, $^{13}CH_4$ and $^{12}CH_4$. A complete list of the binary diffusion coefficients is provided in Appendix 2.

Results and discussion

Vadose zone gas composition: To enable direct comparison to isotopic and CO_2 efflux measurements, the spatial distribution of vadose zone gas composition (collected and analyzed in 2009) is presented. Reactive (O_2, CO_2, CH_4) and non-reactive (Ar, N_2) gases demonstrate that distinct geochemical regions exist within the vadose zone (**Figure 3.2**).

An area of elevated CO_2 and CH_4 and depressed O_2 is found between well 604 and 9101. This region corresponds to the area where oil floats on the water table (**Figure 3.2**) – hereafter termed the 'source zone'. Within the source zone partial pressures of CO_2 range between 0.4 and 18.6 % with an average of 10.1%. A maximum CO_2 partial pressure was measured two mbgs at well 9015, in the region where substantial oil remains at residual saturation (as identified by extensive coring (Dillard et al., 1997) (**Figure 3.2**). In the same region partial pressures of CH_4 range between non-detect and 27%, with an average of 4.7% (**Figure 3.2**). Similar to CO_2, partial pressures of CH_4 are highest in the area where oil remains suspended in the vadose zone

(7.9 mbgs at well 9014). O_2 partial pressures are locally depleted within the area of elevated CO_2 and CH_4 and range between ambient and 0.2% with an average value of 7.1 % (Figure 2a). Minimum partial pressures of O_2 are present near the base of the vadose zone, where oil floats on the water table. Combined, partial pressures of vadose zone gases show a zone of methanogenic degradation surrounded by a region of aerobic methane oxidation (**Figure 3.2**). At the background well (well 310), CO_2 partial pressures did not exceed 0.5 % and no CH_4 was detected.

The sharp transition between high and low partial pressures of CH_4 (**Figure 3.2**), indicates a narrow zone of aerobic oxidation (Conrad et al., 1997; Bekins et al., 2005; Amos et al., 2005; Molins et al., 2010). The presence of a sharp redox interface is further suggested by the strong correlation between O_2 and CO_2 ($r = -0.98$, $p<0.001$) generated from the reaction. In the region where CH_4 is detected, the ratio of CO_2 to CH_4 ranges from 0.005 (4.5 mbgs at well 533) to 1.8 (7.9 mbgs at well 9014) with a mean value of 0.6. The narrow reaction zone (Figure 1) may be the consequence of a discontinuous layer of low hydraulic conductivity and high residual water saturation which inhibits gas transport (Molins and Mayer, 2007; Molins et al., 2010).

Ar partial pressures range from 0.78 % (6.5 mbgs, well 9014) to 1.0 % (several locations; Figure 2d) with an average of 0.95 %. N_2 ranges from 62.1 % (7.9 mbgs, well 9014) to 84.0 % (4.5 mbgs, well 533) with an average of 77.3 % (**Figure 3.2**). Within the source zone, Ar and N_2 are significantly correlated ($r = 0.9$, $P = <0.001$). Amos et al. (2005) demonstrated areas of Ar and N_2 depletion with respect to atmosphere ($Ar^{atm} = 0.93$ %, $N_2^{atm} = 78$ %) are indicative of a methanogenic zone (Revesz et al., 1995), while the reverse suggests methanotrophic conditions (i.e. the oxidation of CH_4). Physically, this distribution of non-reactive gases can be explained by

decreased pressure (caused by the CH_4 oxidation reaction) which drives advective gas transport (Molins and Mayer, 2007).

Comparison of the areal extent of reactive and non-reactive gases to previous studies conducted in 2003 (Amos et al., 2005) and 2007 (Molins et al., 2010) shows minor variations, suggesting that SZNA processes have approached a quasi-steady state, at least in a seasonal context. Already more than a decade ago, Baedecker et al. (1993) and Revesz et al. (1995) indicated that methanogenesis is the dominant pathway for hydrocarbon attenuation. Further increases of CH_4, measured at depth in 2007 (Molins et al., 2010) and 2009 (this study), suggest that methanogenesis continues to gain importance in sustaining NA processes; as anticipated by Amos et al. (2005).

Isotopes in CO_2: To better distinguish between the processes contributing to CO_2 captured in the flux chambers, a detailed isotopic analysis of CO_2 was conducted as part of this study. The focus was on assessing the spatial distribution of stable carbon and radiocarbon in the vadose zone.

Across the site, $\delta^{13}C$ in CO_2 ranged between –16.9 ‰ and –36.8 ‰ ± 0.2 ‰ (**Figure 3.3**). In the source zone, $\delta^{13}C$ values similar to the remaining oil (–28.5 ‰; Baedecker et al., 1993) were measured (–26.5 ‰, 5.5 mbgs at well 533 and –26.0 ‰, 7 mbgs at well 301). Locations of depletion in the abundant isotope (^{12}C) occur near the base of the oil and coincide with the zone where substantial CH_4 is present in the layer directly above the measurement point (**Figure 3.2**). The locations with the greatest depletion in ^{12}C were found 8 mbgs at well 9014 ($\delta^{13}C$: –16.2 ‰), 5.5 and 6.6 mbgs at well 601 ($\delta^{13}C$:–16.9 to –14.0 ‰,); and 6.6 mbgs at well 534 ($\delta^{13}C$: –14.5 ‰) (**Figure 3.3**). CO_2 enriched in ^{12}C is found higher in the vadose zone (near the methanotrophic region) where O_2 concentrations begin to rebound, and CH_4 oxidation has gone to completion (**Figures 3.2 and 3.3**). CO_2 most enriched in ^{12}C was found at well 601 (–34.6 ‰;

2.5 mbgs), well 534 (–36.5 ‰; 4.5 mbgs) and well 9014 (–32.1 ‰; 5 mbgs). Within the source zone significant correlations were noted between $\delta^{13}C_{CO2}$ and partial pressures of N_2 (r = –0.7, P<0.001) and CH_4 (r = 0.7, P<0.001); a weak, yet significant correlation was also observed with the partial pressure of Ar (r = –0.5, P<0.001). These findings indicate that methanogenic and methanotrophic regions can be delineated at this site by non-reactive gases and/or stable carbon isotopes in CO_2.

Observed behaviour of the stable carbon isotopic system is strongly affected by microbially-mediated oil degradation (Revesz et al., 1995). Near the center of the residual oil, anaerobic conditions dominate and oil degradation will generate both CO_2 and CH_4 (**Figure 3.1**). In this region CO_2 is expected to be enriched in ^{13}C; as can be seen in **Figure 3.6.** ^{13}C enrichment is likely explained by a large proportion of CO_2 being generated from acetate fermentation (Aelion, 2010). Near the fringes of the residual oil, aerobic conditions dominate, and the isotopic signature of CO_2 is expected to be similar to that of the oil (as aerobic respiration will not cause significant isotopic fractionation (Conrad et al., 1999; Aelion, 2010)). This behaviour can be seen near the water table, outside the direct vicinity of the residual oil (**Figure 3.3**).

Partitioning of the heavy (^{13}C) and light (^{12}C) isotope between CO_2 and CH_4, respectively, can be explained by the acetate intramolecular isotope fractionation (Whiticar and Faber, 1986). Carbon connected to H is light and more enriched in ^{12}C (Galimov, 2006); in contrast, carbon connected to O is heavy and more enriched in ^{13}C.. As CH_4 is oxidized ^{12}C will be added to CO_2, causing the $\delta^{13}CO_2$ to become more negative. Anaerobic and aerobic regions can be distinguished in the $\delta^{13}C$ signature in **Figure 3.3**, as can the sharp transitions. Overall, stable carbon isotope analysis confirm previous findings by Revesz et al. (1995) for the Bemidji site, but provide a more complete picture on the distribution of ^{13}C for the source zone and

beyond. In contrast to the $\delta^{13}C$ profile in the contaminated zone, the $\delta^{13}C$ of soil CO_2 at the background well (well 310) is relatively constant, with an average $\delta^{13}C$ of –22.7 ‰ - similar to the value reported by Baedecker et al. (1993) (–21.42 ‰) in 1996.

The ^{14}C content of vadose zone CO_2 was analyzed at selected locations – as described in the methods. The oldest CO_2 was found 7.9 mbgs, near the center of the residual oil (6.2 pMC at well 9014; **Figure 3.4**). The youngest CO_2 (92.6 pMC) was found furthest from the center of the oil (1.5 mbgs at downgradient well 530). In the source zone (wells 604 to 9101), pMC ranged from 6.2 % to 45.9 % with an average of 15.9 %. A strong negative correlation was found between pMC values and CO_2 partial pressures ($r = -0.9$, $P < 0.001$).

Conrad et al. (1997, 1999) demonstrated ^{14}C content to provide a direct measure of the fraction of CO_2 attributable to CSR. This suggests that CO_2 generated in the source zone (dominated by high partial pressures of CO_2 and low pMC values) can be attributed to CSR processes. Following Aelion et al. (1997) and Bugna et al. (2005), a two end-member mixing model can be used to estimate the relative contribution of NSR (F_{NSR}) and CSR (F_{CSR}) in the sample:

$$F_{NSR} = \frac{pMC_{sample}}{pMC_{background}} \qquad [5]$$

$$F_{CSR} = 1 - F_{NSR} \qquad [6]$$

where pMC_{sample} is the pMC measured in the sample and $pMC_{background}$ is the pMC measured at a location (unaffected by the contamination). At the Bemidji site, F_{CSR} can be estimated for the source zone, assuming $pMC_{background}$ to be equivalent to pMC_{sample} measured at an unaffected well (Bugna et al., 2005). ^{14}C results from a sample collected ~0.4 mbgs, 45 m north of well 9017 in an area that is completely unaffected by the oil spill was used to define the background

composition. At this location pMC = 107 %, which falls within the range of ^{14}C content found in soil CO_2 in a natural, temperate environment (Trumbore, 2000).

Using ^{14}C contents from affected and background locations, the subsurface region impacted by oil degradation can be delineated between wells 604 and 530 (**Figure 3.4**); within this region F_{CSR} ranges between 0.97 (7.9 mbgs, well 9014) and 0.14 (1.5 mbgs, well 530), with an average value of 0.74. Using a criterion of $F_{CSR} > 0.5$, the area most directly affected by the oil can be defined. This criterion suggests that wells 604 to 531 should be included, coinciding with the earlier delineation of the source zone based on pore gas composition (Sihota et al., 2011), although the limited ^{14}C data in the downgradient region (wells 601 to 533) restricts our ability to positively constrain the termination of vadose zone CSR processes.

Comparison of F_{CSR} calculated for the Bemidji site (30 years following the oil release) can also be made to other sites where ^{14}C content has been used to evaluate NA. In a jet fuel contaminated aquifer, for example, Bugna et al. (2005) used ^{14}C content to estimate the fraction of jet fuel mineralization (as compared to F_{NSR}). F_{CSR} varied from 0 and 0.47 across the site between 4 and 16 years following contamination (release dates were not well documented). At a former refinery site where contamination occurred between 90 – 130 years prior to measurement, Conrad et al. (1999) found F_{CSR} of 0.9 and 0.97, indicating more than 90 % of carbon was generated from NA at some locations. The deviation of F_{CSR} from F_{NSR} in CO_2 measured in the natural environment (1.1 – 1.2 for temperate soils (Trumbore, 2000)) confirms the efficacy of radiocarbon analysis to distinguish between NSR and CSR.

CO_2 effluxes: Sihota et al. (2011) measured CO_2 effluxes above the North Pool transect and found that elevated CO_2 effluxes correlate well with the presence of oil suspended in the vadose

zone and floating on the water table. Consequently, CO_2 effluxes that can be attributed to SZNA (defined as J_{CSR}^{BGC}) were estimated by using the BGC method. This is done by subtracting the average CO_2 efflux from all background locations (representing NSR) from the total measured CO_2 efflux above the source zone, which includes contributions from both NSR and CSR. A maximum average CO_2 efflux of 7.1 ± 0.7 μmol m^{-2} s^{-1} was measured adjacent to well 9017. A minimum CO_2 efflux of 2.6 ± 0.4 μmol m^{-2} s^{-1} was measured adjacent to well 531. Based on inferred J_{CSR}^{BGC}, the source zone was found to encompass wells 9017, 9016, 301, 9015, 9014, and 601 (**Figure 3.5**), which is slightly narrower than the zone delineated based on vadose zone gas composition and shallow vadose zone isotopic signatures (wells 604 to 9101, **Figures 3.2 and 3.4**). In the source zone, CO_2 efflux averaged 5.9 ± 0.7 μmol m^{-2} s^{-1}, while in the unaffected area, the CO_2 efflux averaged 6.3 ± 0.5μmol m^{-2} s^{-1}. An estimate for depth-integrated CSR in the source zone was identified as J_{CSR}^{BGC} = 2.6 μmol m^{-2} s^{-1}. However, the BGC method assumes that average background effluxes do not vary spatially and are also valid for the source zone, which leaves some uncertainty regarding the magnitude and accuracy of J_{CSR}^{BGC}.

Comparison of efflux estimates related to contaminant degradation: As an alternative for background correction using an average NSR value (Sihota et al., 2011), the contribution of CSR to CO_2 measured in the chamber can be estimated using results from soil gas ^{14}C contents. To estimate CSR using the results of ^{14}C analysis, the CO_2 efflux (measured in the chamber) is corrected to account for the fraction of ancient carbon. This can be done using F_{CSR} (as defined by Eq. [6]). The calculation assumes that the pMC in CO_2 does not change significantly as it travels through the upper soil layer, and that SZNA is the major source of carbon with pMC = 0

%. Based on the half-life of ^{14}C and carbon turnover in soils, the latter assumption is defensible (e.g.: Trumbore, 2000), however, the contribution of NSR at shallow depth likely affects ^{14}C. To minimize this error, the analysis requires that only the pMC values that were measured most closely to the ground surface are used. Based on these assumptions, F_{CSR} can be used to estimate the fraction of CO_2 efflux derived from contaminant degradation:

$$J_{CSR}^{14C} = J_{CO2} \cdot F_{CSR} \qquad [7]$$

where J_{CSR}^{14C} is the estimated CO_2 efflux attributable to contaminant degradation [μmol m^{-2} s^{-1}] based on radiocarbon correction.

The areal extent of SZNA based on ^{14}C contents and analysis of vadose zone gas composition can be compared to that delineated using the BGC method (Sihota et al., 2011; **Figure 3.5**). Although representing a weaker signal, ^{14}C contents in CO_2 indicate that the effect of CSR extends to the downgradient wells 532, 518 and 531, while J_{CSR}^{BGC} in this region suggests the contribution of CSR to the total efflux is negligible (Sihota at al. (2011); **Figure 3.5**). Results of ^{14}C analysis demonstrate that a portion of the CO_2 generated in this region is attributable to SZNA (e.g. F_{CSR} = 0.36 at well 532). This finding also suggests that NSR in the region of wells 532 to 530 is lower than the average background value, implying that the contribution of CSR has been underestimated using the BGC method, when correcting for NSR. This result is not unexpected, because the BGC method has a limited sensitivity to lower SZNA rates (Sihota et al., 2011), which may fall into the range of natural variability of NSR. It should be noted that in areas devoid of vegetation, this limitation is expected to be less pronounced due to a lower influence from NSR. Radiocarbon analysis also confirms that the higher CO_2 efflux measured at downgradient well 530 is not mainly due to CSR (F_{CSR} = 0.14%), but can be attributed to

enhanced NSR, as was suspected by Sihota et al. (2011) – likely due to the proximity of the measurement location to large trees.

A comparison can also be made between estimated depth-integrated SZNA rates obtained from J_{CSR}^{14C} and J_{CSR}^{BGC}. Results of this analysis (**Figure 4.5**) show that J_{CSR}^{BGC} and J_{CSR}^{14C} agree reasonably well ($R^2 = 0.80$). In the source zone, average J_{CSR}^{BGC} = 2.6 µmol m^{-2} s^{-1} with a range of 1.9 µmol m^{-2} s^{-1} (well 9015) to 6.8 µmol m^{-2} s^{-1} (well 9017). Estimates for J_{CSR}^{14C} are consistently higher and yield an average of 6.9 µmol m^{-2} s^{-1} with a range of 2.4 µmol m^{-2} s^{-1} (well 604, ^{14}C: 0.5 mbgs) to 5.5 µmol m^{-2} s^{-1} (well 9017, ^{14}C: 0.4 mbgs), when the upgradient and downgradient wells, which exhibit a weak signal (upgradient: 310, 603, and downgradient: 9101, 532, 518, 530) are excluded. Considering all wells yields an average J_{CSR}^{14C}= 2.4 µmol m^{-2} s^{-1} with a minimum of 0.4 µmol m^{-2} s^{-1} (well 531, ^{14}C: 1.5 mbgs). The systematic differences in magnitude of CSR using the two methods are likely due to the assumption that the pMC value measured in the shallow vadose zone is representative of the gas that reaches the surface (i.e. without dilution by CO_2 produced from NSR). Another possibility for the discrepancy in estimates of CSR between the two methods is that the background correction for NSR is not fully representative for the entire site. For example, it is likely that NSR varies due to changes in vegetation and soil conditions (Hanson et al., 2000). It is also possible that, in the source zone, NSR is inhibited due to the presence of compounds toxic to soil microorganisms (Baran et al., 2004). However, this argument is speculative, as no tests were conducted to distinguish the effects of the presence of oil on NSR.

Sihota et al. (2011) also estimated total CO_2 effluxes using the concentration gradient method (J_{CSR}^{CGM} (Lundegard and Johnson, 2006)) at well 301 and 9016. However, this estimate did

not account for the contribution of NSR processes to soil gas CO_2. Using measured ^{14}C content at these locations, J_{CSR}^{CGM} can be refined to consider only ^{14}C-free CO_2. This is achieved by correcting the partial pressure of CO_2 at depth using F_{CSR} [equation 6], prior to conducting the efflux calculation. Using the gas phase saturations (S_g) estimated from analysis of fluid saturations in core samples collected by Dillard et al. (1997) (see Sihota et al., 2011 for discussion of estimates), this calculation yields J_{CSR}^{CGM} = 2.3 μmol m^{-2} s^{-1} (S_g = 0.65) at well 301; and J_{CSR}^{CGM} = 2.6 μmol m^{-2} s^{-1} without correction. For comparison, J_{CSR}^{BGC} = 2.4 μmol m^{-2} s^{-1}; J_{CSR}^{14C} cannot be estimated at well 301 as the shallowest ^{14}C sampling depth is 3 mbgs. Using the same approach at well 9016, J_{CSR}^{CGM} spanned 0.8 – 2.0 μmol m^{-2} s^{-1} (for a range of S_g = 0.6 and 0.8, respectively); while uncorrected for ^{14}C content, the J_{CSR}^{CGM} estimate ranges from 1.3 – 6.5 μmol m^{-2} s^{-1}. For comparison, J_{CSR}^{14C} = 6.2 μmol m^{-2} s^{-1} and J_{CSR}^{BGC} = 2.2 μmol m^{-2} s^{-1}.

The variability in CSR estimates obtained from J_{CSR}^{CGM} at well 9016 illustrates the high sensitivity to S_g, while spatial variability of S_g is not accounted for. The concentration gradient method also assumes that the CO_2 efflux is constant along the migration path, implying that biodegradation does not occur along the diffusion path and that no CO_2 is added from NSR. This assumption implies that the concentration gradient method will tend to underestimate CO_2 effluxes, at least if corrected for pMC. When uncorrected for pMC the gradient method will tend to overestimate CSR if samples are collected from the zone where NSR and atmospheric mixing add ^{14}C and dilute the CSR signal. It should be noted, however, that uncertainties in porosity and S_g may cause larger error than uncertainty in ^{14}C content, especially when ^{14}C content is low.

Values for CSR delineated in this study can further be compared to SZNA estimates from previous studies at the Bemidji site (**Table 3.4**). Revesz et al. (1995), for example, estimated a SZNA rate for the Bemidji site from field measurements resulting in a vertical flux through the unsaturated zone equivalent to 6.2 μmol m^{-2} s^{-1}, within a factor 2 uncertainty. Similarly, results of simulated SZNA rates at the Bemidji site give a range of 0.12 to 6.6 μmol m^{-2} s^{-1} through the first 28 years since the spill occurred (Chaplin et al., 2002; Molins et al, 2010). This comparison indicates a good agreement of the current measurements based on non-invasive CO_2 efflux techniques with previous results.

***Reactive transport modeling*:** Contributions of reaction processes considered in our conceptual model (**Figure 3.1**) were further investigated using the reactive transport code MIN3P-DUSTY (Molins and Mayer, 2007). The simulations focused on a vertical profile at well 9017, for which a complete set of radiocarbon data was collected. The model domain is comprised of a one-dimensional, 5.8 m soil column, representative of the vadose zone thickness at well 9017. Use of a one-dimensional soil column is justified as transport behaviour is predominantly vertical in the region of 9017 (Molins et al., 2010). To reflect geologic conditions (observed in core samples collected adjacent to well 9017), two material zones were included: the sandy glacial outwash sediments and a low K silt layer located at intermediate depth. This unit has previously been identified in core samples (Smith and Hult, 1993), and its presence was reconfirmed by visual inspection of cores collected in 2009. Physical properties of the porous medium are described in Table 1. Infiltration was assumed to be at a steady state with a recharge rate of 300 mm yr^{-1}, which is within the range reported at a nearby well (Bekins et al., 2005).

Oil degradation was considered for a single compound only as C_7H_{16}. C_7H_{16} was selected as within the range of labile compounds expected to remain under conditions in 2009 (Molins et al., 2010). The flow and reactive transport simulation was run under transient conditions until a quasi steady-state was reached (after appr 1.75 years). At the upper boundary of the domain CO_2 composition was assumed to be represented by atmospheric conditions (in the absence of site-specific information) with $\delta^{13}C$ = –7 ‰ and pMC = 114 % (Aelion, 2010). Reactions considered as contributing to SZNA include anaerobic oil degradation, methane oxidation, and aerobic oil degradation. Following Trumbore (2000), NSR was simulated as two pools: fast soil carbon (top 0.3 m of the soil zone) and slow soil carbon (0.3 mbgs – 1 mbgs) (**Table 3.2**). The ratio between fast and slow carbon was set to 2.7, which lies within the bounds reported by Bond-Lamberty et al. (2004) and Hanson et al. (2000) for heterotrophic and autotrophic carbon pools in the upper vadose zone. Carbon derived from NSR was assumed to have a uniform ^{14}C age of 114 pMC, representing recent interaction with atmospheric carbon (Aelion, 2010). Although soil carbon is more accurately represented by an age-structured model (Trumbore, 2000), the use of a uniform age carbon pool in the soil zone is unlikely to induce significant error given the large contrast to the ^{14}C content of oil. The ratio of ^{12}C, ^{13}C and ^{14}C within the soil zone was further constrained by assuming a $\delta^{13}C$ of –27 ‰ to represent NSR (**Table 3.2**; Aelion, 2010). Aerobic degradation was assumed to generate CO_2 with ^{13}C slightly depleted in comparison to the residual oil ($\delta^{13}C$: –29 ‰ (Aelion, 2010)).

Following Revesz et al. (1995) anaerobic degradation was assumed to generate CH_4 by acetate fermentation. Due to the location of the ^{13}C in acetate, the fermentation reaction leads to ^{13}C enrichment in inorganic products (e.g. CO_2) and depletion in CH_4 (Revesz et al., 1995). Consequently, CO_2 highly enriched in ^{13}C (exceeding +10 ‰) frequently accompanies

methanogenic fermentation (Carothers and Kharaka, 1980; Whiticar and Faber, 1986) and results in CH_4 with a typical $\delta^{13}C$ range of –52 ‰ to –80 ‰ (**Table 3.2**; Kendall and Doctor, 2011). At the Bemidji site Revesz et al. (1995) found fermentation to produce CH_4 with $\delta^{13}C$ between –50 ‰ and –62 ‰. In the model a $\delta^{13}CH_4$ of –60 ‰ was assumed. The lower end of the range measured by Revesz et al. (1995) was selected, as transport from the location of reaction can be expected to dilute the $\delta^{13}CH_4$ signal. CH_4 more depleted in $\delta^{13}C$ may suggest the presence of CO_2 reducing methanotrophs (Chanton et al., 2005) previously identified at the site (Bekins et al., 1999). Oxidation of CH_4 within and above the low K (silt) layer was assumed to produce CO_2 with $\delta^{13}C$ equivalent to the CH_4 source (Kendall and Doctor, 2011). A portion of the carbon consumed in the CH_4 oxidation was allocated to the growth of biomass within the low K layer (**Table 3.2**). This was required to allow a successful calibration of the model, and is justified by variations in CH_4 conversion efficiencies observed in the natural environment (Rolsev et al., 1997) and at retired landfill sites (e.g.: Whalen et al., 1990). Furthermore, at the Bemidji site, Molins et al. (2010) documented locations of high simulated CH_4 oxidation to correspond with large populations of methane oxidizing microbes, as determined using the most probable number (MPN) method (Bekins et al., 1999).

Unlike Gibson et al. (2011) and Mahieu et al. (2008), isotopologue-specific reactions were not considered. This approach is justified as a consequence of the large volume of oil present at the Bemidji site, and because simulations were conducted for steady state conditions (Richnow et al., 2003). Furthermore, as CH_4 oxidation occurs rapidly in a narrow band within and above the low K layer (**Figures 3.6, 3.7, and 3.9**), field data to document fractionation within this region is not available. The simple approach adopted is, therefore, unlikely to cause significant error in isotopic evolution of CO_2 due to the CH_4 oxidation reaction.

The model was calibrated using 2009 field data for gas composition (Ar, N_2. O_2, CO_2, and CH_4), stable ($^{13}CO_2$) and radioactive ($^{14}CO_2$) isotopic composition, and surficially measured CO_2 efflux. As $^{13}CH_4$ was not evaluated in this study, results from Revesz et al. (1995) were used to evaluate the $\delta^{13}C$ of CH_4 produced in the anaerobic degradation.

Overall, simulated gas profiles provide a good match to field measurements for the reactive and non-reactive gases (**Figures 3.6a and b**, respectively). Simulated partial pressures of O_2, CO_2 and CH_4 reproduce the sharp gradients observed in the field data, capturing the narrow zone of CH_4 oxidation near the top of the low K layer **(Figures 3.6 and 3.7**). Simulated reaction rates show substantial CH_4 generation at depth, while CO_2 is produced throughout the soil profile (**Figure 3.7**). Results show a zone of CH_4 oxidation within the upper region of the low K layer (**Figure 3.7**), consistent with simulations conducted by Molins et al. (2010).

Simulated gas fluxes (**Figure 3.8**) show that the system is diffusion dominated, which is also consistent with previous simulations (Molins et al., 2010). Downward diffusion of O_2 with a slight contribution of advection (**Figure 3.8**) can be explained by its consumption in the aerobic oxidation of CH_4 within the low K layer. Reactions in the oxidation layer also control the transport of CH_4 (**Figure 3.8**). Examination of $^{12}CH_4$ and $^{13}CH_4$ fluxes reveals diffusion-dominated transport with a small contribution of upward advection toward the reaction zone where they are consumed. The sharp decrease of partial pressure of $^{12/13}CH_4$ in the low K layer result from the oxidation of CH_4 to CO_2, which drives CH_4 transport into this zone (Figure 8c).$^{12}CO_2$ and $^{13}CO_2$ transport is dominated by diffusion away from the oxidation zone towards the surface (**Figure 3.8**). This can be explained by the production of CO_2 from NSR and CSR processes, including CH_4 oxidation. However, due to relatively limited CO_2 production below the low K layer (**Figure 3.7**), concentration gradients for CO_2 are limited in this region (**Figure**

3.6), and advective processes contribute significantly to CO_2 transport (both for $^{12}CO_2$ and $^{13}CO_2$). $^{14}CO_2$ produced from NSR in the upper 1 m of the domain causes a steep gradient driving upward ^{14}C diffusive transport (**Figure 3.8**). Small advective fluxes also contribute to $^{14}CO_2$ transport throughout the vadose zone.

For comparison with field measurements, simulated partial pressures of each isotopologue were converted to δ notation using Eq. [1]. Although $\delta^{13}CH_4$ was not measured in 2009, conversion of modeled $^{13}CH_4$ and $^{12}CH_4$ to $\delta^{13}CH_4$ enables a first-order comparison to the measurements collected by Revesz et al. (1995) and shows the model was able to approximate the isotopic signature observed in 1995 at a neighboring well ($\delta^{13}CH_4$ = –52‰ to –60‰). More importantly, the model provides a reasonable match for $\delta^{13}CO_2$ collected in 2009 (**Figure 3.9**), although there is some scatter in the field data. The steep gradient in $\delta^{13}CO_2$ near the surface is an artifact due to the specification of a first type boundary condition at the top of the domain, which fixes the isotopic composition to that of atmospheric CO_2 ($\delta^{13}C$: –7‰). The addition of CO_2 enriched in ^{12}C from the CH_4 oxidation reaction is well reproduced and can be seen in the shift to more negative δ values near the top of the low K layer.

Conversion of simulated ^{14}C and ^{12}C partial pressures to pMC shows good agreement with field measurements (**Figure 9c**). Within the soil zone (simulated as the upper 1 m of the vadose zone) modeled results suggest substantial addition of modern carbon. At the base of the soil zone (1 mbgs), model results show ~20% of the CO_2 is derived from modern sources, implying downward diffusive transport of ^{14}C derived from NSR, whereas in the soil 0.15 m below the chamber modeled results show ~35% of the CO_2 is of modern origin, approaching the contribution of NSR to the CO_2 efflux. Similar to the results for $\delta^{13}CO_2$, the rapid increase to ~100% pMC near the ground surface is an artifact of the boundary condition.

***Synthesis and integration of results**:* At the Bemidji site, comparison of vadose zone pore gas composition to results of previous studies in 1995 (Revesz et al.,1995), 2003 (Amos et al., 2005) and 2007 (Molins et al., 2010) shows biodegradation within the vadose zone to be approaching quasi steady-state conditions. In contrast to $\delta^{13}CO_2$, ^{14}C contents show large variations in the CO_2 source between contaminated and background regions. High fractions of ancient carbon present in CO_2 within the source zone confirm SZNA is occurring near the residual oil (Conrad et al., 1997). In addition, combining results of ^{14}C content with CO_2 efflux measurements enables direct separation of NSR from CSR. Resulting SZNA rate estimates are within the range of previous estimates for the Bemidji site (Table 4).

Comparing methods to estimate CSR shows that J_{CSR}^{CGM}, J_{CSR}^{14C}, and J_{CSR}^{BGC} agree reasonably well (**Table 3.3**). Highest estimates of SZNA are obtained from J_{CSR}^{14C}; this method also gives the widest range in values (**Table 3.3**). This can be explained by CO_2 production from NSR within the upper soil column. Lowest estimates are obtained from J_{CSR}^{CGM}, however, it should be noted that only two locations were considered for J_{CO2}^{CGM} estimates (as compared to 9 for J_{CO2}^{14C} and 17 for J_{CO2}^{BGC}). Low CSR estimates obtained from J_{CO2}^{CGM} can be explained at least in part by the assumption of linear transport from the measurement point to the surface (i.e. no addition or reaction of CO_2 along the flowpath). Regardless of differences in number of estimates and major assumptions (Table 3); the comparison between the methods suggests that J_{CO2}^{BGC} is an attractive and economical way to delineate depth-integrated SZNA rates. Comparison of the three methods illustrates the advantages and disadvantages of each, and shows that appropriate method selection depends on site conditions and experimental goals (**Table 3.3**).

Reactive transport modeling, when constrained by measured CO_2 effluxes, partial pressures of vadose zone gases and their isotopic composition, proves a powerful tool to integrate information. Building on previous work by Molins et al. (2010), simulation conducted at well 9017 are constrained by field measurements of partial pressures of pore gases, as well as the total carbon efflux. The good match with field measured stable and radiocarbon data (**Figure 3.9**) provides further evidence that the model quite closely captures processes at the site. Sensitivity analyses conducted demonstrated that varying the origin of the gas flux (i.e. aerobic CSR, anaerobic CSR and NSR) quickly leads to a degradation of the model fit. It should also be noted that the model clearly reveals that the isotopic signatures in the soil gas are not representative of the reaction processes alone (**Table 2**), but are strongly affected by transport processes (**Figure 3.8**). For example the simulation introduces CO_2 from the anaerobic reaction with $\delta^{13}C = +15$ ‰, yet $\delta^{13}C$ in the soil column is much more negative due to gas exchange with the region above. Similarly, downward transport of $^{14}CO_2$ explains that $F_{NSR} > 0$ in the NAPL containing region near the water table, although pMC is expected to be 0 in this region based its origin. Examination of gas fluxes within the domain shows that, while the system is diffusion dominated (**Figure 3.8**), advection plays a role in gas transport. Advective transport most strongly influences species consumed and produced by the CH_4 oxidation reaction within a narrow zone near the top of the low K layer (i.e. O_2, CH_4 and CO_2, respectively) and in regions with low concentration gradients. Future work will include evaluation of changes in ^{14}C contents across the soil surface by sampling CO_2 directly from the chamber as well as a more thorough comparison of J_{CSR}^{BGC} and J_{CSR}^{CGM}.

Tables

Table 3.1. Summary of soil parameters used in model simulation for well 9017.

Parameter	Background aquifer	Low K layer	Units	Reference
Hydraulic conductivity	5.0×10^{-5}	1.0×10^{-6}	[ms^{-1}]	Molins and Mayer (2007)
Van Genuchten Parameters				Dillard et al. (1997)
alpha	9.34	9.34	[m^{-1}]	
n	2.5	2.5	[-]	
exponent	1	0.5	[-]	
Residual Saturation	0.05	0.30	[m^3 H_2O m^{-3} void]	Dillard et al. (1997)
Porosity	0.38	0.38	[m^3 void m^{-3} porous medium]	Dillard et al. (1997)
Dispersivity	0.1	0.1	[m]	Molins and Mayer (2007)

Table 3.2. Reaction stoichiometries, rate constants, and isotopic ratios used in model simulation for well 9017. K_i^I: inhibition constant for species i; K_i^S: half-saturation constant; for species i; k_i: rate constant for species i. Reaction parameters' were selected based on Molins et al. (2010) and fitted through model calibration.

Process	Stiochiometry Rate Expression (R)	Rate, Monod, and Inhibition Constants	Units	Isotopic Ratio	Reference for Isotopic Ratio's
Soil respiration (NSR)	$CH_2O + O_2 \rightarrow CO_2 + H_2O$ $R = -k_{CH_2O}$	Fast Carbon: k_{CH2O} = 6.9 x 10^{-9} Slow Carbon: k_{CH2O} = 2.6 x 10^{-9}	[mol $dm^{-3}s^{-1}$] [mol dm^{-3}-s^{-1}]	$\delta^{13}CO_2$ = -27‰ pMC = 114 %	Aelion (2010) Aelion (2010)
Aerobic oxidation (CSR)	$C_7H_{16} + 11O_2 \rightarrow 7CO_2 + 8H_2O$ $R = -k_{C_7H_{16},ae}\left(\frac{C_{O_2}}{K^S_{O_2} + C_{O_2}}\right)$	$k_{C7H16,\ ae}$ = 1.9 x 10^{-10} K^S_{O2} = 1.0 x 10^{-5}	[mol dm^{-3} s^{-1}] [mol L-H_2O^{-1}]	$\delta^{13}CO_2$ = -29‰ pMC = 0 %	Aelion (2010) Kirtland et al. (2005)
Methane oxidation (CSR)	$CH_4 + 1.515O_2 \rightarrow 0.515CO_2 + 1.515H_2O + 0.485CH_2O(biomas$ $R = -k_{CH_4}\left(\frac{C_{CH_4}}{K^S_{CH_4} + C_{CH_4}}\right)\left(\frac{C_{O_2}}{K^S_{O_2} + C_{O_2}}\right)$	k_{CH4} = 9.8 x 10^{-7} K^S_{12CH4} = 1.0 x 10^{-5} K^S_{13CH4} = 8.1 x 10^{-8} K^S_{O2} = 6.1 x 10^{-6}	[mol L-H_2O^{-1} s^{-1}] [mol L-H_2O^{-1}] [mol L-H_2O^{-1}] [mol L-H_2O^{-1}]	$\delta^{13}CO_2$ = -60‰ $\delta^{13}CH_4$ = -60‰ pMC = 0 %	Revesz et al. (2005); Whiticar and Faber, (1986) Kirtland et al. (2005)
Anaerobic oxidation (CSR)	$C_7H_{16} + 3H_2O \rightarrow 1.5CO_2 + 5.5CH_4$ $R = k_{C_7H_{16},an}\left(\frac{K^I_{O_2}}{K^I_{O_2} + C_{O_2}}\right)$	$k_{C7H16,\ an}$ = 1.7 x 10^{-10} K^I_{O2} =1.0 x 10^{-6}	[mol dm^{-3} s^{-1}] [mol L-H_2O^{-1}]	$\delta^{13}CO_2$ = 15‰ $\delta^{13}CH_4$ = -60‰ pMC = 0 %	Carothers and Kharaka (1980); Whiticar and Faber (1986) Kirtland et al. (2005)

Table 3.3. Comparison of methods for estimation of SZNA rate. †assumes that the pMC of background CO_2 is 107%. ‡assumes well 531 can be excluded.

Method		Background correction:	Correction based on ^{14}C in soil†‡:	Gradient method:
Depth-integrated SZNA Rate Estimate [$\mu mol\ m^{-2}\ s^{-1}$]	Average (range)	2.6 (1.9)	Strong signal: 6.9 (6.1) All wells: 2.4 (4.5)	1.7 (1.6)
	Minimum	1.9 (well 9015)	Strong signal: 2.2 (well 604) All wells: 0.6 (well 518)	0.7 (well 9016)
	Maximum	6.8 (well 9017)	5.2 (well 9017)	2.3 (well 301)
Number of estimates		17	9	3
Pros		Rapid, simple measurement. Useful in regions where CSR is >> NSR (due to high CSR rates, or low NSR rates).	Good to identify outliers in NSR. Provides upper boundary for CSR.	Well established (easy comparison to other sites). Provides information on suite of gases (potentially including hydrocarbon vapors) analyzed. Enables identification of other processes (e.g. methanogenesis, methane oxidation).
Cons		Does not account for variability of NSR.	Expensive. Requires special sample preparation in the laboratory. Tends to over predict CSR if based on subsurface sample, because NSR and influences of transport between measurement location and surface are not accounted for.	Time intensive and expensive (requires installation of monitoring wells). Requires laboratory (or field) gas chromatography for sample analysis. Affected by uncertainty in porosity, moisture content, tortuosity and spatial distribution of these parameters (areally and vertically). Best constrained by measurement of the effective diffusion coefficient.

Table 3.4. Comparison of SZNA rate estimates for the Bemidji site from this and other studies. †assumes that the pMC of background CO_2 is 107%. ‡assumes well 531 can be excluded.

Method	**SZNA Rate (as CO_2 efflux [μmol m^{-2} s^{-1}])**	**Reference**
Background correction	2.6 (1.9)	This study
Correction based on ^{14}C in soil†‡	strong signal: 6.9 (6.1) all wells: 2.4 (4.5)	This study
Gradient method	1.7 (1.6)	This study
Gradient method	6.2 (1.6)	Revesz et al. (1995)
Modeled	1985: 0.12 - 0.14 1997: 1.3 - 1.5	Chaplin et al. (2002)
Modeled	6.6	Molins et al. (2010)

Figures

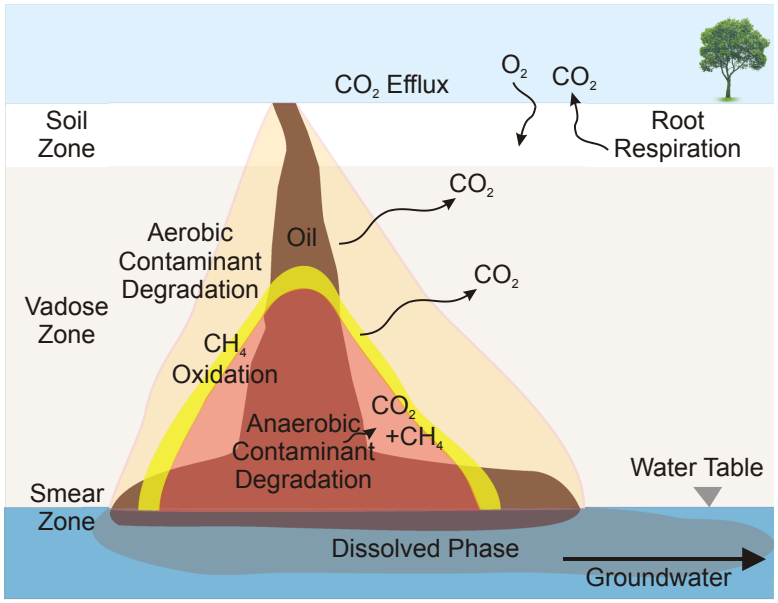

Figure 3.1. Conceptual model of contamination in the vadose zone at the Bemidji site.

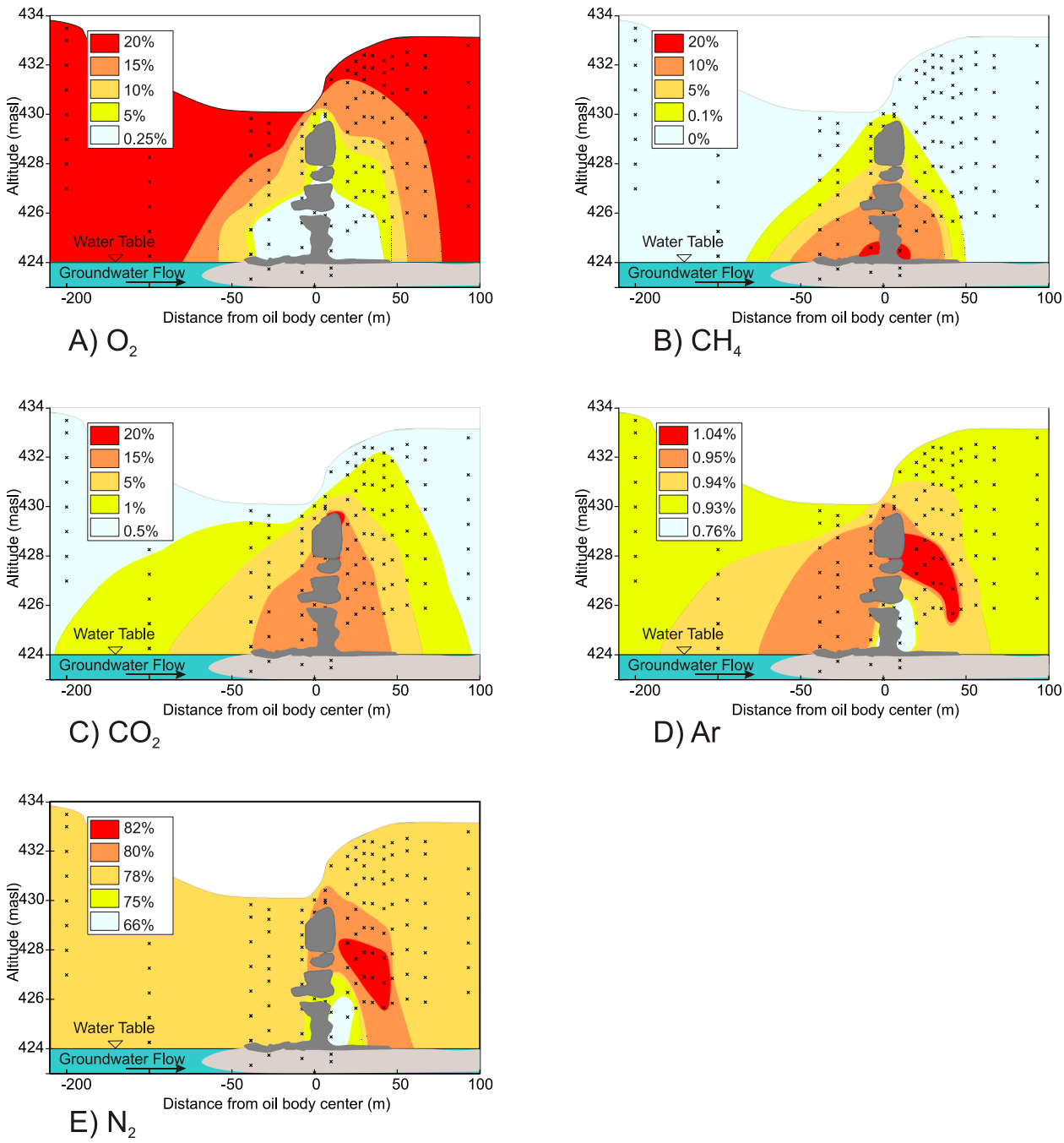

Figure 3.2. Cross section of vadose zone gas composition (August, 2009) along the North pool transect at the Bemidji site. (a) O_2, (b) CH_4, (c) CO_2, (d) Ar, (e) N_2.

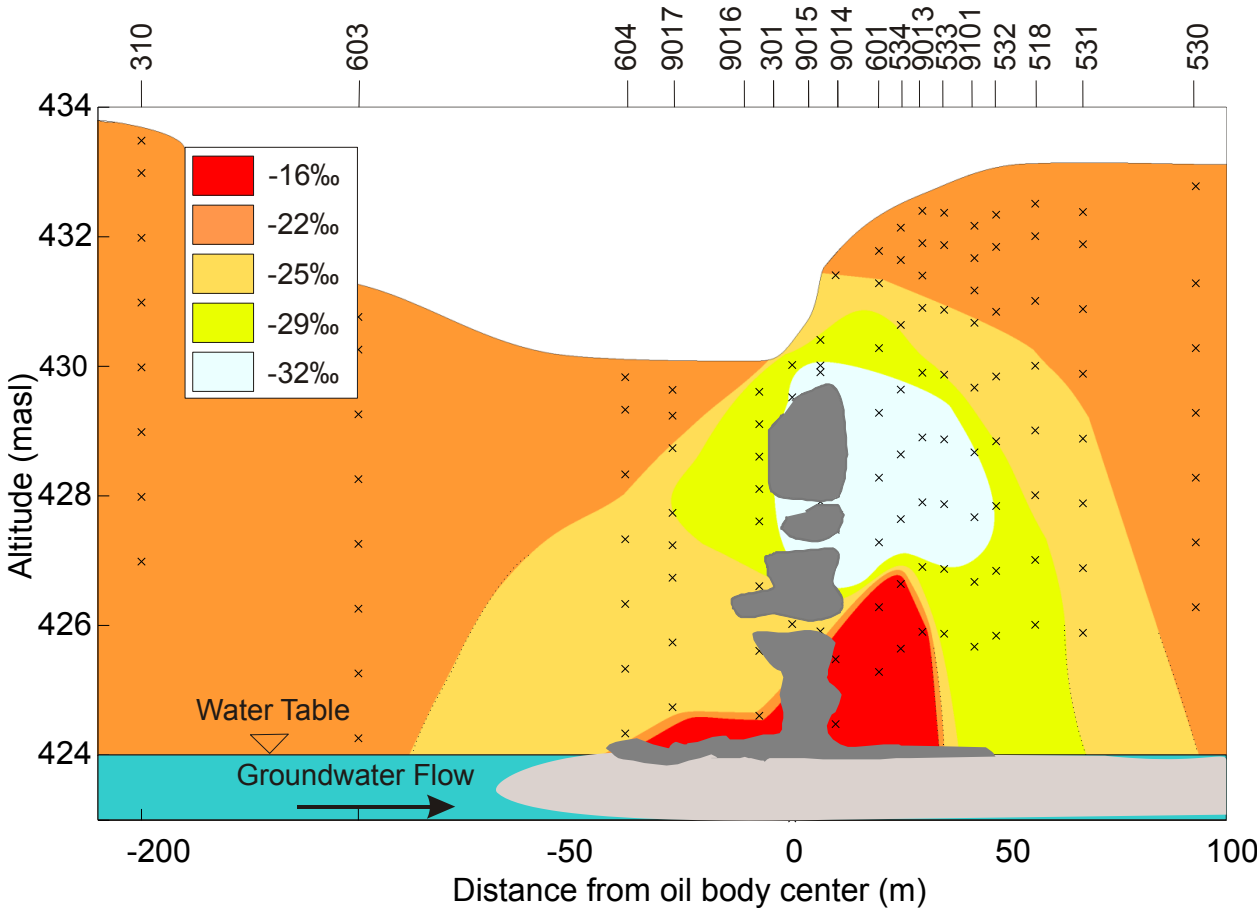

Figure 3.3. Cross section of vadose zone $\delta^{13}CO_2$ composition (August, 2009).

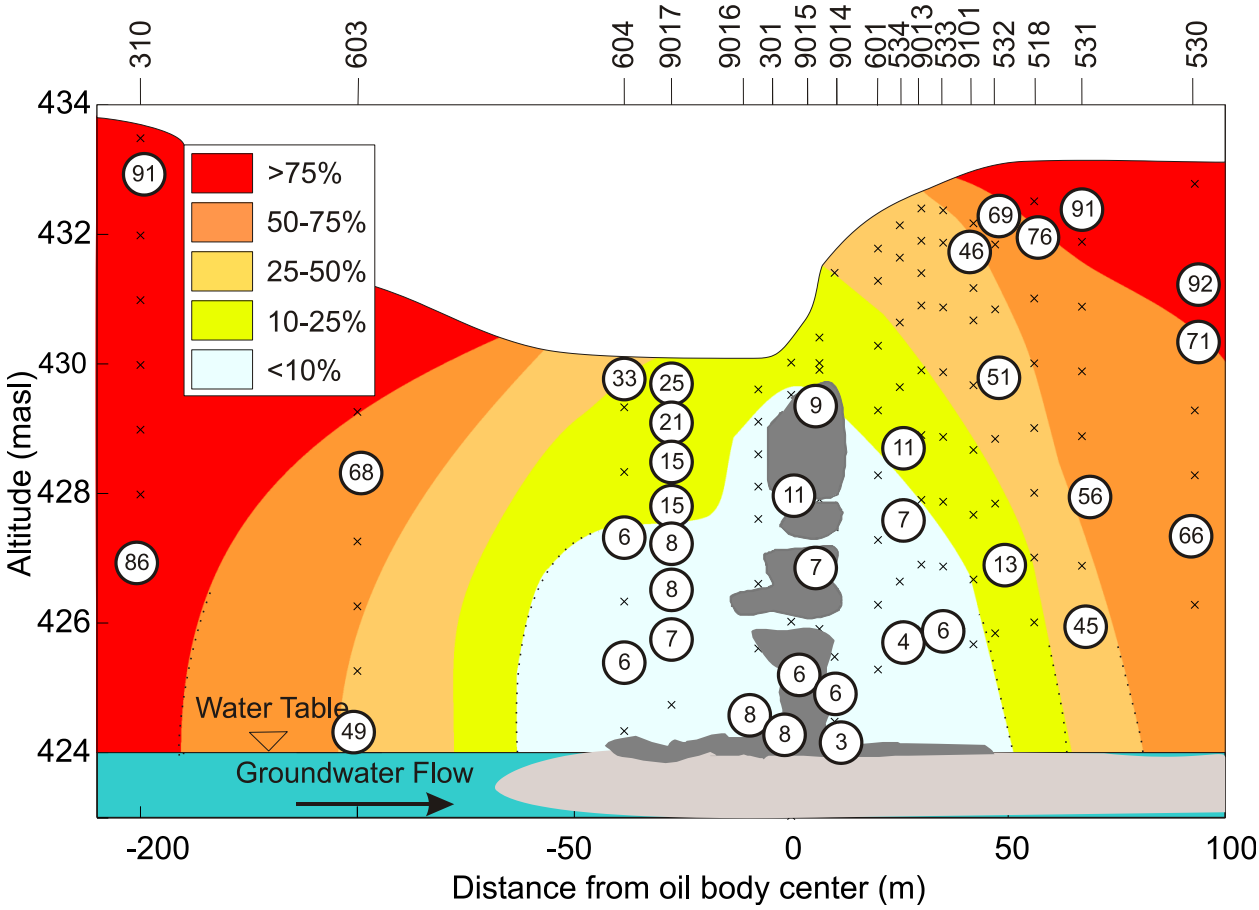

Figure 3.4. Cross section of pMC in vadose zone CO_2 along the North pool transect at the Bemidji site (August, 2009). Circled values show pMC measurements.

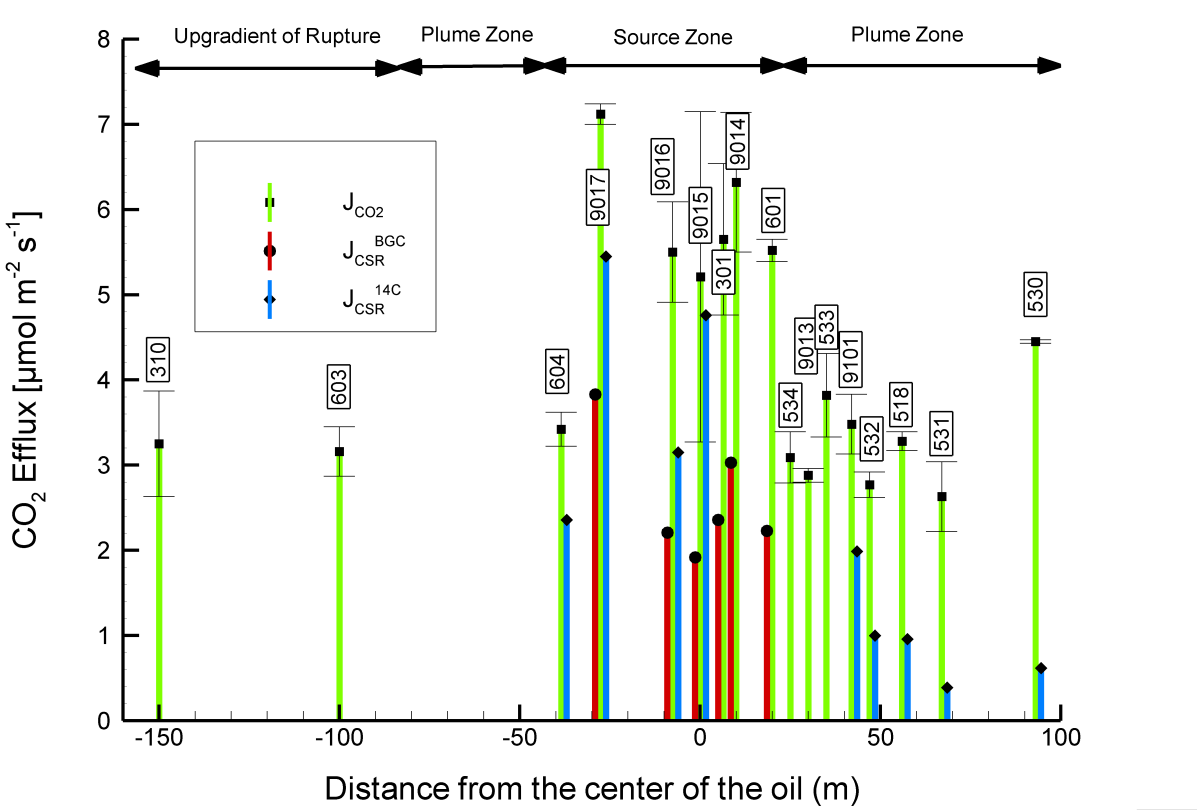

Figure 3.5. CO_2 effluxes above the North Pool transect at the Bemidji site (J_{CO2} = total measured surficial CO_2 efflux, J_{CSR}^{BGC} = CO_2 efflux related to contaminant degradation, J_{CO2} corrected for background soil respiration, J_{CSR}^{14C} = CO_2 efflux related to contaminant degradation, J_{CO2} corrected using radiocarbon data from shallow monitoring points.

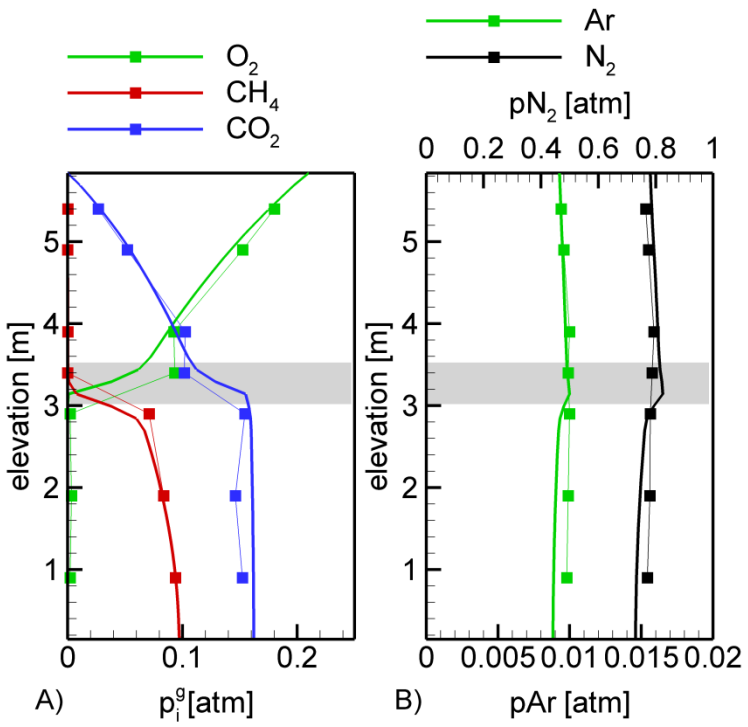

Figure 3.6. Simulated and measured partial pressures at well 9017: a) CO_2, O_2, and CH_4 b) Ar and N_2. Grey shaded area delineates extent of low K layer.

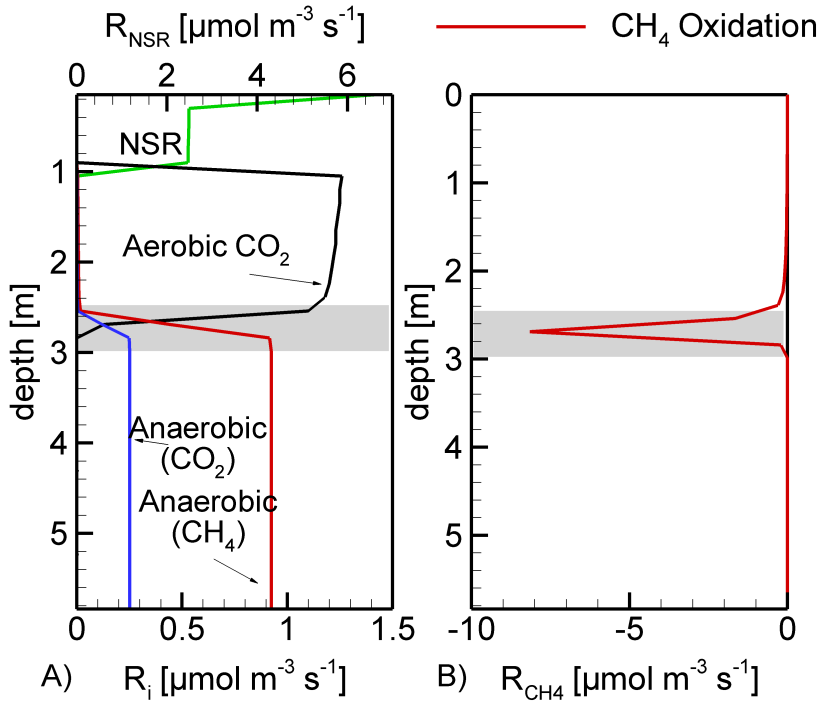

Figure 3.7. Simulated reaction rates at well 9017: a) CO_2 production from soil respiration (NSR), aerobic and anaerobic CO_2 production (CSR), and anaerobic CH_4 production (CSR) b) CH_4 oxidation. Grey shaded area delineates extent of low K layer.

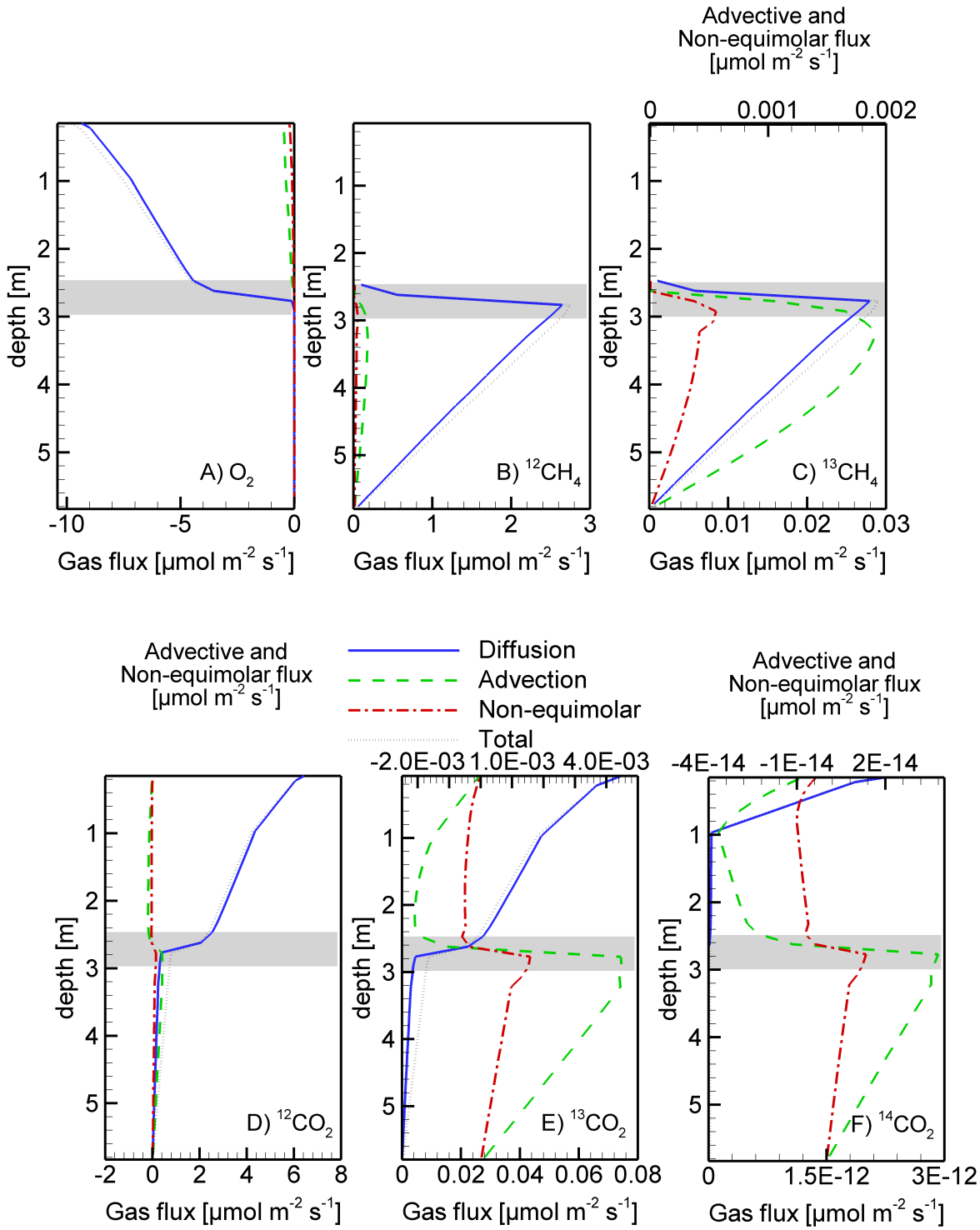

Figure 3.8. Simulated gas fluxes at well 9017: a) O_2, b) $^{12}CH_4$, c) $^{13}CH_4$, d) $^{12}CO_2$, e) $^{13}CO_2$ and F) $^{14}CO_2$. Grey shaded area delineates extent of low K layer.

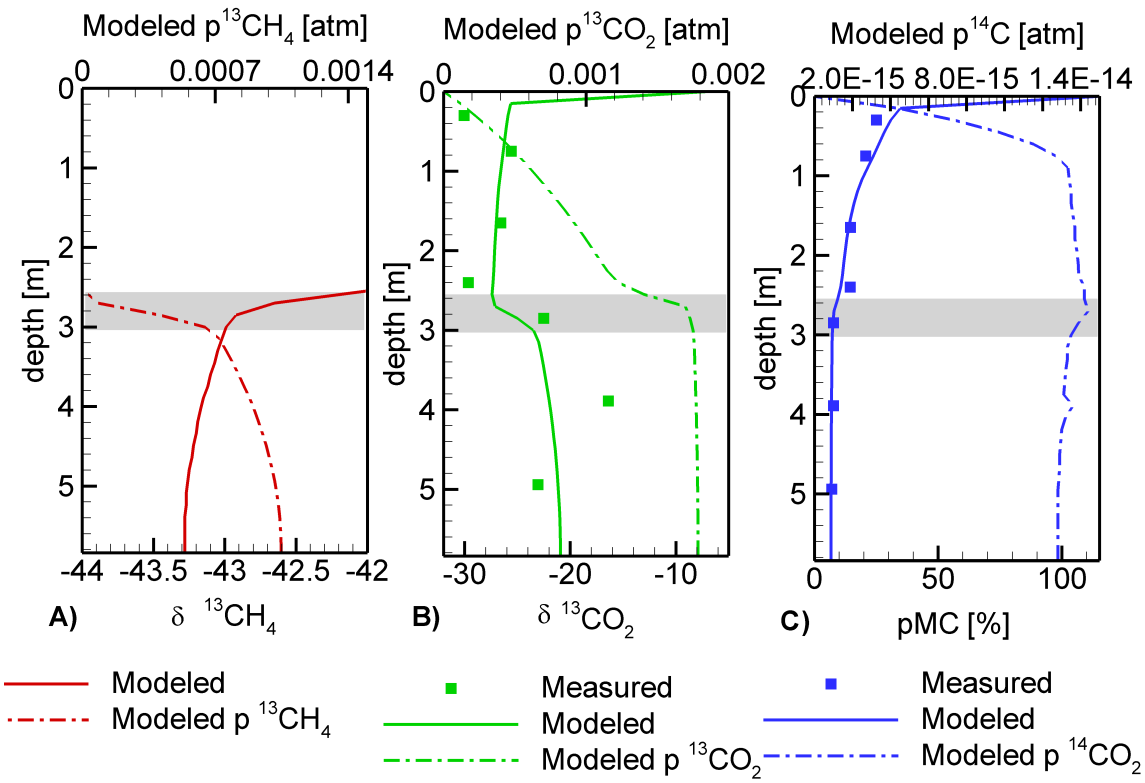

Figure 3.9. Simulated and measured isotopic profiles at well 9017: a) $\delta^{13}CH_4$ b) $\delta^{13}CO_2$ and c) pMC. Grey shaded area delineates extent of low K layer.

Chapter 4: Comparison of surficial CO_2 efflux to other measures of subsurface crude oil degradation

Introduction

Subsurface microbial activity at contaminated sites has been measured using a variety of approaches including molecular methods, contaminant mass loss rates, and production of degradation products (Weiss and Cozzarelli, 2008). However molecular methods do not always clearly correlate with other measures of activity (Röling, 2007). In this study, we examined the relationship among biodegradation populations, contaminant mass losses, and degradation products in the vadose zone at a crude oil spill site near Bemidji, Minnesota.

The crude oil source zone at the study site constitutes a coupled reaction system in which methane (CH_4) is produced in the oil body at the water table and oxidized in the overlying vadose zone. The entire supply of methane diffusing upward from the crude oil contaminant source is oxidized to carbon dioxide (CO_2) and water in the vadose zone. Thus, methane oxidation rates should be proportional to methane flux from the underlying oil, assuming steady-state microbial concentrations. Methane flux is difficult to infer from gas profiles because of variations in sediment diffusivities (Molins et al., 2010). However, because the methane is completely oxidized, CO_2 efflux measured at the surface can be directly related to the methane flux from the source despite subsurface reactions and dissolution. Previous studies have established that surficial CO_2 efflux at the Bemidji site varies with location (Sihota et al., 2011), suggesting spatial variations in degradation rates of the underlying contaminant source.

We selected a range of sites with varying surficial CO_2 efflux and measured four parameters expected to reflect methane production and oxidation rates: surficial CO_2 efflux, population densities of methanogens and methanotrophs using molecular methods, and crude oil degradation state. Microbial concentrations were measured using quantitative Polymerase Chain Reaction (qPCR), a method to determine microbial concentrations using function-specific DNA

fragments that has been shown to correlate with the Most Probable Number (MPN) growth method (Wang et al., 2011; Laskin et al., 2011). Quantitative PCR has been shown to be less labor-intensive than the MPN method, but perhaps more importantly, qPCR data have been shown in some cases to correlate with reaction rates at other sites (Braker and Conrad, 2011; Wang et al., 2011). Thus, we measured concentrations of methanogens in the oil body to assess whether these correlate with variations in crude oil degradation rate. Also, methanotroph concentrations in the vadose zone were measured, since methane oxidation was expected to vary with methane production. Finally, the degradation state of the crude oil is a cumulative measure of degradation rates that have occurred since the spill in 1979 (Peters et al., 2007), so we present analyses of currently degrading hydrocarbon homologs from oil samples at each location.

The study site, located near the town of Bemidji, MN, USA, was contaminated in 1979 when a high pressure pipeline ruptured spilling about 1.7×10^6 L (10,700 barrels) of crude oil. Despite of a major cleanup effort, about 25% of the spilled oil infiltrated into the surficial aquifer and is now present in the unsaturated zone and at the water table (6-8 m below the surface) (Essaid et al., 2011). **Figure 4.1** shows a plan view map of the site near the largest subsurface oil body. The direction of groundwater flow is to the northeast. The surficial aquifer is an ~ 20-m-thick unconsolidated glacial outwash deposit of mostly sand and gravel with some local silt layers (Bennett et al., 1993). The microbial population within the sediments containing residual oil is dominated by fermenters and methanogens (Bekins et al., 1999). Previous results from the site showed that methane from methanogenic degradation of the subsurface oil diffuses upward where it mixes and reacts with oxygen from the surface at 2-4 m depth to create an active methanotrophic zone (Amos et al., 2005; Sihota and Mayer, 2012). **Figure 4.2** shows a

conceptual model depicting the production of methane in the subsurface oil and upward diffusion through the vadose zone to the methanotrophic zone.

Biodegradation of *n*-alkanes under methanogenic conditions occurs at the Bemidji site (Bekins et al., 2005). Other studies have shown methanogenic biodegradation of *n*-alkanes at other sites (Siddique et al., 2006) as well as in laboratory microcosms (Anderson and Lovley, 2000; Zengler et al., 1999). Multiple lines of evidence indicate that methanogenic conditions have existed in the Bemidji oil body since 1988. These include aqueous data (Cozzarelli et al., 2001), gas data (Amos et al., 2005; Chaplin et al., 2002) and microbial data (Bekins et al., 2001; Bekins et al., 1999; Bekins et al., 2005). These methanogenic conditions are stable because oxygen in soil gas and recharge are consumed by methane oxidation in the vadose zone and do not reach the oil body at the water table (Amos et al., 2005; Molins et al., 2010). Analyses of oil from the Bemidji site showed a major difference in the degradation state between the upgradient and downgradient ends of the oil body (Bekins et al., 2005). Whereas both ends exhibited some methanogenic degradation of the *n*-alkane fraction, the upgradient end had mostly degraded by 2003. This area is overlain by a local topographic depression (elevation 430 m) where focused recharge during heavy rains results in recharge estimated to be twice the regional rate (Bekins et al., 2005). The increased recharge transports greater supplies of nutrients N and P from the surface to the oil body leading to more rapid degradation (Bekins et al., 2005). In contrast, at the downgradient end of the oil (elevation 433 m) there was little loss of *n*-alkanes by 2003 indicating that the oil degradation rate is much slower in this area. In this location, recharge was estimated to be comparable to the regional value.

Surficial CO_2 efflux measurements were conducted over the oil body by Sihota et al. (2011). Their results indicated that average CO_2 effluxes were almost twice as high over the oil

compared to background values. The highest values occurred near site 9017G (**Figure 4.4**) and the lowest were east of well 534G (Sihota et al., 2011). These efflux results are broadly consistent with higher activity at the west end of the oil.

Methods

Four active sites above the oil and two background sites were chosen to measure microbial activity. The three active sites (sites 2, 3, and 4 between July 26 to 28, in Supplementary **Table 4.1**). At these sites, three sample locations for methanotrophs were selected to lie above, within, and below the methanotrophic zone. The methanotrophic zone in this area occurs at a grain-size discontinuity where clean, coarse fill added during site clean-up overlies undisturbed fine grained lacustrine sediments typically containing some residual oil (Molins et al., 2010). This grain-size boundary was identified by visual inspection through the transparent core tubes. At site 5, a single core spanning the water table was collected on July 17, 2008. At all sites, samples from two locations spanning the water were used to determine methanogenic concentrations in the oil body. One sample was located 20-40 cm above the water table and the second was from 20-40 cm below the water table.

Reactive gases: As described by Sihota et al. (2011), oxygen and methane gas samples were collected from pre-existing vadose zone multilevel gas monitoring wells constructed of 6.4 mm stainless steel tubing with 10 cm screens (Chaplin et al., 2002; Amos et al., 2005). Three monitoring wells were sampled, each with eight sample ports (Hult and Grabbe, 1985). Samples were extracted using a peristaltic pump (GeoPump, Geotech Environmental Equipment Inc. Denver, CO) operated at a flow rate of 0.5 L min^{-1}. Three line-volumes of soil gas were purged

prior to sample collection via 10 cm^3 gastight syringes (Hamilton Co.). Compositional analysis of all samples was carried out in the field immediately after collection using a Varian CP-4900 dual channel gas chromatograph equipped with TCD detectors and a Molsieve 5A PLOT column to separate Ar, O_2, and N_2, and a PoraPLOT U column to separate CH_4 and CO_2. Column operating temperatures were 110 and 50 °C, respectively. Helium was the carrier gas (at 50 psi) and calibration and periodic verification were performed with air and two calibration gases (Scotty; 9.99% CH_4 and 5.04% O_2).

Carbon dioxide efflux: Carbon dioxide (CO_2) efflux measurements were conducted along a transect centered at gas well 9017 and running parallel to the pipeline (**Figure 4.1**). All measurement locations aside from the background location are situated above the floating oil pool (as identified by the USGS, based on core samples). It should be noted that vegetation along the measurement transect is sparse, and that the vegetation at the background location is comparable to the vegetation at other locations along the transect.

Following the method described by Sihota et al. (2011), CO_2 effluxes were measured using a dynamic closed chamber, coupled to an infrared gas analyzer (LI-COR Inc., Lincoln NE). CO_2 effluxes are calculated using the increase in CO_2 content within the chamber over the measurement interval, after removal of early time data (while mixing is established within the chamber). A minimum of three measurements were conducted at each location (allowing at least 30 min between measurements). CO_2 efflux was measured on August 19, 2009 at site 1a and gas wells 534G (located 6.7 m from site 5) and 9017G (located 2.8 m from site 4) and on June 14, 2011 at sites 1a, 1b, 2, 3, and 4 and gas well 534G. Following Sihota et al. (2011), contaminant mass loss rates are calculated from measured CO_2 effluxes by subtracting the CO_2 efflux

measured at the background location (i.e., site 1a or 1b) from the CO_2 efflux measured at each of the other locations.

Microbial concentrations: Cores were collected in vertical profiles through the unsaturated zone to below the water table from sites 1b, 2, 3, and 4 in 2010 (**Supporting Information Table 1 (provided in Appendix 3**)) using a freezing drive shoe (Murphy et al., 1997). At these sites three sample locations for methanotrophs were selected to lie above, within, and below the methanotrophic zone. The methanotrophic zone in this area occurs at a grain-size discontinuity where clean, coarse fill added during site cleanup overlies undisturbed fine grained lacustrine sediments typically containing some residual oil (Molins et al., 2010). This grain-size boundary was identified by visual inspection through the transparent core tubes. At site 5, a single core spanning the water table was collected in 2008. At all sites, samples from two locations spanning the water were used to determine methanogenic concentrations in the oil body. One sample was located 20-40 cm above the water table and the second was from 20-40 cm below the water table.

For each sample 10-20 g of sediment were placed into Whirl-Pak bags and frozen with dry ice. As described in Amos et al. (2011), DNA was extracted from about 10 g of sediment according to manufacturer's instructions using the Ultraclean MegaPrep Soil DNA kit (MoBio Laboratories, Inc., Carlsbad, CA). DNA was quantified in a Stratagene MX3000P using the Quant-it picogreen dsDNA assay kit (Molecular Probes, Eugene, OR). Real-time quantitative PCR reactions were then performed in a Stratagene MX3000P to assess the abundance of the organisms of interest using the primer sets pmoA for aerobic methanotrophs (Costello and Lidstrom, 1999), mcrA (mcrAf and mcrAr) for methanogens (Luton et al., 2002), DSR for

sulfate reducers (Wagner et al., 1998; Geets et al., 2006), GEO for iron reducers (Anderson et al., 1998; Holmes et al., 2002), and AMO for ammonium oxidizers (Rotthauwe et al., 1997). qPCR reactions were performed as previously described (Amos et al., 2011). Aerobic methanotroph concentrations were measured at sites 1b, 2, 3, and 4; methanogen concentrations were measured at all sites except site 1a. Abundances are presented in gene copies per gram of fresh (wet) sediment.

Hydrocarbon concentrations: Procedures used to collect and analyze samples of petroleum hydrocarbons are detailed elsewhere (Hostettler and Kvenvolden, 2002). Briefly, Bemidji crude oil samples (except for the archived oil) were collected using a freezing drive shoe (Murphy et al., 1997) and extracted using dichloromethane (DCM) from two separate oil-contaminated sediment samples taken from each site. The sediment is mostly sand with very low organic carbon and no confounding organic constituents. An archived sample of pre-spill Bemidji oil was used as a reference standard for comparison with the biodegraded samples to evaluate the biodegradation progression. The extracted hydrocarbons were analyzed by gas chromatography/mass spectrometry either as whole oils dissolved in DCM or after being separated into aliphatic and aromatic fractions by liquid chromatography on a mixed silica-alumina column. Profiles of *n*-alkylcyclohexanes were extracted from ion chromatograms using m/z 86. Compounds in the profile were normalized to C_{23} tricyclic terpane as a conserved internal standard in order to evaluate relative concentration levels between samples of the suite of compounds.

Results

Reactive gases: Methane and oxygen data for gas well 9017G (located 2.8 m from site 4) and gas well 534G (located 6.7 m upgradient from site 5) are plotted in **Figure 4.6.** To facilitate comparisons, the concentration data are plotted against relative distance between the land surface and the average water table. (**Table A6.1** lists for each site the actual elevations of the land surface and the water table). At both sites, oxygen concentrations are the same as atmospheric at land surface and decrease to zero at half way to the water table (**Figure 4.3**). Methane concentrations are high near the water table but decrease to zero near the point half-way from the water table to the land surface for 9017G and one-third of the way for 534G.

These data are consistent with previous results and the conceptual model depicted in **Figure 4.1**. Methane is produced in the oil body at rates sufficient to maintain the soil gas at 10-20% methane by volume immediately above oil body. The produced methane is oxidized before reaching the surface over a very short interval between 0.3 and 0.7 of the distance between the land surface and water table where both methane and oxygen are present. This interval is referred to in the remainder of the paper as the methanotrophic zone.

Carbon dioxide efflux: Measurements of CO_2 efflux, collected in June 2011, are presented in **Figure 4.4**. Efflux for well 534G was 5.0 µmol $m^{-2}s^{-1}$ and for site 1a was 2.5 µmol $m^{-2}s^{-1}$ indicating a net efflux from oil degradation of 2.5 µmol $m^{-2}s^{-1}$. At sites 2, 3, and 4, the efflux values were 5.4, 9.1, and 5.6 µmol $m^{-2}s^{-1}$, respectively while the value at the background site 1b was 1.9 µmol $m^{-2}s^{-1}$. Thus, the highest efflux over the oil was at site 3 while sites 2, 4, and 534G had similar values within 0.6 µmol $m^{-2}s^{-1}$. Efflux values over the two background sites were also within 0.6 µmol $m^{-2}s^{-1}$ of each other.

Microbial concentrations: The microbial concentrations were measured using qPCR at several elevations at sites 1b, 2, 3, and 4 (**Table A3.2**). Concentrations of aerobic methanotrophs ranged from non-detect to 10^7 gene copies per gram (**Figure 4.5**). At the background site 1b, values were below detection. For the locations above the oil body, values peaked at relative depths of 0.4-0.6 with the highest value at site 3 of $9x10^6$ gene copies/g, and similar values at sites 2 and 4 of $1x10^6$ gene copies/g. **Figure 4.6** shows the maximum concentration of methanogens from samples located in the oil body smear zone within 40 cm of the water table. At the background site 1b, methanogen concentrations were below detection. Within the oil body, methanogen concentrations were lowest at site 5 while the highest values for both methanogens and methanotrophs were found at site 3, which is consistent with the observed peak CO_2 efflux there.

Oil degradation state: Two oil samples from each site in the oil were analyzed for *n*-alkanes and *n*-alkylcyclohexanes. In all samples from sites 2-4, the *n*-alkane fraction is absent, indicating that this fraction has been removed by biodegradation. These new data are consistent with previous results documenting complete loss of the *n*-alkane fraction in the more degraded end of the oil (Bekins et al., 2005). At site 5, located in the less degraded end of the oil, the *n*-alkane fraction was still present in both samples but was partially degraded compared to the undegraded reference sample of spilled oil (data not shown). The *n*-alkylcyclohexane suite of compounds (m/z 83) is the next major aliphatic family to biodegrade after the *n*-alkanes. The distributions of this suite of compounds allow relative differentiation of the level of degradation among sites 2-5. The non-degraded *n*-alkylcyclohexanes in Bemidji source oil occur in a roughly bell-shaped distribution from C-11 to about C-31 (**Figure 4.7**). The sample from site 5 in the less degraded

area of the oil body lost very little of this hydrocarbon fraction compared to the source oil, with slightly more loss in the C-10 to C-16 compounds than in the higher molecular weight compounds. In samples from the more degraded area of the oil body (sites 2, 3, and 4), C-15 and higher hydrocarbon concentrations decreased by more than half for most *n*-alkylcyclohexanes.

The observed minor degradation of *n*-alkylcyclohexanes at site 5 is consistent with the methanogen concentrations and CO_2 efflux data which all indicate this site has the lowest degradation activity. Sites 2, 3, and 4 had similar *n*-alkylcyclohexane losses, with the degradation at site 3 progressing a little more than at other two sites with losses in the range of C-17 and higher. Greater *n*-alkylcyclohexane losses at site 3 are consistent with the methanogen, methanotroph, and CO_2 efflux data, which all indicate the highest activity at this site. Considering the entire dataset, the sites can be ranked in order of activity as site 3>site 4>site 2>>site 5.

Correlation of data: Correlation statistics were calculated to quantify the degree of relationship among the five data sets. The values used in the correlations are shown in **Table 4.1**. The base 10 log of the maxima of aerobic methanotroph concentrations in the unsaturated zone and methanogenic concentrations in the oil were used for microbial data. For the *n*-alkylcyclohexanes the entire set of peak heights were averaged for the two samples at each site. Finally, efflux data from June 14, 2011 were used. **Table 4.2** gives the results of the Pearson correlation analysis. The correlation coefficient (r) between the oil degradation state and the two microbial concentrations was very high for aerobic methanotrophs (-1.00) and for methanogens (-0.96). The very high correlations indicate that there is a strong relationship between microbial concentrations measured using qPCR and about 30 years of cumulative microbial activity

measured by degradation state. The coefficient between the two microbe types was similarly significant (0.99). The methanogens produce the methane consumed by the methanotrophs, so correlation of these populations is expected if qPCR data provide a valid measure of activity.

The correlation coefficients between CO_2 efflux and the concentrations of methanogens and methanotrophs (0.92 and 0.90, respectively) and oil degradation state (-0.91) are consistent with the conceptual model that the methanogens consuming the oil compounds are the source of methane, which is oxidized to CO_2 and contributes to surface efflux. However, the significance (p) of the relationship between the CO_2 efflux and concentrations of methanotrophs was greater than 0.05 whereas the p values for the other relationships were less than 0.05.

Discussion

In this study, we have compared several proxies for microbial activity in the vadose zone at a crude oil spill site. The source zone constitutes a coupled reaction system in which methane is produced in the oil body at the water table and oxidized the overlying vadose zone. Up to 60% of the oil is comprised of saturated hydrocarbons, including *n*-alkanes and *n*-alkylcyclohexanes, which are degrading under methanogenic conditions (Anderson and Lovley, 2000; Hostettler and Kvenvolden, 2002). The high correlation between the mcrA abundance and present degradation state of the *n*-alkane and *n*-alkylcyclohexanes in the oil at this site indicates that current mcrA concentrations are indicative of long-term methanogenic activity. A correlation between activity and concentrations of phylogenetic genes (Wang et al., 2011) or functional genes (Chin et al., 2004; Kazy et al., 2010) has been observed by others. However, Carini et al. (2005) found that methanotrophic activity was not directly proportional to gene copies in a seasonally varying lake and (Freitag and Prosser, 2009) showed that transcript/gene ratios of mcrA were only weakly

correlated with rates of methanogenesis. Reviews on this topic concluded that in addition to enumeration of genes it is necessary to understand controls of cellular activity (Röling, 2007) and community structure (Laskin et al., 2011). The strong relationship in this study may be due to the long-term stability of the system, which has been active for almost 30 years. In addition, the relationship is simply a correlation of mcrA concentration and cumulative loss and not a direct measure of instantaneous rate.

The fact that the surface CO_2 effluxes are not as closely correlated to the other measures of activity may be due to the separation between the surface and the underlying methane production and oxidation zones. Based on field measured gas concentrations at gas well 9017, the methane oxidation zone is located at a depth of about 3 m. Unless flow is strictly vertical and the travel time is negligible, the surface efflux may differ from the CO_2 flux leaving the CH_4 oxidation zone. Factors that may cause lateral flow or dispersion of gases include the presence of low permeability layers, variations in moisture content and atmospheric pressure changes. The CO_2 travel time from the production location to the ground surface can be estimated using model results from Sihota and Mayer (2012) who estimate the upward methane flux to be 2.6 μmol m^{-2} s^{-1}. Assuming that methane undergoes complete oxidation prior to its escape across the ground surface (Sihota et al., 2011; Sihota and Mayer, 2012), and using a porosity of 0.38, a methane partial pressure of 0.15 atm (Sihota et al., 2011) and a temperature at 3 m depth of 10 °C, the estimated travel time is 33 days. This suggests that the CO_2 efflux measurements reflect activities in the methane oxidation zone from the previous month. The extent of temporal variations in methane production and oxidation rates is the subject of ongoing studies at the site.

The CO_2 efflux is also affected by the subsurface diffusivity, which depends on moisture content and sediment type. The sediments at the site are part of a surficial glacial

outwash formation and include sands and gravels and lacustrine silts. During recharge events, soil moisture is perched on the lacustrine layers lowering their diffusivity. Such transient events may lead to horizontal migration of CO_2, preventing a direct connection between the zone of CO_2 production and efflux at the overlying surface location. In some locations residual oil is present in the lacustrine sediments which also creates a barrier to vertical migration (Dillard et al., 1997). Finally, the use of the background correction method for calculating contaminant mass loss rates (Sihota et al., 2011), assumes that the CO_2 efflux measured at the background location (i.e., 1a) is representative of the natural component of the CO_2 efflux in the area affected by the crude oil. A comparison of methods to constrain the component of the CO_2 efflux derived from the degradation of the crude oil is provided by Sihota and Mayer (2012).

The samples analyzed in this study were collected in the summers of 2008 and 2010. The combination of samples from different years is justified by the stability of the observations since 2003, including soil gases, degradation patterns, and microbial population differences. Soil gas concentration profiles measured in 2003 (Amos et al., 2005) were similar to those from 2007 (Molins et al., 2010) and 2009 (Sihota and Mayer, 2012). Changes in oil composition between the up- and down-gradient ends of the oil body were noted in Bekins et al. (2005), with much higher *n*-alkane losses in upgradient oil samples based on a combined dataset from 1999-2003. Finally, Bekins et al. (2005), using Most Probable Number (MPN) methods, found higher concentrations of fermenters and methanogens in oily sediments at the upgradient end of the oil compared to downgradient sediments. While we cannot directly compare microbial concentrations from MPN and qPCR methods, the trends of concentrations are comparable to those in this paper. Thus, previously published gas, microbial and *n*-alkane concentrations

indicate similar spatial patterns as we have observed here, making our combination of data from 2008-2010 reasonable.

Conclusions

In a measurement of CO_2 efflux, *n*-alkylcyclohexane loss, and concentrations of methanogens and methanotrophs at a crude oil spill site in Bemidji, Minnesota, we found a close correlation between the concentrations of microbes and hydrocarbon loss. Carbon dioxide efflux was similarly correlated, though not as strongly. The correlation calculations were possible due to the relatively unusual natural experiment of having different conditions at the two ends of the oil body. These conditions allowed for a comparison of the data types. Further, these results indicate that microbial concentrations can be used to infer microbial activity at contaminated sites.

Tables

Table 4.1. Microbial concentrations ($\log_{10}$ copies/g), *n*-alkylcyclohexanes (nC total; sum of GCMS response), and CO_2 efflux (μmol m^{-2} s^{-1}) data used in correlation statistics.

Site	*Methano-gens*	*Methano-trophs*	*nC total*	*CO_2 efflux*
1a			61.72	2.5
1b	1.75	1.75	61.72	1.9
2	6.13	6.19	29.07	5.4
3	7.51	6.96	24.21	9.1
4	6.54	6.06	31.38	5.6
5	5.24		46.75	5.0

Table 4.2. Pearson correlation statistics (r) between microbial concentrations (log_{10} copies/g), n-alkylcyclohexanes, and CO_2 efflux. (p value; number of samples).

	Methanogens	*Methanotrophs*	*nC total*	*CO_2 efflux*
Methanogens	1.00			
Methanotrophs	0.99 (p<0.006; 4)	1.00		
nC total	-0.96 (p<0.010; 5)	-1.00 (p<0.001; 4)	1.00	
CO_2 efflux	0.92 (p<0.027; 5)	0.90 (p<0.100; 4)	-0.91 (p<0.014; 6)	1.00

Figures

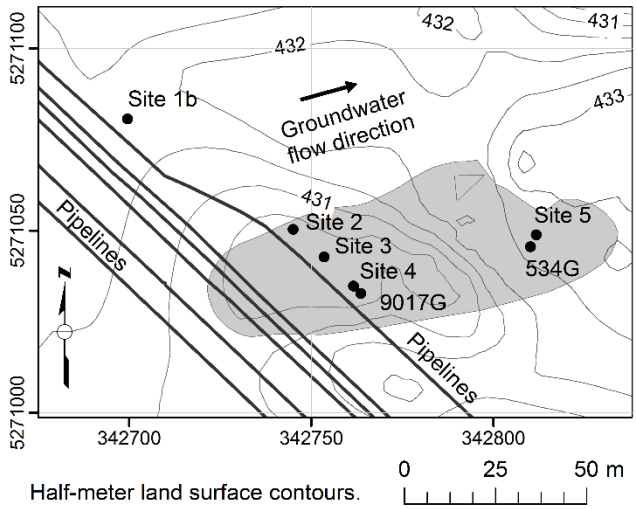

Figure 4.1. Plan view of the Bemidji site showing surface topography, locations of the oil body (grey shading), pipelines (dark lines), wells and sample sites, and direction of groundwater flow (arrow). Site 1a is located 177 m upgradient from site 4. The coordinate system is NAD 1983 UTM Zone 15N.

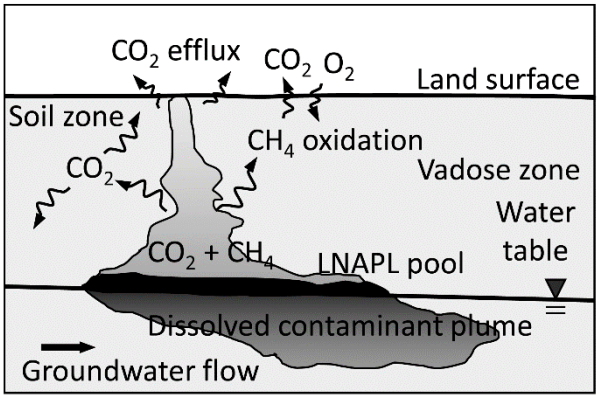

Figure 4.2. Conceptual model of methane generation and oxidation in the unsaturated zone above the light non-aqueous phase liquid (LNAPL) (modified from Sihota et al., 2011).

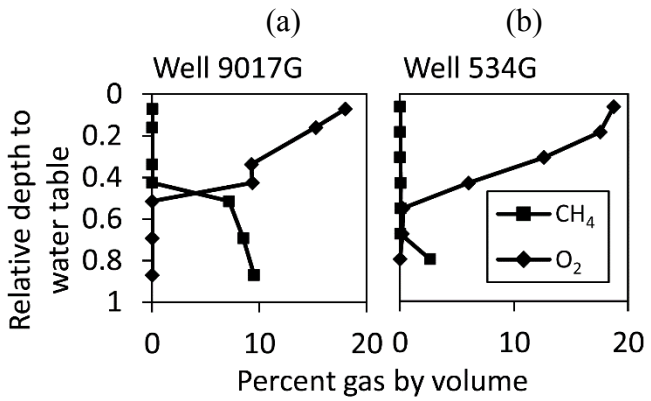

Figure 4.3. Reactive gases, methane and oxygen, by volume in the unsaturated zone measured in September 2009 plotted against relative depth from land surface (0) to water table (1) at (a) well 9017G (near site 4) and (b) well 534G (near site 5).

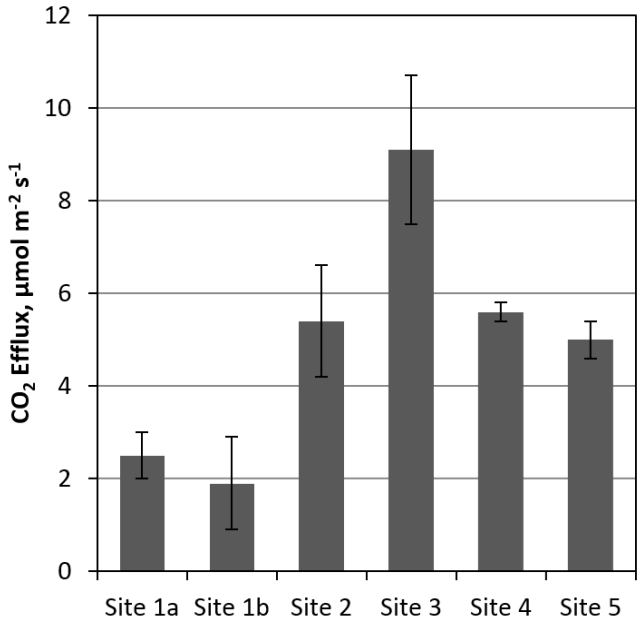

Figure 4.4. CO_2 effluxes with standard deviations based on three measurements on June 14, 2011. Well 534G data was taken near site 5, 6.7 m away (Figure 4.1).

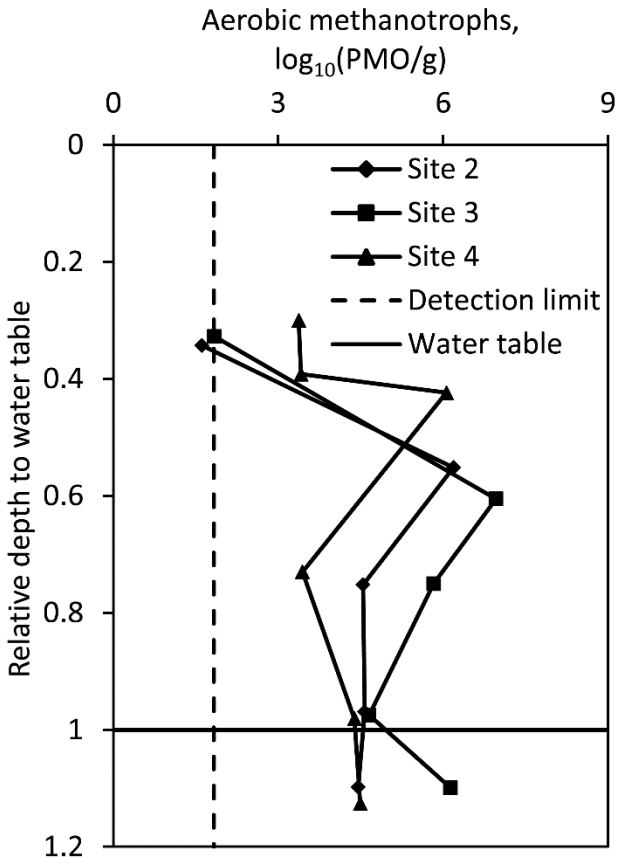

Figure 4.5. Microbial concentrations of aerobic methanotrophs at sites 2-4 as determined by qPCR using pmoA primers sets plotted against relative depth from land surface (0) to water table (1).

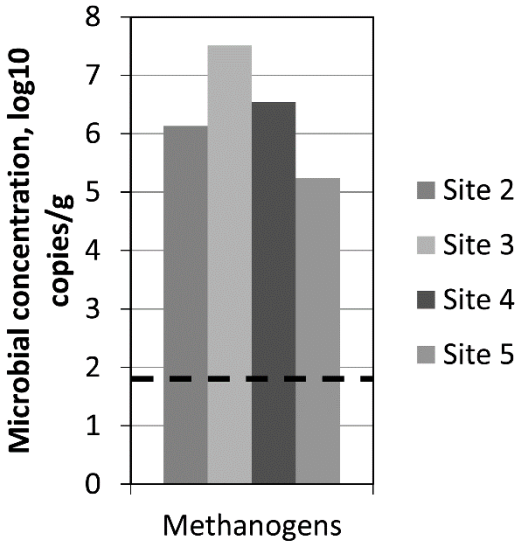

Figure 4.6. Maximum microbial concentrations of methanogens above the water table at sites 2-5 as determined by qPCR. Dashed line represents minimum detection limit.

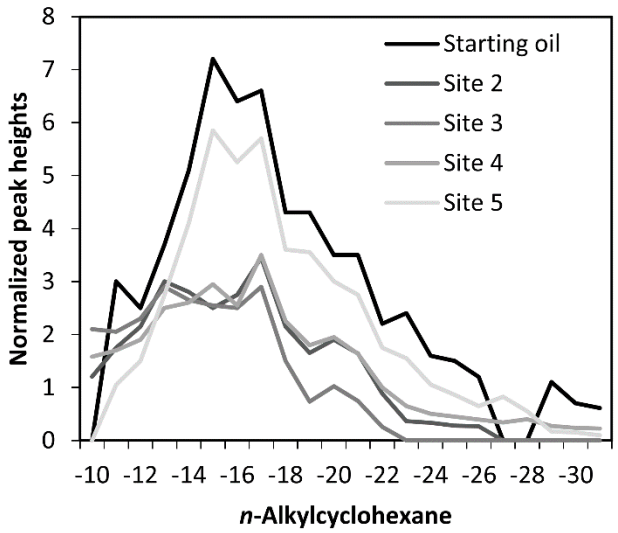

Figure 4.7. Average n-alkylcyclohexane peak heights normalized to triC23 measured in two oily sediment samples taken just above and below the water table at each of the contaminated sites along with an archived sample of pre-spill Bemidji oil.

Chapter 5: Seasonal variability in vadose zone biodegradation at a crude oil pipeline rupture.

Introduction

Seasonal dynamics strongly regulate environmental processes and the resulting stability of ecosystem functions, including the maintenance of energy flows in estuaries (Baird and Ulanowicz, 1989), resource assimilation in arid environments (Schwinning and Sala, 2004), and microbial biomass cycling in forests (Devi and Yadava, 2006). Understanding how seasonal dynamics influence these processes is key for maintaining and managing benefits from and impacts to ecosystem functions (Daily et al., 2012). In subsurface ecosystems, seasonal controls may manifest via a combination of physical and/or biological mechanisms including the regulation of gas emissions (Castro et al., 1995) and enzymatic processes (Baldrian et al., 2013). Increased precipitation falling on soils, for example, will result in short term saturation of pore space, altering gas transport régimes, while on longer time-scales recharge water can stimulate microbial respiration, leading to changing patterns of gas generation and consumption (Hawley and Altizer, 2011; Conant et al., 2011; Suseela et al., 2012). In an investigation of deep soil heterotrophic respiration in a mesic ecosystem, Suseela et al. (2012) showed a seasonally-dynamic temperature sensitivity, which was coupled to changes in soil moisture availability, while in a tidal mudflat, Segarra et al. (2013) found methane (CH_4) generation and emission rates were controlled by seasonal changes in sediment saturation.

As in the natural environment, processes in engineered and anthropogenically-perturbed environments are also regulated by seasonal dynamics. In a permeable reactive barrier, Benner et al. (2001) and Mayer et al. (2006) found seasonal variations in temperature-controlled sulfate reduction rates, while transport processes also affected the spatial distribution of sulfate concentrations. Similarly, seasonal variations have been documented for acid generation from mine waste (Molson et al., 2005), as well as for mineralization rates in oil contaminated coastal

marshes (Jackson and Pardue, 1997; Horel et al., 2012). In perturbed environments, understanding seasonal drivers of contaminant transformation and migration is important for evaluating *in situ* management options (including mineralization by natural microbial communities (i.e., source zone natural attenuation (SZNA)), developing source zone longevity estimates, and evaluating risk potential for receptors (Gantzer et al., 2001).

Source zone natural attenuation processes can be assessed by evaluating changes in microbial community composition (Bekins et al., 2005), and isotopic fractionation signatures in reactants and end products (Revesz et al., 1995; Conrad et al., 1997; Bouchard et al., 2008; Sihota and Mayer, 2012), while SZNA rates can be assessed by evaluating changes in the concentrations of both electron acceptors and contaminants within the vadose and saturated zones (Cozzarelli et al., 2001; Lundegard and Johnson, 2006). However, all of these methods provide limited spatial information, and results are applicable to the measurement period only. Moreover, the time and cost associated with sample collection and analyses often precludes high-resolution temporal and spatial monitoring (Höhener and Ponsin, 2014), making estimates of time-integrated mass loss rates challenging. Recently, Sihota et al. (2011) and Sihota and Mayer (2012) demonstrated that surficial CO_2 fluxes and isotopic measurements could be used for evaluating the extent and rate of SZNA above a crude oil containing vadose zone. The application of surficial CO_2 flux measurements for high-resolution temporal and spatial monitoring is attractive, as recurrent spatial survey measurements are relatively fast and inexpensive, and the equipment is well-suited to longer-term deployment at specific locations (Jassal et al., 2012).

Here we investigate seasonal variations in the distribution and rate of SZNA at a subsurface crude oil spill site using surficial CO_2 fluxes and shallow $^{14}CO_2$ samples. We assess

seasonal variations in soil temperature, moisture and vadose zone gas composition, and evaluate potential implications for the use of surficial CO_2 flux measurements to estimate time-integrated SZNA mass loss rates. Specific objectives include: 1) estimating a mean annual SZNA rate using CO_2 effluxes, 2) comparing SZNA rates obtained during different periods of the year to the mean annual mass loss rate, and 3) evaluating the seasonality in and importance of physical processes on regulating CO_2 effluxes measured at ground surface.

Methods

The study was conducted at the National Crude Oil Study site near Bemidji MN. Contamination occurred as the result of a crude oil pipeline rupture on August 20th 1979, which released ~ 1.7 x 10^6 L of crude oil into the glacial outwash aquifer and overlying soils (Hult and Grabbe, 1988). Following remediation efforts, ~ 4.0 x 10^5 L remained in the subsurface, forming three oil bodies (Hult and Grabbe, 1988). The evolution of SZNA processes at the north oil body (the focus of this study) has been the subject of intense interdisciplinary research for more than 30 years (Essaid et al., 2011). Results show aerobic and anaerobic degradation is occurring within the source zone, resulting in the production of considerable CH_4 and CO_2 at depth (e.g., Revesz et al., 1995, Amos et al., 2005, Sihota and Mayer, 2012). Oxygen depletion occurs in the upper vadose zone due to consumption in aerobic oil degradation and CH_4 oxidation (**Figure 5.1**). Comprehensive site reviews can be found in Hult and Grabbe (1988), Baedecker et al. (1993), Bekins et al. (2001) and Essaid et al. (2011).

Sampling was conducted on a monthly basis between June 2011 and June 2013, aside from gaps (due to logistical constraints between July – September 2011 and 2012, February – April 2012 and May 2013. Vadose zone gas samples were collected from the multilevel ports at

wells 9015G, 534G and 531G (**Figure 5.1**). Well construction details are described in Hult and Grabbe (1988) and sampling and analytical procedures are described in Sihota et al. (2011) and Sihota and Mayer (2012). Samples for evaluation of $^{14}CO_2$ content were collected in June 2009 (Sihota and Mayer 2012), and January of 2011 and 2013. Precipitation data was continuously logged from a tipping bucket located near well 604G (**Figure 5.1**). Soil moisture and temperature data were continuously logged from a multilevel sensor array located adjacent to well 9015G (**Figure 5.1**; Delin and Herkelrath, 2005))

CO_2 fluxes were measured using an infrared gas analyzer (LI-8100) coupled to a dynamic closed chamber system (LI-COR Inc., Lincoln, NE). Sampling was conducted on the same days as vadose zone gas samples were collected and was performed following the procedures described in Sihota et al. (2011). Source zone natural attenuation rates were obtained from contaminant soil respiration (CSR) rates, which were calculated by correcting total CO_2 fluxes (total soil respiration (TSR) rates) for natural soil respiration (NSR) rates. Following Sihota et al. (2011), this was done by identifying sampling locations as 'affected' or 'unaffected' by the oil, based on their proximity to the residual and free phase oil (**Figure 5.1**). To evaluate seasonal changes in the extent of the 'affected area', measurement locations were further classified as either 'vegetated' or 'non-vegetated'. Site 310G (~ 150 m to the southwest of 604G), was used as the reference for vegetated sites (530G, 531G, 532G, 518G, 533G, 534G, 601G, 9014G, 9101G, 9103G, and 603G). Site F (60 m to the northwest of 9017G) was used as the reference for non-vegetated sites (9015G, 9016G, 9017G, A, B, C, D, E, 604G, 301G, and 1212G). Using this approach, sites where CO_2 fluxes were greater than the respective reference site were considered part of the 'affected area'.

Implications of seasonal changes in environmental parameters (e.g., soil moisture) were

further investigated using quantitative reactive transport modeling. Two-dimensional simulations were conducted using the MIN3P-DUSTY code (Molins and Mayer, 2007), which accounts for geochemical reactions in the vadose zone, multicomponent solute transport, and advective-diffusive multicomponent gas transport with gas diffusion described through the Dusty Gas Model (Mason and Malinauskas, 1983) and the tortuosity factor described through the Millington, 1959 formulation. The code has previously been applied to simulate biodegradation in the source zone at the Bemidji site, but only representative for summer conditions (Molins and Mayer, 2007; Molins et al., 2010; Sihota and Mayer, 2012). Reactions considered as important for evaluating SZNA in the context of CO_2 flux measurements included aerobic oil degradation, CH_4 oxidation, and anaerobic oil degradation. Aerobic and O_2-constrained anaerobic degradation reactions were specified within the zone where oil remains at residual saturation and floating on the water table (Dillard et al., 1997). To capture processes within the direct vicinity of the source zone, the model domain was set to represent a 5.8 m vertical by 85 m horizontal slice though the vadose zone. A low permeability layer was specified across a portion of the domain at intermediate depth (Sihota and Mayer, 2012), representing the presence of a well-documented silt layer (Essaid et al., 2011). A complete list of model input parameters is provided in the Supporting Information (**Appendix 4**).

Results and discussion

CO_2 flux measurements and SZNA rates: Seasonal changes in gas emissions were evaluated by comparing the distribution and magnitude of total CO_2 fluxes (TSR). Maximum CO_2 fluxes were typically measured in the late spring and early summer, while minimum CO_2 fluxes were typically measured in winter (**Table 5.1; Figure 5.2**). Across both years, average CO_2 fluxes in

the spring (March – May), summer (June – Aug.), fall (Sept. – Nov.), and winter (Dec. – Feb.) were 2.6, 6.3, 2.8, and 1.7 μmol m^{-2} s^{-1}, respectively (**Table 5.1**). Comparison of the components of the CO_2 flux showed that patterns of NSR followed TSR, with maximum values measured in the summer (5.1 μmol m^{-2} s^{-1}) and minimum values measured in the winter (0.3 μmol m^{-2} s^{-1}) (**Figure 5.3, Table 5.1**). Patterns of CSR (obtained by subtracting NSR) were slightly offset from total fluxes with maximum values measured in the early summer and fall (2.2 – 2.4 μmol m^{-2} s^{-1}) and minimum values measured in the early spring (0.2 μmol m^{-2} s^{-1}) (**Table 5.1; Figure 5.3**). The seasonally weighted average CSR rate was 1.3 μmol m^{-2} s^{-1} (**Figure 5.3**). This value is lower than the average SZNA reported for the site by Sihota et al. (2011) (who conducted measurements in August) and closer to the carbon emissions rate of 1.8 μmol m^{-2} s^{-1} reported in a recent modeling study focusing on a mass balance for the site (Ng et al., 2014).

To evaluate annual contaminant mass loss rates occurring via SZNA, the area under the CSR curve (**Figure 5.3**) was integrated. Results showed an apparent average annual mass loss rate of ~4.1 x 10^7 μmol m^{-2} y^{-1} (~0.5 kg-C m^{-2} y^{-1}, or ~ 0.6 L of diesel equivalents m^{-2} y^{-1} (assuming a diesel carbon density of 0.73 kg-C L-diesel^{-1})). Extending the normalized SZNA rate from the m^{-2} scale to the areal extent of the oil body (~2,970 m^2) resulted in an annual average contaminant mass loss rate of 1.2 x 10^5 mol C y^{-1} (1.5 x 10^3 kg-C y^{-1} or 2.0 x 10^3 L diesel equivalents y^{-1}).

To further evaluate seasonality in the surficial CO_2 flux signal arising from SZNA, the fractional contributions of NSR and CSR were calculated. This revealed a seasonal switching of the dominant source of CO_2 measured in the chamber, with NSR dominating in the spring and summer, and CSR dominating in the fall and winter (**Figure 5.3; Table 5.1**). The decrease in CSR in the winter and early spring could suggest a near shut-down of oil degradation processes

or the presence of physical limitations on gas efflux during these periods. For example, increased soil moisture contents associated with spring snowmelt and precipitation could restrict gas transport during this period and lead to an under-representation of the corresponding seasonal SZNA rate based on CO_2 flux measurements.

Based on the seasonal changes observed in the CSR flux, the implications of snapshot sampling during different seasons for calculating SZNA rates was assessed by comparing average CSR rates obtained from spring, summer, fall, and winter measurements. Results showed the fraction of the flux represented by CSR was highest in the fall and winter and lowest in the spring and summer (**Figure 5.3; Table 5.1**). To estimate the variability associated with each season, the standard error associated with the CSR estimate was calculated. Results showed the error of the measurement was relatively stable in the spring, summer and winter (~ 0.4 μmol m^{-2} s^{-1}) but higher in the summer (0.6 μmol m^{-2} s^{-1}), consistent with an increase in natural soil respiration during the growing season. To further evaluate the implications of the CSR variability in each season, coefficients of variation were calculated for each season from all CSR rates obtained across the site. Results showed variability was greatest for the spring and least for the fall (~ 70% vs. ~25%). Overall, these results suggest the fall is a suitable time for measuring SZNA rates at this site, as the fraction of CSR is high and the measurement variability is relatively low.

To more rigorously investigate seasonal shifts in the fraction of CO_2 derived from CSR and NSR, the $^{14}CO_2$ content within the shallow subsurface (~ 0.5 m bgs) in the summer and winter was compared. Results showed a seasonal shift in the percentage of ancient carbon (pac; **Table 5.2**) with a greater contribution from CSR in winter as compared to the summer, consistent with seasonal changes in the fraction of CSR and NSR observed at the ground surface

(**Figure 5.3; Table 5.1**). Largest relative shifts between the summer and winter pac values occurred in the downgradient region, with a 54% change at 531G, while the smallest changes occurred directly above the center of the oil (with an ~ 4% change, at well 9015G) and ~ 93 m downgradient (with an ~ 2% change, at well 530G). This suggests a near constant contribution of CSR above the most contaminated area, and a shift in the dominant source of respiration near the fringes of the subsurface CO_2 plume towards CSR in the winter. These results are consistent with a seasonal near shut-down of NSR processes in the winter months, having a stronger effect near the fringes of the contaminant source zone. Observations of carbon cycling in other continental ecosystems corroborate the strong seasonal decline of NSR (Parkin and Kaspar, 2004; Herbst et al., 2008). These results are also consistent with surficial CO_2 flux measurements that showed persistently elevated CO_2 fluxes above the center of the oil, and a decline in CO_2 fluxes in the downgradient region (**Figure 5.2**).

Based on observed changes in the rate, fraction, and distribution of CSR, we next investigated seasonal changes in reaction kinetics by constructing an annual average Q_{10} model (which represents the rate of change in a biological reaction due to a 10°K change in temperature (Lloyd and Taylor, 1994; equation 1)) using measured CSR rates and subsurface temperatures:

$$Q_{10} = \left(\frac{R_2}{R_1}\right)^{10/(T_2 - T_1)} \qquad \text{[eq. 1]}$$

where R is the flux [μmol m^{-2} s^{-1}], T is the temperature [°K] and Q_{10} is the unitless change factor; subscripts 1 and 2 represent the reference state and state of interest, respectively. Assuming the annual average CSR rate calculated from flux measurements represents the true CSR rate (**Figure 5.3**), and that degradation occurs over ~ 6 m between land surface and the water table (i.e., neglecting the upper m, where NSR was expected dominate) the average degradation rate

per meter depth (reference SZNA rate) was calculated as ~ 0.2 μmol m^{-1} s^{-1}. The Q_{10} model was then constructed taking the reference temperature as 9 °C (the mean annual temperature measured in the lower vadose zone – **Figure 5.4**). Fitting the CSR rate determined from CO_2 flux measurements with temperatures constrained by data from the soil temperature array (**Figure 5.1**) resulted in an annual average Q_{10} value in the range of ~2.3 - 2.5 (**Figure 5.3**). For comparison, Q_{10} values of 1.3 to 3.3 have been reported across a wide range of natural soils (Raich and Schlesinger, 1992; Tipping et al., 2007), while Q_{10} values in the range of 2 – 3.5 have been reported for environmental hydrocarbon degradation (Brakstad, 2008; Bagi et al., 2014). The Q_{10} values found here and reported for other measurements of environmental hydrocarbon degradation are consistent with an increasing temperature sensitivity of degradation rates when available carbon pools are large (Bujalský et al., 2014). Largest deviations between measured and modeled CSR rates (**Figure 5.3**) occur in winter, and can be explained by a combination of factors, including: increased error associated with surficial flux measurements (e.g., although permanent soil collars were used, surficially frozen soils complicated CO_2 measurements in January of 2013); a threshold response of Q_{10} (i.e., a non-linear response of CSR rates at lower temperatures (Kirschbaum, 1995)); and the interplay between soil moisture and soil temperature in regulating reaction rates and fluxes (Qi et al., 2002)).

To further evaluate results of the Q_{10} model, we compared modeled respiration rates to those obtained using a form of the Arrhenius equation based on a constant activation energy (Lloyd and Taylor, 1994; equation 2), which has previously been shown to provide an unbiased estimation of respiration rates across a range of ecosystem types and soil temperatures (Lloyd and Taylor, 1994; Kätterer et al., 1998; Qi et al., 2002):

$$R = R_{10} e^{308.56\left(\frac{1}{56.02} - \frac{1}{T-227.13}\right)} \qquad \text{[eq. 2]}$$

where R_{10} is the respiration rate at 10 °C (283.15 ° K) and T is the temperature [°K]. This equation is based on an integration of empirical data obtained for a range of soil processes and ecosystem types and has previously provided robust estimates of respiration rates in soil systems (Lloyd and Taylor, 1994; Kätterer et al., 1998; Qi et al., 2002). Comparison of results from the Q_{10} model and those obtained from equation 3 using a R_{10} in the range of ~ 0.23 – 0.25 μmol m^{-1} s^{-1} showed good agreement ($r^2 > 0.9$), providing confidence in the estimated temperature sensitivity of respiration in this system and the applicability of equation 2 at this site. To relate modeled respiration rates to annual mass loss rates calculated from CO_2 fluxes, the area under the Q_{10} curve was integrated (**Figure 5.3**). Results showed an annual average mass loss rate of ~ 4.6 x 10^6 μmol m^{-2} y^{-1} or ~ 0.55 kg-C m^{-2} y^{-1}, which is in relatively good agreement with the ~ 0.5 kg-C m^{-2} y^{-1} calculated from CO_2 flux measurements.

Temperature exerts an important control on reaction rates; however, its influence on gas transport must also be considered due to the temperature sensitivity of diffusion coefficients. Consequently, we next investigated the relative impact of temperature changes on the effective diffusion coefficient D_{eff} by considering a temperature increase from 5 – 15°C as observed within the vadose zone at the Bemidji site. The temperature-dependent effective diffusion coefficient D_{eff} can be calculated according to Webb and Pruess (2003):

$$D_{eff} = \beta D_0 \left(\frac{T + 273.15}{273.15}\right)^{1.8} \qquad \text{[eq. 3]}$$

where β is the porous medium factor (representing the combined effect of porosity, tortuosity, and gas saturation), D_0 is the free air diffusion coefficient [m^2 s^{-1}], 1.8 is an exponent used to represent diffusion in a system with an air-water vapour mixture (Pruess 1987), and T is the

temperature [°K]. This change resulted in an ~ 4% change in D_{eff}, consistent with empirical measures of changes in D_{eff} for CO_2 in air (Wilke and Lee, 1955). In contrast, results of the Q_{10} model show a 10°C change in temperature resulted in a 225 – 250 % change in the reaction rate, demonstrating the relative importance of the temperature sensitivity of D_{eff} is minor in this system.

Similar to the effects of soil temperature, soil moisture affects both gas transport processes and degradation rates, as infiltrating rainwater delivers of a new supply of nutrients and electron acceptors to the reaction zone, while also removing reaction byproducts that may hinder degradation processes (Bekins et al., 2005). To evaluate the potential for infiltrating rainwater to impact degradation rates and alter subsurface gas concentrations, the travel time for a parcel of water entering the vadose zone to reach the oil floating on the water table was calculated. Based on recharge estimates obtained from soil moisture sensors (Delin and Herkelrath, 2005) travel times of 0.5 – 0.6 m month^{-1} were calculated for oily soils in the source zone (**Figure 1**). Using this estimate, arrival of spring recharge water at the CH_4 oxidation zone occurred in the early fall, consistent with the increase in CO_2 concentrations during this period (**Figure 7**), suggesting that natural recharge could also play a role in regulating SZNA processes in this system. However, set in the context of the declining CO_2 fluxes, results indicated that the system was more strongly limited by physical processes relating to gas transport than changes in the rate of degradation.

Seasonal variability in apparent SZNA extent: Given the seasonal differences in the rate of measured and modeled CSR we hypothesized that the areal extent of degradation, as determined by CO_2 flux measurements, would also be impacted by seasonal dynamics. The areal extent of

degradation is therefore an 'apparent' measure that changes as a function of degradation rates and soil conditions, and may be better defined as a seasonally variable 'surficial footprint' of subsurface biodegradation. For example, in areas where degradation is already low during periods of peak productivity (e.g., the fringes of the oil during the summer months) declining temperatures could further inhibit microbial activity, leading to a signal loss at the ground surface and a reduction of the surficial footprint. Similarly, if high degradation rates lead to lateral gas transport, seasonally lower degradation rates could decrease the extent of lateral transport, also resulting in a decline of the surficial footprint. To investigate the extent to which these factors impacted the surficial footprint we compared total CO_2 fluxes measured at each location along two transects parallel and perpendicular to the floating oil body to the CO_2 fluxes measured at the assigned reference location and contoured the resultant CSR estimates to a distance of 15 m from the measurement point. Results showed a seasonal dynamic, with the largest surficial footprint observed in the summer (2.9×10^3 m^2, June 2011), and the smallest surficial footprint observed in the winter (1.2×10^3 m^2, December 2011; **Figure 5.5, Table A5.1**). Comparison of the surficial footprint to the areal extent of the oil body floating on the water table showed the surficial footprint represented 105 % of the floating oil body in the summer and 40 - 45 % of the floating oil body in the fall and winter (**Figure 5.5**). These results confirm that at this site the surficial footprint of biodegradation identified by CO_2 efflux measurements is a good measure for the extent of the oil body or the affected area, in particular during the summer months. Although CO_2 flux measurements did underestimate the size of the floating oil body in the winter, they did show reasonable agreement with the extent of the oil suspended in the vadose zone (**Figures 5.1 and 5.2**), suggesting CO_2 flux measurements are most suitable for evaluating vadose zone impacts.

To evaluate the extent to which changes in CSR processes declined and/or vertical and lateral gas transport changed in the winter months, we next investigated the seasonal changes in vadose zone gas composition (focusing on degradation reactants and end products: O_2, CH_4, and CO_2). First, to provide a baseline for comparison, we evaluated the composition and distribution of these gasses within the entire vadose zone, using snapshot samples collected from ~ 150 vadose zone monitoring points in June 2012. Results showed a significant source of CH_4 at depth, with declining concentrations closer to land surface. Oxygen ingress from the atmosphere resulted in a narrow zone of CH_4 oxidation, ~ 3 mbgs directly above the remaining oil (with some variability in oxidation depth along the oil body axis (**Figure 5.6**)). Carbon dioxide generated from oil and CH_4 oxidation resulted in elevated CO_2 concentrations, which extended into the shallow vadose zone. Ar and N_2 distributions showed enrichment associated with CH_4 generation, and depletion associated with CH_4 oxidation. Overall, these results are consistent with previous studies documenting the extent and composition of atmospheric gasses at the Bemidji site during the summer months (Amos et al., 2005; Molins et al., 2010; Sihota and Mayer, 2012).

To relate seasonal changes in subsurface gas composition to changes in the distribution of CO_2 fluxes measured at ground surface, variability in subsurface gas composition was evaluated at source zone well 9015G (**Figure 5.7**) and plume zone well 534G (**Figure 5.8**). At 9015G, results revealed an unexpected seasonal dynamic to gas distributions (**Figure 5.7**); because periods of strongest CH_4 and CO_2 enrichment in the subsurface occurred in the late fall and early winter, corresponding to times of declining surficial CO_2 effluxes and a contraction of the surficial footprint of biodegradation. Indeed, periods of elevated CH_4 and CO_2 concentration were not consistent with elevated soil temperatures. Moreover, declining O_2 concentrations

observed during the same periods were also unexpected. It was anticipated that during times of reduced degradation rates ingress of atmospheric O_2 would rapidly replenish O_2 consumed in aerobic respiration and CH_4 oxidation. These observations point to a more complex relationship between the processes governing surficial gas emissions and can only be explained by the presence of a barrier to gas transport during the late fall and early winter. Moreover, evaluation of the gas composition at 534G also showed an increase in CO_2 concentrations during fall and winter, consistent with the temporary presence of a barrier to gas transport, promoting lateral gas transport away from the source zone (**Figure 5.8**).

To investigate the potential for seasonal changes in soil moisture contents to create a transient barrier to gas transport and alter the extent of the surficial footprint measured at ground surface, we evaluated changes in the precipitation rates and soil moisture contents using data obtained from a tipping bucket located near 604G and the soil moisture array located adjacent to 9015G (**Figure 5.1**). Results showed substantial precipitation events corresponding to infiltration fronts occurred in the late spring to summer of each of the study years (**Figure 5.9**), suggesting the importance of snow melt and spring rains in controlling soil moisture contents. However, moisture content increases appear to be insufficient to substantially inhibit gas transport during these periods of high biodegradation activity. Lower moisture contents were measured in the late fall and winter (**Figure 5.9**), which seems counter-intuitive considering the observed gas accumulation in the vadose zone during this period of time. However, frozen soil conditions may explain the low observed moisture contents during this time period, as total water content is typically substantially higher in frozen soil than measured by TDR sensors (Spaans and Baker, 1995). Indeed, the decline in surficial CO_2 fluxes and concomitant increases in vadose zone CO_2 concentrations coincided with periods when surficial soils were frozen, suggesting a substantial

decrease in soil gas permeability due to the presence of an ice layer that affects communication between the zone of gas generation and the ground surface. These arguments are in agreement with the co-occurrence of elevated subsurface CO_2 concentrations and reduced surficial CO_2 fluxes when temperatures are below 0°C (fall and winter; **Figure 5.10**).

Based on integration of the field results, a conceptual model emerges whereby changes in temperature drive both respiration rates and increases in surficial CO_2 fluxes when transport is not limited. However, when declining temperatures lead to reductions in SZNA rates, frozen soil conditions restrict communication between the reaction zone and the atmosphere, simultaneously leading to CO_2 buildup and a substantial depression of surficial CO_2 fluxes (**Figure 5.10**). To further understand the implications of seasonal changes in degradation rates and gas transport barriers, and quantitatively evaluate the conceptual model developed based on field observations, we next conducted reactive transport simulations. Specifically, we developed three scenarios to represent different periods of the year; model parameters are provided in **Tables A5.2-3**. The summer base-case (scenario 1) used reaction rates reported in Sihota and Mayer (2012). Results of this simulation (**Figure 5.11**) showed the rate and extent of surficial gas effluxes as well as the spatial distribution of O_2, CH_4, and CO_2 within the vadose zone were consistent with measurements collected in June of 2011 (**Figures 5.2-3 and 5.6**). The extended region of O_2 depletion and CO_2 enrichment between 10 and -25 m from the center of the oil is related to the presence of the low permeability layer (**Figure 1**, Sihota and Mayer (2012)), and is supported by field measurements of gas concentrations within this region (**Figure 5.6**). The second scenario investigated a fall/winter base case, which considered the effects of decreased SZNA rates and the elimination of shallow soil respiration (i.e., NSR; scenario 2). Results of this simulation showed the rate and extent of surficial gas effluxes, as well as the spatial extent of CH_4, and CO_2

within the vadose zone declined, while the spatial distribution of O_2 was extended (**Figure 5.12**). These results are reasonably consistent with field measurements of CO_2 fluxes collected in the fall (**Figures 5.2**), and indicated that a declining SZNA rate could explain a reduced surficial CO_2 flux. To evaluate the effects of a transient barrier to gas transport, we next modified scenario 2 through the inclusion of a low-permeability 'ice layer' at the ground surface (scenario 3). Results of this simulation showed a substantial decline in the rate and extent of surficial gas effluxes coupled with an increase in the concentration and spatial distribution of CH_4 and CO_2, and a decrease in the concentration and spatial distribution of O_2 (**Figure 5.13**), consistent with measurements collected in the winter (**Figures 5.2-3, 5.7-8, and 5.10**). To reproduce the winter field measurements, a high soil moisture content was needed in scenario 3, leaving only 10% gas saturation within the surficial soils. The modeling results provide additional evidence for a barrier to gas transport during the winter period – likely due to ice formation in surficial soils. Indeed, results of scenario 3 lend weight to the argument that gas migration becomes limited during periods when the soil is frozen. This is particularly relevant to the low-lying source zone area where rainwater has been observed to pool between wells 604G and 9014G (**Figure 5.1**). Such conditions facilitate the development of an ice layer when temperatures fall below freezing.

Conclusions

In this study we investigated *in situ* responses of SZNA processes to seasonal dynamics through evaluation of surficial CO_2 flux measurements conducted across a two-year period. We further evaluated the potential for changes in soil temperature and soil moisture contents to influence SZNA measurements using the surficial CO_2 flux method. Datasets were integrated using reactive transport simulations to evaluate the conceptual model developed based on field data.

Results highlighted the importance of the interplay between soil temperature and soil moisture in modulating both gas emissions and subsurface gas concentrations, and revealed the role of transient barriers to gas transport in regulating surficial CO_2 fluxes and subsurface gas concentrations. In addition, travel time calculations pointed to the potential for spring recharge to influence changes in subsurface gas concentrations in the early fall – potentially as a result of nutrient delivery.

Variability in the magnitude and distribution of surficial CO_2 fluxes suggested seasonal processes affected measurements of the mean annual crude oil SZNA rate at the study site. Comparison of seasonal changes in the magnitude and distribution of SZNA delineated at the ground surface also demonstrated that CO_2 efflux measurements are able to estimate the extent of the source zone within a factor of 2, independent of the seasons.

Evaluation of the error associated with SZNA rate estimates, and the relationship of SZNA rates obtained in different seasons to the mean annual rate, suggested CO_2 fluxes measured in the late fall or early winter would represent the best estimators of SZNA rates at the study site. In the winter, the decreased contribution of NSR to the total CO_2 flux was consistent with the decreased contribution of modern carbon to the age signature of samples collected from the shallow vadose zone. However, the presence of frozen ground conditions in 2012 likely resulted in an underestimation of the SZNA rate. Indeed, comparison of seasonal variations in vadose zone temperatures and surficial CO_2 fluxes showed periods of lower temperatures and wet or frozen surficial soils coincided with depressed fluxes. These observations pointed to a combination of biological and physical effects that modulated surficial CO_2 fluxes, whereby the transient presence of elevated soil moisture contents and/or an ice layer acted as a barrier to gas transport despite ongoing degradation processes at depth. In support of these arguments, periods

of frozen soils corresponded with elevated subsurface CO_2 concentrations, and a reduction of the CO_2 efflux signal at the ground surface, supporting the transient presence of an ice layer. Quantitative reactive transport simulations, constrained using field measurements, confirmed a barrier to gas transport could result in a depressed surficial CO_2 flux, even when the gradient between the reaction zone and the atmosphere was high, further supporting the interpretation of the field measurements and providing additional evidence that the system was subject to periodic transport limitations.

Taken together, the results of this study have important implications for evaluation of annual mass loss rates using surficial flux measurements and demonstrate that seasonal and physical changes must be considered when assessing contaminant degradation rates. However, as this study represents the first assessment of seasonal variations in SZNA rates using surficial CO_2 flux measurements, additional work is needed to understand the processes leading to the observed SZNA rates, and also how SZNA rates vary on a seasonal basis in other climates.

Tables

Table 5.1. Results of average surficial CO_2 efflux measurements' and SZNA estimates obtained using the background correction method and comparison of seasonally-weighted values.

Sampling period	**CO_2 flux** [μmol m^{-2} s^{-1}]						**Respiration Fraction** [-]	
	Total	**Total** (SD)	**NSR**	**NSR** (SD)	**CSR**	**CSR** (SE)	**NSR**	**CSR**
6/16/2011	6.6	0.8	4.2	0.8	2.4	0.4	0.64	0.36
10/27/2011	2.8	1.0	1.0	0.3	1.8	0.3	0.35	0.65
11/21/2011	2.4	1.3	0.7	0.4	1.7	0.4	0.29	0.71
12/20/2011	2.3	0.4	1.0	0.5	1.4	0.2	0.42	0.58
1/24/2012	0.7	0.3	0.3	0.1	0.4	0.1	0.36	0.64
5/14/2012	3.9	0.8	2.6	0.7	1.3	0.4	0.67	0.33
6/15/2012	5.4	1.3	4.1	1.2	1.4	0.7	0.75	0.25
10/2/2012	3.6	1.5	1.4	0.6	2.2	0.5	0.40	0.60
11/18/2012	2.2	0.9	1.1	0.6	1.1	0.4	0.51	0.49
12/11/2012	1.6	1.4	0.4	0.5	1.2	0.5	0.24	0.76
2/15/2013	2.3	2.0	1.2	1.6	1.1	0.3	0.53	0.47
3/8/2013	1.2	0.6	0.8	0.8	0.3	0.9	0.71	0.29
4/5/2013	1.8	0.9	1.6	0.6	0.2	0.3	0.88	0.12
7/12/2013	6.8	1.8	5.1	1.1	1.7	0.5	0.75	0.25
Season								
Spring	2.3	0.8	1.7	0.7	0.6	0.4	2.3	0.25
Summer	6.3	1.3	4.5	1.1	1.8	0.6	6.3	0.29
Fall	2.8	1.2	1.1	0.5	1.7	0.4	2.8	0.61
Winter	1.7	1.0	0.7	0.7	1.0	0.4	1.7	0.61

Table 5.2. Percent ancient carbon in vadose zone CO_2 samples collected from the shallow vadose zone (based on results of $^{14}CO_2$ measurements). 2009 values are taken from Sihota and Mayer (2012).

Location (well-port)	Percent Ancient Carbon in Vadose Zone CO_2		
	09-Aug	12-Jan	13-Jan
604G-7	66.9	20.1	87.3
9017G-8	74.9	83.2	88.7
9016G-8	-	63.1	69.4
9015G-8	90.9	92.6	93.9
9101G-7	54.1	67.6	64.9
518G-6	24.2	29.4	22.8
531G-7	9	14	-
530G-6	7.8	7.6	7.6

Figures

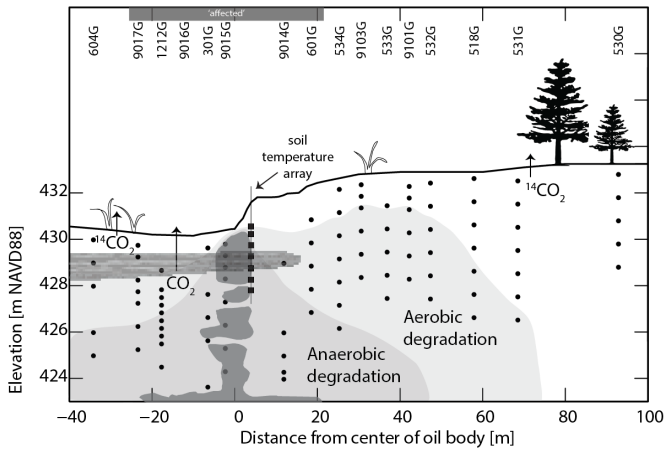

Figure 5.1. Conceptual overview of the vadose zone at the Bemidji site. Textured zone shows extent of an area of reduced hydraulic conductivity between ~ 428 and 430 m NAVD88. 'Affected' refers to wells affected by the residual oil (Sihota et al., 2011).

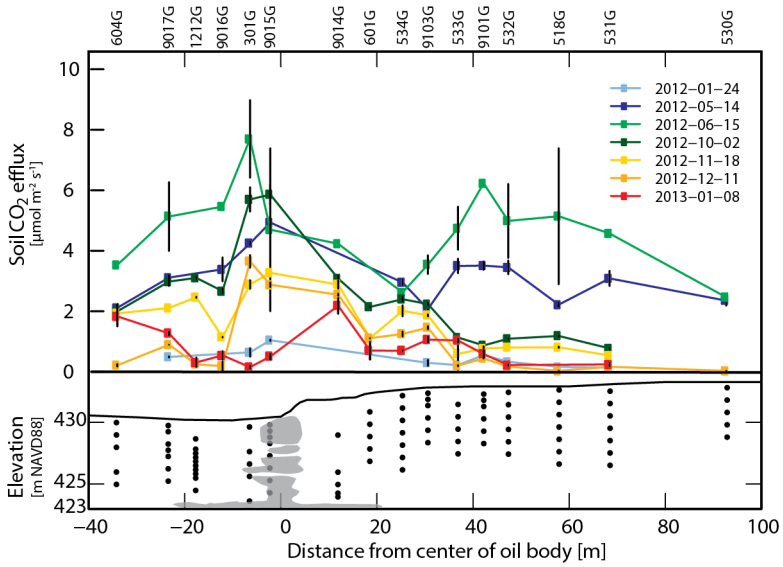

Figure 5.2. Seasonal variations in total surficial CO_2 efflux above the North Oil Pool. Locations of gas wells are identified on the upper x-axis.

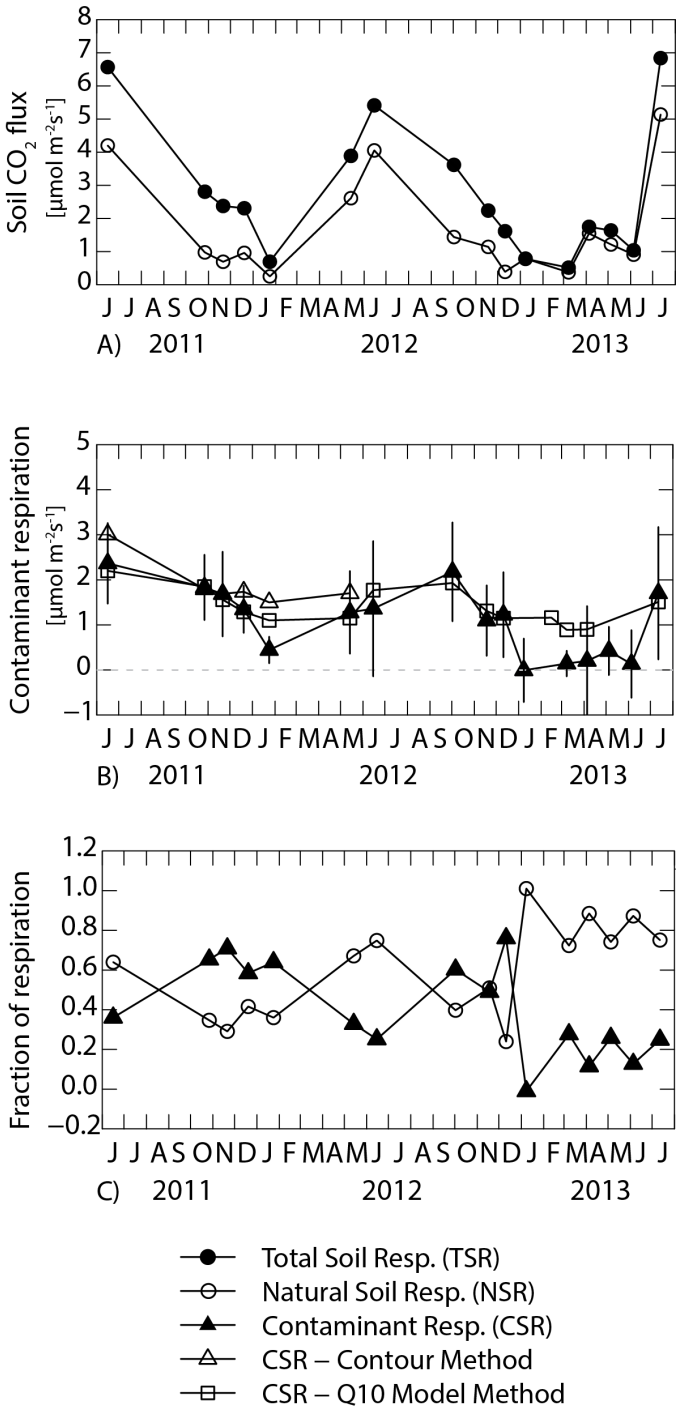

Figure 5.3. Seasonal variations in fraction of CSR and estimates of SZNA using the background correction method above the North Oil Pool. A) total and natural CO_2 fluxes, B) measured and modeled contaminant soil respiration, and C) fraction of natural and contaminant related CO_2 flux. Error bars represent standard deviations on the measurements.

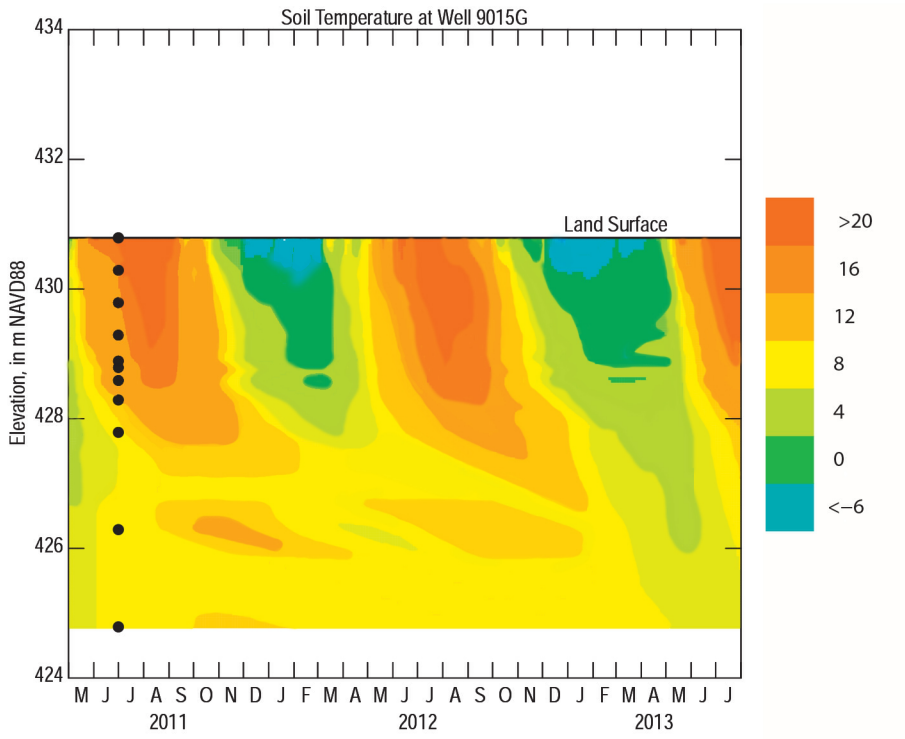

Figure 5.4. Soil temperature in the source zone [° C]. Circles represent measurement locations.

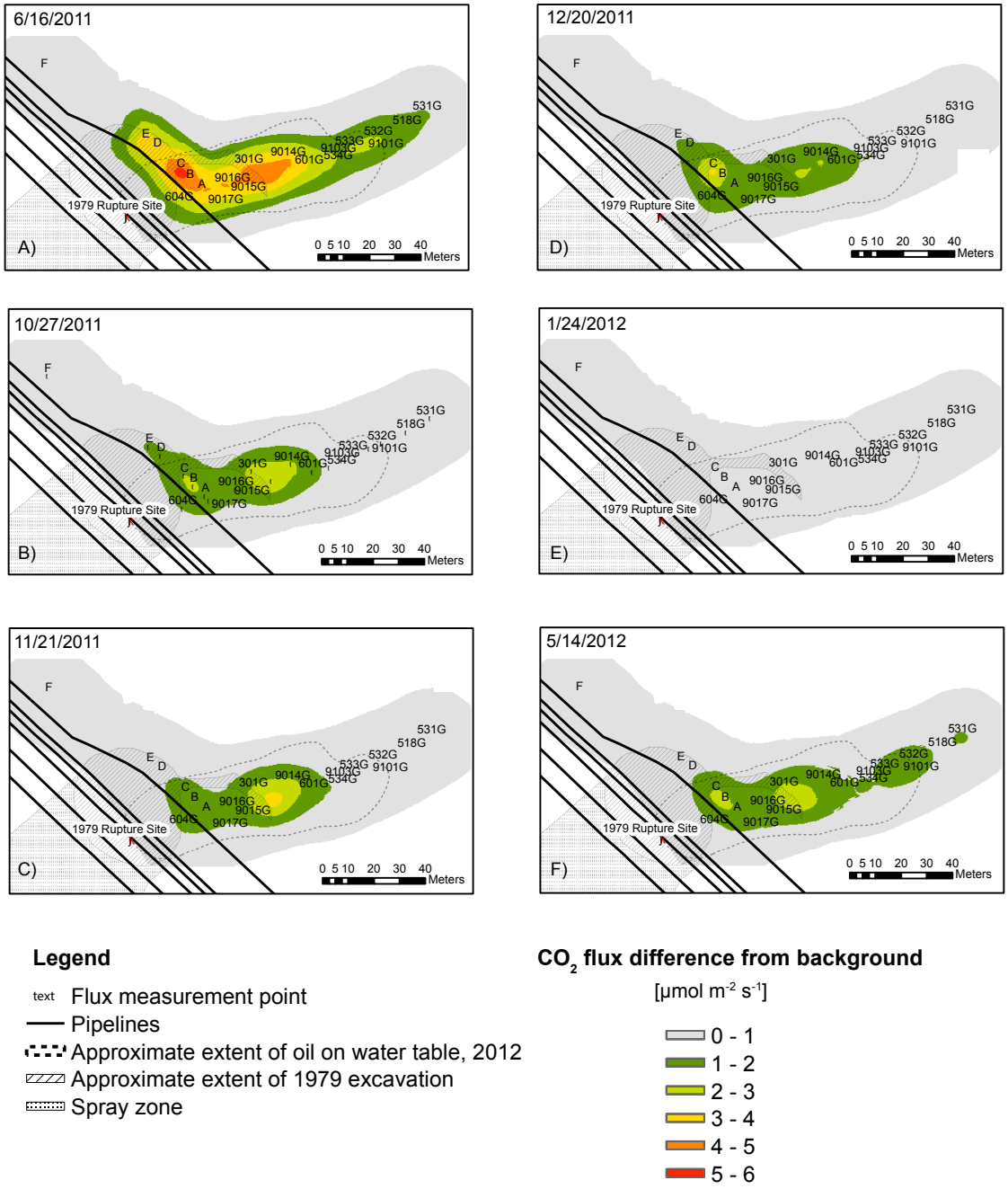

Figure 5.5. Seasonal variations in the extent of the surficial footprint of biodegradation above the North Oil Pool measured in 2011. Contour intervals show differences from background flux values in A) June 2011, B) October 2011, C) November 2011, D) December 2011, E) January 2012, and F) December 2012.

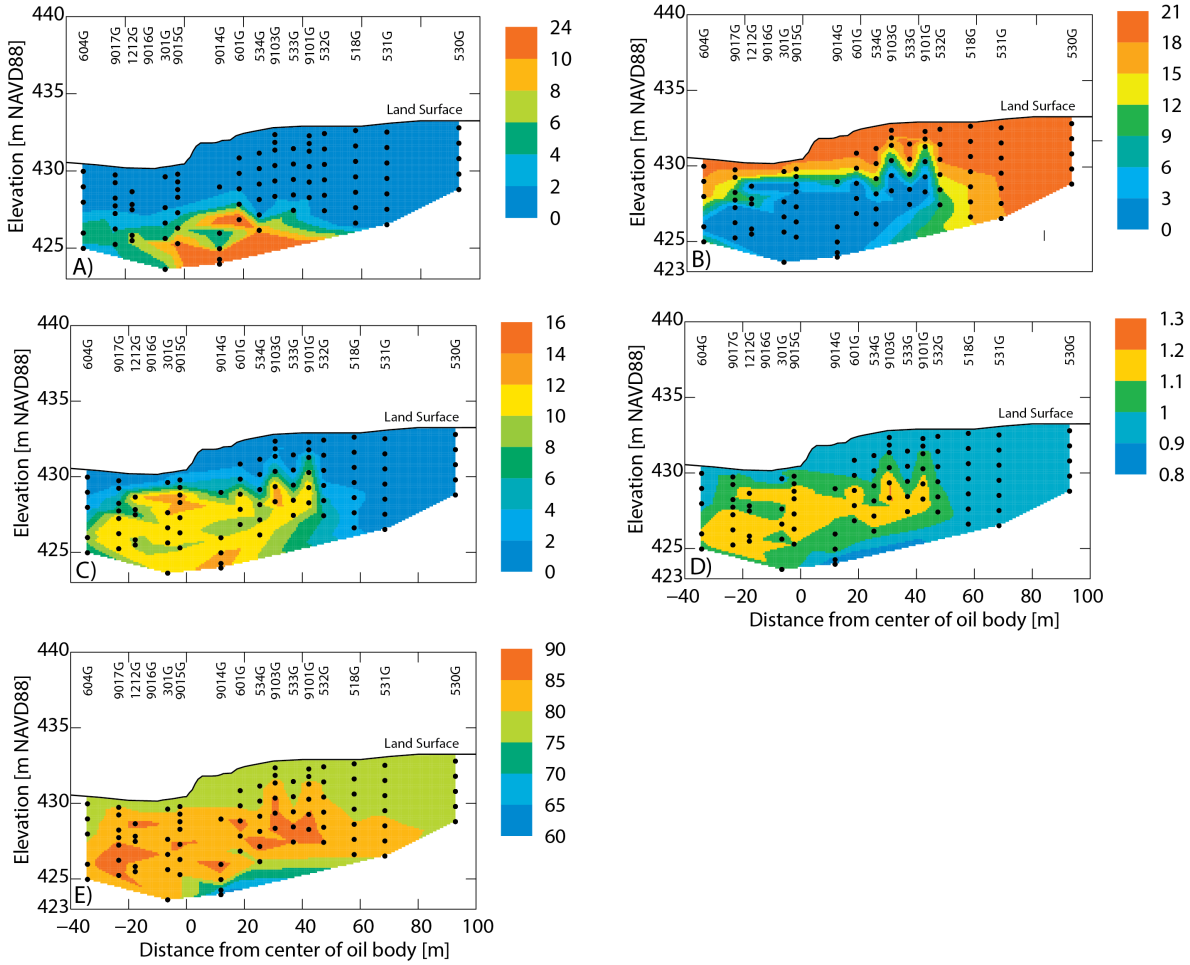

Figure 5.6. Composition of the vadose zone gases in the North Oil Pool in June 2011. Gas concentrations in % v/v for A) CH_4, B) O_2, C) CO_2, D) Ar, and E) N_2.

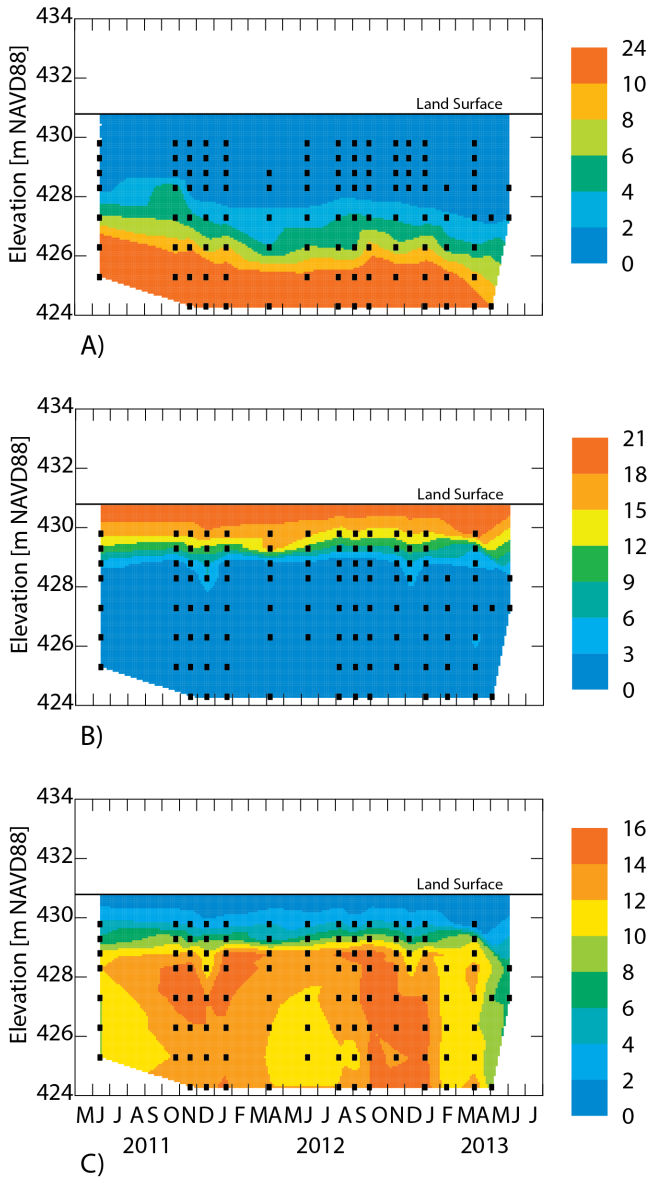

Figure 5.7. Seasonal variations in gas composition at the source zone well 9015G. Gas concentrations in % v/v for A) CH_4, B) O_2, and C) CO_2.

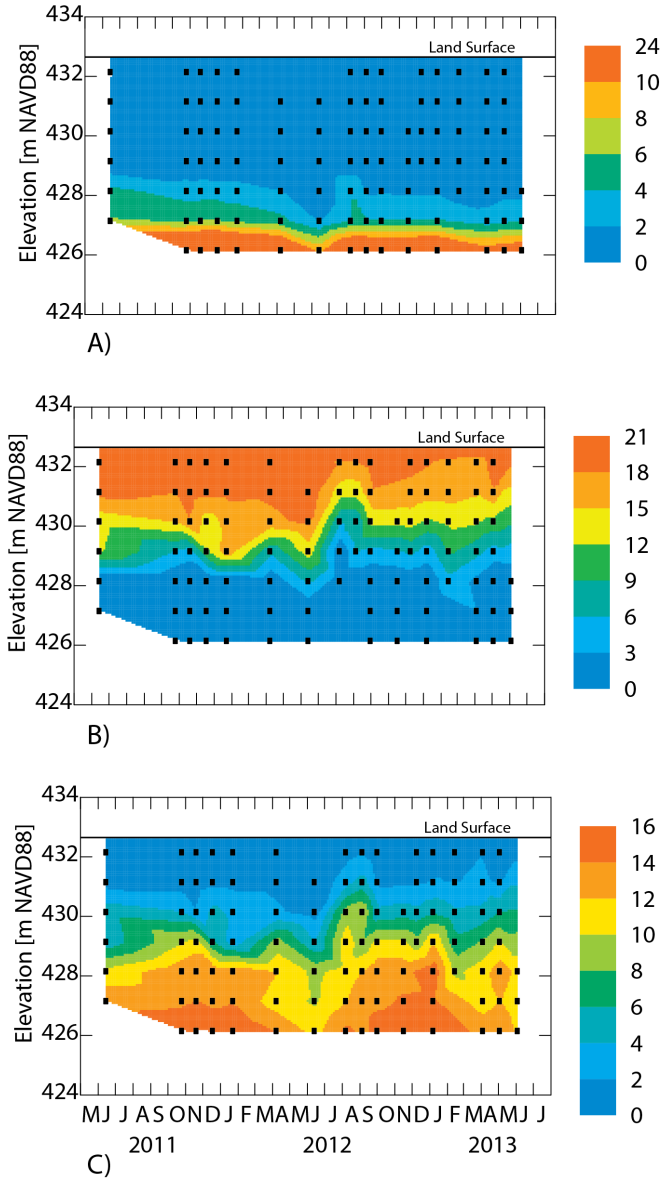

Figure 5.8. Seasonal variations in gas composition at the plume zone well 534G. Gas concentrations in % v/v for A) CH_4, B) O_2, and C) CO_2.

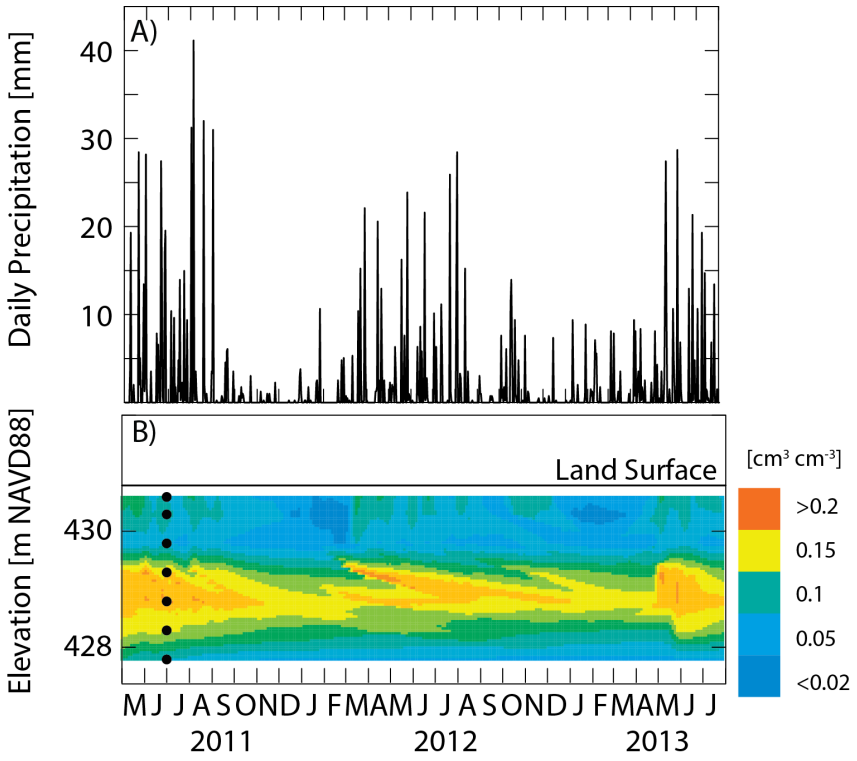

Figure 5.9. Seasonal changes in precipitation and soil water contents. A) daily precipitation and B) volumetric water content in the source zone.

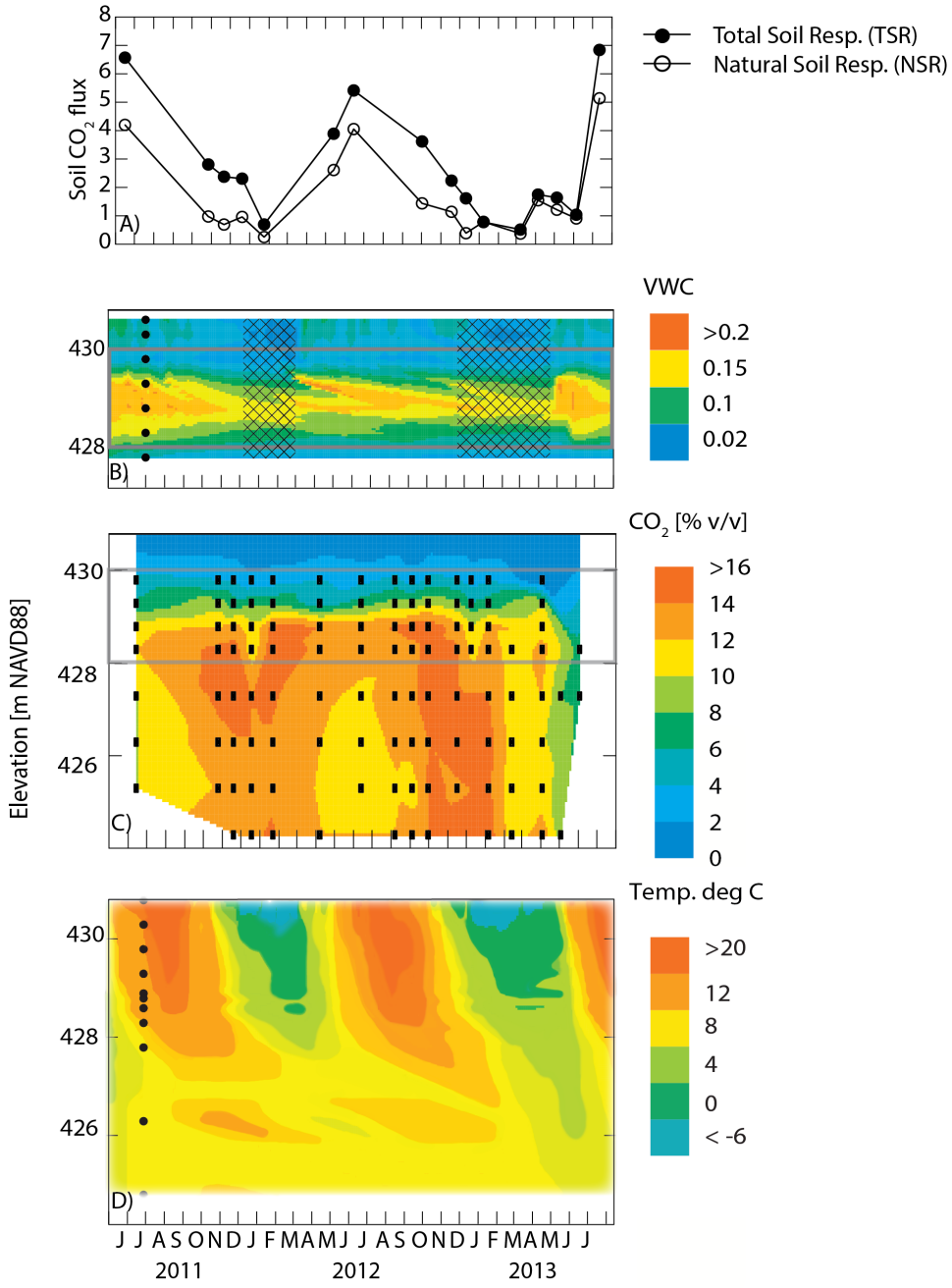

Figure 5.10. Field data supporting conceptual model of vadose zone processes at the Bemidji site. A) total and natural soil respiration, B) volumetric water content [cm^3 cm^{-3}], C) vadose zone CO_2 concentrations, and D) vadose zone temperatures. Grey box shows inset of volumetric water content measurement locations on vadose zone CO_2 concentrations. Hashed lines show periods where volumetric water content is underestimated based on frozen soil conditions.

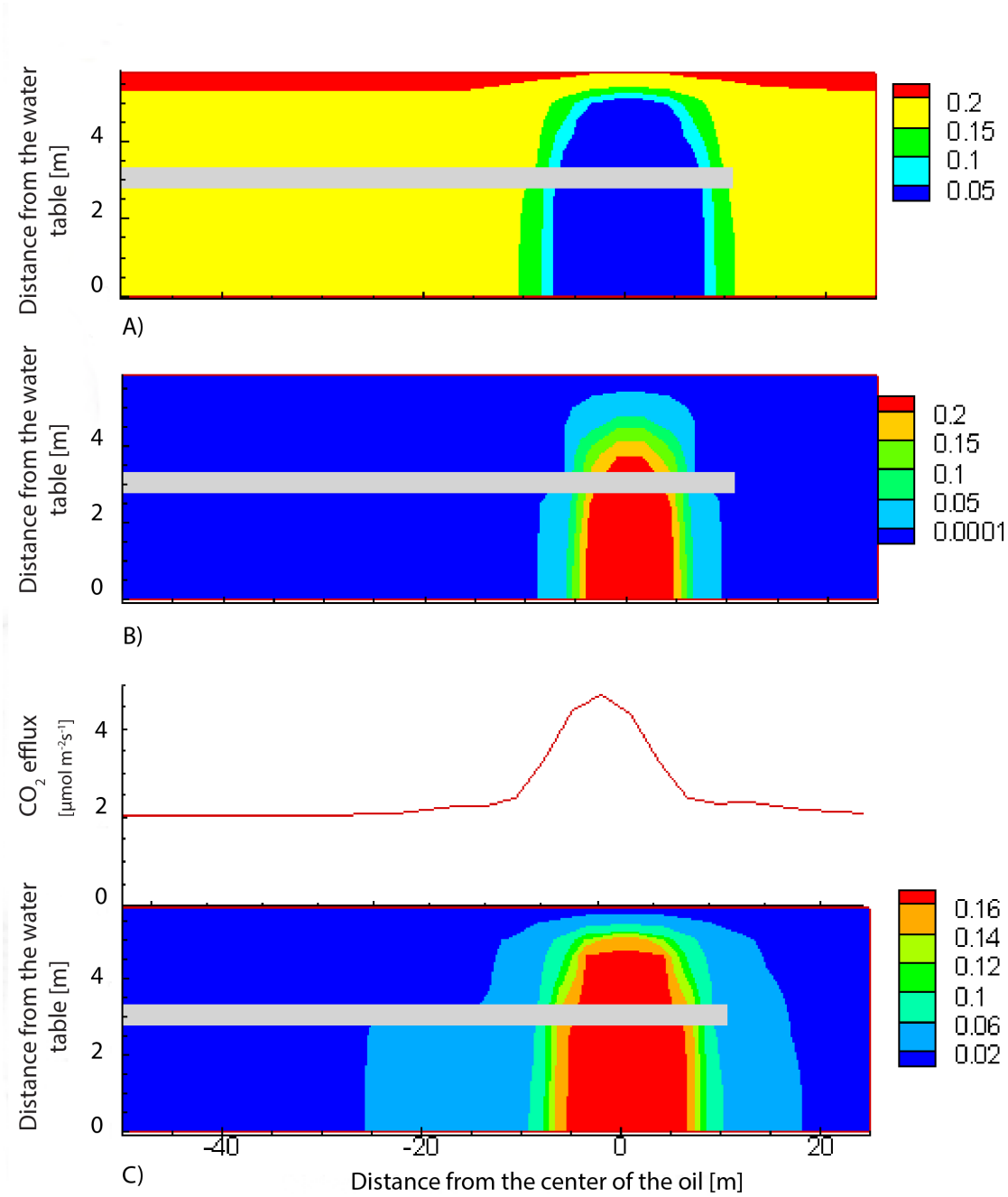

Figure 5.11. Scenario 1 simulation results. A) vadose zone O_2 concentration, B) vadose zone CH_4 concentration, and C) surficial CO_2 flux and vadose zone CO_2 concentration. Gas concentrations shown in % v/v. Grey rectangle shows extent of low permeability layer.

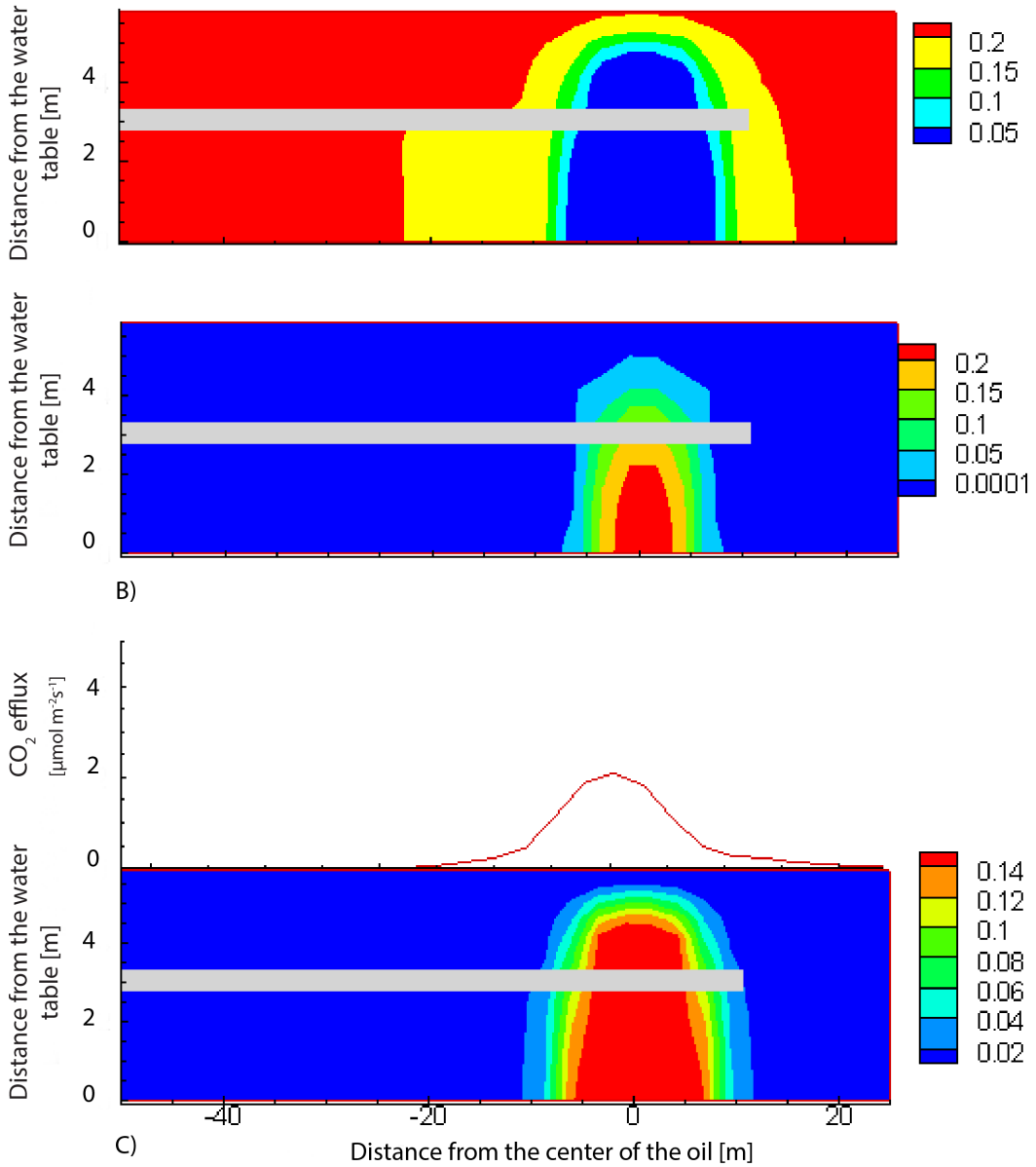

Figure 5.12. Scenario 2 simulation results. A) vadose zone O_2 concentration, B) vadose zone CH_4 concentration, and C) surficial CO_2 flux and vadose zone CO_2 concentration. Gas concentrations shown in % v/v. Grey rectangle shows extent of low permeability layer.

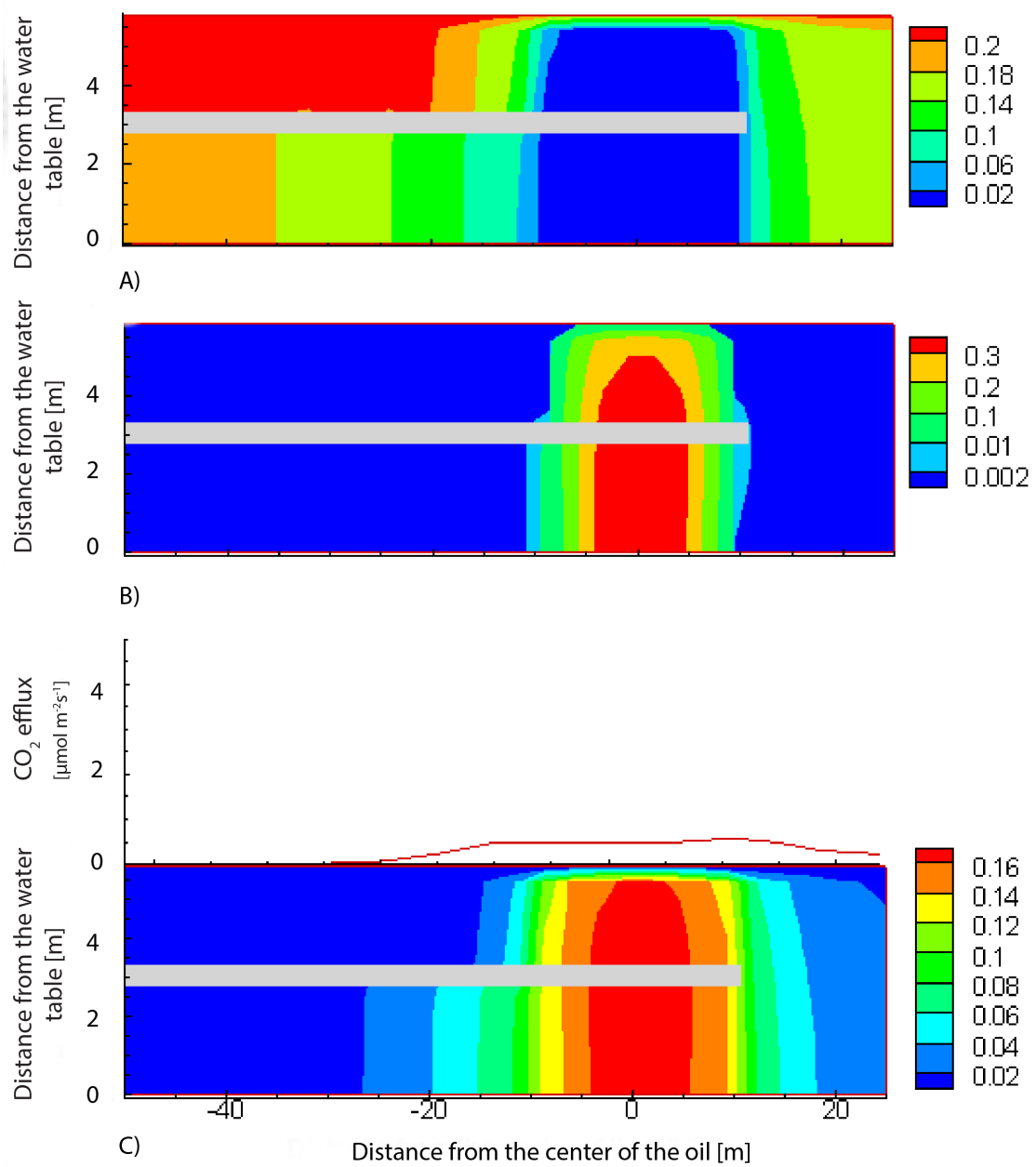

Figure 5.13. Scenario 3 simulation results. A) vadose zone O_2 concentration, B) vadose zone CH_4 concentration, and C) surficial CO_2 flux and vadose zone CO_2 concentration. Gas concentrations shown in % v/v. Grey rectangle shows extent of low permeability layer.

Chapter 6: CO_2 efflux and radiocarbon measurements for assessing SZNA at a large industrial site

Introduction

As demand for refined oil products has decreased and public concerns related to gasoline pricing has increased, the number of operating refineries in the United States has declined (IEA 2014). In 2010, for example, 124 refineries were in operation in the US, down from the 158 in operation in the 1990's. Based on the long lifetime of refineries (many being in operation for over 100 years), hydrocarbon contamination related to historical operating practices and accidental releases is to be expected (Andrews et al., 2010). Once refineries close, there is a need to characterize the extent of the contamination in order to evaluate options for site management and/or redevelopment. Source zone natural attenuation (SZNA; here defined as contaminant mass losses resulting from naturally occurring biodegradation (Kao et al., 2010)) can provide an important means for mass removal (Soga et al., 2004). Identifying areas where SZNA is occurring as well as areas with a lack of degradation (i.e., either unimpacted or unable to degrade) is valuable for site management purposes, including selection of remedial measures (Khaitan et al., 2006). Furthermore, quantifying natural mass loss rates is useful for estimating source zone longevity and assessing the utility of implementing engineered remediation measures under different conditions (Khaitin et al., 2006). However, measuring SZNA remains challenging, particularly due to the influence of subsurface heterogeneities on local scale contaminant degradation processes (e.g., variations in geology and contaminant morphology which influence delivery of electron acceptors and nutrients to the reaction zone (Bekins et al., 2005; Höhener and Ponsin, 2014)). This proves particularly challenging at large scale industrial sites, where the area of investigation can be substantial, and the heterogeneity of subsurface contamination can be significant. Historically, source zones have been delineated using invasive, and time and cost-intensive methods (Khaitin et al., 2006). Even for detailed site-investigations,

it is common that only a limited interpretation of the contaminant distribution and the processes controlling contaminant degradation is possible (Khaitin et al., 2006), despite substantial investments.

In many cases, the extent and rate of SZNA can be delineated based on the measurement of reactants and/or products resulting from SZNA (e.g., O_2 (Johnson et al., 2006) and CO_2 (Sihota et al., 2011), respectively). A conceptual representation of SZNA processes occurring within a contaminated vadose zone is presented in **Figure 6.1**. Johnson et al. (2006), for example, related a decrease in vadose zone O_2 content to a mass loss of total petroleum hydrocarbons (TPH) attributable to aerobic degradation through the measurement of subsurface concentration gradients. Recently, Sihota et al. (2011) equated the elevated CO_2 efflux above a crude oil containing vadose zone to a carbon flux from SZNA using a real time dynamic closed chamber method (LI-COR Inc., Lincoln, NE). A background correction (BGC) was used by subtracting measured CO_2 fluxes at locations unaffected by the contaminant (i.e., background locations) from CO_2 flux measurements at areas known (or suspected) to be impacted by the contaminant. Sihota and Mayer (2012) further evaluated the validity of this approach through a detailed investigation of the radiocarbon content of vadose zone CO_2, which was combined with quantitative reactive transport modeling to assess the processes resulting in the CO_2 flux measured at the ground surface. The measurement of radiocarbon is valuable as it provides a direct indication of the contribution of contaminant respiration to the total CO_2 flux measured with the chamber. This can be explained as the half-life of radiocarbon is relatively short (~5,730 years) in comparison to the age of the hydrocarbon (Conrad et al., 1997). Consequently, it can be expected that CO_2 derived from degradation of the hydrocarbon would be devoid of radiocarbon (e.g., Conrad et al., 1997; Sihota and Mayer, 2012) (**Figure 6.1**). In contrast, material in recent

contact with the atmosphere will have a high radiocarbon content, which may exceed 100%, due to radiocarbon releases associated with atomic bomb testing related to the Second World War (Trumbore, 2000)). As a consequence of the large discrepancy in radiocarbon between CO_2 produced from hydrocarbon destruction and CO_2 produced from natural soil processes, measurement of the radiocarbon content of the total flux captured in the chamber can be expected to provide a reasonable measure of the proportion of the CO_2 attributable to contaminant destruction. Results of the study conducted at the Bemidji crude oil spill site (Sihota and Mayer, 2012) showed the majority of CO_2 within the vadose zone was generated from oil degradation – likely associated with residual oil suspended in the vadose zone, and the exposed portion of the smear zone (although gas release from degradation within the submerged portion of the smear zone may also occur (Amos et al., 2005; Jones et al., 2014)). However, an investigation of the radiocarbon content of the CO_2 measured within the chamber itself was not conducted.

Source zone natural attenuation mass loss rates delineated using the surficial CO_2 flux method at the Bemidji site (Sihota et al., 2011; Sihota and Mayer, 2012) were shown to be comparable to other SZNA rates reported for the site (Revesz et al., 1995; Molins et al., 2010) indicating that the method can be used to obtain non-invasive estimates of SZNA rates. However, the spill at Bemidji consists of a single contaminant type (namely crude oil), which was released over a short period of time, and can be considered a point source. Large scale industrial sites are inherently more complex, providing motivation to evaluate how the CO_2 efflux method can be applied most effectively for site investigation of SZNA mass losses where the distribution of contaminant sources is more wide-spread and heterogeneous in distribution, composition and age (e.g., former refineries).

Specifically, the objectives of this work include:

1. Evaluating the spatial distribution of contaminant respiration (including identification of rapidly degrading 'hotspots', and inactive zones - possibly uncontaminated or not degrading) using CO_2 flux measurements with background correction (BGC) and radiocarbon correction (RCC) approaches (based on samples collected directly from the chamber) at a large industrial site;
2. Calculating and comparing the distribution and rate of SZNA mass losses obtained from the BGC and RCC approaches;
3. Correlating SZNA mass loss rates obtained from the BGC and RCC to site attributes to evaluate the suitability of either approach for subsurface site characterization;
4. Evaluating the suitability of the more cost-effective BGC approach for delineating SZNA.

Methods

Study site: The study site is a former refinery in the north-central USA. The climate in the region is characterized as semi-arid and natural vegetation at the site is sparse. Where present, it is dominated by a mixture of grasses and short brush. The refinery was operational between 1923 and 1982. During its lifetime, the facility processed crude oil from local sources into gasoline, diesel, and other fuels; asphalt and petroleum coke were also produced. The refinery was closed in 1982 and decommissioned beginning in 1996. By the end of 1999, buildings, processing units, tanks, underground piping, and other components had been removed. The vadose zone and aquifer that underlies much of the property is generally comprised of alluvial medium-coarse sands with some interbeds of fine sands and silts (based on soil boring logs collected by the site

consultants). A bedrock subcrop is located in the northeastern portion of the property, and in that location the alluvial aquifer is absent (**Figure 6.2**). Depth to groundwater ranges from approximately 1.5 to 11 meters below ground surface (mbgs), with the greatest depths observed at the southeastern corner of the property.

Since 1999, multiple subsurface investigations have been conducted on the property to support development of an LNAPL Site Conceptual Model, and inform the selection of remedial measures. The LNAPL distribution and chemical / physical properties have been characterized across the entire site covering approximately 4 ha (~150 acres). Nested vapor well data indicate that the smear zone LNAPL acts as a source of volatile constituents to soil gas, with possible smaller sources from sorbed hydrocarbons in the shallow subsurface. Based on the soil gas profiles determined from vadose zone monitoring points, the volatilized hydrocarbons are mineralized to CO_2 either directly (aerobic biodegradation) or indirectly (methanogenesis followed by aerobic biodegradation of methane (**Figure 6.1**)). Thus, the fossil fuel CO_2 effluxes at ground surface can generally be considered as representative of hydrocarbon losses from the vadose zone soils and smear zone.

CO_2 flux measurements: CO_2 flux measurements were conducted between September 9 and 12th, 2012. Following Sihota et al., (2011), measurements were conducted using a LI-8100A soil CO_2 flux system with a 20 cm survey chamber. For a detailed discussion of the method, the reader is referred to Sihota et al. (2011, 2013). In order to develop a high-resolution map of the SZNA processes, CO_2 flux measurements were conducted at 93 locations across a regular grid (hereafter referred to as the high-resolution background correction (HR-BGC) dataset; **Figure 6.2**). At each location, soil collars (20 cm ID PVC) were installed ~ 5-8 cm into the soil several

days prior to conducting the flux measurements, as recommended by Jassal et al. (2012). Replicate measurements at a single location were averaged. Background locations were selected based on data from previous site assessments that identified areas at the perimeter of the site as devoid of an LNAPL smear zone (**Figure 6.2**).

Radiocarbon measurements: To constrain results of the BGC correction approach, a second CO_2 flux dataset was collected at a subset (~ 1/3) of the sampling locations described in section 2.2. In this dataset (hereafter referred to as the medium-resolution radiocarbon correction (MR-RCC) dataset), the radiocarbon content of the measured flux was evaluated, to provide a more direct measure of TPH degradation. Measurements were conducted between September 12th – 14th, 2013. At each location, samples for radiocarbon analyses were collected at two time periods. To evaluate the ambient radiocarbon content, an initial sample was collected from inside the soil collar. This was necessary, as the potentially large area undergoing SZNA at the site may have affected the age signature of CO_2 present directly above the soil surface. Consequently, it cannot be assumed that the composition is 100% modern. Samples collected prior to the chamber measurement were collected ~ 5 cm above the ground surface from inside the collar and at the location where the chamber would be placed (to avoid any interference with the flux measurement itself). To assess the flux of radiocarbon from the subsurface, a final radiocarbon sample was collected from the chamber at the end of the measurement cycle. Samples were collected directly from a septum installed in-line to the chamber system (Sihota et al., 2013), using a gas tight syringe (VICI Inc., Magnum Series) and injected into pre-evacuated glass vials, which were immediately sealed with silicon to prevent sample loss or atmospheric contamination through the pierced septum. Samples were transported to the laboratory at UBC, where the CO_2

was isolated (following the methods described in Sihota and Mayer (2012)). Isolated samples were analyzed using accelerated mass spectrometry.

Calculation of SZNA rates: For comparison of mass loss rates across approaches and studies, results are presented in TPH equivalents. Following Lundegard and Johnson (2006), TPH is represented as $C_{10}H_{22}$. To calculate SZNA rates using the BGC, measured CO_2 fluxes were corrected for measured natural soil respiration rates (NSR) following Sihota et al. (2011). To calculate SZNA rates using the RCC with samples collected directly from the chamber, the initial and final CO_2 content within the chamber (measured using the infra-red gas analyzer in the LI-8100A) are corrected using the results of the radiocarbon content of the initial and final sample, respectively (equation 1).

$$\frac{\partial ac}{\partial t} = \frac{(C_1 * pac_1) - (C_0 * pac_0)}{t_1 - t_0} \qquad [1]$$

where ∂ac is the change in ancient carbon [ppm_v] over the measurement period (∂t [s]), C_0 is the initial CO_2 concentration in the chamber [ppm_v] and C_1 is the CO_2 concentration in the chamber at the second sampling time, pac_1 and pac_0 are the initial and final radiocarbon contents in the chamber (with pac (i.e., the percent of ancient carbon) = 100-pmc). The corrected CO_2 increase over time is then used to calculate a CO_2 flux resulting from degradation of the contaminant using the equations described in LI-COR (2007), and Sihota et al. (2013). While longer time periods (up to 20 minutes) were required to minimize the sample volume extracted from the chamber headspace, time intervals used for CO_2 flux calculations were consistent between the datasets and with standard practice (Jassal et al., 2012).

Site metadata: To evaluate the ability of SZNA rates calculated from surficially measured CO_2 fluxes to identify site attributes relevant for assessing remediation goals, a suite of subsurface parameters was selected for comparison to CO_2 fluxes and SZNA rates (calculated using the BGC and RCC). Metadata evaluated include: thickness of the smear zone; thickness of the smear zone above the average water table (under pumping conditions); LNAPL persistence (i.e., the frequency of LNAPL occurrence above 3 cm thickness in wells from 2000 to 2010); toluene, benzene and naphthalene mole fraction in LNAPL (analyzed in samples collected from the smear zone LNAPL and soil); benzene and toluene concentration in soil from 0.15 to 1.8 mbgs (mg kg^{-1}); and maximum fluorescence intensity for a given laser-induced fluorescence (LIF) push, normalized to the maximum for the full LIF data set (Supporting Information (provided in **Appendix 5**) **Figure A5.1**). Statistical analyses of CO_2 flux datasets and correlations with site parameters were conducted, using methods as outlined in the SI Methods.

Results and discussion

HR-BGC dataset: Total CO_2 fluxes measured using the chamber ranged from 0.4 to 46.2 μmol m^{-2} s^{-1} with an average of 4.5 μmol m^{-2} s^{-1} (**Table 6.1, Figure 6.3**). Lowest fluxes were measured in the north-western and south-eastern regions of the site, while highest fluxes were clustered into two areas near the center of the property (**Figure 6.3**). The mean background CO_2 flux was 1.8 μmol m^{-2} s^{-1}, consistent with CO_2 fluxes measured at natural sites under similar conditions (Raich and Schlesinger, 1992; Dugas, 1993). Above the contaminated region, the mean CO_2 flux was 4.2 μmol m^{-2} s^{-1}. For this calculation and further statistical analysis, the high value of 46.2 μmol m^{-2} s^{-1} was considered an outlier and omitted for reasons discussed below, resulting in a

conservative estimate of the CO_2 flux above the contaminated region with a range of 0.4 – 14.2 μmol m^{-2} s^{-1}.

Using the BGC, SZNA was identified at 80% (73/92) of the measurement locations, resulting in an average SZNA rate of 2.5 μmol m^{-2} s^{-1} (SE = 0.3 μmol m^{-2} s^{-1}, n = 92) with a range of 0.2 to 12.4 μmol m^{-2} s^{-1}. When weighted for the area represented by the measurement (**SI Figure 2B, 3B**), the average SZNA rate was 2.7 μmol m^{-2} s^{-1}. SZNA 'hotspots' were identified as fluxes significantly greater than NSR. Using a threshold of ~ 2.5 x the NSR rate, SZNA hotspots were identified at 15 locations pointing to local variations in natural degradation potential (**Figure 6.3**).

To evaluate the sampling density required for adequately characterizing overall SZNA mass losses, the sensitivity of the average SZNA rate to the number of samples included in the estimate was assessed. Using multiple realizations from the dataset shows reduced benefit of sampling above ~ 50 locations (**Figure 6.4, Figure A5.4**), suggesting this site could have been adequately characterized using one point per 1.2 x 10^4 m^2.

MR-RCC and MR-BGC datasets: Results of radiocarbon measurements from samples collected both prior to, and at the end of the measurement (directly above the soil surface, and from the chamber, respectively) show variability in the age of emitted CO_2 across the site. The oldest initial sample (8.1 percent modern carbon – pmc) was collected at B7 (**Figure 6.2**). The youngest initial samples were collected close to the periphery of the site (104.3 and 99.6 pmc at H3 and I9, **Figure 6.2**). The average initial carbon composition was 88 pmc, with a median of 76.6 pmc. These results highlight the variability in NSR across the site and reinforce the need for assessing the initial radiocarbon content of CO_2 prior to chamber closure. The oldest and youngest final

samples were collected at B7 (26.9 pmc) and C6 (94.2 pmc), respectively (**Figure 6.2**). The average final carbon composition of CO_2 in the chamber was 46.6 pmc and the median was 66.3 pmc. These results highlight the variability in CSR across the site and demonstrate the utility of collecting radiocarbon measurements for informing local estimates of SZNA rates. It should be noted that, depending on the relative magnitude of the natural and contaminant-related CO_2 flux, a carbon mass loss from SZNA may occur even when overall pmc of the sample increases between the initial and final sample.

To evaluate the areal extent of degradation processes and identify hotspots of SZNA, contaminant degradation rates obtained using the BGC and RCC were mapped onto the site grid (**Figure 6.5**). Using the BGC, CO_2 fluxes attributable to SZNA above the 1.8 μmol m^{-2} s^{-1} NSR threshold were identified at (77%) 24/31 locations resulting in an average SZNA rate of 2.1 μmol m^{-2} s^{-1} (SE = 0.4 μmol m^{-2} s^{-1}, n = 32) with a range of 0.3 to 8.8 μmol m^{-2} s^{-1}. When weighted for the area represented by the measurement (**Figures A5.2B, A5.3B**), the average SZNA rate was 2.3 μmol m^{-2} s^{-1}. Applying the RCC results in a SZNA rate of 2.0 μmol m^{-2} s^{-1} (SE = 0.4 μmol m^{-2} s^{-1}, n = 32) with a range of 0.2 to 8.3 μmol m^{-2} s^{-1}. When weighted for the area represented by the measurement (SI Figure 3C), the average SZNA rate was also 2.0 μmol m^{-2} s^{-1}. Evaluation of SZNA 'hotspots' shows 6 and 5 locations using the BGC and RCC, respectively (**Figure 6.5**)).

Comparison between SZNA rates calculated using the BGC and RCC shows reasonably good agreement in total mass loss rates (**Table 6.1**) with results of bootstrapped distributions providing additional confidence in the comparability of these estimates (**Figure A5.4**). However, differences exist in the spatial distribution of the SZNA rates (**Figure 6.6**). This can be explained by the lack of sensitivity of the BGC to variations in NSR, which remove SZNA rates below the NSR threshold, and overestimate SZNA rates in areas where actual NSR is greater than the

average NSR value used in the BGC. Overall, this suggests that the BGC provides a reasonable estimate of mass loss rates, and a conservative estimate of the area undergoing SZNA. Moreover, these results highlight both the importance of initial radiocarbon measurements, and the utility of the RCC for identifying location-specific SZNA rates and hotspots. This information could be used to inform well placement and identify both areas to target with enhanced remediation and areas where SZNA is operating efficiently, suggesting the more labor and cost intensive RCC approach (~ a 10 and 300 fold time and dollar increase, respectively) is warranted in some scenarios.

Variability in NSR rates across the site can be further explored using results of radiocarbon measurements. The mean NSR rate calculated using radiocarbon measurements is 1.9 μmol m^{-2} s^{-1} (SE = 0.3), with a range of 0.1 – 5.5 μmol m^{-2} s^{-1}; on average NSR represents ~ 53 % of the total flux. These values are well within the range of natural CO_2 fluxes in similar environments (Raich and Schlesinger, 1992; Dugas, 1993) and further suggest the 46.2 μmol m^{-2} s^{-1} flux (of which ~ 68 % of the flux represented NSR) represents an outlier. The discrepancy between the NSR rate used for the BGC, and the NSR rate determined from radiocarbon measurements suggests the BGC approach may slightly overestimate the SZNA rate in this study. However sensitivity analyses shows that the 0.1 μmol m^{-2} s^{-1} difference yields only a 0.07 and 0.08 μmol m^{-2} s^{-1} change in SZNA rates calculated using the BGC on the HR and MR datasets, respectively, which is within the error of the estimates (**Table 6.1**).

Evaluation of SZNA mass losses*:* SZNA rates calculated in this study can be converted to mass loss rates for the entire area of the refinery (60 ha), and then compared to both historical data from the study site, and mass loss rates reported in the literature. To facilitate these comparisons,

mass loss rates are calculated using TPH equivalents per day (as $C_{10}H_{22}$). Longer-term extrapolations are not attempted, as conditions controlling degradation (e.g., temperature) are expected to show seasonal variability. For example, soil frost up to a meter deep can be expected in the study region (Soil Survey Staff 2014).

Using average SZNA rates for each dataset and correction approach, results in mass loss rates of ~ 1.5, 1.3 and 1.2 x 10^3 kg-TPH day^{-1} (for the HR-BGC, MR-BGC, MR-RCC datasets, respectively). Taking another approach, the area represented by each measurement point (typically ~ 6.6 x 10^3 m^2 and 2.3 x 10^4 m^2 for the HR-BGC and MR-RCC/BGC datasets, respectively; **Figures A5.3, A5.4**) is assigned the SZNA rate obtained from that location. Results of these calculations provide mass loss rate of ~ 2.0, 1.6 and 1.5 x 10^3 kg-TPH day^{-1} (for the HR-BGC, MR-BGC, MR-RCC data sets, respectively). Finally, mass loss rates can be calculated based on an integration of the contour areas presented in **Figures 6.3 and 6.5**, resulting in mass loss rates of ~ 1.7, 1.3 and 1.1 x 10^3 kg-TPH day^{-1} (for the HR-BGC, MR-BGC, and MR-RCC data sets, respectively).

Overall, mass loss rate comparisons demonstrate reasonable agreement between the different datasets and correction approaches. The higher value obtained from the HR-BCG approach is explained by increased sampling density, which resulted in several additional areas of elevated effluxes being identified (compared to the MR-RCC dataset (**Figures 6.3 and 6.5**)). Furthermore, evaluation of the sampling density needed to achieve a stable estimate of the site-wide SZNA rate (**Figures 6.4**) suggests the 32 samples collected in the MR-RCC may be insufficient to capture the variation across the site. Within the medium resolution dataset, the lower average mass loss rate obtained from RCC (as compared to the BGC) results from sensitivity to variations in natural soil respiration and, consequently, its ability to constrain

SZNA mass losses when natural soil respiration is high. Comparing the different areal-based corrections (i.e., point-based and contoured) also suggests the resolution of the MR-RCC dataset was insufficient to capture the site-wide variation in SZNA rates, and indicates that higher-resolution sampling is important, particularly for constraining the local distribution of mass loss rates (**Figures 6.3 and 6.5; Figures A5.2 and A5.3**).

To compare mass loss rates determined from this study to those reported in the literature, total mass loss rates obtained from the point based mapping are converted to TPH equivalents per m^2. This set of values was selected as the most characteristic representation of SZNA processes at the site and results in values of ~ 2.9, 2.1, and 1.8 g TPH m^{-2} day^{-1} (for the HR-BGC, MR-BGC, MR-RCC data sets, respectively; **Table 2**). For comparison, within the direct vicinity of the highly-impacted source zone at the site of a crude oil pipeline rupture near Bemidji, MN, Sihota et al. (2011) estimated an average mass loss rate of ~ 6.3 g TPH m^{-2} day^{-1} (using CO_2 flux measurements). At the Guadalupe Oil Field in California, Lundegard and Johnson (2006) estimated natural mass loss rates of diluent in the range of 0.14 – 6.6 g TPH m^{-2} day^{-1} (using vadose zone gas concentration profiles). Using O_2 profiles reported by Luo et al. (2009) near a maintenance warehouse (**Figure 6.2**), concentration gradient calculations result in mass loss estimate of ~ 1.9 g TPH m^2 d^{-1}, which is similar to the values estimated based on CO_2 fluxes (**Figures 3,4; Table 1, 2**). Using O_2 consumption rates below a building where vadose zone sediments were impacted by a tarry LNAPL source, Lundegard et al. (2008) estimated SZNA on the order of 2 – 5 g TPH m^{-2} day^{-1}. Overall, natural mass loss estimates obtained in this study are within the range of those obtained from the literature, and also demonstrate variability in mass loss rates within and among study sites.

To set mass loss rates obtained from CO_2 fluxes into the broader context of remediation at the site, hydrocarbon mass removal rates achieved by active remedial systems are evaluated. Most recently, LNAPL has primarily been recovered via groundwater interceptor trenches adjacent to the barrier wall (a hydraulic barrier between the aquifer and the adjacent river; **Figure 6.2**). To maintain the potentiometric surface below the water level in the river, pumping draws water and LNAPL into the collection system. The maximum annual LNAPL recovery rate since 2000 was 5.4 x 10^3 kg-TPH day^{-1}, with an average of 2.7 x 10^3 kg-TPH day^{-1}, and much lower rates in recent years. These mass loss rates are comparable to those achieved from SZNA across the site (~1.1 to 2.0 x 10^3 kg-TPH day^{-1}, demonstrating that, when placed in the context of the entire area undergoing degradation, SZNA mass loss rates can rival those achieved by engineered systems. LNAPL mass was also removed in a partial smear zone excavation (~ 6,300 m^2; **Figure 6.2**) conducted in 2013, which involved extraction of ~ 1.2 x 10^5 kg of LNAPL, followed by land farming of recovered soils. For comparison, an equivalent mass could be removed by SZNA in 0.2 – 0.4 years, based on SZNA rates estimated for the entire site, further emphasizing the efficiency of SNZA processes.

Finally, calculated mass loss rates obtained from SZNA estimates can be contrasted against mass removal rates obtained from other sites where active recovery has occurred. However, it must be stressed that direct comparison of mass losses obtained from SNZA and active recovery measures is challenging. Consequently, this represents a first order comparison for illustrative purpose only. For a dual-pump recovery system (i.e., a coupled groundwater and skimmer pump) at the Bemidji site, for example, Delin and Herkelrath (2014) reported a crude oil recovery rate of ~ 25 – 300 L day^{-1} (roughly equivalent to 500 – 6,000 kg day^{-1} of $C_{10}H_{22}$), over the five years that the system was in operation. Peak removal rates were recorded for ~ the

first year, with a substantial decrease at later times. Assuming mass recovery occurred evenly across the 2.8 x 10^2 m^2 footprint of the crude oil (J. Trost, pers. comm.) results in an estimated mass loss rate of ~ 0.18 – 2.1 kg of $C_{10}H_{22}$ m^{-2} d^{-1}. It is worth noting that, at the Bemidji site, the remedial effort also resulted in the development of a secondary anoxic groundwater plume, which persisted for over five years following the cessation of remediation (Delin and Herkelrath, 2014), underlining the potentially uncertain and complex results of remediation efforts, even for engineered systems in relatively favorable conditions. Although natural source zone attenuation results in lower mass removal rates, this is contrasted by the observation that SZNA tends to occur across the full contamination footprint, rather than just an area undergoing remediation. Broadly, this comparison suggests that both engineered systems and SZNA are effective for contaminant mass removal, and that consideration of site management goals will inform the suite of approaches selected.

Site metadata: Using the HR-BGC dataset correlation analyses show both total CO_2 fluxes and SZNA rates to have significant associations with source zone thickness; source zone thickness above the water table (measured in 2012); maximum fluorescence intensity in LIF; LNAPL persistence; and toluene, naphthalene and benzene mole fractions (**Table A5.1, Figure A5.1**). In the HR-BGC dataset, strongest associations are found for source zone thickness and naphthalene mole fraction, while weaker, yet significant, associations were found for other parameters (**Table A5.1**).

To further compare results obtained from the BGC and RCC, results of correlation analyses are explored using the MR-RCC dataset. Source zone thickness above the water table, LNAPL persistence, and benzene mole fraction were significantly correlated with SZNA rates

obtained from the RCC. This suggests areas with relatively elevated amounts of mass in place above the water table are degrading most rapidly at this site, consistent with increased degradation rates found for elevated contaminant concentrations in weathered LNAPL samples (Björklöf et al., 2008). Results show correlations between SZNA rates obtained using the RCC are stronger than those obtained using the BGC (**Table A5.1**), suggesting the RCC provides a more direct indication of subsurface parameters of concern. However, when SZNA rates obtained using the BGC for the MR and HR datasets are compared, results show correlations between site parameters and SZNA rates are stronger for the HR than the MR dataset. This suggests that, with sufficient sampling resolution, the BGC can also provide a useful indication of subsurface contamination characteristics.

To further investigate the relationship between rapidly degrading areas and contaminant characteristics, the distributions of site parameters at SZNA hotspots are considered. Results show elevated SZNA rates tend to occur in locations where total LNAPL mass and volatile content is relatively high. For example, using the HR-BGC dataset, the area-weighted average value of each subsurface parameter is higher at hotspot locations, as compared to locations where lower CO_2 fluxes were measured (**Table 6.3**). As treatment often prioritizes areas where LNAPL mass and content of toxicologically relevant chemicals are elevated an understanding of the distribution of these parameters is important for site remediation (ITRC 2009). The correlation of CO_2 fluxes with parameters of concern suggests surficial CO_2 fluxes could be used as a rapid and cost-effective screening tool for identifying contaminated areas, and providing insight on areas to target with active remediation.

Conclusions

This study represents both the first application of high-resolution CO_2 flux measurements for evaluating areas undergoing SZNA at a large-scale industrial site and the first direct comparison of the radiocarbon and background correction approaches for evaluating SZNA. The spatial distribution of measured SZNA rates shows variability across the site. However, evaluation of the sampling density required to characterize an average mass loss rate indicates this could be achieved with roughly half the measurements collected in the high-resolution dataset. Comparison of SZNA rates obtained from the BGC and RCC approaches demonstrate that, while overall mass loss estimates are reasonably consistent, local differences in mass loss rates exist. These discrepancies are attributed to the BGC's lack of sensitivity to variability in NSR, which results in an inability to measure SZNA rates below the assumed NSR value, or constrain SZNA rate estimates in areas where NSR values are large, implying that the BGC provides a less accurate depiction of the spatial distribution of the effluxes at this site. Overall, the results suggest that the rapid and inexpensive BGC provides a reasonable estimate of average mass losses, and that the approach can be most useful when rapid assessment of a site-wide mass loss rate is desirable. In comparison, the RCC approach is better suited for assessing variability in NSR processes and is therefore more valuable when accurate knowledge regarding local mass loss rates is important (e.g., for informing well-placement decisions).

Comparison of SZNA rates to subsurface parameters reveals CO_2 flux measurements are most influenced by LNAPL abundance and composition in the vadose zone, supporting the use of the surficial CO_2 flux method for identifying the presence of contaminants within the shallow subsurface. Correlations between SZNA rates and subsurface contaminant characteristics show strongest correlations are obtained for RCC mass loss rates, lending weight to the assertion that

radiocarbon results are a good indicator of SZNA processes. However, with an increased number of sampling locations (i.e., comparing the BGC for the HR and MR datasets), the correlations between BGC mass losses and site parameters are stronger, suggesting the BGC approach represents a useful tool, provided the number and spatial distribution of sampling locations is sufficient.

Mass loss rates calculated from CO_2 fluxes in this study are within the range of those estimated from other sites where SZNA or enhanced source zone depletion is occurring (**Table 6.2**). The variability in SZNA rates estimated across the large footprint for the current study supports the within-site variation documented elsewhere, and adds the observation that this variation is related to subsurface source zone characteristics. Interestingly, comparison of mass loss rates attributed to SZNA to examples of engineered mass removal show that, when normalized over the entire study area, natural mass losses can rival those obtained from engineered systems, under some conditions. However it should be stressed that engineered systems are often needed to achieve goals other than mass removal (e.g., the barrier wall at the study site evaluated in this work, or when a sensitive receptor may be impacted by the contaminant). In addition, while it is tempting to scale the results of the snapshot measurements of SZNA obtained in this study to annual mass loss rates, strong seasonal fluctuations in environmental parameters (e.g., temperature) suggest that the annual variations in mass losses obtained from CO_2 flux measurements requires evaluation before annual mass loss trends can be properly calculated. Consequently, future work will focus on evaluating SZNA mass loss rates obtained from CO_2 fluxes over seasonal timescales.

Tables

Table 6.1. Comparison of SZNA mass loss rates using the BGC and RCC methods. Fluxes are reported in μmol m^{-2} s^{-1}. * determined from radiocarbon measurements

Dataset	**HR-BGC**	**MR-RCC**	
Correction applied	**BGC**	**BGC**	**RCC**
Raw CO_2 flux Range [μmol m^{-2} s^{-1}]	0.4 – 46.2	0.4 – 41.5	
BGC value [μmol m^{-2} s^{-1}]	1.8	1.8	1.9*
SZNA rate Average (SE) [μmol m^{-2} s^{-1}]	2.5 (0.3)	2.1 (0.5)	2.0 (0.4)
SZNA rate Minimum [μmol m^{-2} s^{-1}]	0.1	0.3	0.2
SZNA rate Maximum [μmol m^{-2} s^{-1}]	12.4	8.8	8.3
Number of locations with SZNA identified	73	31	24
Total num. sample locations	92	31	31
% SZNA identification	80	-	77

Table 6.2. Comparison of SZNA mass loss rates reported in this study to mass loss rates obtained for other technologies and sites. TPH is reported as ($C_{10}H_{22}$). + point based area correction *shown in Figure 1. ^normalized to total site area.

	Site	**Condition**	**Mass loss rate** [g TPH m^{-2} day^{-1}]	**Reference**
Passive Remediation	Former refinery	BGC (HR-BGC dataset)	2.9^{+}	this study
	Former refinery	BGC (MR-RCC dataset)	2.1^{+}	this study
	Former refinery	RCC correction (MR-RCC dataset)	1.8^{+}	this study
	Former refinery	O_2 gradients	1.9	Luo et al. (2009)
	Guadalupe Oil Field (diluent in sand)	O_2 gradients	0.14 – 6.6	Lundegard and Johnson (2006)
	Crude oil pipeline rupture in sand (Bemidji, MN)	Source Zone CO_2 fluxes (BGC correction)	6.3	Sihota et al. (2011)
Active Remediation	Substructure in sand with tarry LNAPL	O_2 consumption	2 – 5	Lundegard et al. (2008)
	Former refinery*^	Interceptor trench	4.4 – 8.9^	this study
	Former refinery*^	Smear zone excavation	19,000 [g TPH m^{-2}]	this study
	Crude oil pipeline rupture in sand (Bemidji, MN)^	Dual-pump extraction	180 – 2,100^	Delin and Herkelrath (2014)

Table 6.3. Comparison of site metadata and SZNA hotspots identified using the BGC method and the HR-BGC dataset. CO_2 flux threshold set as ~ 6.5 x background NSR.

Parameter	**Non-hotspot**	**Hotspot**
CO_2 Flux **[**μmol m^{-2} s^{-1}]	**< 6.6**	**> 6.6**
Smear Zone Thickness (m)	1.7	2.4
Smear Zone Thickness Above Water Table (m)	0.9	1.6
LNAPL Persistence	0.3	0.4
Toluene Mole Fraction in LNAPL	2×10^{-4}	4×10^{-4}
Benzene Mole Fraction in LNAPL	1×10^{-4}	4×10^{-4}
Naphthalene Mole Fraction in LNAPL	4×10^{-4}	7×10^{-4}
LIF Intensity	0.3	0.4

Figures

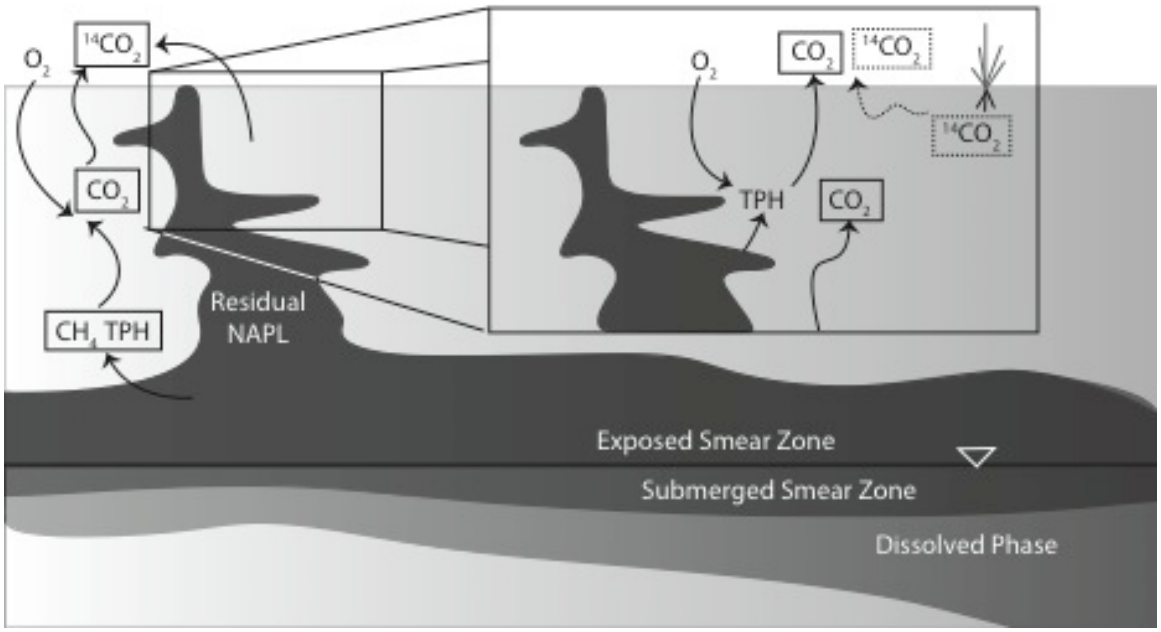

Figure 6.1. Conceptual model of radiocarbon and CO_2 in a NAPL containing vadose zone.

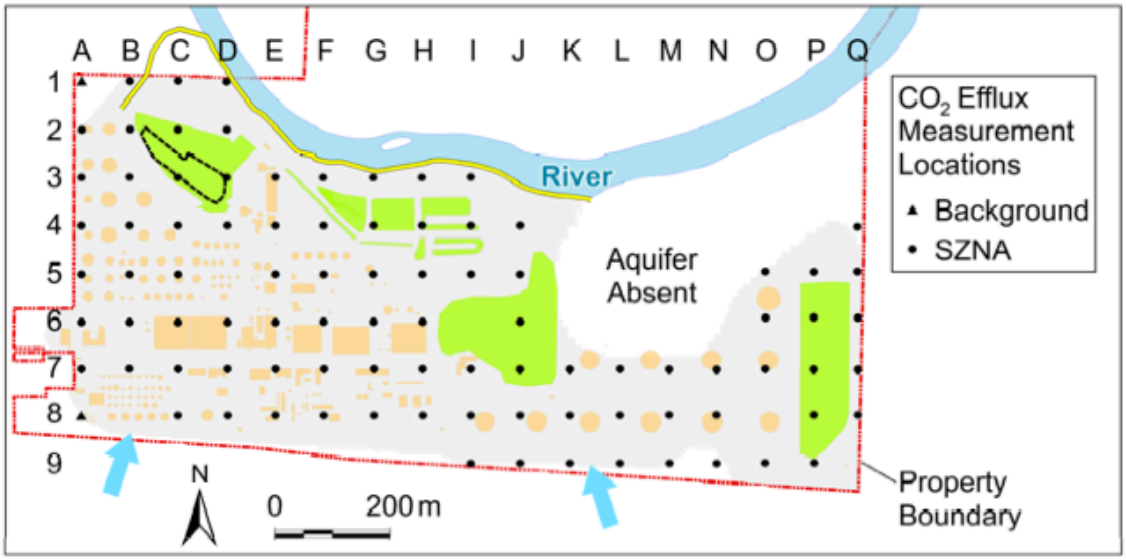

Figure 6.2. Overview of the study site with sampling locations (Background: measurement locations used for BGC; SNZA: measurement locations used for SZNA rate estimates). Dashed line shows extent of 2013 smear zone excavation. Grey regions shows extent of smear zone. Blue arrows show regional groundwater flow directions. Yellow line shows extent of barrier wall. Green and tan shapes show outlines of historical releases and site buildings, respectively.

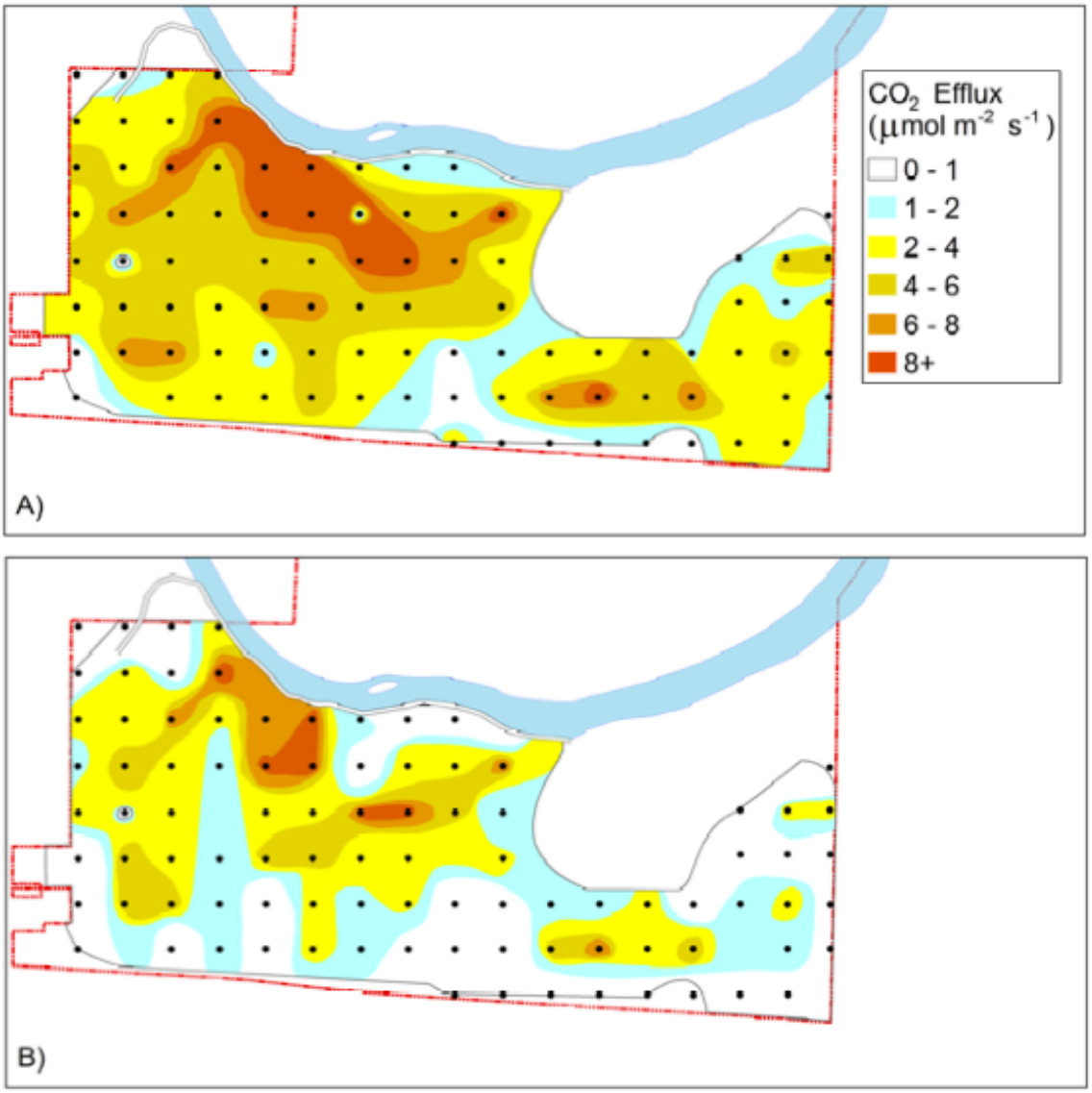

Figure 6.3. Results of CO_2 flux measurements conducted for the HR-BGC dataset. A) Distribution of total CO_2 fluxes, B) Distribution of SZNA rates calculated using the BGC. Dashed lines show 'hotspot' regions of SZNA.

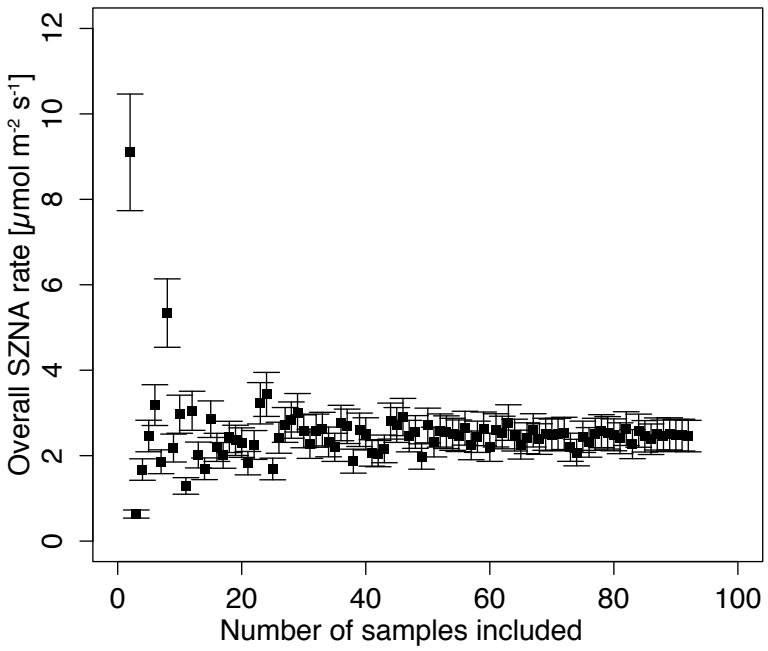

Figure 6.4. Comparison of SZNA rates obtained for the HR-BGC dataset based on random data subsets.

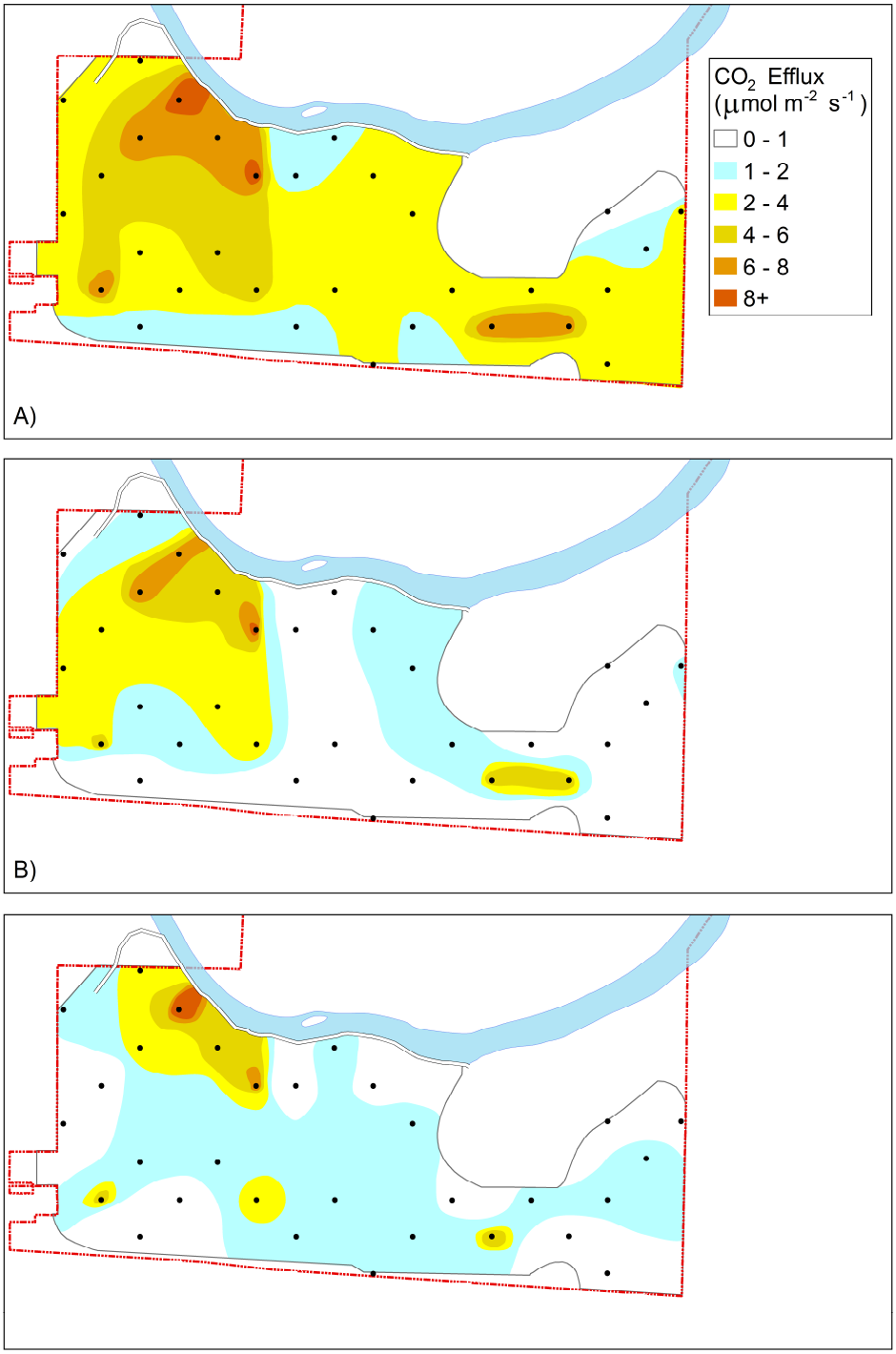

Figure 6.5. Results of CO_2 flux measurements conducted for the MR-RCC dataset. A) Distribution of total CO_2 fluxes, B) Distribution of SZNA rates calculated using the BGC, C) Distribution of SZNA rates calculated using the RCC.

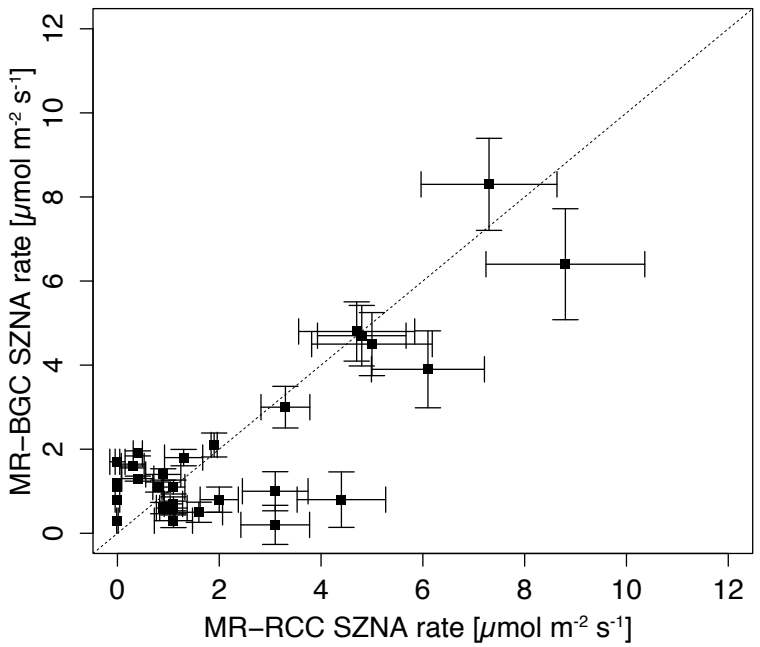

Figure 6.6. Comparison of SZNA rates obtained for the MR-RCC dataset obtained for the BGC and RCC fluxes. Error bars represent average standard error for the measurements.

Chapter 7: Methane emissions and contaminant degradation rates at sites affected by accidental releases of denatured fuel-grade ethanol

Introduction

As the search for sustainable fuel alternatives to offset carbon emissions has intensified, so has the production and use of a variety of biofuels. Recent legislation promoting a range of higher percentage EtOH-blended fuels (USEPA, 2012) has increased the production, transportation and use of denatured fuel-grade EtOH (DFE), raising the probability of accidental releases. Although high concentrations of EtOH can inhibit or halt microbial degradation (e.g.: Powers et al., 2001; Nelson et al., 2010), natural attenuation (NA) has been documented at sites where large volume EtOH releases have occurred (e.g.: (Buscheck et al., 2001; Spalding et al., 2011)). Once below the toxicity threshold, EtOH's degradation potential may rapidly exhaust the local supply of terminal electron acceptors (including O_2 derived from the atmosphere) and culminate in methanogenic conditions (**Figure 1**; Buscheck et al., 2001; Spalding et al., 2011; Corseuil et al., 2011)). In addition, because acetate (a primary intermediate product of EtOH degradation) is also highly labile (Powers et al., 2001), the potential exists for rapid and sustained CH_4 generation in the shallow subsurface.

For high CH_4 generation rates, it can be envisioned that elevated CH_4 concentrations develop in the subsurface, increasing the probability of CH_4 releases at the ground surface (**Figure 7.1**). Buscheck et al. (2001) measured CH_4 partial pressures exceeding 15 percent by volume (v/v %) in soil gas above a 7.2×10^4 (19,000 gallon) neat EtOH release at a bulk fuel terminal in the Pacific Northwest. Similarly, Spalding et al. (2011) measured elevated CH_4 partial pressures in the vadose zone at two large volume DFE spill sites in Minnesota, with soil gas CH_4 concentrations locally exceeding 50 v/v %. At these sites, Spalding et al. (2011) confirmed the occurrence of CH_4 emissions at the ground surface by capturing CH_4-containing soil gas in inverted steel tubs; however, the rate of CH_4 release was not measured in this study.

Using a static chamber, Ma et al., (2013) measured the CH_4 efflux above a small, continuous release (0.4 L d^{-1}) of 10 v/v % EtOH-augmented tap water in a model aquifer. Results showed that the CH_4 content in the chamber reached a maximum of ~21 ppm_v after ~15 hours. However, the spatial distribution and magnitude of CH_4 effluxes at large scale DFE-spill sites has not been documented to date.

If sites with high CH_4 migration rates are located in close proximity to buildings, it is theoretically possible that an explosive or asphyxiate atmosphere develops in poorly ventilated basements or other confined spaces. This situation could result, if ingressing soil gas with a high CH_4 content mixes with ambient air (Jewell and Wilson, 2011) and the resulting CH_4 content exceeds 5 v/v % (Lundegard et al., 2000). Consequently, an understanding of the potential for, and occurrence of, CH_4 accumulation in confined spaces, and for the associated transport of other hydrocarbons towards the ground surface, is valuable for delineating conditions which may result in an enhanced risk of soil vapor intrusion (SVI) near DFE spill sites.

The objectives of this study are to: 1) evaluate the occurrence, distribution, and magnitude of surficial CH_4 and CO_2 effluxes at two DFE-impacted field sites by means of soil gas efflux measurements; 2) use gas efflux measurements to delineate DFE-containing source zones at both sites; 3) quantify depth-integrated DFE degradation rates, based on total background-corrected carbon emissions at the ground surface (CO_2 + CH_4); 4) discuss characteristic differences between the two sites based on field observations and illustrative reactive transport modeling; 5) assess the magnitude of carbon emissions (CO_2 and CH_4) in relation to sites with petroleum hydrocarbon spills, landfill sites, and natural environments (e.g., peat bogs, wetlands); and 6) evaluate the potential for CH_4 accumulation in confined spaces leading to the development of an explosive atmosphere or asphyxiation hazard.

Methods

Method for measurement of real time gas fluxes: The application of CO_2 effluxes for measuring depth-integrated hydrocarbon mineralization rates was demonstrated at a crude oil spill site by Sihota et al. (2011) using a dynamic closed chamber and an infra-red gas analyzer (IRGA) system (LI-COR Inc., Lincoln, NE). To calculate total CO_2 effluxes, the increase in chamber CO_2 content during the period when the chamber is closed is combined with measured water content, pressure, temperature and system volume using (LI-COR, 2007):

$$F = \frac{10VP_0(1-\frac{W_0}{1000})}{RA(T_0+273.15)}\frac{\partial C}{\partial t} \qquad [1]$$

where F is the gas efflux in μmol m^{-2} s^{-1}, W_0 is the initial water vapour mole fraction [mmol mol^{-1}], T_0 is the initial air temperature [°C], V is the total volume of the system (chamber, analyzers, tubing and the soil collar) [cm^3], P_0 is the initial pressure [kPa], A is the soil surface area [cm^2], R is the gas constant (8.314 [Pa m^3 K^{-1} mol^{-1}]), $\partial C/\partial t$ is the change in the dry air concentration of the gas species of interest (i.e., corrected for the water vapour flux) within the chamber headspace over the measurement period [μmol mol^{-1} s^{-1} or ppm_v s^{-1}].

In contrast to CO_2 effluxes, CH_4 effluxes are often calculated by manually collecting a time-series of discrete gas samples from a closed chamber (e.g., deMello and Hines, 1994). Analysis of the CH_4 content within the samples is then performed by gas chromatography (GC). Results are used to determine the increase in CH_4 content within the chamber headspace. This approach is well-suited to many sites where slow, diffusion-driven CH_4 effluxes require long time periods for CH_4 accumulation in the chamber and the increase in CH_4 content is linear. However, the method may become less efficient at sites where high CH_4 effluxes lead to rapid

concentration changes, or where ebullition events (rapid buoyancy driven release of gas bubbles from saturated media) complicate the analysis (Tokida et al., 2007; Guimbaud et al., 2011).

To address the limitations of the GC-based method, Guimbaud et al. (2011) and Santoni et al. (2012) integrated laser-based CH_4 analyzers and gas flux chambers to enable real-time, concurrent measurement of CO_2 and CH_4 effluxes. Similarly, in this study, a commercially available CO_2-IRGA and dynamic closed chamber system (LI-COR Inc., Lincoln, NE) for measurement of CO_2 effluxes was modified to include an instrument using cavity ring down laser spectroscopy (CRDS) (Los Gatos Research Inc., Mountain View, CA) for the measurement of CH_4 content within the chamber. This was achieved by splicing the gas line between the IRGA and the chamber to include the CRDS analyzer (Supporting Information is provided in **Appendix 6, Figure A6.1**). Since both the IRGA and the CRDS instruments have internal pumps, a bypass line was added to prevent interference due to different pumping rates (based on discussions with both manufacturers; **Figure A6.1**).

In addition to CH_4, the CRDS analyzer concurrently measures the CO_2 and H_2O content of the gas stream. This enables a comparison of CO_2 effluxes calculated from changes in CO_2 content within the chamber reported by both the IRGA and the CRDS instrument. Consistency between the measurements was evaluated in the laboratory using a flux generation column (following Widen and Lindroth, 2003; Martin et al., 2004; and Jassal et al., 2005) and during field deployment. Good agreement between the two CO_2 efflux measurements was obtained from the laser and the IRGA instruments under both laboratory conditions ($R^2 = 0.99$, n = 190; **Figure A6.2**) and in the field ($R^2 = 0.99$, n = 366; **Figure A6.3**), providing confidence in the instrument set-up.

To confirm the ability of the CRDS system to measure CH_4 effluxes under field conditions, and to evaluate if the measurements are affected by interferences due to variations in humidity, volatile fatty acids or other organic vapors, samples for CH_4 analysis via GC were collected from the chamber headspace. To this extent, samples were extracted using a gas-tight syringe from a septum in the gas line between the IRGA and the chamber at the end of the efflux measurement period. After collection, gas samples were immediately injected into pre-evacuated glass vials. To minimize the potential for diffusive exchange through the pierced septum of the vial, samples were collected to ~200 kPa (~2 atm) pressure. To further reduce the possibility of contamination via the pierced septum, sample vials were sealed with silicon (Dow Corning 732) in the field. The samples were analyzed in the laboratory at UBC using a Varian CP-4900 gas chromatograph, equipped with a Molsieve 5A Plot column and a Poraplot U column.

To evaluate the potential for the development of an explosive atmosphere under confined conditions, custom-designed gas collection chambers were installed at one of the field sites (with the selection of locations guided by real-time CO_2 and CH_4 gas efflux measurements). The collection chambers consist of machined plastic buckets (**Figure A6.4**), which were inserted into the soil along an impact-gradient above the DFE-affected region. Similar to the design of the chamber used in the real-time gas efflux measurements (LI-COR, 2007), a vent tube was installed in the collection chambers to minimize the effects of barometric pressure changes and to avoid a pressure build up inside the chamber due to ebullition and advective soil gas effluxes. To prevent substantial removal of gas from the chamber due to the Venturi effect, the atmospheric end of the tube was shielded with a plastic cylinder. Holes were drilled into the cylinder, near the base, to allow air flow past the end of the vent tube (Xu et al., 2006). A gas

sampling port was installed by drilling a hole into the side of the collection chamber, and covering the hole with silicon to create a septum.

Field sites: The Balaton site is located in a vacant lot which straddles a rail line (**Figure 7.2**). Vegetation at the site, where present, is sparse, and consists of short, patchy grass, aside from a row of trees and taller grasses adjacent to the creek that feeds into Lake Yankton. A lumber yard and abandoned wooden train loading station are located in the southwest corner of the site. A recycling depot is located in the southeast corner of the site. Depth to groundwater across the Balaton site varies from ~ 1.5 – 6.5 m (5 – 11.5 ft) below ground surface (Pinnacle Engineering, 2004). Soils are mainly comprised of poorly sorted sand with some silty lenses; these overlay a highly variable silty/sandy/clay layer (based on core logs provided by the Minnesota Pollution Control Agency (MPCA), unpublished data).

At the Balaton site, a multi-railcar derailment on July 28, 2004, led to the release of 1.5 x 10^5 L (40,000 gallons) of DFE (EtOH denatured with 5% gasoline) and soybean oil (Pinnacle Engineering, 2004) (**Figure 7.2**). To protect Lake Yankton (a popular recreational lake), clay berms were constructed and pooled free product was pumped off and removed from the area. In addition, ~1.6 x 10^3 m^3 (2,100 cu. yards) of soil (primarily originating from the poorly sorted sand layer) was excavated from the main source area and replaced with clean fill (Pinnacle Engineering, 2004). Groundwater flow at the site is directed to the north-east, but is seasonally influenced by a municipal pumping well to the south-west of the site.

Following site clean-up, Spalding et al. (2011) estimated, ~ 6.8 x 10^4 L (10,000 gallons) of DFE remained in the soils and aquifer. Chemical analysis performed on soil samples collected from post-clean-up soil borings showed residual EtOH to be heterogeneously distributed within

the poorly sorted sand layer (Pinnacle Engineering, 2004), in agreement with findings of Freitas and Barker (2011) for the distribution of ethanol following a release of EtOH to the unsaturated zone at a different field site. Dissolved CH_4 appeared near saturation in shallow groundwater below the source zone by the fall of 2008 (Pinnacle Engineering, 2004). Although dissolved CH_4 was continuously detected from 2008 through 2011, EtOH has not been detected in the monitoring wells since December 2007 (Spalding et al., 2011). Previous work at the site, conducted by Spalding et al. (2011), documented (through the use of static chambers) that surficial CH_4 releases were occurring, with maximum concentrations in the chamber reaching 2.7 v/v %.

The Cambria site is located within the Minnesota River valley. The site is bisected by an elevated rail line (**Figure 7.3**). To the north of the rail line, surficial soils are dominated by sandy floodplain deposits and vegetation consists of ~1 m tall grasses. In the south-east region of the site, soils are comprised of a mixture of silty sand and loam (based on field observation and core collected by the MPCA) and vegetation consists of patchy areas of relatively dense underbrush (including shrubs and trees). Groundwater flow is directed east-northwest (Spalding et al., 2011). Areas of ponded water occur in some locations, particularly during the spring (although this has also been noted after heavy summer rainfall events) (**Figure 7.3**). Where a vadose zone exists, depth to water table is typically less than 1 m (6.3 ft) below ground surface. During the field study, significant standing water was present above a portion of the investigated area (**Figure 7.3**); consequently, gas effluxes were measured only in areas free of standing water.

At the Cambria site, a multi-railcar derailment in November 2006, released ~9.5 x 10^4 L (~ 25,000 gallons) of DFE (**Figure 7.3**; Pinnacle Engineering, 2007). Approximately 4.9 x 10^4 L

(~ 13,000 gallons) of DFE remained in the subsurface following the cleanup efforts (Spalding et al., 2011). In contrast to the Balaton site, no soil excavation occurred at the Cambria site.

Percent levels of EtOH were initially detected in groundwater (Pinnacle Engineering, 2007), with measurable concentrations remaining (held within the capillary fringe) in June of 2010 – 4 years after the release (Spalding et al., 2011). Significant dissolved CH_4 was not observed at Cambria for a year following the release (Spalding et al., 2011). Highest aqueous CH_4 concentrations were measured in source zone wells MW1, MW10, and MW11 (**Figure 7.3**), following the appearance of acetate. As at the Balaton site, Spalding et al. (2011) demonstrated that surficial CH_4 releases were occurring (using static chambers), with a maximum CH_4 concentration of 1.6 v/v % within the chamber.

Field measurements: Real time CH_4 and CO_2 effluxes were measured at the Balaton and Cambria sites between May 8th and 20th, 2012 using the dynamic closed chamber and dual gas analyzer system described in 2.1.2. The measurements were conducted following the method described in Sihota et al. (2011). First, to minimize the contribution of CO_2 produced by plants and microbes within the upper soil layer, surfical vegetation was removed from the measurement location (Sihota et al., 2011). To minimize gas leaks between the chamber and the soil, a 0.2 m ID PVC soil collar was then inserted ~0.05 m into the soil (LI-COR, 2007; Jassal et al., 2012). As suggested by Norman et al. (1997), the soil collar was allowed to equilibrate with the soil for several hours prior to measurement. Measurements were conducted by placing the base of the chamber onto the soil collar, where it seals with a rubber gasket. Once the chamber is secured to the collar, the chamber closes. In this study, the measurement period (the time the chamber is closed) was set to five minutes, to allow for sufficient time for CH_4 accumulation (e.g.: Norman

et al., 1997; Jassal et al., 2011). Due to the potential for increasing gas concentrations within the chamber to alter the diffusion gradient (Jassal et al., 2012), only the early time data was used for calculation of gas effluxes when rapid concentration changes were observed during data processing. At select sample locations, gas samples for GC analysis were collected manually from the chamber headspace for verification of the CH_4 effluxes.

At the Cambria site, the custom-designed gas collection chambers were installed on May 16th, 2012 at selected locations (**Figure 7.3**). Consistent with the dynamic chamber measurements, installation was accomplished by securing approximately 0.05 m of the chamber into the ground (to ensure gas fluxes did not escape around the edges of the chamber due to poor sealing (LI-COR, 2007; Jassal et al., 2012)). Gas samples were collected from each chamber directly following installation (~8:30 pm, May 16th), as well as ~13 hrs (~9:30 am, May 17th) and 61 hrs (~9:50 am, May 19th) after installation. Gas samples were collected from the septum in the sample chamber.

***Reactive transport modeling*:** Reactive transport modeling was conducted with an emphasis on illustrating the processes that control the composition of the observed gas effluxes at the two field sites, specifically the CH_4:CO_2 ratio measured in the chambers. The simulations were conducted using the MIN3P-DUSTY code (Molins and Mayer, 2007), which accounts for geochemical reactions in the vadose zone, multicomponent solute transport, and gas transport by advection and diffusion, with diffusion described by the Dusty Gas Model (Molins and Mayer, 2007). The code has previously been used to simulate biodegradation in the source zone at the National Crude Oil Spill Research Site in Bemidji, MN (Molins and Mayer, 2007; Molins et al., 2010; Sihota and Mayer, 2012).

The simulations were constrained by measured gas fluxes, observed water table locations, and soil textures noted in the field (Spalding et al., 2011; this study) and interpreted from soil borings collected by Pinnacle Engineering (2004, 2007) and the MPCA (unpublished data). Precipitation was specified within the range of annual average precipitation reported for each region by the USDA (Soil Survey Staff, 2012). A CH_4 : CO_2 release ratio of 3 : 1 was specified at the base of the domain (representing the top of the water table, as described below) to reflect EtOH degradation under methanogenic conditions:

$$CH_3CH_2OH \rightarrow \tfrac{3}{2}CH_{4(g)} + \tfrac{1}{2}CO_{2(g)} \qquad [2]$$

Gas generation rates were specified to reflect the total surficial carbon efflux measured at a representative location within the source zone at each field site. CH_4 oxidation is limited to within the aerobic zone, and specified using a dual-Monod formulation (Molins and Mayer, 2007).

$$R = -k_{CH_4}\left(\frac{C_{CH_4}}{K^S_{CH_4} + C_{CH_4}}\right)\left(\frac{C_{O_2}}{K^S_{O_2} + C_{O_2}}\right) \qquad [3]$$

Where R is the CH_4 oxidation rate [μmol L-H_2O^{-1} s^{-1}], k_{CH4} is the CH_4 oxidation rate constant [μmol L-H_2O^{-1} s^{-1}], K_i represents the half-saturation constant of species i [μmoles L-H_2O^{-1}] and C_i is the species concentration [μmol L-H_2O^{-1}]. CH_4 oxidation rates were bounded by rates reported by Molins et al. (2010) for the Bemidji crude oil spill site and Scheutz et al. (2011) for a landfill cover soil. Within this range, oxidation rate constants (k_{CH4}) were calibrated to reproduce CH_4 : CO_2 ratios observed in field-measured gas effluxes. Model input parameters are summarized in **Table 7.1**.

Two scenarios were considered to represent the distinct conditions observed at the different field sites. In the Balaton scenario, silty sand with a relatively low residual water

saturation (0.0403; **Table 7.1**) was used to represent the poorly sorted sand and fill material. The vertical extent of the vadose zone in the Balaton simulation is 2.25 m, constrained by the average depth to water table reported in Spalding et al. (2011). These conditions are representative for most of the site, but not for the area close to the creek (see **Figure 7.2**). In the Cambria scenario, a silty loam with a relatively high residual water saturation (0.067; **Table 7.1**) was deemed representative for the source area. The vertical extent of the vadose zone in the Cambria simulation is 0.25 m, constrained by the depth to water table reported in Spalding et al. (2011) and conditions observed in the field. In the absence of more specific data, the simulations were run to steady state with the goal to provide a process-based interpretation that illustrates the distinct behavior at the two sites.

Results

Real-time gas flux measurements: Across the Balaton site, CO_2 effluxes ranged from 0.6 to 178.4 μmol m^{-2} s^{-1} (n = 189; **Figure 7.4 and Table 7.2**). CH_4 effluxes above 0.3 μmol m^{-2} s^{-1} were measured at 25 locations with a maximum of 9.1 μmol m^{-2} s^{-1} (**Figure 7.4 and Table 7.2**). Total carbon effluxes ranged from 0.6 to 179 μmol m^{-2} s^{-1}. At the Cambria site, CO_2 effluxes ranged from 0.5 to 174.7 μmol m^{-2} s^{-1} (n = 206; **Figure 7.5 and Table 7.2**). Where present, CH_4 effluxes ranged from 0.2 to 393 μmol m^{-2} s^{-1} (n = 63; **Figure 7.5 and Table 7.2**). Total carbon effluxes ranged from 0.5 to 506.3 μmol m^{-2} s^{-1} (n = 206).

The largest CH_4 and carbon effluxes at the Cambria site were measured at locations with ebullition events – as identified by rapid changes in the CH_4 content within the chamber headspace (Guimbaud et al., 2011). To illustrate the difference between the linear changes in headspace gas content under a diffusive regime and the abrupt and intermittent changes in

headspace gas content under ebullition conditions, **Figure 7.6** provides an example of each. The efflux calculated from CH_4 concentration increases presented in **Figure 7.6** results in a CH_4 efflux of ~393 μmol m^{-2} s^{-1} (over 30 s) for the gas release that occurred at ~100 s and 311 μmol m^{-2} s^{-1} (over 38 s) for the gas release that occurred at ~340 s. Alternately, the gas efflux over the total measurement interval (following the establishment of mixing within the chamber − here 260 seconds) can be calculated, resulting in a lower average CH_4 release rate of ~94 μmol m^{-2} s^{-1}. The ability to observe rapid changes in gas concentration within the chamber headspace highlights the advantage of the real-time measurements to identify ebullition events, as rapid gas releases would be challenging to characterize using discrete samples and GC analysis.

As a result, the maximum effluxes reported for the Cambria site (**Table 7.2**) are valid for ebullition conditions only. However, ebullition was only identified at two locations near areas of standing water implying that the method of data interpretation for the ebullition events has a negligible effect on the evaluation of site-wide gas effluxes. CH_4 effluxes in the range of 10 – 100 μmol m^{-2} s^{-1} were observed at several locations without ebullition events (**Figure 7.5**). In general, gas effluxes have been estimated for time periods showing linear concentration increases, as is common practice.

A comparison of the CH_4 content in the chamber headspace at the end of the efflux measurement period yielded generally good agreement between the GC and the laser-based measurements (**Figure 7.7**). However, a systematic difference of ~10% between CH_4 content reported by the CRDS system and samples analyzed using gas chromatography was observed with lower values obtained from the GC samples. Although these differences are significant, they do not affect interpretation of the study results. This comparison provides confidence that the CH_4 measurements conducted under field conditions are not substantially affected by volatile

fatty acids (VFAs) or petroleum or EtOH vapours potentially present in the gas phase (as has been documented for several gas field meters (Jewell and Wilson, 2011)). Aside from interferences or instrument performance in the field, the systematic discrepancies may also be due to rapid changes in the chamber headspace CH_4 content and time required for collection of the gas sample (~10 s). The differences may be further attributed to contamination with air during collection, transport, and processing of the GC samples, which all would decrease CH_4 concentrations.

***Potential for a confined space hazard*:** At the Cambria site, results of GC analysis on gas samples taken from the collection chambers, show variability in gas composition between the locations at both the 13 hour and 61 hour sampling periods. It should be noted that chambers B, C and D were all located directly within the source zone (**Figures 7.3 and 7.5**); however, each chamber was located on soil with visibly different moisture content. The soil beneath chamber B was damp, implying an intermediate moisture content; the soil beneath chamber C was close to saturation (the chamber was surrounded by ponded conditions); and the soil beneath chamber D was relatively dry, with the water table ~0.3 m below ground surface (estimated based on nearby ponded water). Chambers A and E were located outside the source area (**Figures 7.3 and 7.5**), with soil conditions similar to those beneath chamber B.

Chamber B (**Figure 7.3**) showed maximum CH_4 accumulations of 6.6 v/v % and 22 v/v % 13 hours and 61 hours following installation (**Table 7.3**). Increased CH_4 concentrations correlated with substantial O_2 depletion (to 72% and 14% of atmospheric levels after 13 and 61 hours respectively; **Table 7.3**). O_2 depletion was also found in samples collected from chambers C and D, coinciding with increases of CH_4 to concentrations of up to 2.2 v/v %. Observed

nitrogen (N_2) and argon (Ar) depletion (with respect to atmospheric values of 78 and 0.93 v/v %, respectively) suggests a pressure buildup within the chamber due to gas emissions may have occurred (particularly at location B), resulting in displacement of atmospheric gasses through the chamber's vent tube.

Outside the source zone, chamber A did not show significant O_2 depletion and CH_4 was below detection. Although outside the immediate source zone, chamber E was located directly adjacent to the ponded area (**Figure 7.3**). Gas composition in this chamber showed a slight increase in CH_4 and CO_2 (**Table 7.3**), while a substantial decrease in O_2 combined with increases in N_2 and Ar concentrations relative to atmospheric values suggest that O_2 ingress and consumption in the soil was substantial and caused air inflow through the vent tube.

Discussion

Occurrence, distribution and magnitude of gas effluxes: At both field sites, observations clearly demonstrate substantially elevated CO_2 and CH_4 effluxes within the source zone. Increased CO_2 effluxes are ubiquitous within the affected region and are clearly distinguishable from background conditions. CO_2 effluxes are in average 4-5 times higher than background conditions (**Table 7.2**) and locally exceed 100 μmol m^{-2} s^{-1} at both field sites. Although CH_4 effluxes of substantial magnitude (>100 μmol m^{-2} s^{-1}) did also occur; they were much more localized, with the highest effluxes attributed to ebullition events. It is well known that O_2 ingress from the atmosphere can lead to partial or complete oxidation of CH_4 within the soil column, facilitated by methanotrophic microbes (e.g.: Molins et al., 2010; **Figure 7.1**). This process is likely active at both sites, as is evidenced by low average CH_4 : CO_2 ratios of 0.04 and 0.5 derived from the real time measurements at Balaton and Cambria, respectively (**Table 7.2**).

However, results also suggest that a high rate of DFE degradation, combined with shallow water table conditions and high moisture contents (in particular relevant to the conditions at the Cambria site), can limit O_2 ingress and overwhelm the capacity of methanotrophic bacteria to completely oxidize CH_4. Comparison of gas effluxes, measured at the two sites shows largest effluxes to be located in the areas where the water table is shallow. Furthermore, CH_4 : CO_2 ratios exceeding 0.5 are restricted to the area directly above the initial EtOH pool at the Cambria site (**Figures 7.3 and 7.5**).

At the Balaton site, CH_4 effluxes are weakly, but significantly correlated with soil volumetric water content (R^2 = 0.5, $p<0.01$, data not shown). At the Cambria site, soils were often close to saturation, precluding the ability to correlate moisture content with measured efflux. However, field observations of soil moisture accompanying the gas collection chambers are in agreement with the results from the Balaton site, with higher CH_4 releases occurring under moist, but not saturated conditions (i.e., chambers B and C). In relatively wet soils, it is likely that the increased moisture content inhibits O_2 ingress, thereby limiting the ability of methanotrophs to completely oxidize CH_4 generated from anaerobic degradation.

In soils approaching saturation, gas diffusion is severely restricted and ebullition events control gas migration to the ground surface. Gas release by ebullition has previously been noted in saturated bog and peat environments, where it can be responsible for releases of biogenic gasses that are large in comparison to diffusive fluxes (e.g.: Baird et al., 2004; Tokida et al., 2007; Guimbaud et al., 2011). Within the source zone of the Cambria site, periodic ebullition events were observed in time intervals < 1 min in areas of standing water. Results of chamber data collected from locations close to ponded water (N=2) also suggest ebullition was a mechanism for gas release (as evident by sudden increases in concentration observed in real time

measurements within the chamber headspace (**Figure 7.6, Table 7.2**; Guimbaud et al., 2011)) and ratios of CH_4 : CO_2 approaching 6.

***DFE source zone delineation*:** Similar to the approach used by Sihota et al. (2011), the contaminant containing source zone can be delineated by identifying locations where the total carbon efflux is substantially greater than carbon efflux in areas unaffected by the contaminant (i.e., from natural soil respiration). In the context of a DFE site, the 'source zone' can be extended beyond the area where ethanol is held at residual within the capillary fringe (Spalding et al., 2011), to include the area affected by acetate (which is also a highly labile carbon source). At the Balaton site, the presence of a lumber yard, train loading station, a recycling depot, and a nearby residential area restricted the selection of the background locations (**Figure 7.2**). At the selected locations, the estimated natural soil respiration rates (the geometric mean of location-averaged CO_2 effluxes (**Table 7.2 and Figure 7.4**)) range from 6.7 to 6 μmol m^{-2} s^{-1}. The lower effluxes fall within the range of CO_2 effluxes typically measured for grassy vegetation and similar climatic conditions (Reiners, 1968; McCulley et al., 2004), while the higher observed effluxes may be explained by the proximity to the lumber yard and train loading station (**Figure 7.2**) − a potential source for labile carbon.

At the Cambria site the estimated natural soil respiration value ranged between 5.4 to 7 μmol m^{-2} s^{-1} (**Table 7.2 and Figure 7.5**), which is similar to values reported by Stoffel et al. (2010) for a Wisconsin hardwood forest and Mielnick and Dugas (2000) for a Texas tallgrass prairie. The lower bound of the natural soil respiration rate for the Cambria site was measured far from the source zone, in a grassy area (not shown on **Figure 7.5**). The upper bound of the natural soil respiration value measured at the Cambria site was measured in a swampy area, adjacent to

the ponded water (**Figure 7.5**) and is similar to the values reported for May CO_2 effluxes in a South Dakota wetland by Gleason et al. (2009) and Sulman et al. (2009) in a Wisconsin wetland.

To account for the variability in natural CO_2 effluxes, the source zone area is delineated using only those effluxes which are greater than twice the efflux used to represent natural soil respiration. Based on these consideration, the source zone at the Balaton site is delineated by an area that is located adjacent to the creek and extends over a length of approximately 100 m and is up to 30 m wide (**Figure 7.4**). The surficial soil consists of dry, orange, fine sand and clay. Removal of the upper ~0.15 m (6") revealed damp, black soil with a characteristic butyrate odour. Within this area, CH_4 effluxes were found in ~35% (19/55) of the measurements, and CO_2 effluxes were elevated in comparison to other locations across the site (**Figure 7.4a**), with an average of 21 μmol m^{-2} s^{-1} (±4.0 μmol m^{-2} s^{-1}).

At the Cambria site, substantial carbon effluxes were restricted to localized areas north and south of the rail line (**Figure 7.5**). At this site the remaining source area is roughly circular with a diameter of approximately 60-70 m, although a substantial fraction of this zone was covered by water at the time of the measurements (**Figure 7.5**). The soils range from a fine grey sand and silt to a darker soil with a silty or loamy texture. Also similar to the most impacted area at the Balaton site, a characteristic butyrate odour was pervasive within the southern source zone at the Cambria site. Within the source zone areas measureable CH_4 effluxes were present at ~36 % of the measurements (46/128), and CO_2 effluxes were elevated in comparison to other locations across the site (Figure 5a), with an average of 26 μmol m^{-2} s^{-1} (±2.3 μmol m^{-2} s^{-1}).

Estimation of depth-integrated DFE degradation rates: Using measured surficial CO_2 effluxes, Sihota et al. (2011) showed that it is necessary to correct for natural soil respiration when

estimating the CO_2 efflux associated with contaminant mineralization at petroleum hydrocarbon spill sites (i.e., subtracting the CO_2 efflux associated with natural soil respiration from the CO_2 efflux associated with contaminant degradation). This makes accurate determination of carbon loss rates directly associated with contaminant degradation more difficult. In principle, this is also true for DFE sites; however, due to the substantial inferred degradation rates, the error introduced by uncertainties regarding natural soil respiration rates is more limited. It is not required to apply a similar correction for the CH_4 effluxes, because CH_4 effluxes were not resolved at the background locations at either site.

At the Balaton site, the correction for natural soil respiration yields a total carbon efflux attributable to DFE degradation, which ranges from non-detect to ~174 μmol m^{-2} s^{-1} over 55 measurements within the source zone (**Table 7.2 and Figure 7.4**). The average carbon efflux from DFE degradation within this region is 22 μmol m^{-2} s^{-1} (**Table 7.2**). At the Cambria site, this correction yields a range in total carbon effluxes attributable to DFE degradation from non-detect to ~ 500 μmol m^{-2} s^{-1} over 128 measurements within the source zone (**Table 7.2 and Figure 7.5**. In this case, the average DFE-related carbon efflux is 32 μmol m^{-2} s^{-1} (**Table 7.2**).

Assuming EtOH to represent the main carbon source, the total carbon release rate can be converted into an estimated EtOH mass loss rate. This calculation is approximate, as it assumes that CH_4 and CO_2 are not affected by reactions within the vadose zone that will sequester or release carbon (e.g., sequestration to biomass Schoefs et al. (2004), exchange with carbonate minerals, or dissolution to groundwater). Within the source zone, estimated EtOH loss rates at the Balaton site range from non-detect to 3 mg-EtOH m^{-2} s^{-1} with an average of 0.3 mg-EtOH m^{-2} s^{-1}. Estimated EtOH loss rates at the Cambria site range from non-detect to 8 mg-EtOH m^{-2} s^{-1} with an average of 0.5 mg-EtOH m^{-2} s^{-1}. As the transient evolution of the gas fluxes was not

measured, a long-term mass loss calculation over time periods of years is not appropriate. Furthermore, it must be stressed that reported degradation rates are representative of field conditions at the time of measurement only.

Evaluation of characteristic differences between effluxes at the Balaton and Cambria sites: It is evident that both maximum and average carbon loss rates measured at the Cambria site are much greater than those measured at the Balaton site. The relatively lower degradation rate measured at the Balaton site may be explained because the release at the Balaton site occurred two years prior to the release at the Cambria site. It also seems reasonable that the excavation of the majority of impacted soils from the source zone at the Balaton site resulted in earlier substrate exhaustion and lower degradation rates at the time of the investigation. This finding is in agreement with the conclusion of Spalding et al. (2011) in regards to the importance of soil excavation at sites impacted by large DFE releases. Furthermore, at the Balaton site, in the area where EtOH pooled, and soil was not excavated (adjacent to creek in **Figure 7.2**), CH_4 effluxes and total carbon release rates were within the range of the larger carbon release rates measured at the Cambria site (**Table 7.2**). It should be noted that this area slopes toward the creek and the water table is locally much shallower than at other locations across the site.

Differences between the composition of the measured effluxes at the two field sites can be further explored through reactive transport modeling scenarios that illustrate the importance of contrasting site-specific conditions at the two field sites. The Balaton site is characterized by a deeper water table, soils composed of silty sand with lower moisture contents, and average lower gas generation rates. For these conditions, simulated vadose zone gas profiles show O_2 penetration well into the vadose zone (**Figure 7.8**). CO_2 partial pressure exceeds that of CH_4

throughout the profile, and reaches a maximum directly above the source zone. CH_4 oxidation occurs within the soil column, removing CH_4 before it can reach the ground surface (Figure 8b). Profiles of Ar and N_2 show slight enrichment with respect to atmospheric values close to the CH_4 reaction zone (**Figure 7.8**), consistent with Ar and N_2 signature reported in regions of methane oxidation (Amos et al., 2005). Pore water saturation is relatively low (~0.15), consistent with conditions observed at many locations in the field. It should be noted that these simulations were performed to represent average conditions at the Balaton site, but are not applicable to conditions close to the creek, where the water table is very shallow and a CH_4 efflux was observed.

In contrast, the Cambria site is dominated by a shallow water table, soils are composed of silty loams, and average gas generation rates are higher. For this scenario, simulated vadose zone gas profiles show O_2 is available only in the upper soil profile (**Figure 7.9**); this corresponds to a sharper CH_4 oxidation front than in the Balaton scenario (**Figure 7.9**). The partial pressure of CH_4 is greatest at depth and remains above CO_2 throughout the profile (**Figure 7.9**). As can be seen from **Figure 7.9**, CH_4 oxidation does not go to completion within the soil column, and CH_4 escapes across the ground surface. Profiles of Ar and N_2 show depletion with respect to atmospheric values as they are absent in the source and their downward transport is limited due to the high water saturations and upward gas advection. In the Cambria scenario, pore water saturation is high (~0.8), consistent with the nearly saturated conditions observed in the field. These simulations are representative for conditions close to the ponded area, but not for locations with ebullition events.

Simulated gas fluxes for the Balaton scenario show gas transport to be diffusion dominated, with the total gas flux closely following the diffusive gas flux (**Figure 7.10**). Simulated O_2 profiles also indicate diffusion dominates transport downward as it is consumed in

the CH_4 oxidation reaction, although advection can be seen to play a minor role (**Figure 7.10**). Similarly, the upward transport of CH_4 and CO_2 is diffusion-dominated with advection contributing to CO_2 transport to a limited extent – mostly restricted to the lower section of the soil column.

In contrast to the Balaton scenario, simulated results for the Cambria case show that O_2 transport is affected by both advection and diffusion (**Figure 7.11**). Downward O_2 diffusion is inhibited by upward advection of O_2 which moves along with CH_4 and CO_2 in a bulk gas flow towards the surface. Also in contrast to the Balaton site, advection plays an important role in the upward transport of CH_4 and CO_2 to the CH_4 oxidation zone. Above the CH_4 oxidation zone the fluxes of CH_4 and CO_2 are driven by both advection and diffusion (**Figure 7.11**).

Simulated results for scenarios representing the conditions at Balaton and Cambria provide gas fluxes and CH_4 : CO_2 flux ratios within the range of values measured in the impacted area at each site (**Tables 7.1 and 7.3**). Results of the simulations (**Figures 7.8 - 7.11**) can be used to further evaluate the processes driving the differences in magnitude and composition of gas fluxes at the two sites. The greater vertical extent of the soil column above the zone of gas release, as well as the lower residual water saturation for conditions at the Balaton site results in the near complete oxidation of CH_4 within the vadose zone (**Figure 7.8**). In contrast, the narrow vertical extent and higher water saturations in the Cambria scenario results in a greater proportion of the generated CH_4 escaping across the ground surface (**Figure 7.9**). Sensitivity analysis performed by increasing the CH_4 oxidation rate by an order of magnitude showed the resultant surficial gas fluxes were relatively insensitive to this parameter, with a corresponding change in the CH_4 : CO_2 flux ratio of 28%, underlining the import control of O_2 ingress in this system.

Comparison of CH_4 and total carbon effluxes between DFE sites and other environments: To place CH_4 effluxes into context, the magnitude of CH_4 effluxes measured at DFE spill sites in this study can be compared with CH_4 effluxes found in natural and other anthropogenically-influenced environments. In natural environments, CH_4 effluxes show large variations and range from local net uptake (e.g., peatlands (Maljanen et al., 2001)) to effluxes of >0.5 μmol m^{-2} s^{-1} (e.g., the drainage ditch of a wetland Schrier-Uijl et al. (2011)). Similarly, in anthropogenically-influenced environments CH_4 fluxes range from net intake to large effluxes (**Table 7.4**). For example, despite the presence of CH_4 at depth, a net intake of CH_4 was observed at a crude oil spill site (unpublished data) while, at an active landfill with an operational gas collection system, Lohila et al. (2007) estimated average and maximum emissions of 37 and 187.5 μmol m^{-2} s^{-1}, respectively. At an active landfill site with no gas collection system, Mosher et al. (1999) reported an average CH_4 emission of 94 μmol m^{-2} s^{-1}.

To place total EtOH degradation rates into context, total carbon effluxes can be compared with carbon effluxes occurring in natural (e.g., wetlands, bogs and peatlands) and anthropogenically-influenced environments (e.g., petroleum hydrocarbon spills and landfills, **Table 7.4**). In a wetland, Elberling et al. (2011) measured a total carbon efflux of ~3 μmol m^{-2} s^{-1}. In a temperate wetland, Schrier-Uijl et al. (2011) found total carbon effluxes in drainage ditches and lakes of 1.39 and 0.45 μmol m^{-2} s^{-1}, respectively. In a peat deposit, Maljanen et al. (2001) measured larger emissions, ranging from 2.9 - 8.1 μmol m^{-2} s^{-1}. Effluxes from anthropogenically-impacted environments can also vary widely. For example, Sihota et al. (2011) measured total carbon effluxes at the Bemidji crude oil spill site of 5.9 μmol m^{-2} s^{-1}, with

2.6 μmol m^{-2} s^{-1} attributable to oil degradation. At landfill sites, maximum carbon effluxes can exceed 300 μmol m^{-2} s^{-1} (Lohila et al., 2007).

Overall the magnitude of CH_4 and total carbon emissions measured in this study are larger than those found in the natural CH_4 emitting environments. The observed CO_2 and CH_4 effluxes in large DFE source zones substantially exceed those at the Bemidji crude oil spill site and other petroleum hydrocarbon sites (unpublished data) and are more similar to CH_4 and total carbon emissions at landfill sites (**Table 7.4**).

***Potential for development of hazardous conditions in confined spaces*:** Decreased O_2 content and elevated CH_4 concentrations measured in samples collected from the gas collection chambers installed at the Cambria site (**Table 7.3**) suggest the possibility exists for accumulation of CH_4 in confined spaces above a rapidly degrading DFE source. Furthermore, the depletion of Ar and N_2 in samples collected from chamber B is consistent with gas composition expected under methanogenic conditions (Amos et al., 2005) and indicates advective displacement from the soil. This result is also in agreement with simulation results for the Cambria scenario (**Figures 7.9 and 7.11**), which reproduce the measured fluxes and CH_4 : CO_2 ratios determined near chamber B .

Evaluation of the CH_4 : CO_2 ratios on gas samples collected from the collection chambers shows ratios greater than 0.5 exist only in the area directly affected by the source (**Table 7.3 and Figure 7.2**). As the degradation of EtOH is expected to produce CH_4 and CO_2 in a 3:1 ratio (**Figure 7.1**), the measured ratios suggest that the gas composition in the chambers is somewhat influenced by a combination of CH_4 oxidation within the soil column and aerobic degradation of the DFE due to the ingress of atmospheric O_2 or oxygenated water.

Overall, it can be concluded that, although the possibility exists for accumulation of CH_4 in confined spaces at concentrations exceeding the LEL (5 v/v %), a unique set of conditions is required, such as the large DFE release at the Cambria site into low permeability soils with a shallow water table. It is expected that a more typical case would involve the partial or complete oxidation of CH_4 before it is released at the ground surface.

Conclusions

Results of gas efflux measurements conducted at both field sites demonstrate that biodegradation of the DFE is occurring, leading to the production of CH_4 and CO_2. Field measurements, reflective of environmental conditions at the time of measurement, also confirm that both gasses are escaping across the ground surface – even years after the spill (eight and six years for Balaton and Cambria, respectively), and despite soil excavation (Balaton). These findings agree with those of Buscheck et al. (2001), and indicate that, although there may be an extended time lag in the initial occurrence of CH_4 following a highly concentrated DFE spill (e.g., a year passed before CH_4 was detected at the Cambria site (Spalding et al., 2011)), the potential for CH_4 generation remains. However, large total carbon fluxes, and CH_4 fluxes in particular, were closely related to the soil type and moisture content (observed and measured in the field, and illustrated through simulation results) suggesting gas fluxes may vary with environmental (e.g., seasonal) conditions.

It was previously shown that high subsurface degradation rates can lead to advective gas transport in the vadose zone (Molins et al., 2010) or gas ebullition from the saturated zone and capillary fringe (Amos and Mayer, 2006). For the Balaton scenario, illustrative simulations designed to reproduce gas effluxes measured in the field suggest the role of advection is minor.

For the Cambria scenario, in contrast, the combination of nearly saturated soils and high carbon emissions suggests the importance of gas migration by ebullition and advection. Vigorous ebullition, observed during field work at the Cambria site and recorded during gas efflux measurements (in the standing water adjacent to the measurement locations and in shallow source zone wells) provides additional direct evidence that ebullition contributes locally to surficial gas effluxes. Illustrative simulations for the Cambria scenario suggest that, as the vertical extent of the vadose zone above the gas generation source decreases and moisture content increases, advection begins to play a more important role (**Figure 7.11**).

Large measured CH_4 effluxes and high inferred subsurface biodegradation rates, particularly at the Cambria site, have implications for SVI investigations at DFE release sites. For example, SVI conceptual models for petroleum releases often assume that vapor phase transport is diffusion limited (e.g., Johnson et al. (2006)). In addition, these SVI conceptual models generally assume that volatilization from groundwater to soil gas is limited by diffusive mass transfer, whereas ebullition can more effectively strip BTEX and other volatile organic compounds from groundwater and transfer them to the ground surface. Furthermore, high fluxes of flammable gas (CH_4) that can be transported by advection may not be assessed as part of a routine SVI investigation, although results from both field sites investigated in this study show that localized CH_4 effluxes are possible above DFE source zones. However, it must be stressed that the conditions at the Cambria site likely represent a 'worst-case' scenario and that, even at this site, large CH_4 effluxes are highly localized.

Overall, it can be concluded that DFE spills may lead to CH_4 emissions, particularly at sites with high moisture contents and a shallow water table; conditions which inhibit O_2 ingress from the atmosphere. At such sites, conditions may also hinder the aerobic oxidation of BTEX

and other volatile organic compounds (present in blended fuel mixtures) (Molson et al., 2002), which may increase the risk of migration of these compounds to the ground surface (i.e., increase the potential for soil vapour intrusion into subsurface structures). The magnitude of CH_4 effluxes measured at both field sites and their association with the DFE source zone provides evidence that the CH_4 generated is due to the degradation of the DFE, rather than degradation of natural organic matter (Lundegard et al., 2000). However, it must be emphasized that measured gas fluxes are reflective of environmental conditions at the time of measurement only. To enhance the understanding of variability in gas emissions, seasonal monitoring could be conducted. Furthermore, to definitively identify the source of the CH_4, isotopic analysis could be performed (e.g., Freitas et al. (2010)). It is expected that stable isotopic analysis on ^{13}C and ^{3}H can provide insight into the production pathway of CH_4 (Lundegard et al., 2000; Freitas et al., 2010); ^{14}C analysis has also been shown as beneficial in identifying the component of the total carbon efflux attributable to degradation of the petroleum hydrocarbon fraction (e.g., Sihota and Mayer, 2012). Evaluation of priority compounds from within the chamber headspace (e.g., BTEX vapors) can provide insight for assessing the potential for SVI risk related to petroleum hydrocarbons above DFE-impacted sites.

Tables

Table 7.1. Parameters used in the reactive transport model.

	Scenario			
Model Parameter	**Balaton**	**Cambria**	**Units**	**Reference**
Soil type	Silty sand	Silty loam	-	Pinnacle Engineering (2004, 2007); Spalding et al. (2011); field observations
Vadose zone extent	2.25	0.25	[m]	Spalding et al. (2011); field observations
Van Genuchten Parameters Alpha n exponent	 4.3 2.3 0.5	 2.0 1.4 0.5	 [m^{-1}]	Based on soil type Rosetta Rosetta Rosetta
Hydraulic conductivity	5.4×10^{-4}	1.3×10^{-6}	[$m\ s^{-1}$]	Pinnacle Engineering (2004, 2007); Rosetta
Residual saturation	0.040	0.067	[-]	Rosetta
Porosity	0.39	0.45	[-]	Rosetta
Precipitation	0.56	0.71	[$m\ y^{-1}$]	USDA
CO_2 release rate	2.5	38	[$\mu mol\ m^{-2}\ s^{-1}$]	constrained by field data
CH_4 release rate	7.5	113	[$\mu mol\ m^{-2}\ s^{-1}$]	constrained by field data
CH_4 oxidation rate	0.7	0.7	[$\mu mol\ L\text{-}H_2O^{-1}\ s^{-1}$]	based on Molins et al. (2008), Scheutz et al. (2011) and calibrated
CO_2 efflux Diffusion Advection	 10 -	 35 12	 [$\mu mol\ m^{-2}\ s^{-1}$] [$\mu mol\ m^{-2}\ s^{-1}$]	constrained by field data
CH_4 efflux Diffusion Advection	 - -	 69 35	 [$\mu mol\ m^{-2}\ s^{-1}$] [$\mu mol\ m^{-2}\ s^{-1}$]	constrained by field data
$CH_4 : CO_2$ of gas efflux	-	2.2	[-]	constrained by field data

Table 7.2. Real time CO_2 and CH_4 effluxes measured at Balaton and Cambria sites in 2012. [1]within the area defined as the source zone and CH_4 fluxes were detected. [2]assumed (geometric mean of replicate measurements). ND: non-detect. BG: background CO_2 efflux correction used. SE = Standard error, n = number of measurements. [3]based on an ebullition flux.

		Balaton	**Cambria**
CO_2 Efflux [μmol m^{-2} s^{-1}]	Minimum	0.6	0.5
	Maximum	178.4	174.7
CH_4 Efflux [μmol m^{-2} s^{-1}]	Minimum	ND	ND
	Maximum	9.1	392.9
Approximate background CO_2 efflux[2] (±SE, n) [μmol m^{-2} s^{-1}]		5 (1, 2)	6 (0.8, 2)
Average CO_2 efflux attributable of DFE degradation in the source zone (±SE, n) [μmol m^{-2} s^{-1}]		21 (4, 55)	26 (2, 128)
Average CH_4 efflux attributable of DFE degradation in the source zone (±SE, n) [μmol m^{-2} s^{-1}]		1.4 (0.5,19)	24 (9, 46)

	Balaton	**Cambria**	
Total carbon flux from DFE degradation in the source zone	Average	22	32
	(±SE, n)	(4, 55)	(5, 128)
	Minimum	5	6
[μmol m^{-2} s^{-1}]	Maximum	174	500
Source Zone CH_4:CO_2 ratio[1]	Average	0.04	0.5
	(±SE, n)	(0.01, 19)	(0.1, 46)
	Minimum	0.003	0.005
	Maximum	0.12	6.43
Depth-integrated DFE degradation rate in the source zone	Average	0.3	0.5
	(±SE, n)	(0.06, 55)	(0.07, 128)
	Minimum	0.07	0.1
[mgEtOH m^{-2} s^{-1}]	Maximum	3	8

Table 7.3. Complete gas composition measured within the gas collection chambers at the Cambria site. [1]Ar contents are corrected based on Ar content in air. [2]sample contamination by air suspected. BD: below detection (< 15 ppm_v)

			Gas content [% v/v]						
Location	**Date**	**Time**	**CH_4**	**CO_2**	**Ar[1]**	**O_2**	**N_2**	**O_2** [% atmospheric]	**CH_4:CO_2**
A	5/16/2012	9:02	BD	0.06	0.93	20.8	78.4	99	-
A	5/17/2012	9:51	BD	0.2	0.93	20.6	77.8	99	-
A	5/19/2012	9:58	BD	0.5	0.93	20.6	77.8	99	-
B	5/16/2012	8:30	BD	0.1	0.93	20.9	78.3	100	-
B	5/17/2012	9:36	6.6	6.6	0.91	15.0	74.8	72	1.9
B	5/19/2012	10:00	22.0	12.7	0.84	6.0	61.5	14	1.7
C	5/16/2012	8:36	BD	0.1	0.93	20.1	77.8	96	-
C	5/17/2012	9:48	1.0	1.1	0.93	19.4	77.9	93	0.9
C	5/19/2012	10:15	2.2	6.4	0.95	16.2	77.8	77	0.7
D	5/16/2012	8:40	BD	0.09	0.93	20.1	78.4	96	-
D	5/17/2012	9:26	1.7	1.6	0.94	18.5	77.9	88	1.0
D[2]	5/19/2012	10:18	1.4	2.4	0.90	17.1	77.7	82	0.6
E	5/16/2012	8:52	BD	0.1	0.93	20.9	78.2	100	-
E	5/17/2012	9:33	BD	0.5	0.94	19.9	78.2	95	-
E	5/19/2012	10:22	0.3	2.6	0.98	16.7	80.4	80	0.1

Table 7.4. Total carbon, CO_2 and CH_4 effluxes at Cambria and Balaton DFE spill sites in comparison to other contaminated and natural environments (values in brackets represent contaminant soil respiration i.e. corrected for natural soil respiration).NR: not reported. Average CH_4 : CO_2 presented are calculated using the average of CH_4 : CO_2 obtained from individual measurements.

Environment		**Average Gas Flux** [µmol m^{-2} s^{-1}]			**Ratio**	**Reference**
		CO_2 (CSR)	**CH_4**	**Total C** (CSR)	**CH_4/CO_2**	
Natural	Wetland	3	0.005	3	1.7×10^{-3}	Elberling et al. (2011)
	Wetland (ditch)	0.81	0.58	1.39	0.83	Schrier-Uijl et al. (2011)
	Wetland (lake)	0.38	0.07	0.45	0.18	
	Peat	2.9-8.1	-0.009	2.9-8.1	$\sim 1.0 \times 10^{-3}$	Maljanen et al. (2001)
	Peat (laboratory)	NR	0.06 (max)	NR	NR	Baird et al. (2004)
	Peat	NR	0.001(base)	NR	NR	Tokida et al. (2007)
	(field Plots)		~ 0.043 (max)			

		Average Gas Flux [μmol m^{-2} s^{-1}]			**Ratio**	**Reference**
		CO_2 (CSR)	**CH_4**	**Total C** (CSR)	**CH_4/CO_2**	
Impacted	Crude oil spill	5.9 (2.6)	0	5.9 (2.6)	0	Sihota et al. (2011)
	Landfill (active site-gas recovery)	33	37	70	0.6-1.2	Lohila et al. (2007)
	Landfill (closed site-gas recovery)	NR	6.5	NR	NR	Mosher et al. (1999)
	Landfill (active site-no gas recovery)	NR	94	NR	NR	Mosher et al. (1999)
	DFE (source zone, Balaton)	21	1.4	22	0.04	This study
	DFE (source zone, Cambria)	27	25	33	0.5	

Figures

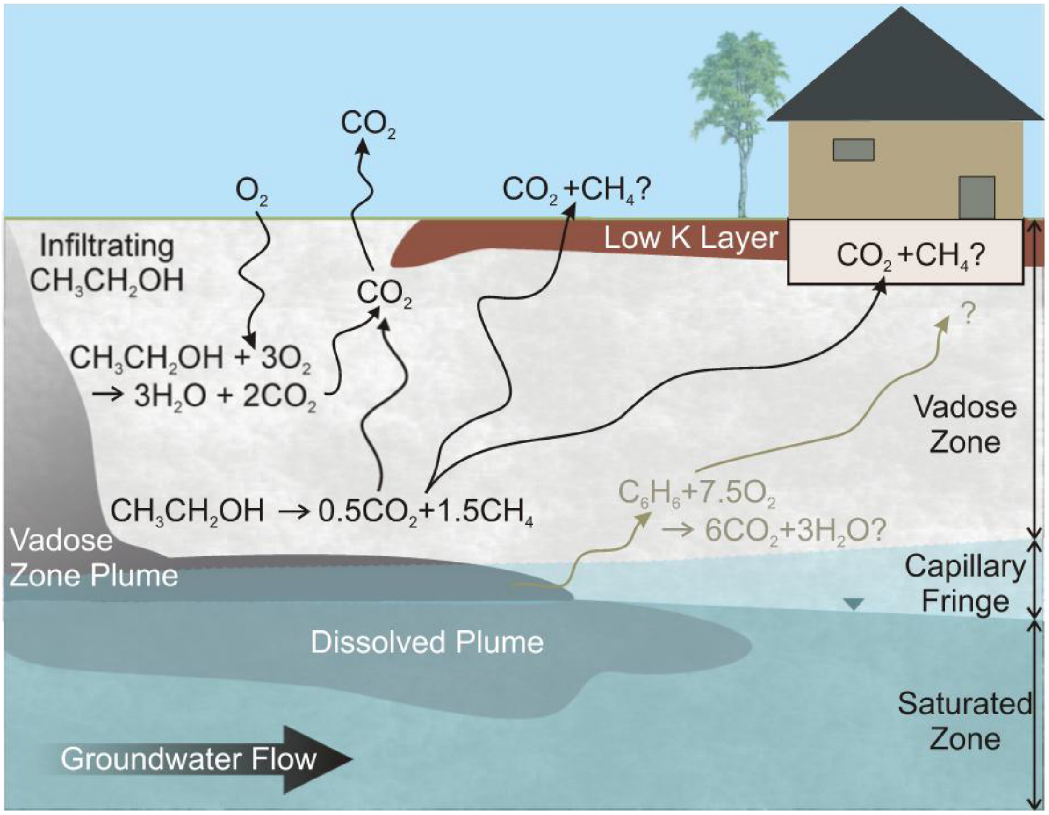

Figure 7.1. Conceptual model of SZNA at sites impacted by EtOH blended fuel.

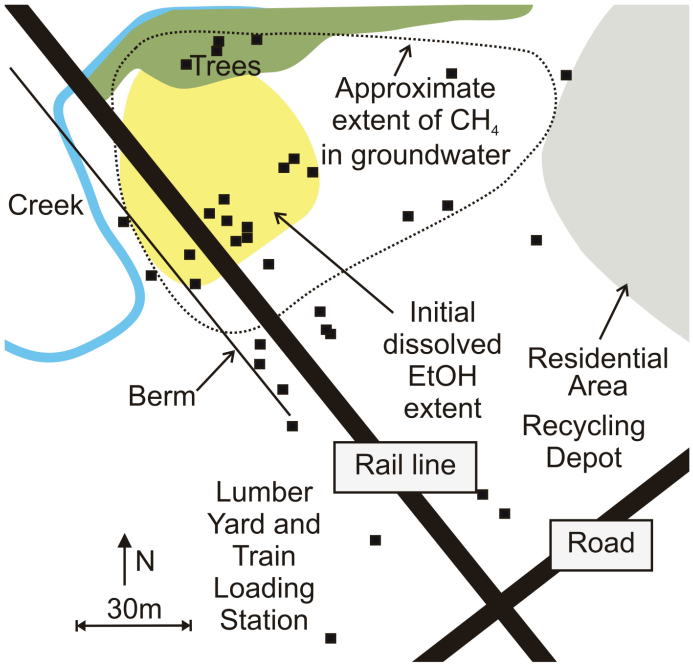

Figure 7.2. Plan view of Balaton site. Squares identify locations of monitoring wells, soil borings and vapour points used to delineate the ethanol and CH_4 containing zones (>1,000 ppb CH_4 contour shown (Spalding et al., 2011)).

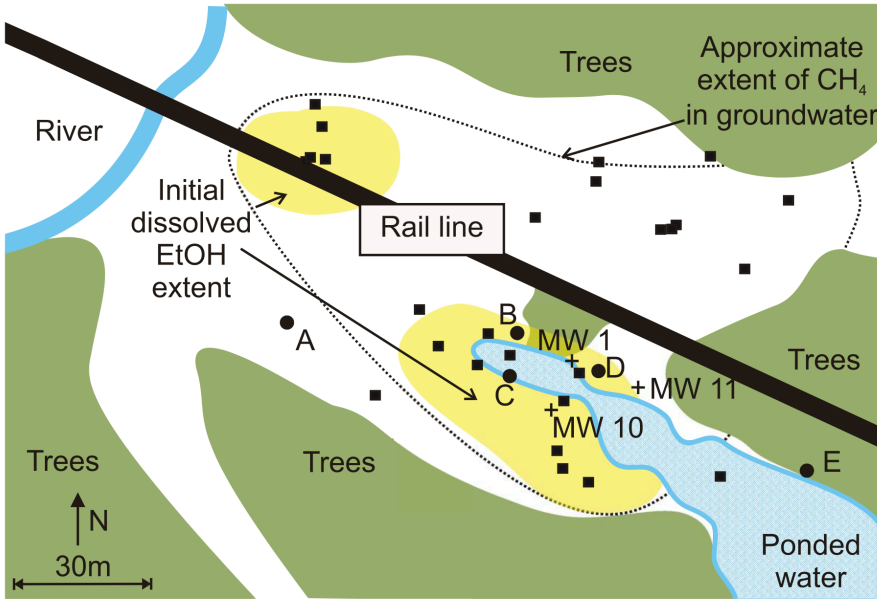

Figure 7.3. Plan view of Cambria site. Squares identify locations of monitoring wells, soil borings and vapour points used to delineate the ethanol and CH_4 containing zones (>1,000 ppb CH_4 contour shown (Spalding et al., 2011)). Crosses identify locations of monitoring wells. Black circles identify locations of gas collection chambers.

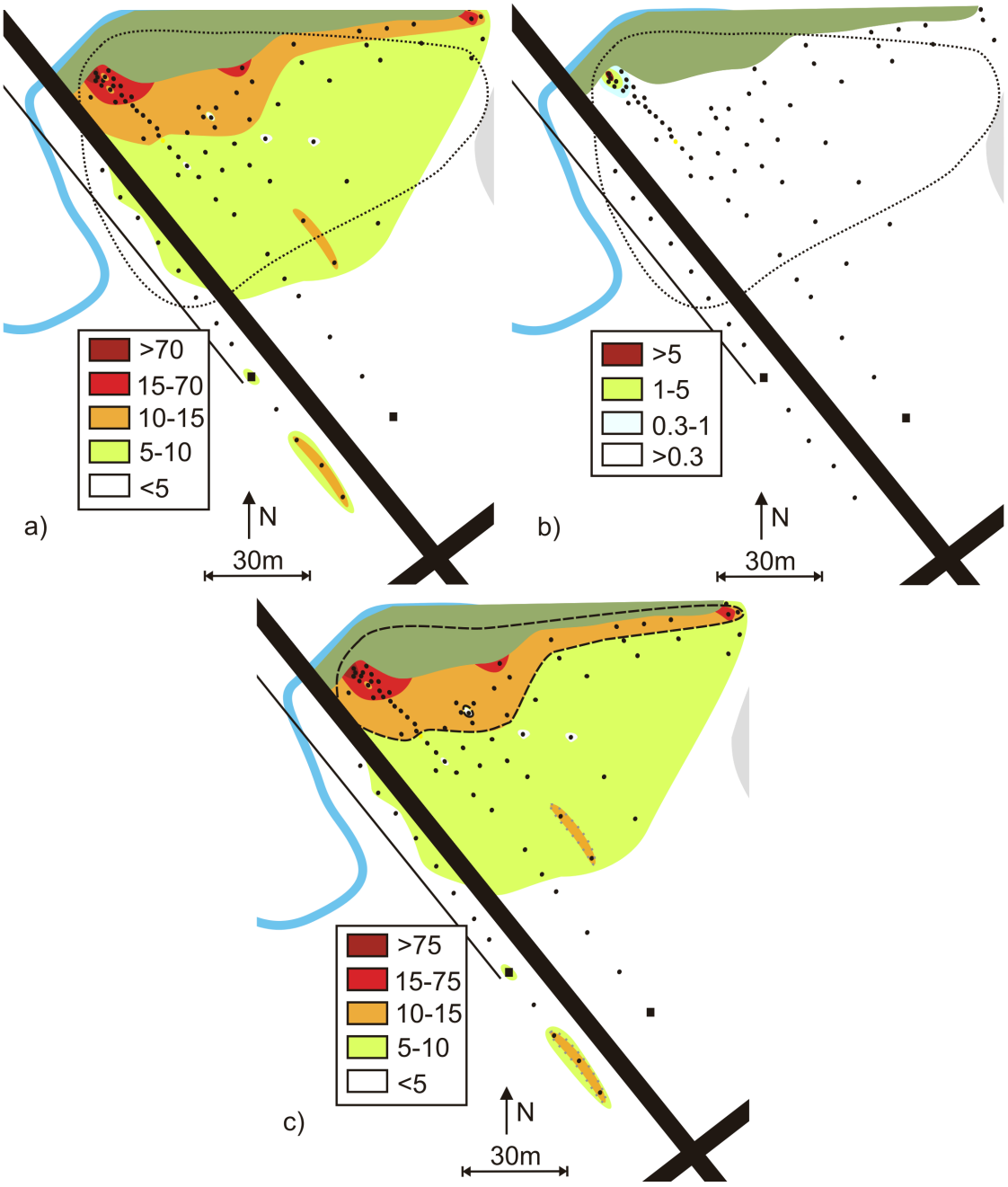

Figure 7.4. Distribution of measured gas effluxes [μmol m^{-2} s^{-1}] at the Balaton site. Small black circles denote measurement locations. Green squares denote measurement locations used to define background conditions. a) CO_2, b) CH_4, and c) total carbon efflux, black dashed line denotes the extent of the delineated source zone.

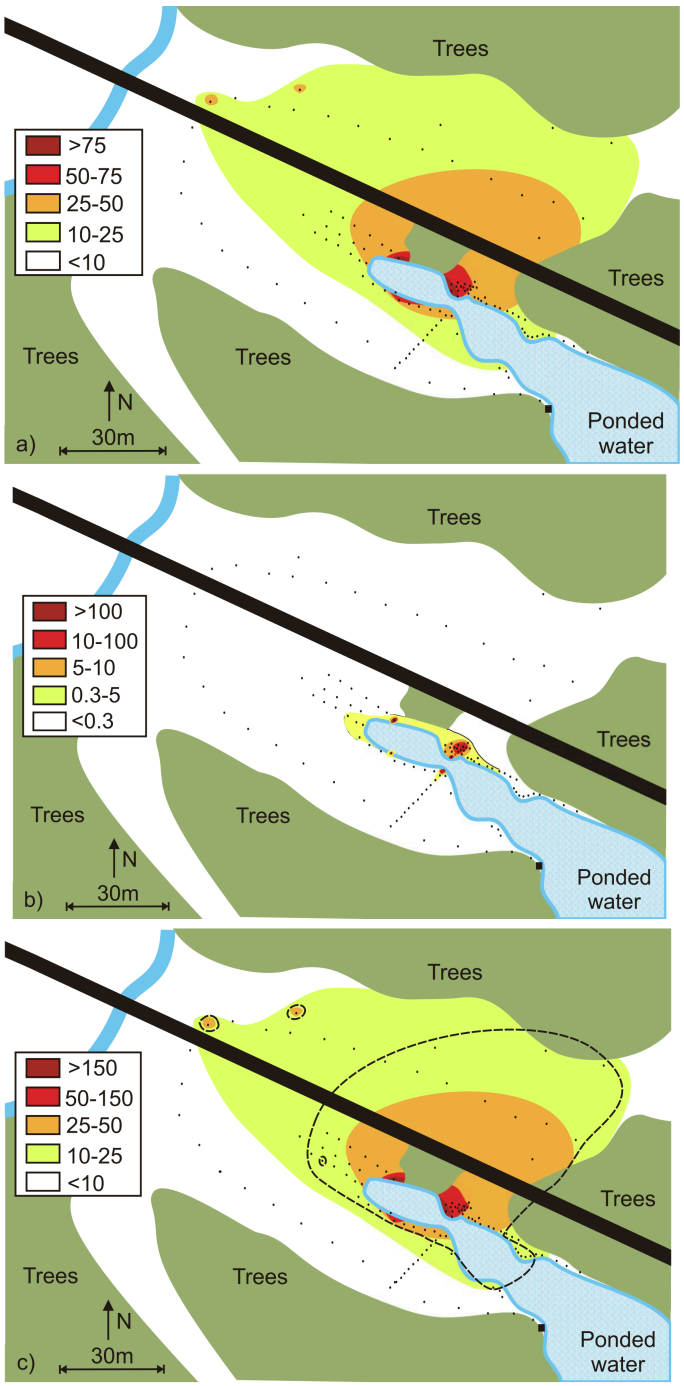

Figure 7.5. Distribution of gas effluxes [μmol m^{-2} s^{-1}] calculated for the Cambria site. Small black circles denote measurement locations. Green squares denote measurement locations used to define background conditions. a) CO_2 and b) CH_4 and c) total carbon efflux, black dashed line denotes the extent of the delineated source zone.

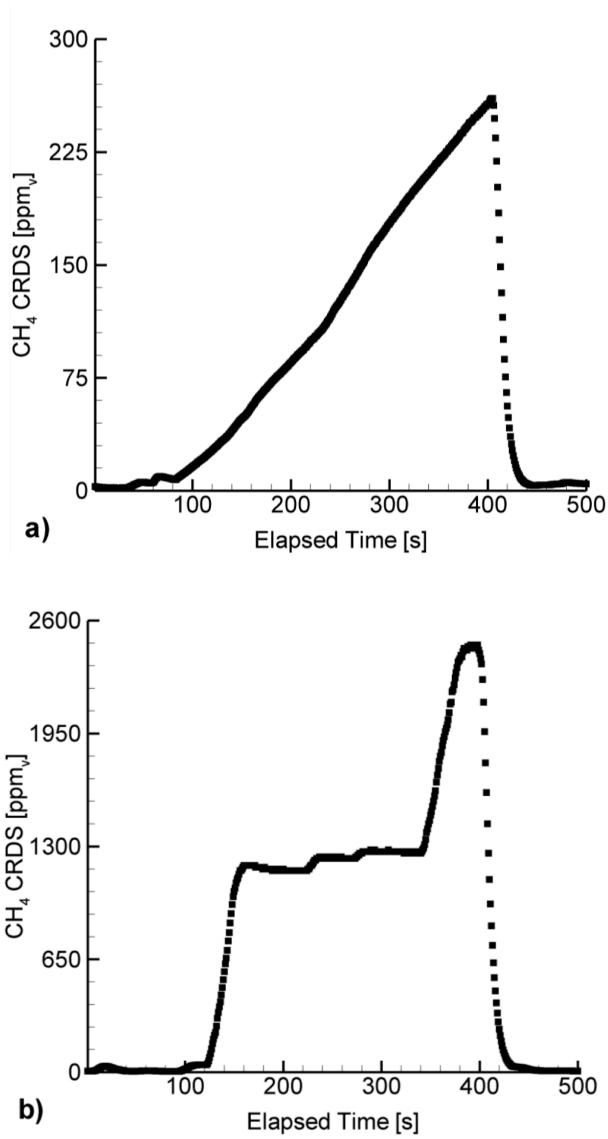

Figure 7.6. Example of data used in estimation of gas fluxes at the Cambria site. a) diffusive regime and b) ebullitive regime.

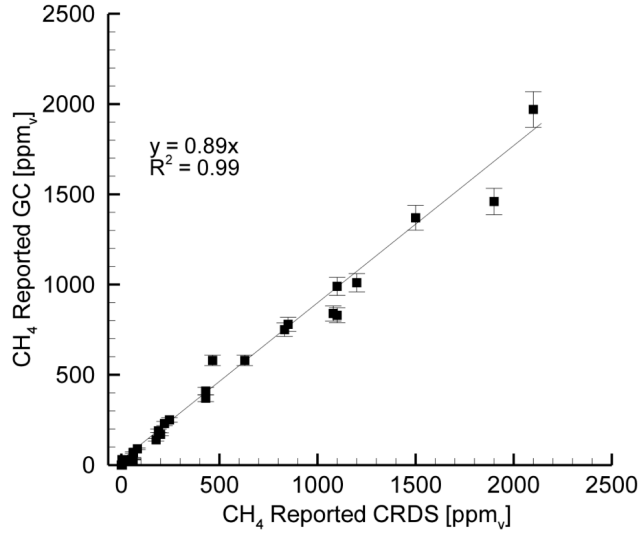

Figure 7.7. Comparison of CH_4 content in reported by the CRDC in the field and CH_4 content determined by GC analysis of samples collected from the chamber headspace. Error bars for GC analyses represent 5% error, based on reproducibility of replicate standard material.

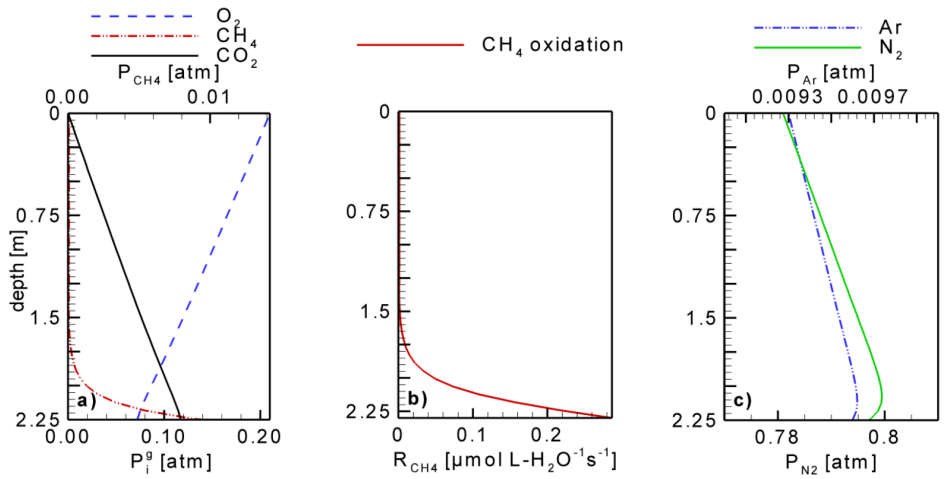

Figure 7.8. Simulated vadose zone gas profiles for Balaton scenario under quasi-steady state conditions, a) O_2, CH_4 and CO_2, b) CH_4 oxidation rate, c) Ar and N_2

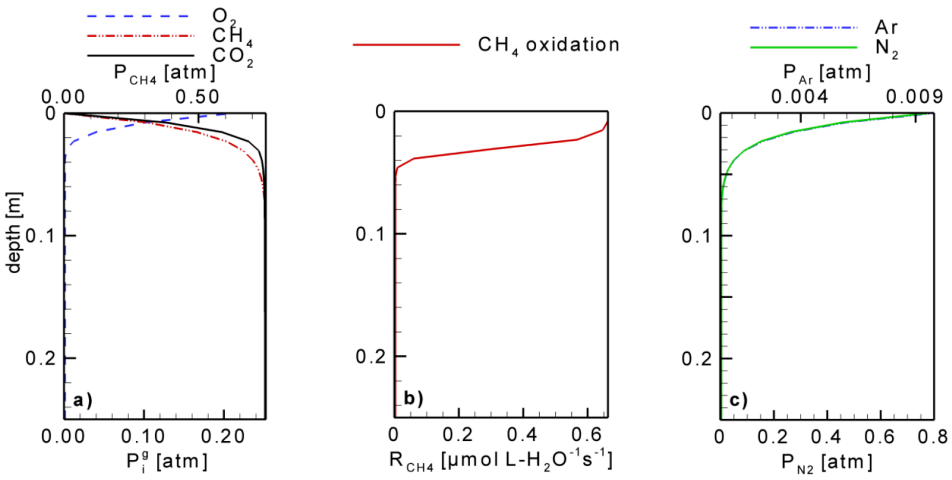

Figure 7.9. Simulated vadose zone gas profiles for Cambria scenario under quasi-steady state conditions, a) O_2, CH_4 and CO_2, b) CH_4 oxidation rate, c) Ar and N_2.

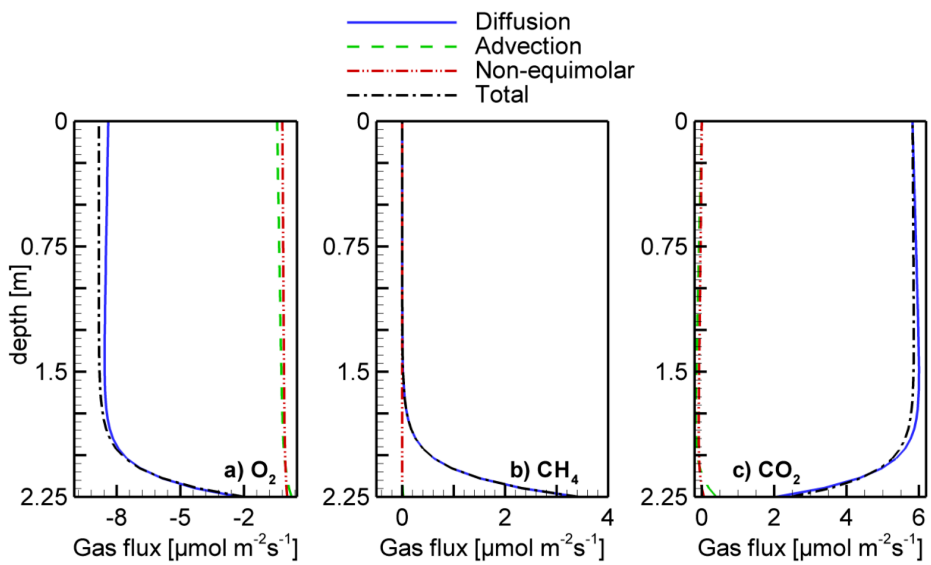

Figure 7.10. Simulated vadose zone gas fluxes for Balaton scenario under quasi-steady state conditions, a) O_2, b) CH_4, and c) CO_2.

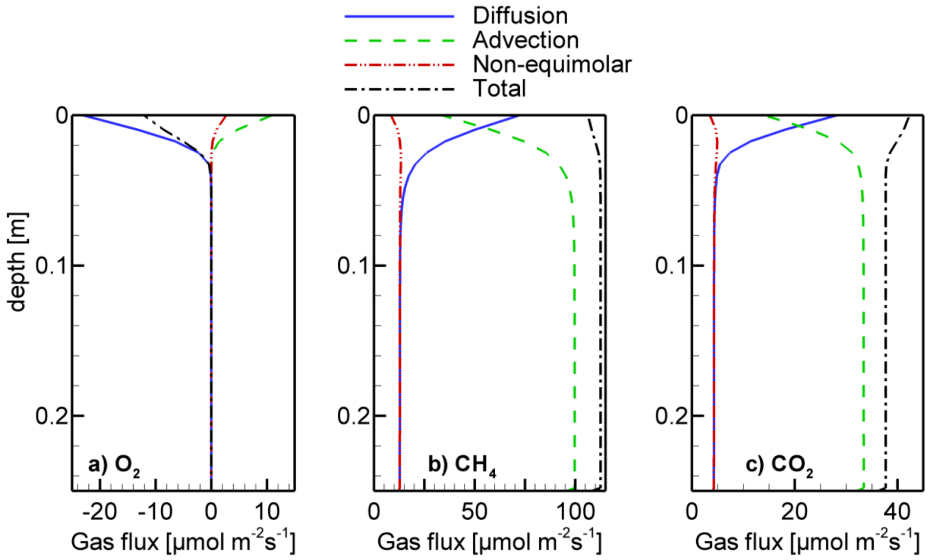

Figure 7.11. Simulated vadose zone gas fluxes for Cambria scenario under quasi-steady state conditions, a) O_2, b) CH_4, and c) CO_2.

Chapter 8: Catastrophic biofuel release activates syntrophic networks in the rare biosphere

Introduction

Microbial communities play integral roles in providing and maintaining ecosystem functions (Falkowski et al., 2008), such as carbon sequestration, nutrient cycling, and pollutant removal and the resulting services that humans enjoy (Daily and America, 1997; Ducklow, 2008). Understanding how microbial communities respond to environmental perturbations is critical for managing and engineering ecosystem services. Environmental perturbations can arise from catastrophic events such as bolide impacts, forest fires and oil spills, or result from cumulative impacts or stressors such as anthropogenic CO_2 release, eutrophication and drought (Nelson et al., 2006). Global energy consumption has resulted in cross-scale environmental perturbations, ranging from local degradation of air, soil and water quality (Groffman and Bohlen, 1999), to intercontinental transport of atmospheric pollutants (Lin et al., 2014), to global warming with the potential to alter ecosystem services arising from microbial community metabolism (Sheik et al., 2011).

Increased awareness of the socioeconomic and environmental costs associated with conventional energy resources has prompted many developed countries to seek alternate and sustainable modes of energy production (Hill et al., 2006). For example, both the United States and the European Union have promoted the use of blended ethanol (EtOH) biofuels derived from renewable plant sources such as corn, switchgrass and algae (Clarens et al., 2010). However, while considerable research has examined trade-offs associated with biofuel production (e.g., CO_2 emissions (Hill et al., 2006)), environmental impacts associated with biofuel spills remain poorly constrained (Sihota et al., 2013). Because biofuel production and transport occur primarily via rail cars and tanker trucks (Sihota et al., 2013), most release scenarios will result in surficial spills impacting the complete soil profile from vadose to saturated zones (**Figure 8.1**).

Contemporary studies examining biofuel releases have focused mainly on microbial processes within the saturated zone, neglecting microbial community responses within the vadose zone where the majority of DFE transformation is likely to transpire (Corseuil et al., 2011).

Recent advances in sequencing technologies (e.g., Caporaso et al., 2010) have enabled a deeper understanding of microbial community structure and function through massively parallel analyses of ribosomal genes (rDNA) and ribosomal RNA (rRNA), respectively. These techniques have been applied to evaluate both pristine (Campbell et al., 2011) and perturbed (Nogales et al., 1999) environments. In addition, the comparison of rRNA:rDNA ratios can be used to gain insight into the contribution of the rare and abundant biosphere to potential community activity (Campbell et al., 2011; Hugoni et al., 2013). For example, rRNA:rDNA ratios have been used to describe microbial community responses to fluctuating redox and moisture conditions in Amazonian rainforest soils (DeAngelis et al., 2010), and the function and activity of members of the rare archaeal biosphere in marine coastal surface waters (Hugoni et al., 2013). Similarly, rRNA:rDNA ratios have been to determine the relative activity of different microbial groups in estuarine surface waters and along a salinity gradient (Campbell et al., 2011; Campbell and Kirchman, 2013). In some cases, correlation networks of rRNA or rDNA have been used to investigate interactions between microbial community members (Ahn et al., 2010; Barberán et al., 2012). However, although understanding interactions among active microbial community members is integral to maintaining and managing ecosystem functions and services, networks combining rRNA and rDNA profiles have not been reported. Here we investigate microbial community responses to a catastrophic biofuel release (denatured fuel-grade EtOH or DFE) caused by a train derailment using pyrosequencing to generate combined rRNA and rDNA

profiles through the vadose and saturated zones at a source site (SS) and a reference site (RS) unaffected by the DFE.

Methods

Sample collection: Samples were taken at 10 cm intervals from sediment core collected at the RS and SS using a GeoProbe in October 2012. At each integral ~ 15 g of sediment was collected to falcon tubes and immediately in liquid nitrogen. Samples were shipped on dry ice to the University of British Columbia where DNA and RNA was extracted**.**

Nucleic acid extraction and cDNA synthesis: Total genomic DNA and RNA were isolated using the PowerMax® Soil DNA and PowerSoil® RNA Isolation Kits, respectively (MoBio, Carlsbad, CA). Resultant yields were quantified using the Picrogreen and Ribogreen assays (Invitrogen). RNA was purified using the RNeasy Mini Kit (Qiagen, Valencia, CA, USA) and an on-column DNase I digestion was applied to remove DNA contamination from RNA. Total RNA was reverse transcribed to complementary DNA (cDNA) using a Superscript® III first-strand synthesis kit (Invitrogen, Carlsbad, CA) with random hexamers. To ensure final cDNA was free of DNA contamination, cDNA synthesis reactions were performed without reverse transcriptase and then evaluated with polymerase chain reaction (PCR; as described below).

PCR amplification and pyrosequencing of SSU rDNA and cDNA: Amplification of the V6-V8 region of the SSU rRNA gene was conducted using DNA and cDNA templates with universal primers 926F (5'-AAACTYAAAKGAATTGRCGG-3') and 1392R (5'-ACGGGCGGTGTGTRC-3'). Primers were modified to include 454 adaptor sequences, and

reverse primers were modified to include a five base-pair barcode following (Engelbrektson et al., 2010; Allers et al., 2013). To minimize PCR bias, reactions were performed in duplicate, and paired with a negative control. Each reaction included 50 µl of substrate including 0.6 µl Taq DNA Polymerase (5U/ µl), 5 µl 10X PCR buffer, 3 µl magnesium chloride, 4 µl 2mM dNTP mix, 1 µl of each primer, 1 µl reverse primer and 10 ng template. Final duplicate reactions were pooled. Sequencing was performed at Genome Quebec (Montreal, Canada) on the Roche 454 GS FLX Titanium platform (454 Life Sciences, Branford, CT, USA) following manufacturer's instructions.

Processing of pyrotag sequences: Quantitative Insights Into Microbial Ecology (QIIME) version 1.4.0 software package (Caporaso et al., 2010) was used to process a total of 275,606 and 127,187 SSU rDNA and rRNA pyrotag sequences. Sequences with less than 200 bases, ambiguous 'N' bases, quality scores below 25, and homopolymer runs were removed before chimera detection (ChimeraSlayer (Haas et al., 2011)). High quality sequences were clustered to operational taxonomic units (OTUs) at 97% with a maximum e-value cut-off of $1e^{-10}$ (Edgar, 2010). Singletons (represented by one read) were omitted to reduce over prediction of rare OTUs (Kunin et al., 2010). Resulting in 29,113 OTUs made up of 224,599 pyrotag sequences in the rDNA dataset and 17,627 OTUs made up of 102,550 pyrotag sequences in the rRNA. Taxonomic assignment was conducted using the Basic Local Alignment Tool (BLAST) and the SILVA database version 111 (www.arb-silva.de; (Pruesse et al., 2007)) using a confidence level of 0.8 and a maximum e-value cut-off of $1e^{-6.}$ Samples containing <400 OTUs in either the rDNA or rRNA fraction were excluded from the datasets. OTUs occurring <1 times in the entire dataset were eliminated from further analyses, resulting in 29,113 and 17,627 OTUs for rDNA

and rRNA datasets. OTU abundance was normalized to the total number of reads recovered per sample, and expressed as normalized percent for analysis.

Data analyses: Statistical analyses were performed in R (version 6.0.2 (2013-09-25)) and using in-house perl scripts. Network analyses was conducted in Gephi (version 0.8.2), following generation of correlation matrices using Spearman's sign rank correlations ($r^2 > 0.8$, $P < 0.01$). To evaluate differences in community structure between the rDNA datasets for the RS and SS and between the rDNA and rRNA datasets for the SS, species richness was estimated using the Chao1 index ((Chao, 1984); Supporting information provided in **Appendix 7 - Figure A7.1**). Diversity was calculated within samples from the RS and SS (alpha diversity) and between the RS and SS sites (beta diversity) using the Shannon and Simpson indices and Fishers alpha, respectively. Analyses were conducted using R software (R version 6.0.2 (2013-09-25)) with the vegan and MASS packages.

Similarity in depth-discrete samples within the rDNA (RS and SS) and rRNA (SS) datasets was identified using Wards hierarchical cluster analysis, conducted using R packages vegan and pvclust. To identify indicator species within resultant clusters, indicator species analyses were performed based on resultant cluster groups using R packages labdsv and cluster.

Network analyses: Networks were constructed using correlation matrices based on OTU tables from rDNA (RS and SS), rRNA (SS) and rRNA:rDNA (SS) datasets using Spearman's sign rank correlations. Inclusion requirements were as follows: $r^2 > 0.8$, $P < 0.01$, OTU present in ≥ 3 samples. Networks were visualized and properties were evaluated using Gephi (version 0.8.2; (Bastian et al., 2009)). Results were compared to random networks constructed using the same

number of nodes as each of the networks listed above. Network properties are provided in **Table A7.1.** To evaluate sub-community motifs, node partitioning was conducted based on modularity class following the approach outlined in (Blondel et al., 2008). Forced-directed layouts were obtained from the Force Atlas 2 algorithm (Jacomy, 2009) to visualize the rDNA and rRNA networks, as this resulted in a clear separation of soil zones (**Figure A7.4** and **Figure A7.5**). For the rRNA:rDNA network, a Fruchterman-Reingold Algorithm (Fruchterman and Reingold, 1991) was used to generate the layout (**Figure 8.4**). This approach was selected as active sub-communities were strongly tied to particular soil zones, resulting in a loss of the inter-community connectivity (and consequently, observable soil structure). This result is reasonable due to the strong chemical and redox stratification at the site. Results of modularity analyses are presented in **Table A7.4**, and were consistent with results obtained using edge clustering algorithms (Link Communities' which creates groups based on shared edges (Ahn et al., 2010)), and PageRank analyses.

Results

Our study site is located in southwestern Minnesota (lat. 44.247083, long. -94.33710598677882). Contamination resulted from a multicar train derailment in November 2006, which released 9.5 x 10^4 L of DFE onto land surface. Analyses of pyrosequence datasets revealed two depth-stratified groups in the RS representing topsoil and subsoil layers respectively, while three depth-stratified groups were resolved in the SS representing vadose, capillary, and saturated zones (VZ, CZ, and SZ, respectively), with EtOH concentrations peaking in the CZ (**Figure 8.1, Appendix 7**).

To evaluate changes in microbial community structure as a consequence of catastrophic DFE exposure, the contributions of rare and abundant taxa at the RS and SS were calculated.

Results revealed 11.3 and 28.4 % of the rDNA OTUs from RS and SS samples were rare when using a stringent threshold of 0.01% (Galand et al., 2009)**,** suggesting an increase in the rare biosphere following EtOH exposure (Lennon and Jones, 2011*)*. Expansion of the rare biosphere could represent an ecological threshold or tipping point associated with catastrophic DFE exposure (Lennon and Jones, 2011)**.** Within the rDNA dataset from the SS, the rare community represented 34.8, 48.1, and 30.9 % of the VZ, CZ, and SZ, respectively. Within the rRNA dataset, the distribution shifted to 0, 36.5, and 39.1%, respectively, consistent with increased activity at the watertable interface, and within the most perturbed soil zones.

To determine relative contributions of rare, intermediate, and abundant OTUs within the SS rDNA dataset, we compared frequency distributions within each category, using ranges of 0 – 0.1, 0.1 - 1 and > 1% (**Figure 8***.2* (Galand et al., 2009)). We observed that 42, 57.4, and 0.6 % of the community was rare, intermediate and abundant, respectively. Comparison of rDNA OTUs between RS and SS indicated that 31, 31, and 27 % were shared within rare, intermediate and abundant categories, consistent with a change in community structure associated with catastrophic DFE exposure and reinforcing the potential ecological roles of low abundance (e.g., rare and intermediate) OTUs during perturbation responses (**Figure 8***.2, Table* **A7***.2*).

To evaluate potential activity of low abundance OTUs in the SS, rRNA:rDNA ratios were calculated (Campbell et al., 2011). We observed only a weak correlation (tau = 0.26) between rDNA and rRNA abundance, consistent with observed frequency distributions within the rDNA dataset (**Figure S2**). Moreover, the distribution of scatter in the rRNA:rDNA frequency plot indicated that rare and intermediate OTUs were active community members (**Figure 8***.2,* (Campbell et al., 2011)*)*. This was further reinforced by the observation that low abundance community members contributed 77, 70, and 60 % of rRNA OTUs within active communities of

the VZ, CZ, and SZ respectively indicating that recruitment from low abundance OTUs was substantial in the active community.

To better resolve how potential activity related to DFE transformation processes, we calculated rRNA:rDNA ratios for dominant microbial groups and mapped previously identified metabolic traits for these groups onto the soil profile (**Figure 8.*3*, Figure A7.3, *Table* A7.*2*, Appendix 7**). We observed functional partitioning consistent with redox transitions between taxonomic groups inhabiting the VZ, CZ, and SZ. Within the VZ, trait-based mapping revealed a primarily aerobic consortium, including groups responsible for nitrite oxidation (Nitrosospirales), CH_4 oxidation (Methylococcales) and aromatic catabolism (Burkholderiales). Within the CZ trait-based mapping revealed a transition to anaerobic metabolism with an increase in active taxa involved in iron and sulfur cycling and volatile fatty acid production (Desulfuromondales, Desulfobacterales) as well as methane production (Methanobacteria and Methanomicrobia). Within the SZ, trait-based mapping indicated declining anaerobic conditions, based on a decrease in activity of taxa involved in methane production and an increase in activity of taxa involved in methane consumption (Methylococcales) at the base of the soil profile. Shifts in methanogen activity were consistent with local competition for syntrophic growth substrates including H_2 and acetate with aceticlastic methanogens and Deltaproteobacteria outcompeting hydrogenotrophic methanogens throughout the soil profile.

Given the potential for syntrophy in the soil profile we evaluated effects of catastrophic DFE exposure using co-occurrence networks constructed from RS and SS rDNA datasets. Network properties are provided in **Table A7.3** and discussed in **Appendix 7**. Within the SS network rare, intermediate and abundant OTUs contributed, 80, 18, and 2 % of the nodes based on the distribution of OTUs presented in **Figure 8.2**. Within the RS network rare, intermediate

and abundant OTUs shared with the SS contributed 6.2, 1.3, and 0.2 % of the nodes. The contrasting structure of RS and SS rDNA networks supports the hypothesis that catastrophic DFE exposure crosses an ecological threshold or tipping point, altering the composition and connectivity of the soil network. To determine the extent to which this tipping point redirected matter and energy flow, we evaluated the co-occurrence of active community members using rRNA and rRNA:rDNA datasets from the SS (**Figures 8.4 and A7.3-4, Table A7.3**). Within the rRNA:rDNA network, 69, 28, and 4 % represented rare, intermediate, and abundant OTUs supporting the importance of low abundance OTUs in responding to catastrophic DFE exposure. When compared to the rDNA network, the rRNA:rDNA network contained lower diversity, but higher connectivity (**Table A7.3**). These findings are consistent with other studies applying network theory to investigate regime shifts in complex systems involved in cellular signaling (Szalay and Csermely, 2013), global climate regulation (Donges et al., 2011), and financial markets (Scheffer et al., 2012).

Given the differences in network properties, we investigated connectivity between OTUs within defined modules of the rRNA:rDNA network. Although a total of 150 modules were identified, 12 modules contained ~ 70% of all OTUs (nodes) and ~ 93 % of all connections (edges) represented in the network (with each module representing > 1% of all the OTUs) (**Table A7.3-4**). Mapping VZ, CZ, and SZ indicators to nodes revealed that modules were mainly comprised of OTUs representative of specific soil zones (**Figure 8.4A, Table A7.4***)*. Across these modules, the contribution of rare and intermediate OTUs (represented in **Figure 8.2**) ranged from 2.1 – 11.2 % and increased with module size ($r^2 = 0.9$, $P<0.01$; **Figure 8.4B**, **Table A7.4**). Average module activity (rRNA:rDNA) ranged from 1.5 to 7.7, with the most active modules being associated with the SZ and CZ. Comparison of average activity to other network

properties revealed that activity correlated well with closeness centrality ($r^2 = 0.7$ $p < 0.01$), suggesting that tightly-connected OTUs were highly active (Table A7.4). The increased activity in the CZ and SZ is consistent with an increase in activity at the water table interface and with the low energy yield of anaerobic degradation, which requires complex syntrophic community interactions (Morris et al., 2013). Overall, the differences in properties between the rDNA and rRNA:rDNA networks are consistent with increased metabolic coupling in the SS, a pattern observed in other anoxic soil settings supporting syntrophic growth (Morris et al., 2013).

To evaluate the extent to which functional partitioning observed between taxonomic groups inhabiting the VZ, CZ, and SZ (Figure 8.3) was reflected in the network, we mapped taxonomic and trait information used previously to nodes (Figure 8.4C). We observed distinct microbial consortia with connectivity patterns consistent with redox zonation (Figure 8.4D). For example, in predominantly VZ modules (M64, M67, M117, M130, M131 – all > 98% VZ) most active OTUs were affiliated with aerobic Alpha- and Deltaproteobacteria, Armatimonadetes and Fungi. In a predominantly CZ module (M26; 96%), OTUs affiliated with Clostridia and Bacilli were highly active. This association is consistent with known syntrophic interactions, whereby Bacilli condition the environment for Clostridia (through removal of O_2 and CH_3COO^- (Chang et al., 2008)). In a module comprised of OTUs mapping to both CZ and SZ (M58; 29% CZ, 71% SZ), OTUs affiliated with Clostridia and methanogens (Methanobacteriales and Methanosarcinales) were most active, while OTUs affiliated with sulphate reducing Deltaproteobacteria were less active. In contrast, in predominantly SZ modules (M37, M50 and M122), sulphate reducing Deltaproteobacteria and Syntrophobacterales (VFA oxidizers) were most active, while OTUs affiliated with methanogens were less active. These results point to functional partitioning between taxonomic groups (**Figure 8.3**), and reveal patterns of

competitive exclusion related to H_2 and potentially acetate utilization, between methanogens and sulphate reducing Proteobacteria in the soil profile. This is consistent with theoretical thermodynamic calculations (as sulphate reduction is more favorable than methanogenesis ($\Delta G_0' = -152.2$ kJ mol^{-1} vs. -131 kJ mol^{-1}, respectively), and empirical evidence for syntrophy observed in anaerobic EtOH-fed biofilms (Parameswaran et al., 2009).

Discussion

Differences in OTU distributions between RS and SS rDNA datasets suggest that expansion of rare and intermediate taxonomic groups represents an ecological response to a threshold or tipping point associated with catastrophic DFE exposure. Indeed, the dramatic drop in microbial abundance and activity in proximity to peak EtOH concentrations is supported by reported EtOH toxicity thresholds reported under laboratory conditions (Nelson et al., 2010). Based on our results, EtOH toxicity changes the fitness landscape allowing rare and intermediate community members to occupy new or vacated niches (Lennon and Jones, 2011). Consistent with this observation, community structure within SS rDNA and rRNA:rDNA datasets indicated recruitment from non-active seed populations that became active participants in community metabolism following catastrophic DFE exposure (Lennon and Jones, 2011). However, care must be taken when interpreting rRNA:rDNA ratios, as elevated levels of rRNA have been attributed to sources other than increased activity (e.g., multiple ribosome copies or dormant cell function (Blazewicz et al., 2013)). Despite these limitations, evaluation of the rRNA:rDNA datasets using network analyses revealed a highly modular active community, with dense intra-module connectivity most notable in modules dominated by OTUs from CZ and SZ. This reinforces the importance of syntrophic interactions in driving matter and energy transformations

in contaminated ecosystems where anaerobic degradation operates near thermodynamic thresholds (Wu et al., 2012).

Overall, our in situ observations are consistent with emerging views of 'obligatory mutualistic metabolism' in natural and perturbed ecosystems (Morris et al., 2013) and provide a framework for understanding bioenergetic cycling in perturbed ecosystems based on active microbial community interaction networks. Indeed, changes in network properties associated with catastrophic DFE exposure can assist in the development of conceptual (Figure 8.4) and numerical (Fang et al., 2011) models for monitoring microbial dynamics in ecosystems subject to periodic or cyclical changes (e.g., isolated catastrophic perturbations or changing redox conditions in soil or aquatic ecosystems). Finally, the outcomes of this study can also be used to inform engineers and decision makers about the attenuation potential of DFE contaminated soils and provide ecological design principles to mitigate or manage risk under catastrophic release scenarios – scenarios that are likely to increase as we become more reliant on biofuels to offset fossil fuel consumption.

Figures

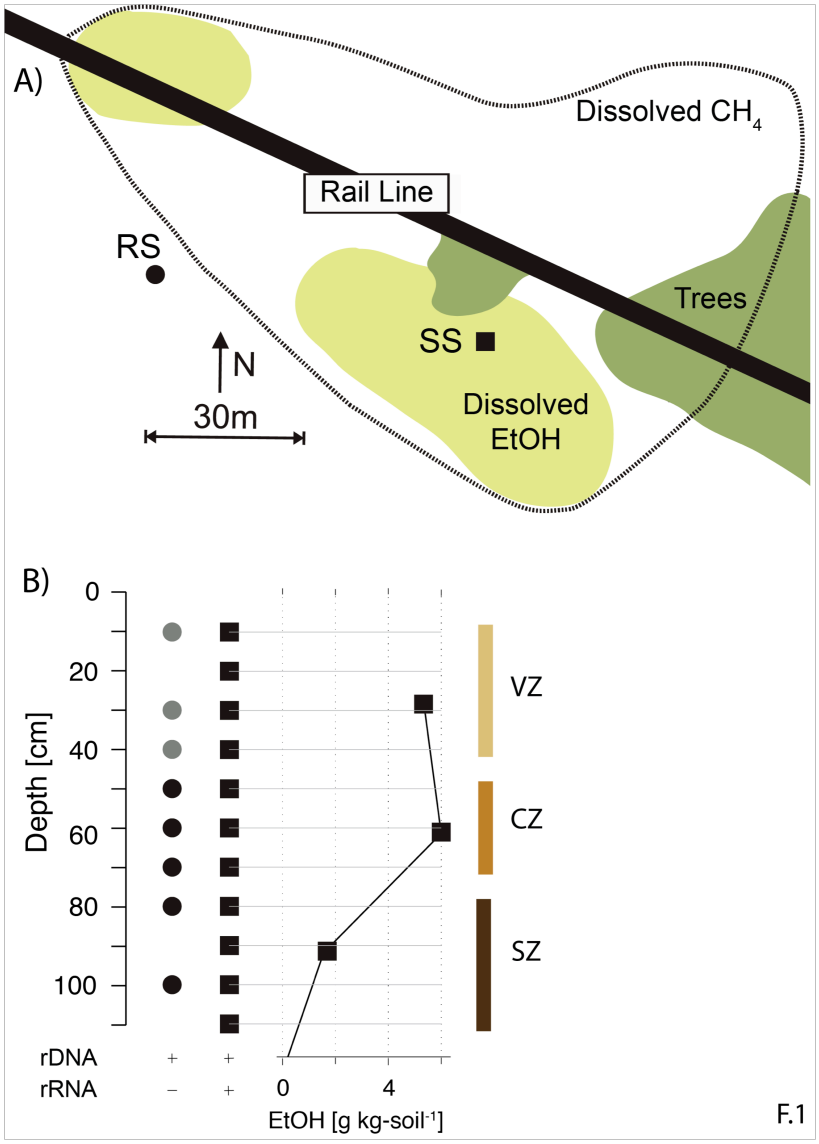

Figure 8.1. Site layout. A) Distribution of DFE at the field site and locations of reference site (RS) and source site (SS) core collection. B) Depths of sample locations at the RS and SS and EtOH concentrations measured in core collected adjacent to the SS; colors show cluster zones.

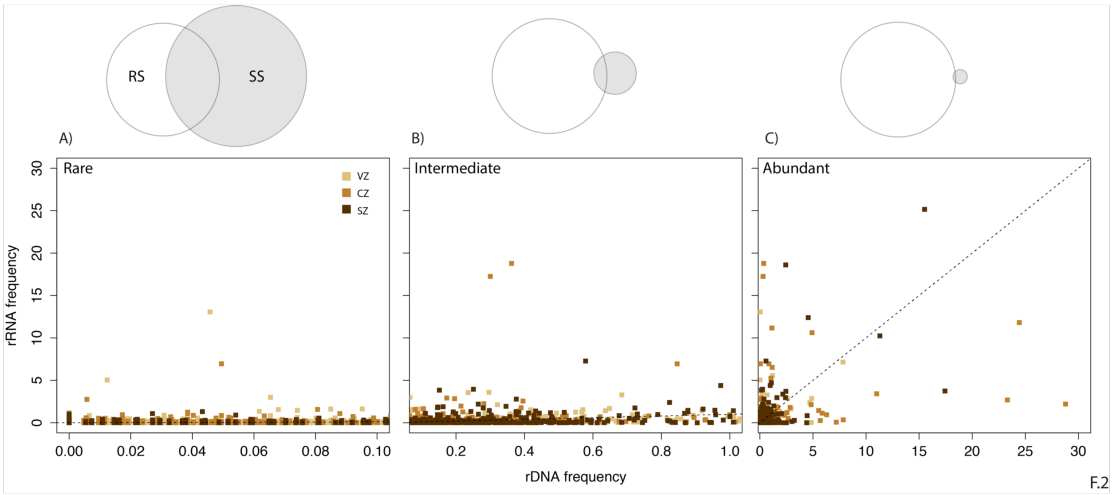

Figure 8.2. Microbial community distribution at the SS. Distribution of A) rare, B) intermediate and C) abundant biosphere. Relationships between frequencies of 16S rRNA and 16S rDNA OTUs defined in the pyrosequence dataset at the SS. Euler circles show OTUs shared between the RS rDNA dataset and the fraction of the SS represented in associated scatterplots. Dashed lines represent 1:1 relationships.

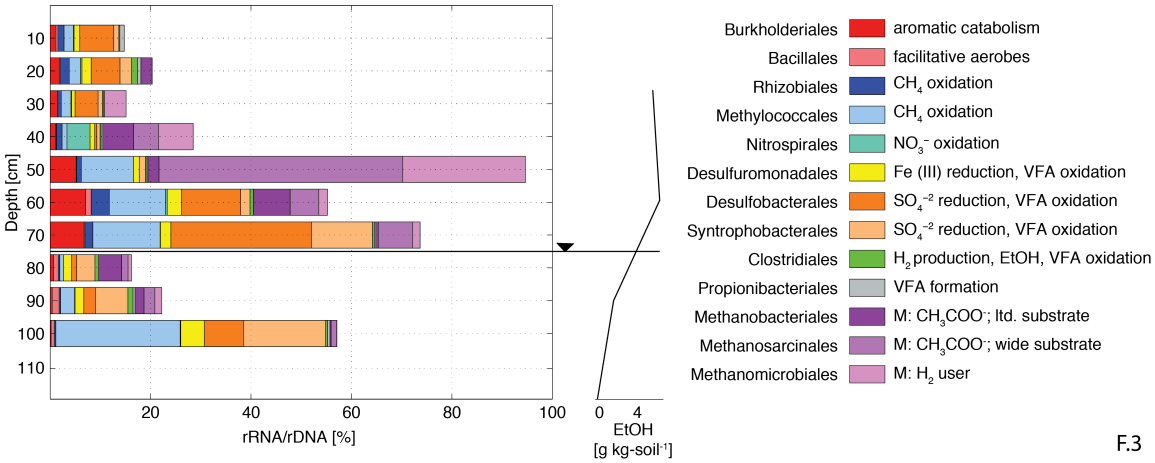

Figure 8.3. Active microbial community members at the SS. Distribution of taxa and traits mapped to the soil profile for the intermediate and abundant active microbial categories at the SS. Spark line shows EtOH concentration; filled triangle shows approx. location of the water table.

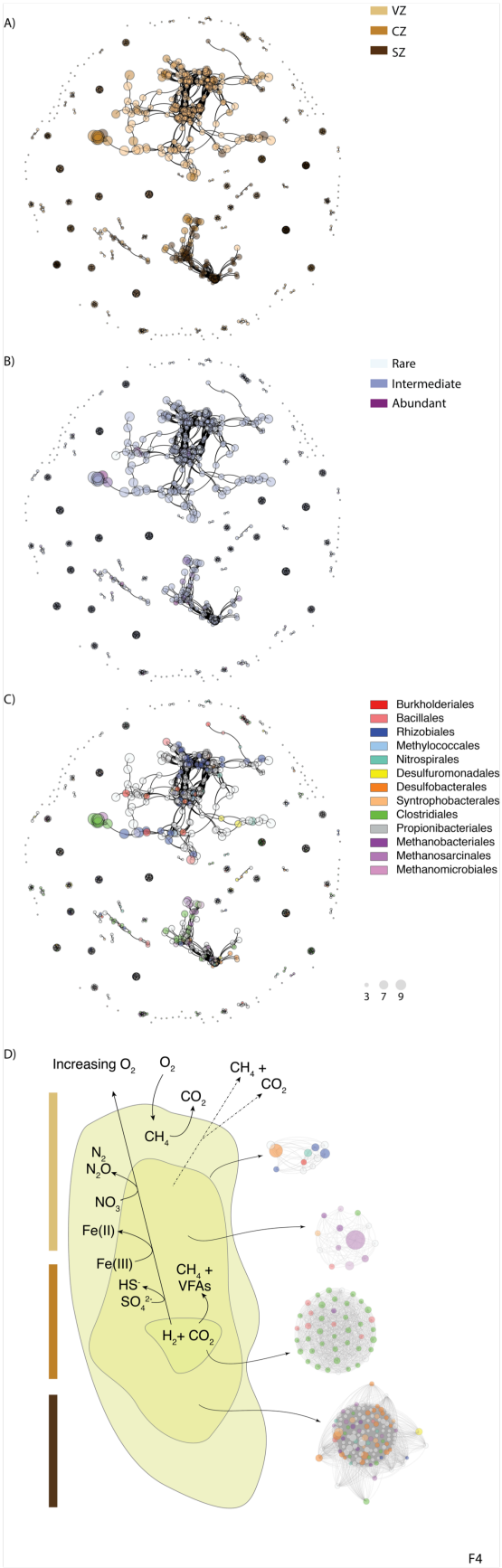

Figure 8.4. Activity network. Network of active community members identified based on interactions between OTUs at the SS. Distribution of OTUs within A) soil zones, B) microbial community categories, C) phylogenetic mappings, and D) conceptual model of bioenergetic cycling and community interactions in perturbed ecosystems. Nodes are sized to closeness centrality.

Chapter 9: Comparison of source zone natural attenuation rates at crude oil and biofuel release sites

Introduction

Anthropogenic contamination occurs across the globe as a result of chemical releases to the natural environment associated with the production, transport, and use of goods for human consumption. For example, the environmental fate of heavy metals (McClintock, 2012), hydrocarbons (Samanta et al., 2002), radionuclides (Lind et al., 2013), herbicides (Laini et al., 2012), and pharmaceuticals (Pal et al., 2010) have been well documented in the scientific literature. Under some conditions, contaminants can be degraded *in situ* by native microbial communities (i.e., via source zone natural attenuation; SZNA), allowing for sustainable management of mass in place. In this context, understanding how specific site characteristics influence natural attenuation processes is critical for informing management decisions (Reed et al., 2011). Laboratory research using samples collected from a range of field sites has demonstrated that differences exist between SZNA potential across environments impacted by the same contaminant (Díaz et al., 2002; Hamamura et al., 2006; Liang et al., 2011). Similarly, unique contaminant characteristics have been linked to differences in degradation potential (Owsianiak et al., 2009). However, translating laboratory or modeling results to field sites is challenging, suggesting direct field measurements of SZNA are needed. Source zone natural attenuation can be quantified in the field through assessment of microbial populations (Bekins et al., 2005a), measurement of degradation products in the vadose (Lundegard and Johnson, 2006) and saturated zones (Revesz et al., 1995), evaluation of isotopic fractionation patterns (Meckenstock et al., 2004), and push-pull tests (Istok et al., 1997). However given the labour intensity and relatively small volume characterized by these methods, combined with the geologic heterogeneity inherent to natural systems, spatial characterization of SZNA remains challenging. This is further complicated by local-scale variability in contaminant biodegradation

potential (Wilson et al., 2004; Thornton et al., 2011). Recently, (Sihota et al., 2011, 2013)) developed a method for rapid evaluation of depth- and terminal electron acceptor-integrated biodegradation rates using surficial gas efflux measurements. This method assumes that degradation reactions culminate in CO_2 and CH_4 generation, and that these gasses report to ground surface. In cases where O_2 ingress is sufficient to oxidize CH_4 within the vadose zone, CO_2 effluxes alone are sufficient to evaluate SZNA processes, while in cases where CH_4 escapes oxidation (e.g., scenarios with high soil moisture contents and/or rapid degradation rates), measurement of CH_4 effluxes is also required (Sihota et al., 2011, 2013). This suggests that both specific site conditions and differences in degradation potential between contaminants would influence the composition and magnitude of gas emissions. For example, in comparison to traditional fuel mixtures, ethanol (EtOH)-augmented fuels provide a large pool of highly labile carbon, yet at elevated concentrations EtOH is toxic to microorganisms (Nelson et al., 2010). Elevated EtOH concentrations can be expected to result directly following large volume, highly concentrated EtOH-augmented fuel releases, such as DFE (95% EtOH, 5% gasoline; (Spalding et al., 2011)). For these scenarios, the combination of initial toxicity coupled with the mass of labile carbon for resilient and/or opportunistic microbes once EtOH falls below toxicity thresholds pose unique challenges for risk assessment and site management. Consequently, to develop robust conceptual models and inform management options, there is a need to evaluate differences in the factors influencing SZNA and identify potential risk drivers under traditional petroleum hydrocarbon and DFE field release scenarios.

Here we use surficial gas efflux measurements to compare and contrast the extent and rate of SZNA processes at two crude oil and two DFE field sites. The objective of this work is to evaluate differences between sites with the same contaminant and across sites with different

contaminants with a particular focus on: 1) the composition and magnitude of total gas effluxes; 2) the ability to delineate the contaminant containing source zone using gas efflux measurements; and 3) magnitude of calculated SZNA rates. Results are set in the context of site-specific environmental conditions influencing degradation to evaluate risk potential under different fuel release scenarios, and identify important parameters for assessing SZNA under field conditions.

Methods

Field sites: Fieldwork was conducted at two crude oil spills and two DFE release sites in Minnesota, USA (**Figure 9.1, Table 9.1**). The Bemidji site is located in a forested region of north-central Minnesota and is underlain by a sand and gravel glacial outwash aquifer. A pipeline rupture on Aug. 20th, 1979 resulted in the loss of ~ 1.7 x 10^6 L of crude oil to the subsurface (Essaid et al., 2011). Following remedial efforts, ~ 4 x 10^5 L remained in the vadose zone, where it formed three oil bodies (Essaid et al. 2011). The north pool (the focus of the present study) was estimated to contain ~1.47 x 10^5 L of crude (Essaid et al. 2011). The main research area is bisected by an abandoned rail line that serves as an access road. The repaired pipeline runs through the south-western extent of the source zone (**Figure 9.2**). Above the oil containing source zone, sparse grasses are present, while to the east and west vegetation becomes denser and pine trees are present in some areas. Interdisciplinary investigation of SZNA processes began in 1983, and has been led by the United States Geological Survey (USGS). Within the vadose zone, results to date show a core of anaerobic degradation focused in the area where oil remains suspended above the water table. CH_4 and CO_2 are locally elevated in this region, and O_2 is absent. Surrounding the anaerobic core is an aerobic zone, where CH_4 is

oxidized by ingressing O_2 from the atmosphere; CH_4 concentrations are below detection at all gas monitoring ports near the ground surface (Sihota et al. 2011). Comprehensive site overviews can be found in (Baedecker et al., 1993; Bennett et al., 1993; Eganhouse et al., 1993; Cozzarelli et al., 2001) CO_2 effluxes were measured in 2009 (Aug. 9th - 21st; Sihota et al. 2011), 2010 (July 20th - 30th), 2011 (June 14th - 18th), and 2012 (June 12th - 18th). In 2012, both CO_2 and CH_4 effluxes were measured.

The Cass Lake site is located adjacent to a pumping station in north-central Minnesota (**Figures 9.1 and 9.3**; ~ 40 km to the east of the Bemidji site; the pipeline which runs beneath each site is the same) and is underlain by a sand and gravel outwash aquifer. A weeping flange associated with the pumping station was first identified in 2001 (although the date of initial release is unknown; Drennan et al. 2010). Remediation included removing ~ 278 m^3 of impacted sediments. To maintain pipeline integrity, not all of the contaminated sediments could be removed (Drennan et al. 2010). Following remediation, ~ 1.82 x 10^5 L was estimated to remain floating on the water table (Drennan et al. 2010). As at the Bemidji site, research at the Cass Lake site has been conducted by the USGS, however no data is available on the distribution of subsurface gas concentrations. Gas efflux measurements were conducted on June 24th, 2011 (CO_2 only) and on June 20th, 2012 (CO_2 and CH_4).

The Balaton site is located in a vacant lot in southwest Minnesota (**Figures 9.1 and 9.4**) and is underlain by poorly sorted sand with some silt lenses (Sihota et al., 2012). A multi-railcar derailment on July 28, 2004, resulted in the loss of 1.5 x 10^5 L of DFE and soybean oil (Spalding et al. 2011) (**Figure 9.4**). Clay berms were constructed, and accessible free product was pumped off and removed. Additional remedial action included excavation of ~ 1.6 x 10^3 m^3 of impacted soils; the area was subsequently backfilled with clean material (Spalding et al. 2011). Spalding et

al. (2011) estimated ~ 6.8 x 10^4 of DFE remained in the soils and aquifer following remediation. Maximum EtOH concentrations of exceeding 5 % were detected for close to a year following the release, but EtOH has not been detected in the monitoring wells since December 2007 (Spalding et al. 2011). Dissolved CH_4 was detected at levels exceeding saturation directly below the source zone by the fall of 2008 and its presence continued through 2012 (Spalding et al. 2011, MPCA *unpublished data*). Within the vadose zone, CH_4 concentrations up to 58 % v/v were reported in 2007 (Spalding et al. 2011), however detailed data is not available on the distribution of subsurface gas concentrations. Vegetation is sparse and is dominated by short, scrubby grass, with the exception of the northern edge of the site, adjacent to the creek, where more substantial grasses and trees are present. Using static chambers, Spalding et al. (2011) documented surficial CH_4 releases with maximum concentrations in the chamber reaching ~ 2.7 v/v %, however emission rates were not evaluated. Gas efflux measurements at the Balaton site were conducted between May 8th and 20th, 2012 (Sihota et al. 2013).

The Cambria site is located within the Minnesota River valley in south-central Minnesota and is underlain by silty loam (**Figures 9.1 and 9.5**). A multi-railcar derailment in November 2006 released ~ 9.5 x 10^4 L of DFE (Spalding et al. 2011), with ~ 4.9 x 10^4 L of DFE remaining after the following cleanup efforts. No soil excavation occurred at the Cambria site (Spalding et al. 2011). Maximum EtOH concentrations exceeding 5 % were detected shortly following the release while lower concentrations were detected through 2012 (Spalding et al., 2011; MPCA, *unpublished data*). Dissolved CH_4 was detected at levels exceeding saturation directly below the source zone by the spring of 2008 and its presence continued through 2012 (Spalding et al. 2011; MPCA, *unpublished data*), however no data is available on the distribution of subsurface gas concentrations. Vegetation to the north of the rail line consists of ~ 1 m tall grasses, while to the

southeast of the rail line, patchy areas of shrubs and trees dominate. Areas of ponded water are found, particularly during the spring, with depth to water table remaining shallow (typically < 1 m) in other areas. Similar to the Balaton site, Spalding et al. (2011) documented the occurrence of surficial CH_4 releases (again using static chambers); here, a maximum CH_4 concentration of 1.6 v/v % was measured. Gas efflux measurements were conducted at the Cambria site between May 8th and 20th, 2012 (Sihota et al. 2013).

Gas flux measurements and delineation of SZNA rates: Measurement of CO_2 effluxes are commonly conducted using infra-red gas analyzers coupled to dynamic closed chambers (Hanson et al., 2000; Jassal et al., 2012). In this approach, the increase in the gas concentration within the chamber headspace is recorded over the measurement interval (typically on the order of minutes). When the water vapour mole fraction, initial air temperature, initial pressure inside the chamber and the total system volume are measured, changes in gas composition within the chamber headspace can be equated to a gas flux (Jassal et al., 2012). In this study, gas flux measurements were conducted using a dynamic closed chamber (DCC) system with an infra-red gas analyzer for measurement of CO_2 (LI-COR Inc., Lincoln, NE) and a laser-based instrument for measurement of CH_4 (Los Gatos Research, Mountain View, CA). For complete instrumentation details, the reader is referred to (Sihota et al., 2013).

To delineate the contaminant containing source zone and calculate SZNA rates, the total carbon flux measured in the chamber was corrected for the carbon fluxes measured at background locations where contamination was absent (Sihota, Singurindy, and Mayer 2011; Sihota et al. 2013). Areas where total gas emissions exceeded those measured at the background locations were considered part of the 'source zone'. At the Bemidji site, the contaminant-

containing source zone is relatively well defined based on isotopic measurements (Revesz et al., 1995); analysis of oil content in core samples (Chaplin et al., 2002); surficial gas effluxes (Sihota et al., 2011); and ongoing measurements of NA parameters (Essaid et al., 2011). In comparison to the Bemidji site, the source zone at the other sites investigated is less well constrained. Consequently, locations where the total carbon flux exceeds twice the value of the carbon flux measured at the background locations were used to delineate the source zone at the other field sites investigated.

Results and discussion

Composition, and magnitude of gas emissions: First, to evaluate differences between each of the crude oil and DFE sites, we compared the magnitude and distribution of gas emissions at each type of site. At the two crude oil sites, CO_2 effluxes were of similar magnitude and CH_4 effluxes were absent (**Table 9.2**). Inter-annual comparisons of CO_2 effluxes showed the magnitude of emissions were relatively constant for the measurement periods (spring/summer (**Table 9.2**)). At the two DFE sites CO_2 effluxes were of similar magnitude, however substantial differences were observed in the magnitude of CH_4 effluxes (**Table 9.2**). At both sites the occurrence of CH_4 effluxes was closely tied to soil conditions and contaminant availability (i.e., locations of high moisture content where DFE pooled and was not excavated (**Figures 9.4 and 9.5**)), suggesting the occurrence of CH_4 effluxes is related to specific conditions rather than only fuel type, consistent with the measurement of CH_4 effluxes in natural wetland and bog environments (Gogo et al., 2011). Comparison of emission rates between the two field sites showed CH_4 effluxes at the Cambria site were an order of magnitude greater than those measured at the Balaton site, pointing to rapid DFE degradation at the Cambria site. This is

supported by the lack of soil excavation and the more recent release at the Cambria site. Comparison of total carbon effluxes between the two DFE sites also showed high variability, mainly as a consequence of the differences in CH_4 effluxes, suggesting differential SZNA rates between the two sites. Based on these observations, we next investigated differences between the distribution and magnitude of gas emissions between the crude oil and DFE sites. To facilitate a direct comparison between all sites, we limited our comparison to measurements collected in 2012 (**Table 9.2**).

Substantial variation in both the magnitude and composition of the gas effluxes is evident between the crude oil and DFE sites. Comparing the range in CO_2 effluxes shows maximum CO_2 effluxes were an order of magnitude greater at the DFE sites than at the crude oil sites, and that the variability in CO_2 emissions was much higher at the DFE sites (**Table 9.2**). Lower minimum CO_2 effluxes measured at the DFE sites were related to areas of barren, compacted sand (Balaton) and locally near-saturated conditions (Cambria). The larger total emissions at the DFE sites is consistent with the labile nature of EtOH, as well as the relative age of the sites, with more recent releases having a greater proportion easily degradable carbon remaining (Peters et al., 2005). The presence of CH_4 emissions at the DFE sites and absence of CH_4 emissions at the crude oil sites is also consistent with differences in the soil types and the depth to the water table. At the crude oil sites, the general geology is characterized by loose sands and gravels with low residual moisture contents and deeper water tables, allowing entry of O_2 and oxidation of CH_4, while at the DFE sites, the general geology is characterized by clays and silts, with higher residual moisture contents and shallower water tables inhibiting the ingress of O_2 (**Table 9.1**). These findings point to the importance of evaluating local scale variations in site geology for assessing hazards related to CH_4 emissions and soil vapour intrusion potential. These

observations also imply that CH_4 emissions may occur at petroleum hydrocarbon spill sites if the geological conditions are suitable, although likely at a lower rate (based on the relatively recalcitrant nature of the crude oil).

Source zone delineation: To evaluate the present-day extent of the source zone at each site, we compared the source zone identified using gas flux measurements to previous estimates of mass in place. At the crude oil sites, the initial mass in place was estimated based on oil saturations documented in core samples (Bemidji (Chaplin et al., 2002) and Cass Lake (Drennan et al., 2010)), while at the DFE sites initial mass in place was estimated based on dissolved EtOH documented in monitoring wells (Balaton and Cambria (Spalding et al., 2011)). At the crude oil sites, results show good agreement between the extent of the source zone delineated using surficial gas effluxes and crude oil documented in the vadose zone and floating on the water table (**Figures 9.2 and 9.3**). At the Bemidji site, the source zone was delineated over a 2.4 x 10^3 m^2 area using surficial gas effluxes as compared to the 6.0 x 10^3 m^2 area of the oil. At the Cass Lake site, the length of the source zone along a transect was determined as 50 m using surficial gas effluxes as compared to an estimated oil pool length of 60 m. Comparing the source zone identified at each of the crude oil sites, shows 80% of the area where oil was estimated to be present was identified using the surficial measurements. The poorer detection ability at the fringes of the oil at each site may be related to lower degradation rates and lateral gas transport, which would mute the CO_2 flux signal arriving at the ground surface, but also represents the combined error associated with each estimate.

At the DFE sites, results show moderate agreement between the extent of the source zone delineated using surficial gas effluxes and the initial mass in place (**Figures 9.4 and 9.5**). At the

Balaton site, the source zone was delineated over 1.8 x 10^3 m^2 using surficial gas effluxes as compared to a DFE pool of 1.5 x 10^3 m^2 (following soil excavation). At the Cambria site, the source zone was delineated over 6.3 x 10^3 m^2 using surficial gas effluxes as compared to an initially present DFE pool of 1.9 x 10^3 m^2. The larger extent of the source zone at the Cambria site is supported by the lack of soil excavation and the larger volume of DFE remaining following remediation, highlighting the potential benefit of soil excavation in mitigating plume expansion associated with DFE releases (**Table 9.1**). Indeed, the relationship between the spatial distribution of elevated effluxes and initially present EtOH showed elevated fluxes were measured far outside the most contaminated regions at both sites. This was most pronounced at the Cambria site, where the identified source zone covered an area ~ 70 % greater than the initially measured EtOH in groundwater. This disparity is consistent with the mobility of both EtOH and its degradation product acetate (also highly labile) in groundwater and is supported by the expansion of the surficial gas plume in the general directions of groundwater flow (**Figures 9.4 and 9.5**). This extension of the source zone has implications for the transport of other contaminants of concern (e.g., BTEX) which are soluble in EtOH and less likely to degrade when mixed with EtOH and acetate, due to thermodynamic constraints (Gomez and Alvarez, 2010). Comparison to the crude oil sites showed the differences between the source zone identified and the extent of initial mass in place was more pronounced at the DFE sites, consistent with the relative mobility of the EtOH in comparison to crude oil (as EtOH is miscible in water and the compounds have kinematic viscosities of 1.5 and 6.8 – 26.2 cSt for EtOH and crude oil, respectively). This comparison points to an advantage of the surficial gas flux method as a tool for the rapid assessment of the extent of a mobile plume in the shallow groundwater, which could assist in site and risk assessment investigations.

In comparing the areal extent of the source zone delineated using surficial carbon effluxes, the sensitivity to measurements of natural soil respiration (i.e., the background value) must be acknowledged. This sensitivity is more pronounced at sites with lower total carbon emissions (here the crude oil sites) than at sites where total carbon emissions are much larger than those commonly found in the natural environment (here the DFE sites). To illustrate this point, a 10 % change in the magnitude of natural soil respiration (consistent with variations observed in CO_2 flux measurements in the natural environment (Jassal et al., 2012)) results in a 10 % change in the source zone delineated at the Bemidji site, as compared with only a 2 % change in the source zone delineated at the Cambria site. Overall, this supports the ability to resolve the agreement noted between the extents of the source zones delineated at the crude oil sites and the disparity between the extents of the source zones delineated at the DFE sites.

Source zone natural attenuation rates: To compare the contaminant mass loss rates between the crude oil and DFE sites, we calculated SZNA rates obtained from total gas effluxes at each site. At the crude oil sites, average SZNA rates were relatively low in keeping with total gas emissions. The average SZNA rate at the Bemidji site was 2.4 (0.2, n = 107) μmol m^{-2} s^{-1} or ~ 2.5 g-C m^{-2} d^{-1}. The average SZNA rate at the Cass Lake site was 6.2 μmol m^{-2} s^{-1} (±0.9, n = 23) or ~ 6.4 g-C m^{-2} d^{-1}. The higher SZNA rate calculated for the Cass Lake site is consistent with differences in the age of the spill (with the last release documented 12 years ago vs. 33 years ago at the Bemidji site) and in agreement with simulations of the transient evolution of SZNA processes at the Bemidji site reported by Molins et al. (2010), which showed that the majority of the volatile fraction had been removed from the oil within the first 28 years following the release (~ 55 % by volatilization and ~ 45 % by degradation). Moreover, the slow leak at the Cass Lake

site would have delivered a longer-term source of volatile substrate as compared to the large volume instantaneous release at the Bemidji site. The higher average SZNA rate found for the Cass Lake site is also supported by differences in site geology, as a low permeability layer at the Bemidji site contributes to O_2 limitation at depth, resulting in a substantial contribution from anaerobic degradation (Revesz et al., 1995), while the coarse gravels underlying the pumping station at the Cass Lake site, in contrast, would support O_2 ingress and extend the range of aerobic respiration. Furthermore, high residual oil contents in the source zone at the Bemidji site associated with the oil infiltration from ground surface (Essaid et al., 2011), would additionally restrict gas transport within the vadose zone and contribute to O_2 limitation, while at the Cass Lake site, the presence of the leak at depth would limit the vadose zone pore space occupied by the oil and allow for freer gas transport.

At the DFE sites the average SZNA rates were relatively high, in keeping with total gas emissions. The average SZNA rate at the Balaton site was ~ 22 (±4, n = 55) μmol m^{-2} s^{-1} or ~ 23 g-C m^{-2} d^{-1} and the average SZNA rate at the Cambria site was ~ 32 (±5, n = 128) μmol m^{-2} s^{-1} or ~ 33 g-C m^{-2} d^{-1}. The higher SZNA rate calculated for the Cambria site is consistent with differences in weathering associated with the age of the spill, and is also in agreement with the differences in SZNA rates and release ages at the two crude oil sites. Similarly, differences in site geology between the DFE sites also appear to contribute to differences in SZNA processes. At the Cambria site the combination of lower permeability sediments, a highly labile contaminant, and a shallow water table contributed to both substantial O_2 depletion leading to anaerobic conditions and a shift in the dominant gas transport regime, with an increased contribution of advective flow – particularly for CH_4. This suggests that advective transport is important in regulating CH_4 emissions (and the potential for transport of other contaminants of

concern, such as benzene, in the gas stream; Sihota et al., 2013). These results are further supported by the minor contribution of advection at the Bemidji site, where CH_4 effluxes did not occur, despite a substantial CH_4 presence at depth (Molins et al., 2010; Sihota and Mayer, 2012). Overall, comparison of SZNA rates at the DFE sites showed contaminant age and site hydrogeology played important roles in controlling SZNA rates and the potential for CH_4 hazards, underlining the necessity of evaluating these parameters. Moreover, the comparison between the implications of low permeability media, degradability of the contaminant, and the depth to water table at the Bemidji and Cambria sites points to the importance considering the interactions of these parameters under site-specific conditions.

To further evaluate the processes contributing to observed differences in SZNA rates between the field sites, we compared climatic variables across the field sites (**Table 9.1**). Results showed the highest annual average temperature and greatest annual precipitation rate occurred at the Cambria site, suggesting the importance of recharge waters and temperature in regulating degradation rates. Indeed, higher precipitation rates could deliver nutrients to and remove reaction by-products from the microbial communities responsible for the degradation reactions (Bekins et al., 2005b). This process is likely to be particularly important at the DFE sites, as EtOH is toxic to microorganisms at elevated levels (Nelson, LaPara, and Novak 2010), while accumulation of reaction intermediates (including volatile fatty acids such as acetate and butyrate – measured at elevated levels at the Cambria and Balaton sites (Spalding et al., 2011)) and associated changes in pH, can also inhibit degradation (Freitas et al., 2010). However regional differences in climate must again be placed in the context of the site geology. For example at the Bemidji site, Bekins et al. (2005) documented elevated oil weathering in samples collected from within a local depression where water can pond during substantial precipitation, while at the

Cass Lake site, rapid infiltration through the permeable gravel courtyard has been suggested as a path for nutrient delivery to microorganisms mediating degradation processes (Drennan et al. 2010). Moreover, as all sites investigated in this study are located in Minnesota, the range of climatic conditions observed was narrow, suggesting a more pronounced effect on SZNA could occur across a wider climatic gradient, in agreement with regional changes in hydrocarbon degrading genes (Luz et al., 2004) and results of laboratory experiments evaluating the influence of environmental parameters on SZNA processes (Dibble and Bartha, 1979). Overall, these observations suggests that the interplay between site specific geologic and environmental variables contribute to the evolution of SZNA processes and are important to consider for understanding variations in SZNA rates and drivers of source zone longevity.

Conclusions

In this study we investigated differences in SZNA rates at field sites impacted by crude oil and DFE through comparison of the composition and distribution of surficial gas effluxes. We further evaluated the potential for site-specific contaminant, geologic, and climatic controls to influence SZNA processes and drive risk potential through comparison of gas emissions to site parameters. Results showed the magnitude and composition of gas effluxes and SZNA rates at sites impacted by the same contaminant were similar, while pronounced differences were observed between the magnitude and composition of gas effluxes at crude oil (lower SZNA rates, no CH_4 emissions) and DFE (higher SZNA rates, CH_4 emissions) spill sites. Results also revealed that the areal extent of source zone at the DFE impacted sites can be far larger than the initial extent of the mass in place, suggesting novel monitoring strategies are needed for evaluating SZNA at DFE release sites. Comparisons across sites impacted by different contaminants highlighted the

importance of the interplay between contaminant composition and soil characteristics in mediating respiration rates and modulating gas transport regimes with important implications for risks related to CH_4 emissions, in particular.

Tables

Table 9.1. Comparison of key attributes of the field sites.
[1]Bekins et al. (2005), [2] MCWG (2013), [3]Drennan et al. (2010), [4]Soil Survey Staff (2012)

Site	**Source**	**Release date**	**Soil type**	**Remaining (released) volume** [L]	**Depth to water table** [m]	**Avg. annual temp** [°C]	**GW flow** [m y^{-1}]	**Avg. annual ppt.** [m y^{-1}]
Bemidji, MN	Crude oil	Aug. 20th, 1979	glacial outwash	1.47×10^5 (1.7×10^6)	6-9	5[1]	22	0.66[1]
Cass Lake, MN	Crude oil	Detected 2001	glacial outwash	1.82×10^5	8-9	5[2]	26	0.61[2]
Balaton, MN	E95	July 28th, 2004	silty sand	6.8×10^4 (1.5×10^5)	1-3	6.1[4]	NM	0.56[4]
Cambria, MN	E95	Nov., 2006	sandy loam	4.9×10^4 (9.5×10^4)	0-1	8.9[3,4]	NM	0.71[4]

Table 9.2. Comparison of gas efflux ranges, estimated extent of source zones, and inferred SZNA rates at the field sites. *delineated based on Sihota et al. (2011). **delineated based on those values ≥ twice the background value. ND: small influx detected, but below reporting threshold.

Site	**CO_2 efflux range** [μmol m^{-2} s^{-1}]	**CH_4 efflux range** [μmol m^{-2} s^{-1}]	**Mean CO_2 efflux Source zone** [μmol m^{-2} s^{-1}]	**Mean CO_2 efflux Background** [μmol m^{-2} s^{-1}]	**Mean CH_4 efflux** [μmol m^{-2} s^{-1}]	**Estimated extent of source zone** [m]	**Estimated SZNA rate** [μmol m^{-2} s^{-1}]
Bemidji, MN							
2009	2.6 – 7.1	NA	5.9*	6.3	NA	55	2.6
2010	0.2 – 17.1	NA	5.0*	2.1	NA	55	6.4
2011	1.5 – 16.2	NA	5.3*	6.6	NA	55	2.3
2012	1.3 – 15.1	ND	5.1*	6.8	ND	55	2.4
Cass Lake, MN							
2011	2 – 19	NA	11**	3	NA	60	8
2012	2 – 13	ND	10**	3	ND	44	6.6
Balaton, MN							
2012	0.6 – 178.4	ND – 9.1	21**	5	1.4	1.8×10^3 m^2	22
Cambria, MN							
2012	0.5 – 174.7	ND – 392.9	26**	6	24	6.3×10^3 m^2	32

Figures

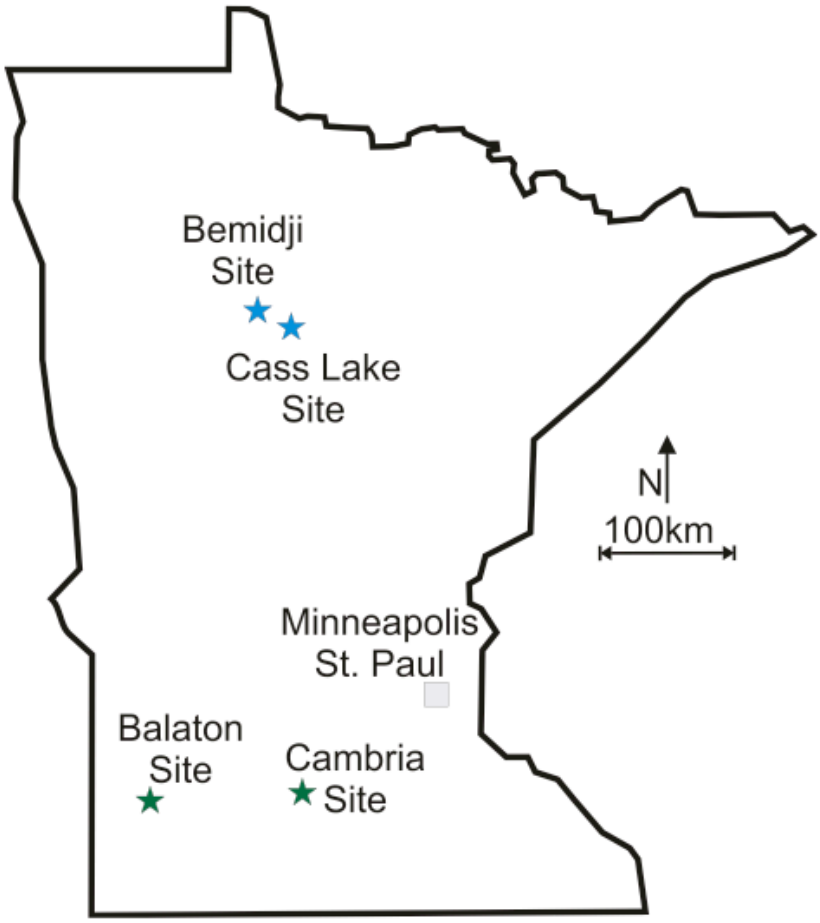

Figure 9.1. Locations of the study sites.

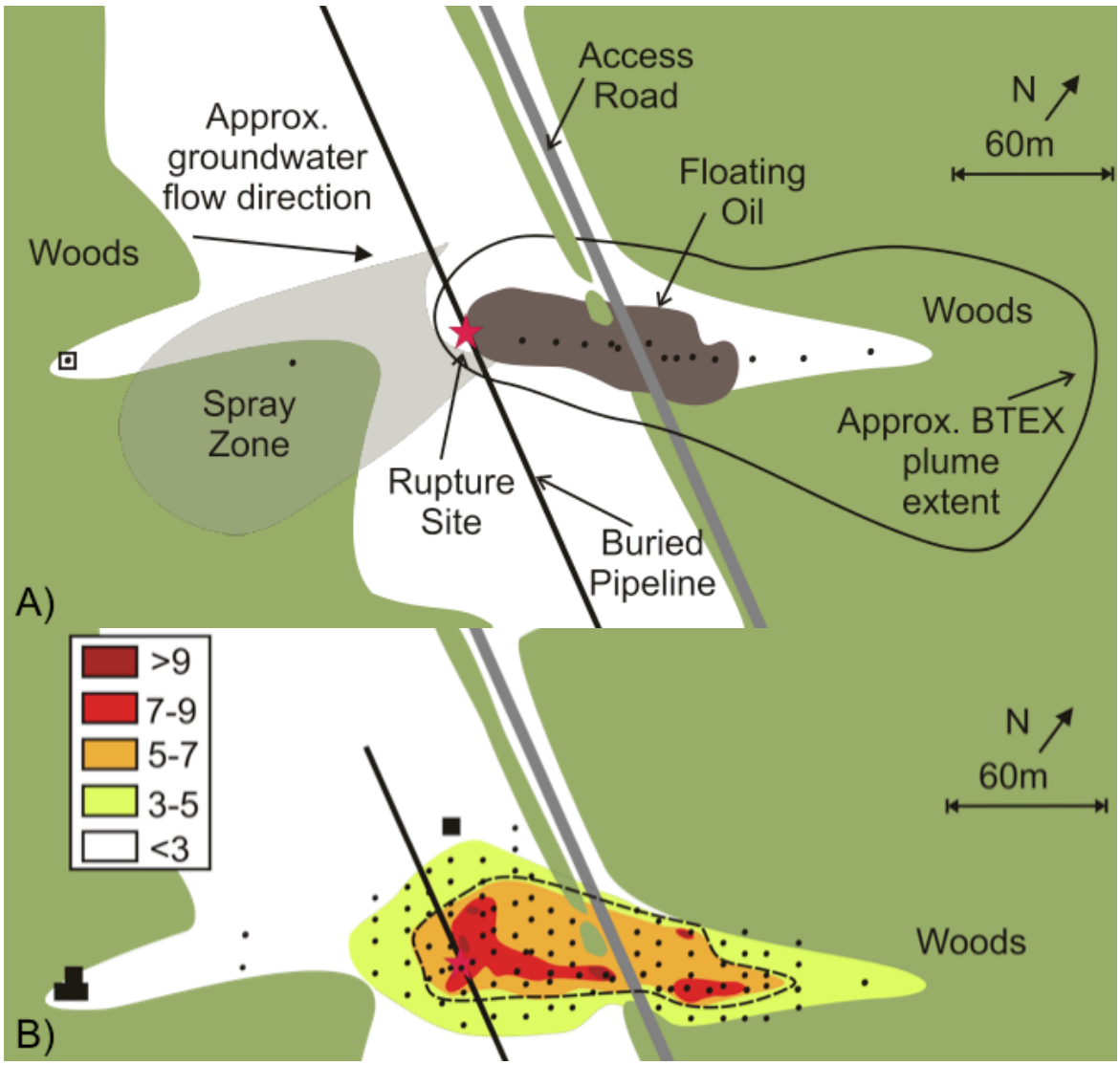

Figure 9.2. Bemidji site. A) Key characteristics, B) total carbon losses and delineated source zone. Black circles show measurement locations. Boxes denote locations used in calculating background soil CO_2 effluxes. Dashed lines denote source zone area identified with surficial gas effluxes.

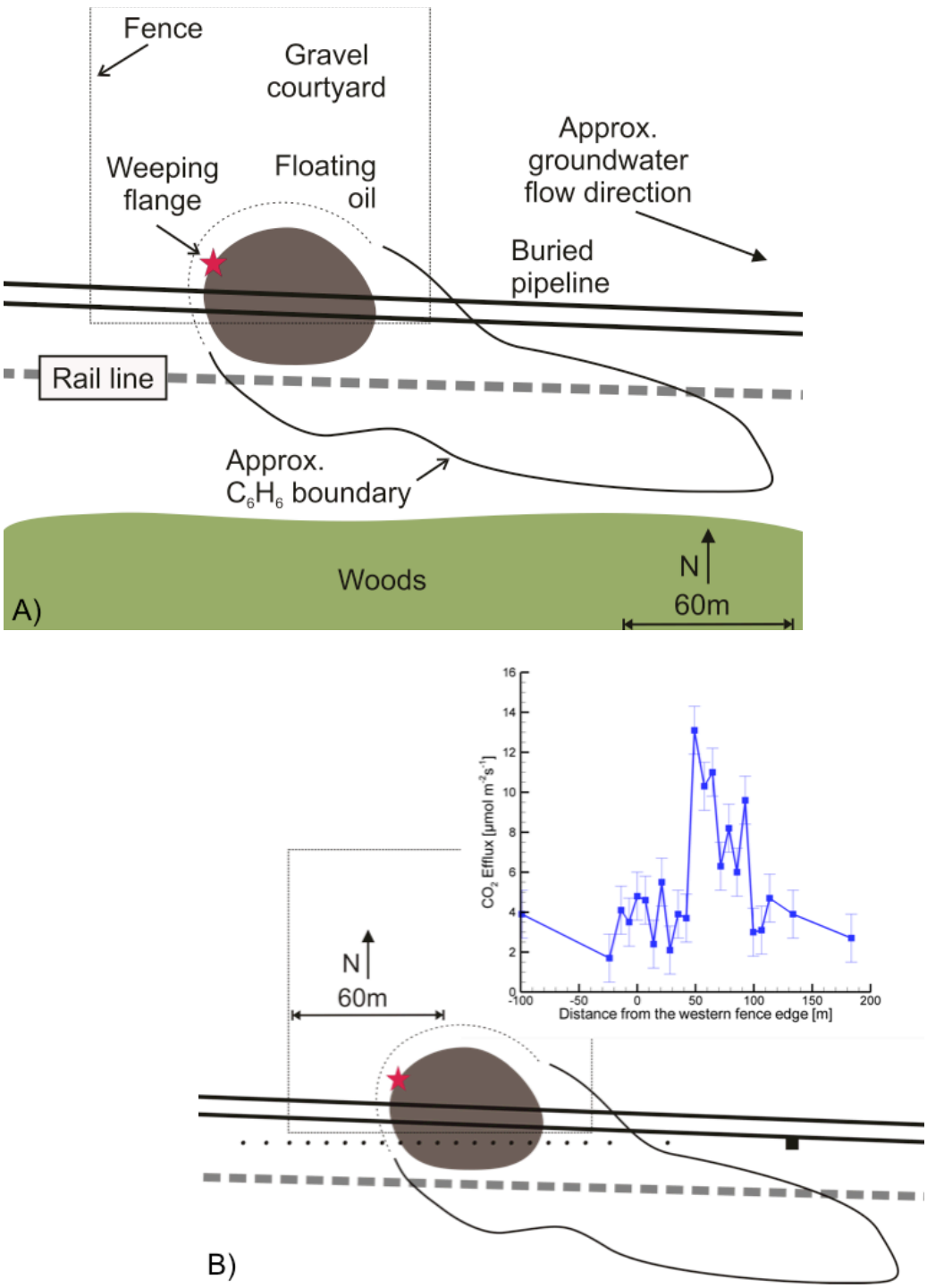

Figure 9.3. Cass Lake site. A) Key characteristics, B) total carbon losses and delineated source zone. Black circles show measurement locations. Boxes denote locations used in calculating background soil CO_2 effluxes. Dashed lines denote source zone area identified with surficial gas effluxes.

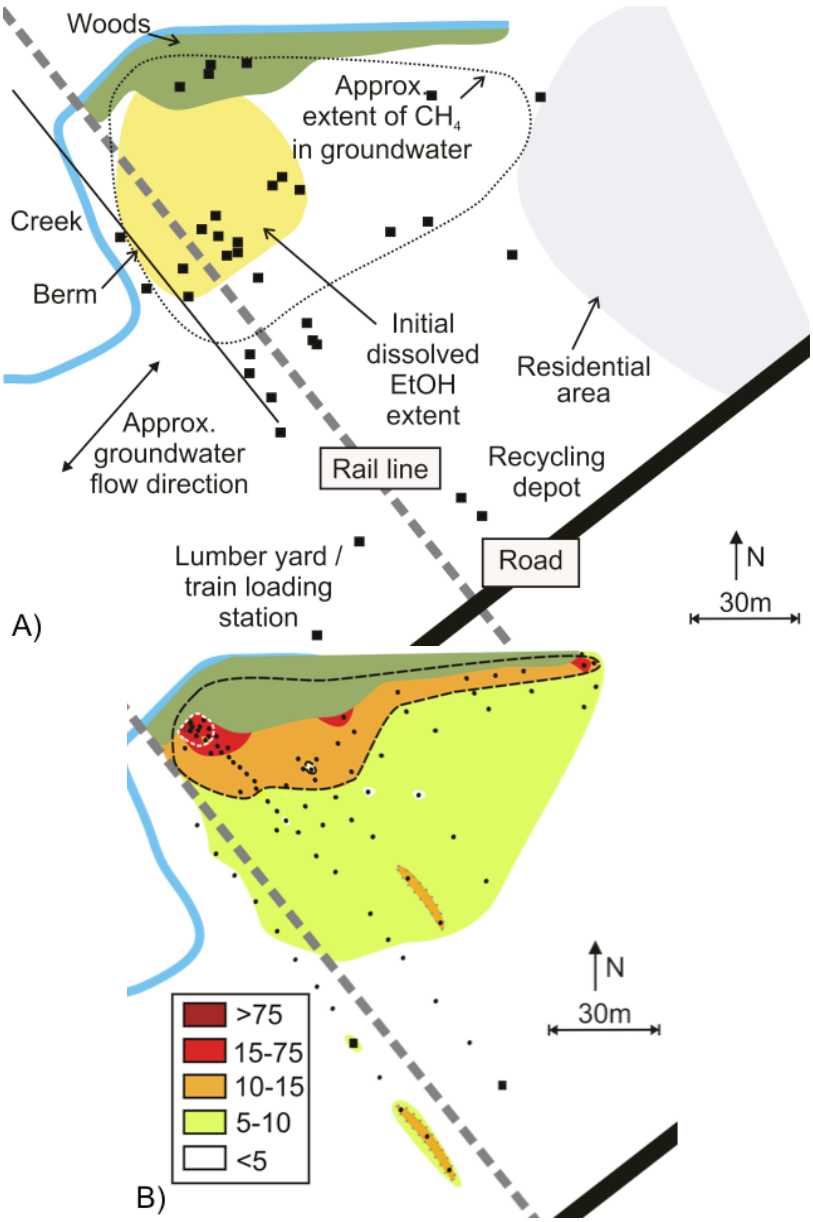

Figure 9.4. Balaton site. A) Key characteristics, B) total carbon losses and delineated source zone. Black circles show measurement locations. Boxes denote locations used in calculating background soil CO_2 effluxes. Dashed lines denote source zone area identified with surficial gas effluxes. White dashed lines indicate area where CH_4 effluxes were present at the time of measurement (modified from Sihota et al., 2013).

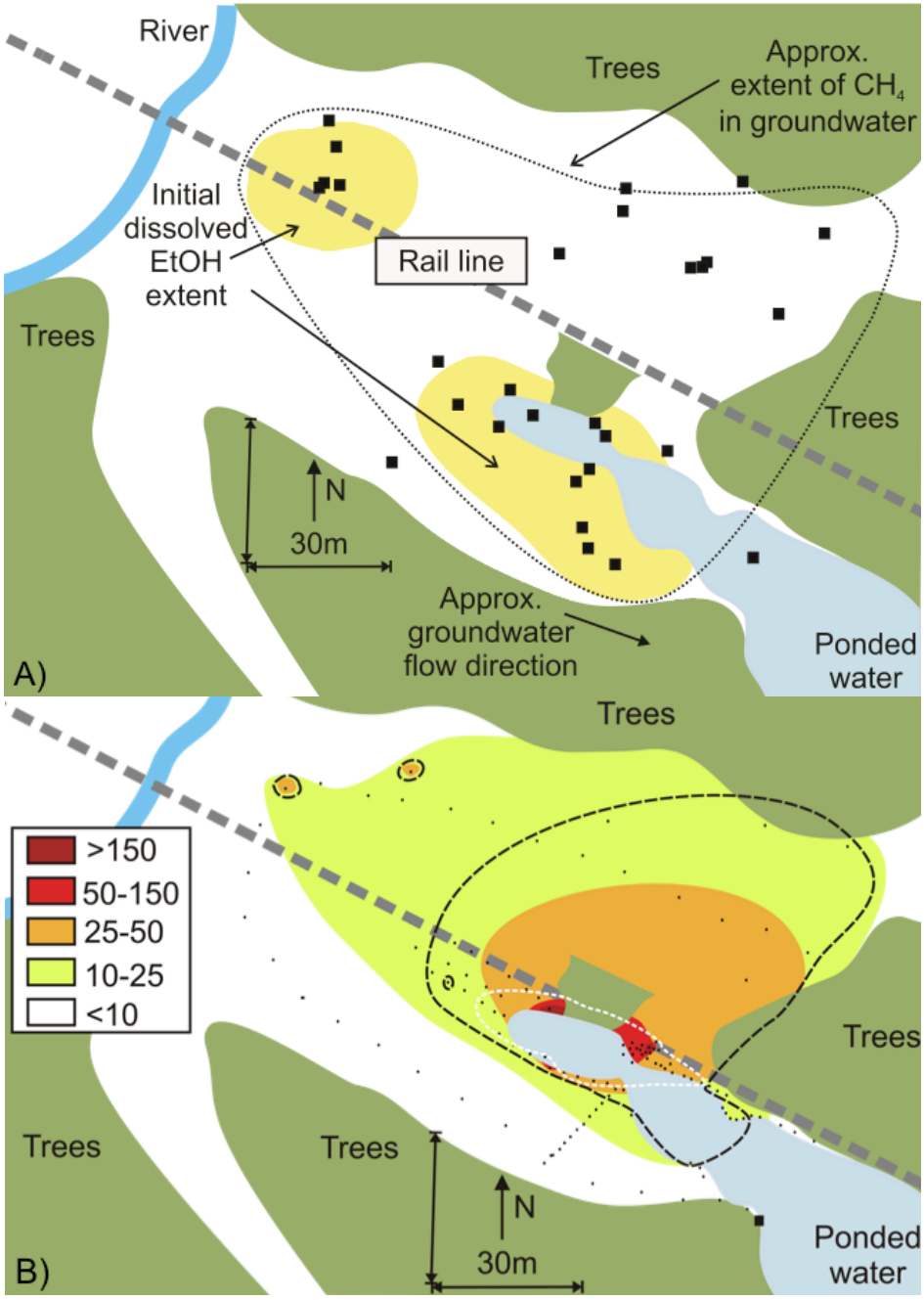

Figure 9.5. Cambria site. A) Key characteristics, B) total carbon losses and delineated source zone. Black circles show measurement locations. Boxes denote locations used in calculating background soil CO_2 effluxes. Dashed lines denote source zone area identified with surficial gas effluxes. White dashed lines indicate area where CH_4 effluxes were present at the time of measurement (modified from Sihota et al., 2013).

Chapter 10: Summary and conclusions

In this work, the question: "***Can the measurement of surficial gas fluxes be used as an integrated representation of SZNA processes at sites impacted by hydrocarbons releases?"*** was addressed by identifying eight hypotheses and then investigating these hypotheses through research described in chapters 2 – 9. The key conclusions of these inquiries are described below.

Based on the CO_2 generated from contaminant respiration, it was hypothesized that the rate and extent of source zone natural attenuation could be delineated using measurements of CO_2 fluxes at the ground surface. Results of the 'proof-of-concept' study described in chapter 2 conducted at a crude oil pipeline rupture site near Bemidji, MN indicated that the surficial CO_2 efflux approach is able to both delineate the source zone, and distinguish between the rates of natural soil respiration and contaminant mineralization (Sihota et al., 2011). The average CO_2 efflux associated with contaminant degradation in the source zone at the Bemidji site was estimated as 2.6 μmol m^{-2} s^{-1} (obtained by subtracting the estimated natural soil respiration rate or 'background correction' from the measured surficial CO_2 efflux). This corresponds to a total petroleum hydrocarbon mineralization rate (expressed as $C_{10}H_{22}$) of 3.3 g m^{-2} day^{-1}, which is in good agreement with previous estimates of SZNA rates for the site (Revesz et al., 1995; Molins et al., 2010) and has been supported by more recent modeling work (Ng et al., 2014).

While the CO_2 efflux approach proved promising, the accuracy of degradation rate estimates was limited by the ability to separate CO_2 effluxes associated with SZNA from those attributable to natural soil respiration. To overcome this limitation, the differences in the age between carbon in recent contact with the atmosphere and carbon held in hydrocarbon compounds was exploited to provide a constraint on the magnitude of natural soil respiration. This was done using measurements of surficial CO_2 effluxes, combined with detailed analysis of soil gas composition – including the radiocarbon and stable isotopic composition of CO_2.

Quantitative reactive transport modeling was used to further evaluate the controls on CO_2 generation and fate, and CH_4 generation and oxidation. Results confirmed that, in the source zone at the Bemidji site, the majority of CO_2 originated from degradation of the oil body and demonstrated that radiocarbon in CO_2 is particularly useful for determining the contribution of contaminant degradation to the measured CO_2 efflux (described in chapter 3 and Sihota and Mayer (2012)).

To further compare microbial activity measurement methods at the Bemidji site, CO_2 effluxes, methanogen and methanotroph concentrations, and oil degradation state were evaluated at multiple locations in the oil body. Results demonstrated good agreement between the different data types. All microbial activity measurement approaches showed locations over the oil body were significantly more active than the background locations and data from the different approaches correlated well at all locations, demonstrating that the approaches evaluated were able to detect gradients in microbial activity (described in chapter 4 and Warren et al. (*accepted*)).

Based on the sensitivity of microbial respiration to changes in climatic variables (i.e., temperature and moisture availability), seasonal variations in SZNA processes were next investigated using *in situ* measurements of surficial CO_2 effluxes, vadose zone gas composition and soil temperature and soil moisture contents over a two-year period. Datasets were integrated using reactive transport simulations to evaluate the conceptual model developed based on field measurements. Results highlighted the importance of the interplay between soil temperature and moisture in modulating SZNA rates, gas emissions, and subsurface gas concentrations, and revealed the role of transient barriers to gas transport in regulating surficial CO_2 fluxes. Overall, the results of this study have important implications for evaluation of annual mass loss rates

using surficial flux measurements and demonstrate that seasonal changes in both biological and physical systems must be considered when quantifying contaminant degradation rates (described in chapter 5 and in Sihota et al. (*in prep.*)).

To evaluate the utility of CO_2 flux and radiocarbon measurements for delineating the extent and rate of SZNA in an industrially setting, the approaches developed in chapters 2 – 4 were applied at a former refinery site with a heterogeneous contaminant distribution. Results demonstrated reasonable agreement between mass loss rates obtained from the background correction and the more involved radiocarbon correction for natural soil respiration. Local scale discrepancies between the correction approaches showed that the radiocarbon correction was most useful for understanding the distribution of SZNA rates, while the background correction was useful for evaluating site-wide mass losses. Comparing SZNA rates calculated from each correction approach to site metadata show CO_2 fluxes were a reasonably good proxy for zones of subsurface contamination – particularly with respect to vadose zone impacts. Overall, results demonstrated that mass loss rates calculated from CO_2 fluxes show SZNA can result in substantial contaminant removal which may rival that obtained from engineered remediation under some conditions, as described in chapter 6 and in Sihota et al. (*in review*).

To further evaluate the applicability of surficial gas efflux measurements for evaluating SZNA processes, and to understand potential risks related to CH_4 emissions at EtOH-blended fuel release sites, surficial gas efflux surveys were conducted at two train car derailment spill sites near Cambria and Balaton, Minnesota. Results of this investigation demonstrate that substantial CO_2 and CH_4 emissions can occur − even years after a spill. However at each site, large total carbon fluxes, and CH_4 emissions in particular, were restricted to localized areas within the DFE source zone. Substantial CH_4 accumulation, coupled with oxygen (O_2) depletion,

measured in samples collected from custom-designed gas collection chambers at the Cambria site suggest that development of an explosion or asphyxiation hazard is possible in confined spaces above rapidly degrading DFE releases. However, results also indicated that the development of these hazards would be localized to areas with a high degree of soil moisture, close proximity to the source zone, a good connection between the soil and the confined space, and poorly aerated conditions. Overall, this study demonstrated that CH_4 emissions do occur at DFE impacted sites, but that CH_4 hazards require a unique set of conditions (described in chapter 7 and in Sihota et al. (2013)).

Based on EtOH's toxicity to microbial populations (Nelson et al., 2010) and the lag time to the onset of SZNA observed at the field sites by Spalding et al. (2011), the underlying characteristics of the microbial community composition were investigated at the Cambria site using samples collected from both an unimpacted reference site and a source site in the core of the contaminated area. Results demonstrated that rare biosphere activity was expanded as a consequence of the DFE release, and that active microbial community interaction networks provide an ecological framework for understanding bioenergetic cycling in perturbed ecosystems. By identifying the ability of microbial activity networks to elucidate microbial mediated bioenergetic cycling, this work makes a fundamental contribution to understanding processes driving environmental matter and energy transformations. This new knowledge enhances monitoring and modeling of the microbial contribution to ecosystem functions and services in both pristine and perturbed ecosystems (described in chapter 8 and Sihota et al. (*submitted*)).

While the work described in chapters 2 – 6 describes SZNA processes at hydrocarbon impacted sites and chapters 7 – 8 describes SZNA processes at DFE impacted sites,

understanding differences in SZNA rates occurring among field sites impacted by the same contaminant, and across field sites impacted by different contaminants is critical for developing effective management strategies. For example, unique site conditions can favour or inhibit biodegradation, while differences between contaminants can lead to variations in biodegradation potential. To better understand the implications of these effects, differences in gas emissions and SZNA rates at two crude oil and two denatured fuel-grade ethanol (DFE) spill sites were evaluated using *on-site* measurements of surficial gas effluxes. At the crude oil sites, CH_4 effluxes were below detection, while CH_4 effluxes occurred at both DFE sites. Similarly, SZNA rates among sites impacted by the same contaminant were comparable, while order of magnitude differences existed between sites impacted by crude oil or DFE. At DFE sites results also revealed source zone expansion in relation to the initial mass in place, suggesting extended spatial monitoring may be required to characterize risk potential. Overall, key differences between crude oil and DFE release sites demonstrated the importance of site-specific interactions between hydrogeology and contaminant composition for mediating gas emissions and SZNA rates, and modulating gas transport regimes under field conditions (chapter 9, Sihota and Mayer (*submitted*)).

Implications and applications

Conclusions from the research presented in this dissertation have gained widespread interest for assessing SZNA processes under a range of field conditions. Several major petroleum companies, environmental consultants, and State regulators in the United States are currently

applying the approaches developed in this work. With continued refinement, this research could greatly improve site characterization and management, as well as risk assessment by reducing the cost and time required to characterize SZNA at spill sites across a range of sizes and site conditions.

Strengths and limitations

Table 10.1. Key strengths and limitations of the approaches developed in this dissertation.

Topic	Key strengths	Key limitations
Gas flux measurement	Rapid characterization of the contaminant containing source zone	Limited sensitivity to smear zone and dissolved phase impacts
	Rapid assessment of SZNA rates	Difficulty of separating natural and contaminant related soil respiration
	Inexpensive measurement	Subjected to seasonal variability
	Limited technical skills required	Gas emissions are impacted by physical changes to the system
	Field based measurement	Limited understanding of detailed processes
Microbiology	Information on community metabolism	Expensive
	Information on community interactions	Time consuming

The advantages of the surficial gas efflux methodology explored in this research are simplicity, rapidity, and reduction in cost over other more traditional ways of measuring both the areal extent of contamination and the rate of SZNA. Furthermore the time necessary for determination using the surficial gas efflux methodology is 1/3 to 1/4 the time required by traditional techniques (i.e. in the order of weeks versus months). Results of this research further illustrated

the difference between EtOH and crude oil biodegradation, and underlined the importance of monitoring and managing spill sites in a manner that is sensitive not only to specific contaminants, but also to seasonal and site-specific characteristics. Results also demonstrated the difficulty of separating natural and contaminant related respiration and, consequently, potential sources of error associated with mass loss estimates. Similarly, field measurement demonstrated a limited sensitivity of surficial gas effluxes to smear zone and dissolved phase impacts – particularly as the vertical extent of the vadose zone increases. However, a fuller understanding of vadose zone processes would be valuable for understanding SZNA processes.

Future work

Outcomes of the research presented in this dissertation suggest surficial gas efflux measurements can be used to evaluate SZNA at crude oil and DFE release sites. This work could be extended through investigating SZNA under other fuel release scenarios (e.g., other biofuels), using gas efflux measurements for monitoring enhanced natural attenuation processes (e.g., nutrient or electron acceptor amendments), augmenting the chamber system to investigate risks for soil vapour intrusion (e.g., through measurement of BTEX), and characterizing emissions under other conditions (e.g., leaking oil and gas wells).

The microbiological work conducted as part of this dissertation demonstrated that catastrophic DFE releases could lead to large-scale alteration of community composition and structure. This work could be extended by conducting time series measurements and comparisons of microbial community responses to different fuel blends and release scenarios. Results of these investigations would be valuable for understanding relative risks related to different release scenarios.

Furthermore, as the focus of this research was on investigation of field-scale processes, detailed laboratory experiments are suggested to evaluate the pathways leading to gas emissions and the changes in microbial communities as degradation processes evolve. Combining these investigations with process-based reactive transport modeling could lead to a more complete understanding of biodegradation processes for a range of scenarios and could inform and refine real world risk assessment and management practices.

References

Aelion, C.M., P. Höhener, D. Hunkeler and R. Aravena (eds). 2010. Environmental isotopes in biodegradation and bioremediation. Taylor and Francis, Boca Raton, FL.

Aggarwal, P.K., and R.E. Hinchee. 1991. Monitoring insitu biodegradation of hydrocarbons by using stable carbon isotopes. Environ. Sci. Technol. 25:1178–1180.

Ahn, Y.-Y., J.P. Bagrow, and S. Lehmann. 2010. Link communities reveal multiscale complexity in networks. Nature 466(7307): 761–764.

Allers, E., J.J. Wright, K.M. Konwar, C.G. Howes, E. Beneze, S.J. Hallam, and M.B. Sullivan. 2016. Diversity and population structure of Marine Group A bacteria in the Northeast subarctic Pacific Ocean. ISME J. 7(2): 256–268.

Amos, R.T., and K.U. Mayer. 2006. Investigating Ebullition in a Sand Column Using Dissolved Gas Analysis and Reactive Transport Modeling. Environ. Sci. Technol. 40(17): 5361–5367.

Amos, R.T., B.A. Bekins, G.N. Delin, I.M. Cozzarelli, D.W. Blowes, and J.D. Kirshtein. 2011. Methane oxidation in a crude oil contaminated aquifer: Delineation of aerobic reactions at the plume fringes. J. Contam. Hydrol. 125: 13–25.

Amos, R.T., B.A. Bekins, I.M. Cozzarelli, M.A. Voytek, J.D. Kirshtein, E.J.P. Jones, and D.W. Blowes. 2012. Evidence for iron-mediated anaerobic methane oxidation in a crude oil-contaminated aquifer. Geobiology 10(6): 506–517.

Amos, R.T., K.U. Mayer, B.A. Bekins, G.N. Delin, and R.L. Williams. 2005. Use of dissolved and vapor-phase gases to investigate methanogenic degradation of petroleum hydrocarbon contamination in the subsurface. Water Resour. Res. 41(2): W02001.

Anderson, R.T., and D.R. Lovley. 2000. Hexadecane Decay by Methanogenesis. Nature 404: 722–726.

Anderson, R.T., J.N. Rooney-Varga, C.V. Gaw, and D.R. Lovley. 1998. Anaerobic Benzene Oxidation in the Fe(III) Reduction Zone of Petroleum-Contaminated Aquifers. Environ. Sci. Technol. 32(9): 1222–1229.

Andreote, F.D., R.T. Carneiro, J.F. Salles, J. Marcon, C.A. Labate, J.L. Azevedo, and W.L. Araújo. 2009. Culture-Independent Assessment of Rhizobiales-Related Alphaproteobacteria and the Diversity of Methylobacterium in the Rhizosphere and Rhizoplane of Transgenic Eucalyptus. Microb. Ecol. 57(1): 82–96.

Andrews, Anthony, and Robert Pirog. The U.S. Oil Refining Industry: Background in Changing Markets and Fuel Policies. Report. Congressional Research Service, Library of Congress, October 29, 2010. United States. http://digital.library.unt.edu/ark:/67531/metadc29627/.

Baedecker, M.J., I.M. Cozzarelli, R.P. Eganhouse, D.I. Siegel, and P.C. Bennett. 1993. Crude oil in a shallow sand and gravel aquifer—III. Biogeochemical reactions and mass balance modeling in anoxic groundwater. Appl. Geochem. 8(6): 569–586.

Baedecker, M.J., I.M. Cozzarelli, R.P. Eganhouse, D.I. Siegel, and P.C. Bennett. 1996. Crude-oil in a shallow sand and gravel aquifer-III. Biogeochemical reactions and mass-balance modeling in anoxic groundwater. Appl. Geochem. 8:569–586.

Bagi, A., D.M. Pampanin, A. Lanzén, T. Bilstad, and R. Kommedal. 2014. Naphthalene biodegradation in temperate and arctic marine microcosms. Biodegradation 25(1): 111–125.

Baird, A.J., C.W. Beckwith, S. Waldron, and J.M. Waddington. 2004. Ebullition of methane-containing gas bubbles from near-surface Sphagnum peat. Geophys. Res. Lett. 31(21): L21505.

Baird, D., and R.E. Ulanowicz. 1989. The Seasonal Dynamics of The Chesapeake Bay Ecosystem. Ecol. Monogr. 59(4): 329–364.

Baldrian, P., J. Šnajdr, V. Merhautová, P. Dobiášová, T. Cajthaml, and V. Valášková. 2013. Responses of the extracellular enzyme activities in hardwood forest to soil temperature and seasonality and the potential effects of climate change. Soil Biol. Biochem. 56: 60–68.

Baran, S., J.E. Bielińska, P. Oleszczuk. 2004. Enzymatic activity in an airfield soil polluted with polycyclic aromatic hydrocarbons. Geoderma 118:221-232.

Barberán, A., S.T. Bates, E.O. Casamayor, and N. Fierer. 2012. Using network analysis to explore co-occurrence patterns in soil microbial communities. ISME J. 6(2): 343–351.

Bastian, M., S. Heymann, and M. Jacomy. 2009. Gephi: An Open Source Software for Exploring and Manipulating Networks. Available at http://www.aaai.org/ocs/index.php/ICWSM/09/paper/view/154 (verified 15 April 2014).

Bekins, B. A., E. M. Godsy, and E. Warren. 1999. Distribution of microbial physiologic types in an aquifer contaminated by crude oil. Microb. Ecol. 37:263 – 275.

Bekins, B.A., E.M. Godsy, and E. Warren. 1999. Distribution of Microbial Physiologic Types in an Aquifer Contaminated by Crude Oil. Microb. Ecol. 37(4): 263–275.

Bekins, B.A., F.D. Hostettler, W.N. Herkelrath, G.N. Delin, E. Warren, and H.I. Essaid. 2005. Progression of methanogenic degradation of crude oil in the subsurface. Environ. Geosci. 12: 139–152.

Bekins, B.A., I.M. Cozzarelli, E.M. Godsy, E. Warren, H.I. Essaid, and M.E. Tuccillo. 2001. Progression of natural attenuation processes at a crude oil spill site: II. Controls on spatial distribution of microbial populations. J. Contam. Hydrol. 53:387–406.

Benner, S.G., D.W. Blowes, and J.W. Molson. 2001. Modeling preferential flow in reactive barriers: implications for performance and design. Ground Water 39(3): 371–379.

Bennett, P.C., D.E. Siegel, M.J. Baedecker, and H. M.F. 1996. Crude oil in a shallow sand and gravel aquifer—I. Hydrogeology and inorganic geochemistry. Appl. Geochem. 8(6): 529–549.

Birkham, T.K., M.J. Hendry, L.I. Wassenaar, C.A. Mendoza, and E.S. Lee. 2006. Characterizing geochemical reactions in unsaturated mine waste-rock piles using gaseous O2, CO2, 12CO2, and 13CO2. Environ. Sci. Technol. 37:496–501.

Björklöf, K., Salminen, J., Sainio, P., and K. Jørgensen. 2008. Degradation rates of aged petroleum hydrocarbons are likely to be mass transfer dependent in the field. Env. Geochem. and Health 30,(2): 101-107.

Black, T.A., G. Den Hartog, H.H. Neumann, P. d. Blanken, P. c. Yang, C. Russell, Z. Nesic, X. Lee, S.G. Chen, R. Staebler, and M.D. Novak. 1996. Annual cycles of water vapour and carbon dioxide fluxes in and above a boreal aspen forest. Glob. Change Biol. 2(3): 219–229.

Blazewicz, S.J., R.L. Barnard, R.A. Daly, and M.K. Firestone. 2016. Evaluating rRNA as an indicator of microbial activity in environmental communities: limitations and uses. ISME J. 7(11): 2061–2068.

Blondel, V.D., J.-L. Guillaume, R. Lambiotte, and E. Lefebvre. 2008. Fast unfolding of communities in large networks. J. Stat. Mech. Theory Exp. 2008(10): P10008.

Bockelmann, A., D. Zamfirescu, T. Ptak, P. Grathwohl, and G. Teutsch. 2003. Quantification of mass fluxes and natural attenuation rates at an industrial site with a limited monitoring network: a case study. J. Contam. Hydrol. 60(1-2): 97–121.

Bolstad, P.V., and J.M. Vose. Forest and pasture carbon pools and soil respiration in the southern Appalachian mountains. Available at http://www.treesearch.fs.fed.us/pubs/25430 (verified 28 May 2014).

Bond-Lamberty, B., C. Wang, and S.T. Gower. 2004. A global relationship between the heterotrophic and autotrophic components of soil respiration? Global Change Biol. 10:1756–1766. doi: 10.1111/j.1365-2486.2004.00816.x.

Bonin, A.S., and D.R. Boone. 2006. The Order Methanobacteriales. p. 231–246. In Dr, M.D.P., Falkow, S., Rosenberg, E., Schleifer, K.-H., Stackebrandt, E. (eds.), The Prokaryotes. Springer New York.

Borken, W., Y.-J. Xu, E.A. Davidson, and F. Beese. 2002. Site and temporal variation of soil respiration in European beech, Norway spruce, and Scots pine forests. Glob. Change Biol. 8(12): 1205–1216.

Bouchard, D., D. Hunkeler, P. Gaganis, R. Aravena, P. Höhener, M.M. Broholm, and P. Kjeldsen. 2008. Carbon Isotope Fractionation during Diffusion and Biodegradation of Petroleum Hydrocarbons in the Unsaturated Zone: Field Experiment at Værløse Airbase, Denmark, and Modeling. Environ. Sci. Technol. 42(2): 596–601.

Brakstad, O.G. 2008. Natural and Stimulated Biodegradation of Petroleum in Cold Marine Environments. p. 389–407. In Margesin, R., Schinner, F., Marx, J.-C., Gerday, C. (eds.), Psychrophiles: from Biodiversity to Biotechnology. Springer Berlin Heidelberg.

Bugna, G.C., J.P. Chanton, T.B. Stauffer, W.G. MacIntyre, and E.L. Libelo. 2005. Partitioning microbial respiration between jet fuel and native organic matter in an organic-rich long time-contaminated aquifer. Chemosphere. 60:177–187. doi:10.1016/j.chemosphere.2004.12.066.

Bujalský, L., S. Kaneda, P. Dvorščík, and J. Frouz. 2014. In situ soil respiration at reclaimed and unreclaimed post-mining sites: Responses to temperature and reclamation treatment. Ecol. Eng. 68: 53–59.

Buscheck, T.E., K. O'Reilly, G. Koschal, and G. Davis. 2001. Ethanol in Groundwater at the Pacific Northwest Terminal. National Ground Water Association, Westerville, Ohio.

Caldwell, M.E., R.M. Garrett, R.C. Prince, and J.M. Suflita. 1998. Anaerobic Biodegradation of Long-Chain n-Alkanes under Sulfate-Reducing Conditions. Environ. Sci. Technol. 32(14): 2191–2195.

Campbell, B.J., and D.L. Kirchman. 2016. Bacterial diversity, community structure and potential growth rates along an estuarine salinity gradient. ISME J. 7(1): 210–220.

Campbell, B.J., L. Yu, J.F. Heidelberg, and D.L. Kirchman. 2011. Activity of abundant and rare bacteria in a coastal ocean. Proc. Natl. Acad. Sci.: 201101405.

Caporaso, J.G., J. Kuczynski, J. Stombaugh, K. Bittinger, F.D. Bushman, E.K. Costello, N. Fierer, A.G. Peña, J.K. Goodrich, J.I. Gordon, G.A. Huttley, S.T. Kelley, D. Knights, J.E. Koenig, R.E. Ley, C.A. Lozupone, D. McDonald, B.D. Muegge, M. Pirrung, J. Reeder, J.R. Sevinsky, P.J. Turnbaugh, W.A. Walters, J. Widmann, T. Yatsunenko, J. Zaneveld, and R. Knight. 2010. QIIME allows analysis of high-throughput community sequencing data. Nat. Methods 7(5): 335–336.

Carini, S., N. Bano, G. LeCleir, and S.B. Joye. 2005. Aerobic methane oxidation and methanotroph community composition during seasonal stratification in Mono Lake, California (USA). Environ. Microbiol. 7: 1127–1138.

Carothers, W.W. and Y.K. Kharaka. 1980. Stable carbon isotopes of HCO3– in oil-field waters—implications for the origin of CO2, Geochim. Cosmochim. Acta. 44:323–332. doi:10.1016/0016-7037(80)90140-4.

Castro, M.S., P.A. Steudler, J.M. Melillo, J.D. Aber, and R.D. Bowden. 1995. Factors controlling atmospheric methane consumption by temperate forest soils. Glob. Biogeochem. Cycles 9(1): 1–10.

Chang, J.-J., C.-H. Chou, C.-Y. Ho, W.-E. Chen, J.-J. Lay, and C.-C. Huang. 2008. Syntrophic co-culture of aerobic Bacillus and anaerobic Clostridium for bio-fuels and bio-hydrogen production. Int. J. Hydrog. Energy 33(19): 5137–5146.

Chanton, J.P., L.C. Chasar, P. Glaser, D. Siegel. 2005. Carbon and hydrogen isotopic effects in microbial methane from terrestrial environments. p. 85–105. In L.B. Flanagan, J.R. Ehleringer, and D.E. Pataki (eds.) Stable isotopes and biosphere-atmosphere interactions. Physiological Ecology Series. Elsevier-Academic Press, Amsterdam.

Chao, A. 1984. Nonparametric-estimation of the number of classes in a population. http://viceroy.eeb.uconn.edu/estimatespages/EstSUsersGuide/References/Chao1984.pdfAvailable at http://ir.lib.nthu.edu.tw/handle/987654321/98798 (verified 15 April 2014).

Chaplin, B.P., G.N. Delin, R.J. Baker, and M.A. Lahvis. 2002. Long-Term Evolution of Biodegradation and Volatilization Rates in a Crude Oil-Contaminated Aquifer. Bioremediation J. 6(3): 237–255.

Cherry, R.S., and D.N. Thompson. 1997. Shift from growth to nutrient-limited maintenance kinetics during biofilter acclimation. Biotechnol. Bioeng. 56(3): 330–339.

Chin, K.-J., A. Esteve-Núñez, C. Leang, and D.R. Lovley. 2004. Direct Correlation between Rates of Anaerobic Respiration and Levels of mRNA for Key Respiratory Genes in Geobacter sulfurreducens. Appl. Environ. Microbiol. 70: 5183–5189.

Clarens, A.F., E.P. Resurreccion, M.A. White, and L.M. Colosi. 2010. Environmental Life Cycle Comparison of Algae to Other Bioenergy Feedstocks. Environ. Sci. Technol. 44(5): 1813–1819.

Conant, R.T., M.G. Ryan, G.I. Ågren, H.E. Birge, E.A. Davidson, P.E. Eliasson, S.E. Evans, S.D. Frey, C.P. Giardina, F.M. Hopkins, R. Hyvönen, M.U.F. Kirschbaum, J.M. Lavallee, J. Leifeld, W.J. Parton, J. Megan Steinweg, M.D. Wallenstein, J.Å. Martin Wetterstedt, and M.A. Bradford. 2011. Temperature and soil organic matter decomposition rates – synthesis of current knowledge and a way forward. Glob. Change Biol. 17(11): 3392–3404.

Conrad, M.E., A.S. Tempeton, P.F. Daley, and L. Alvarez-Cohen. 1999. Isotopic evidence for biological controls on migration of petroleum hydrocarbons. Org. Geochem. 30:843–859.

Conrad, M.E., P.F. Daley, M.L. Fischer, B.B. Buchanan, T. Leighton, and M. Kashgarian. 1997. Combined 14C and δ13C Monitoring of in Situ Biodegradation of Petroleum Hydrocarbons. Env. Sci Technol 31(5): 1463–1469.

Coplen, T. B. 2011. Guidelines and recommended terms for expression of stable-isotope-ratio and gas-ratio measurement results. Rapid Commun.Mass Spectrom. 25:2538–2560. doi: 10.1002/rcm.5129.

Coplen, T.B. 1994. Reporting of Stable Hydrogen, Carbon and Oxygen Isotopic Abundances, Pure Appl. Chem. 66: 273-276.

Corseuil, H.X., A.L. Monier, M. Fernandes, M.R. Schneider, C.C. Nunes, M. do Rosario, and P.J.J. Alvarez. 2011. BTEX Plume Dynamics Following an Ethanol Blend Release: Geochemical Footprint and Thermodynamic Constraints on Natural Attenuation. Environ. Sci. Technol. 45(8): 3422–3429.

Costello, A.M., and M.E. Lidstrom. 1999. Molecular characterization of functional and phylogenetic genes from natural populations of methanotrophs in lake sediments. Appl. Environ. Microbiol. 65: 5066–5074.

Cozzarelli, I.M., B.A. Bekins, M.J. Baedecker, G.R. Aiken, R.P. Eganhouse, and M.E. Tuccillo. 2001. Progression of natural attenuation processes at a crude-oil spill site: I. Geochemical evolution of the plume. J. Contam. Hydrol. 53(3–4): 369–385.

Czepiel, P.M., B. Mosher, R.C. Harriss, J.H. Shorter, J.B. McManus, C.E. Kolb, E. Allwine, and B.K. Lamb. 1996. Landfill methane emissions measured by enclosure and atmospheric tracer methods. J. Geophys. Res. Atmospheres 101(D11): 16711–16719.

Daily, G.C., and E.S. of America. 1997. Ecosystem services: benefits supplied to human societies by natural ecosystems. Ecological Society of America.

Daily, J.P., N.P. Hitt, D.R. Smith, and C.D. Snyder. 2012. Experimental and environmental factors affect spurious detection of ecological thresholds. Ecology 93(1): 17–23.

Davidson, E.A., K. Savage, L.V. Verchot, and R. Navarro. 2002. Minimizing artifacts and biases in chamber-based measurements of soil respiration. Agric. For. Meteorol. 113(1–4): 21–37.

DeAngelis, K.M., W.L. Silver, A.W. Thompson, and M.K. Firestone. 2010. Microbial communities acclimate to recurring changes in soil redox potential status. Environ. Microbiol. 12(12): 3137–3149.

Delin, G.N., and W.N. Herkelrath. 2005. Use of soil moisture probes to estimate ground water recharge at an oil spill site. United States Geological Survey.

Delin, G.N., and W.N. Herkelrath. 2014. Effects of a Dual-Pump Crude-Oil Recovery System, Bemidji, Minnesota, USA. Groundw. Monit. Remediat. 34(1): 57–67.

Devi, N.B., and P.S. Yadava. 2006. Seasonal dynamics in soil microbial biomass C, N and P in a mixed-oak forest ecosystem of Manipur, North-east India. Appl. Soil Ecol. 31(3): 220–227.

Díaz, M.P., K.G. Boyd, S.J.W. Grigson, and J.G. Burgess. 2002. Biodegradation of crude oil across a wide range of salinities by an extremely halotolerant bacterial consortium MPD-M, immobilized onto polypropylene fibers. Biotechnol. Bioeng. 79(2): 145–156.

Dibble, J.T., and R. Bartha. 1979. Effect of environmental parameters on the biodegradation of oil sludge. Appl. Environ. Microbiol. 37(4): 729–739.

Dietrich, D.P., and D.C. Leven. 2006. Direct Push-Technologies. p. 321–340. In Kirsch, D.R. (ed.), Groundwater Geophysics. Springer Berlin Heidelberg.

Dillard, L.A., H.I. Essaid, and W.N. Herkelrath. 1997. Multiphase flow modeling of a crude-oil spill site with a bimodal permeability distribution. Water Resour. Res. 33(7): 1617–1632.

Donges, J.F., R.V. Donner, M.H. Trauth, N. Marwan, H.-J. Schellnhuber, and J. Kurths. 2011. Nonlinear detection of paleoclimate-variability transitions possibly related to human evolution. Proc. Natl. Acad. Sci. 108(51): 20422–20427.

Drennan, D.M., B.A. Bekins, E. Warren, I.M. Cozzarelli, M.J. Baedecker, W.N. Herkelrath, G.N. Delin, R.J. Rosenbauer, and P.L. Campbell. 2010. Fate and transport of petroleum hydrocarbons in the subsurface near Cass Lake, Minnesota: U.S. Geological Survey Scientific Investigations Report 2010-5085, 1-36.

Ducklow, H. 2008. Microbial services: challenges for microbial ecologists in a changing world. Aquat. Microb. Ecol. 53: 13–19.

Dugas, W.A. 1996. Micrometeorological and chamber measurements of CO2 flux from bare soil. Agric. For. Meteorol. 67(1–2): 115–128.

Edgar, R.C. 2010. Search and clustering orders of magnitude faster than BLAST. Bioinformatics 26(19): 2460–2461.

Edwards, E.A., L.E. Wills, M. Reinhard, and D. Grbic-Galic. 1992. Anaerobic degradation of toluene and xylene by aquifer microorganisms under sulfate-reducing conditions. Appl. Environ. Microbiol. 58(3): 794–800.

Eganhouse, R.P., M.J. Baedecker, I.M. Cozzarelli, G.R. Aiken, K.A. Thorn, and T.F. Dorsey. 1996. Crude oil in a shallow sand and gravel aquifer—II. Organic geochemistry. Appl. Geochem. 8(6): 551–567.

el-Din Sharabi, N., and R. Bartha. 1996. Testing of some assumptions about biodegradability in soil as measured by carbon dioxide evolution. Appl. Environ. Microbiol. 59(4): 1201–1205.

Elberling, B., L. Askaer, C.J. Jørgensen, H.P. Joensen, M. Kühl, R.N. Glud, and F.R. Lauritsen. 2011. Linking Soil O2, CO2, and CH4 Concentrations in a Wetland Soil: Implications for CO2 and CH4 Fluxes. Env. Sci Technol 45(8): 3393–3399.

Engelbrektson, A., V. Kunin, K.C. Wrighton, N. Zvenigorodsky, F. Chen, H. Ochman, and P. Hugenholtz. 2010. Experimental factors affecting PCR-based estimates of microbial species richness and evenness. ISME J. 4(5): 642–647.

Essaid, H.I., B.A. Bekins, W.N. Herkelrath, and G.N. Delin. 2011. Crude Oil at the Bemidji Site: 25 Years of Monitoring, Modeling, and Understanding. Ground Water 49(5): 706–726.

Falkowski, P.G., T. Fenchel, and E.F. Delong. 2008. The Microbial Engines That Drive Earth's Biogeochemical Cycles. Science 320(5879): 1034–1039.

Fang, Y., T.D. Scheibe, R. Mahadevan, S. Garg, P.E. Long, and D.R. Lovley. 2011. Direct coupling of a genome-scale microbial in silico model and a groundwater reactive transport model. J. Contam. Hydrol. 122(1–4): 96–106.

Freitag, T.E., and J.I. Prosser. 2009. Correlation of methane production and functional gene transcriptional activity in a peat soil. Appl. Environ. Microbiol. 75: 6679–6687.

Freitas, J.G., and J.F. Barker. 2011. Oxygenated gasoline release in the unsaturated zone — Part 1: Source zone behavior. J. Contam. Hydrol. 126(3–4): 153–166.

Freitas, J.G., B. Fletcher, R. Aravena, and J.F. Barker. 2010. Methane Production and Isotopic Fingerprinting in Ethanol Fuel Contaminated Sites. Ground Water 48(6): 844–857.

Fruchterman, T.M.J., and E.M. Reingold. 1991. Graph drawing by force-directed placement. Softw. Pract. Exp. 21(11): 1129–1164.

Galand, P.E., E.O. Casamayor, D.L. Kirchman, and C. Lovejoy. 2009. Ecology of the rare microbial biosphere of the Arctic Ocean. Proc. Natl. Acad. Sci.: pnas.0908284106.

Galimov, E.M. 2006. Isotope organic geochemistry Org. Geochem. 37:1200–1262.

Gantzer, C., P. Gaspard, L. Galvez, A. Huyard, N. Dumouthier, and J. Schwartzbrod. 2001. Monitoring of bacterial and parasitological contamination during various treatment of sludge. Water Res. 35(16): 3763–3770.

Garcia, J.-L., B. Ollivier, and W.B. Whitman. 2006. The Order Methanomicrobiales. p. 208–230. In Dr, M.D.P., Falkow, S., Rosenberg, E., Schleifer, K.-H., Stackebrandt, E. (eds.), The Prokaryotes. Springer New York.

Geets, J., B. Borremans, L. Diels, D. Springael, J. Vangronsveld, D. Van Der Lelie, and K. Vanbroekhoven. 2006. DsrB gene-based DGGE for community and diversity surveys of sulfate-reducing bacteria. J. Microbiol. Methods 66: 194–205.

Gibson, B.D., R.T. Amos, and D.W. Blowes. 2011. 34S/32S Fractionation during sulfate reduction in groundwater treatment systems: reactive transport modeling. Environ. Sci. Technol.45:2863–2870.

Gleason, R.A., B.A. Tangen, B.A. Browne, and N.H. Euliss Jr. 2009. Greenhouse gas flux from cropland and restored wetlands in the Prairie Pothole Region. Soil Biol. Biochem. 41(12): 2501–2507.

Gogo, S., C. Guimbaud, F. Laggoun-Défarge, V. Catoire, and C. Robert. 2011. In situ quantification of CH₄ bubbling events from a peat soil using a new infrared laser spectrometer. J. Soils Sediments 11(4): 545–551.

Gomez, D.E., and P.J.J. Alvarez. 2010. Comparing the effects of various fuel alcohols on the natural attenuation of Benzene Plumes using a general substrate interaction model. J. Contam. Hydrol. 113(1–4): 66–76.

Grahammer, K., M.D. Jawson, and J. Skopp. 1991. Day and night soil respiration from a grassland. Soil Biol. Biochem. 23(1): 77–81.

Groffman, P.M., and P.J. Bohlen. 1999. Soil and Sediment Biodiversity: Cross-system comparisons and large-scale effects. BioScience 49(2): 139–148.

Guimbaud, C., V. Catoire, S. Gogo, C. Robert, M. Chartier, F. Laggoun-Défarge, A. Grossel, P. Albéric, L. Pomathiod, B. Nicoullaud, and G. Richard. 2011. A portable infrared laser spectrometer for flux measurements of trace gases at the geosphere–atmosphere interface. Meas. Sci. Technol. 22(7): 075601.

Haas, B.J., D. Gevers, A.M. Earl, M. Feldgarden, D.V. Ward, G. Giannoukos, D. Ciulla, D. Tabbaa, S.K. Highlander, E. Sodergren, B. Methé, T.Z. DeSantis, J.F. Petrosino, R. Knight, and B.W. Birren. 2011. Chimeric 16S rRNA sequence formation and detection in Sanger and 454-pyrosequenced PCR amplicons. Genome Res. 21(3): 494–504.

Halihan, T., S. Paxton, I. Graham, T. Fenstemaker, and M. Riley. 2005. Post-remediation evaluation of a LNAPL site using electrical resistivity imaging. J. Environ. Monit. 7(4): 283–287.

Hamamura, N., S.H. Olson, D.M. Ward, and W.P. Inskeep. 2006. Microbial Population Dynamics Associated with Crude-Oil Biodegradation in Diverse Soils. Appl. Environ. Microbiol. 72(9): 6316–6324.

Hanson, P.J., N.T. Edwards, C.T. Garten, and J.A. Andrews. 2000. Separating root and soil microbial contributions to soil respiration: A review of methods and observations. Biogeochemistry 48(1): 115–146.

Hawley, D.M., and S.M. Altizer. 2011. Disease ecology meets ecological immunology: understanding the links between organismal immunity and infection dynamics in natural populations. Funct. Ecol. 25(1): 48–60.

Healy, R.W., R.G. Striegl, T.F. Russell, G.L. Hutchinson, and G.P. Livingston. 1996. Numerical Evaluation of Static-Chamber Measurements of Soil—Atmosphere Gas Exchange: Identification of Physical Processes. Soil Sci. Soc. Am. J. 60(3): 740–747.

Herbst, M., H.J. Hellebrand, J. Bauer, J.A. Huisman, J. Šimůnek, L. Weihermüller, A. Graf, J. Vanderborght, and H. Vereecken. 2008. Multiyear heterotrophic soil respiration: Evaluation of a coupled CO2 transport and carbon turnover model. Ecol. Model. 214(2–4): 271–283.

Hill, J., E. Nelson, D. Tilman, S. Polasky, and D. Tiffany. 2006. Environmental, economic, and energetic costs and benefits of biodiesel and ethanol biofuels. Proc. Natl. Acad. Sci. 103(30): 11206–11210.

Hinchee, R.E., and S.K. Ong. 1992. A rapid in situ respiration test for measuring aerobic biodegradation rates of hydrocarbons in soil. J. Air Waste Manag. Assoc. 42(10): 1305–1312.

Hinchee, R.E., D.C. Downey, R.R. Dupont, P.K. Aggarwal, and R.N. Miller. 1991. Enhancing biodegradation of petroleum-hydrocarbons through soil venting. J. Hazard. Mater. 27:315–325.

Höhener, P., and V. Ponsin. 2014. In situ vadose zone bioremediation. Curr. Opin. Biotechnol. 27: 1–7.

Höhener, P., N. Dakhel, M. Christophersen, M. Broholm, and P. Kjeldsen. 2006. Biodegradation of hydrocarbons vapors: Comparison of laboratory studies and field investigations in the vadose zone at the emplaced fuel source experiment, Airbase Værløse, Denmark. J. Contam. Hydrol. 88(3–4): 337–358.

Holmes, D.E., K.T. Finneran, R.A. O'Neil, and D.R. Lovley. 2002. Enrichment of Members of the Family Geobacteraceae Associated with Stimulation of Dissimilatory Metal Reduction in Uranium-Contaminated Aquifer Sediments. Appl. Environ. Microbiol. 68(5): 2300–2306.

Horel, A., B. Mortazavi, and P.A. Sobecky. 2012. Responses of microbial community from northern Gulf of Mexico sandy sediments following exposure to Deepwater Horizon crude oil. Environ. Toxicol. Chem. SETAC 31(5): 1004–1011.

Hostettler, F.D., and K.A. Kvenvolden. 2002. Alkylcyclohexanes in environmental geochemistry. Environ. Forensics 3: 293–301.

Hugoni, M., N. Taib, D. Debroas, I. Domaizon, I.J. Dufournel, G. Bronner, I. Salter, H. Agogué, I. Mary, and P.E. Galand. 2016. Structure of the rare archaeal biosphere and seasonal dynamics of active ecotypes in surface coastal waters. Proc. Natl. Acad. Sci.: 201216866.

Hult, M.F. and R.R. Grabbe.1988. Distribution of gases and hydrocarbon vapors in the unsaturated zone. p C17–C20, In S.E. Ragone (ed.) U.S. Geological Survey Program on Toxic Waste - Ground-Water Contamination - Proceedings of the second technical meeting, Cape Cod, MA, 21–25 October 1985. U.S. Geological Survey Open-File Report 86–481.

Interstate Technology and Regulatory Council. 2009. Evaluating Natural Source Zone Depletion at Sites with LNAPL. Technology Overview.

Istok, J.D., M.D. Humphrey, M.H. Schroth, M.R. Hyman, and K.T. O'Reilly. 1997. Single-Well, "Push-Pull" Test for In Situ Determination of Microbial Activities. Ground Water 35(4): 619–631.

IUPAC. 1997. Compendium of Chemical Terminology. 2nd ed. (the "Gold Book"). Blackwell Scientific Publications, Oxford. Also available online at http://goldbook.iupac.org (verified 20 Dec. 2011).

Jackson, A., and J.H. Pardue. 1997. Seasonal Variability of Crude Oil Respiration Potential in Salt and Fresh Marshes. J. Environ. Qual. 26(4): 1140.

Jacomy, M. 2009. Force-Atlas Graph Layout Algorithm. Available at http://gephi.org/2011/forceatlas2-the-new-version-of-our-home-brew-layout.

Jassal, R., A. Black, M. Novak, K. Morgenstern, Z. Nesic, and D. Gaumont-Guay. 2005. Relationship between soil CO2 concentrations and forest-floor CO2 effluxes. Agric. For. Meteorol. 130(3–4): 176–192.

Jassal, R., Black, A., Novak, M., Morgenstern, K., Nesic, Z., and D. Gaumont-Guay. 2005. Relationship between soil CO2 concentrations and forest-floor CO2 effluxes. Agric. For. Meteorol. 130, 176–192.

Jassal, R.S., T.A. Black, R. Roy, and G. Ethier. 2011. Effect of nitrogen fertilization on soil CH4 and N2O fluxes, and soil and bole respiration. Geoderma 162(1–2): 182–186.

Jassal, R.S., T.A. Black, Z. Nesic, and D. Gaumont-Guay. 2012. Using automated non-steady-state chamber systems for making continuous long-term measurements of soil CO2 efflux in forest ecosystems. Agric. For. Meteorol. 161(0): 57–65.

Jewell, K.P., and J.T. Wilson. 2011. A New Screening Method for Methane in Soil Gas Using Existing Groundwater Monitoring Wells. Ground Water Monit. Remediat. 31(3): 82–94.

Johnson, P., P. Lundegard, and Z. Liu. 2006. Source Zone Natural Attenuation at Petroleum Hydrocarbon Spill Sites—I: Site-Specific Assessment Approach. Ground Water Monit. Remediat. 26(4): 82–92.

Johnson, P.C., C. Bruce, R.L. Johnson, and M.W. Kemblowski. 1998. In Situ Measurement of Effective Vapor-Phase Porous Media Diffusion Coefficients. Environ. Sci. Technol. 32(21): 3405–3409.

Jones, K.L., M.B.J. Lindsay, R. Kipfer, and K.U. Mayer. 2014. Atmospheric noble gases as tracers of biogenic gas dynamics in a shallow unconfined aquifer. Geochim. Cosmochim. Acta 128: 144–157.

Kabwe, L.K., G.W. Wilson, and M.J. Hendry. 2005. Effects of rainfall events on waste-rock surface-water conditions and CO_2 effluxes across the surfaces of two waste-rock piles. J. Environ. Eng. Sci. 4(6): 469–480.

Kao, C., H. Chien, R. Surampalli, C. Chien, and C. Chen. 2010. Assessing of Natural Attenuation and Intrinsic Bioremediation Rates at a Petroleum-Hydrocarbon Spill Site: Laboratory and Field Studies. J. Environ. Eng. 136(1): 54–67.

Karlen, I., I.U.Olsson, P. Kallburg, and S. Kilici. 1968. Absolute determination of the activity of two 14C dating standards. Arkiv Geofysik. 4:465–471.

Kätterer, T., M. Reichstein, O. Andrén, and A. Lomander. 1998. Temperature dependence of organic matter decomposition: a critical review using literature data analyzed with different models. Biol. Fertil. Soils 27(3): 258–262.

Kazy, S.K., A.L. Monier, and P.J.J. Alvarez. 2010. Assessing the correlation between anaerobic toluene degradation activity and bssA concentrations in hydrocarbon-contaminated aquifer material. Biodegradation 21: 793–800.

Kendall, C. and D.H. Doctor. Stable isotope applications in hydrologic studies. p. 181–226. In Holland, H.D. and K.K. Turekian (ed.) Isotope geochemistry : from the treatise on geochemistry. Elsevier Ltd., San Diego, CA.

Kendall, C. and E. A. Caldwell. 1998. Fundamentals of Isotope Geochemistry. In C. Kendall and J.J. McDonnell (Eds.), Isotope Tracers in Catchment Hydrology. Elsevier Science, Amsterdam, pp. 51-86.

Kendall, C. and E. A. Caldwell. 1998. Fundamentals of isotope geochemistry. p. 51-86. In C. Kendall and J.J. McDonnell (eds.) Isotope tracers in catchment hydrology. Elsevier Science, Amsterdam.

Kendall, M.M., and D.R. Boone. 2006. The Order Methanosarcinales. p. 244–256. In Dr, M.D.P., Falkow, S., Rosenberg, E., Schleifer, K.-H., Stackebrandt, E. (eds.), The Prokaryotes. Springer New York.

Kennith Krupka, and W. Martin. Subsurface Contaminant Focus Area: Monitored Natural Attenuation (MNA)Programmatic, Technical, and Regulatory Issues.

Khaitan, S., S. Kalainesan, L. e. Erickson, P. Kulakow, S. Martin, R. Karthikeyan, S. l. l. Hutchinson, L. c. Davis, T. h. Illangasekare, and C. Ng'oma. 2006. Remediation of sites contaminated by oil refinery operations. Environ. Prog. 25(1): 20–31.

Kim, S.-J., D.H. Choi, D.S. Sim, and Y.-S. Oh. 2005. Evaluation of bioremediation effectiveness on crude oil-contaminated sand. Chemosphere 59(6): 845–852.

Kirk, M.F., A.M. Martini, D.O. Breecker, D.R. Colman, C. Takacs-Vesbach, and S.T. Petsch. 2012. Impact of commercial natural gas production on geochemistry and microbiology in a shale-gas reservoir. Chem. Geol. 332–333: 15–25.

Kirschbaum, M.U.F. 1995. The temperature dependence of soil organic matter decomposition, and the effect of global warming on soil organic C storage. Soil Biol. Biochem. 27(6): 753–760.

Kirtland, B.C., C. M. Aelion, and P. A. Stone. 2005. Assessing in situ mineralization of recalcitrant organic compounds in vadose zone sediments using δ13C and 14C measurements. J. Contam. Hydrol. 76:1–18. doi:10.1016/j.jconhyd.2004.07.007.

Kram, M.L., S.H. Lieberman, J. Fee, and A.A. Keller. 2001. Use of LIF for Real-Time In-Situ Mixed NAPL Source Zone Detection. Ground Water Monit. Remediat. 21(1): 67–76.

Krupka, K.M.; Martin, W.J. Subsurface contaminant focus area: monitored natural attenuation (MNA)-programmatic, technical, and regulatory issues; Report PNNL-13569 Contract DE-AC06-76RL01830 with US Department of Energy; Pacific Northwest National Laboratory: Richmond, WA, July 2001; pp 138. http://www.pnl.gov/main/publications/external/technical_reports/PNNL-13569.pdf

Kunin, V., A. Engelbrektson, H. Ochman, and P. Hugenholtz. 2010. Wrinkles in the rare biosphere: pyrosequencing errors can lead to artificial inflation of diversity estimates. Environ. Microbiol. 12(1): 118–126.

Laini, A., M. Bartoli, L. Lamastra, E. Capri, M. Balderacchi, and M. Trevisan. 2012. Herbicide contamination and dispersion pattern in lowland springs. Sci. Total Environ. 438: 312–318.

Lajtha, K., and R.H. Michener. (eds.) 1994. Stable isotopes in ecology and environmental science. Blackwell Science Publications, Oxford.

Laskin, A.I., G.M. Gadd, and S. Sariaslani. 2011. Advances in Applied Microbiology. Academic Press.

Law, B.E., F.M. Kelliher, D.D. Baldocchi, P.M. Anthoni, J. Irvine, D. Moore, and S. Van Tuyl. 2001. Spatial and temporal variation in respiration in a young ponderosa pine forest during a summer drought. Agric. For. Meteorol. 110(1): 27–46.

Lennon, J.T., and S.E. Jones. 2011. Microbial seed banks: the ecological and evolutionary implications of dormancy. Nat. Rev. Microbiol. 9(2): 119–130.

LI-COR, 2007. Automated Soil CO2 Flux System & LI-8150 Multiplexer Instruction Manual, 3rd Ed. [Online]; LI-COR Inc.: Lincoln, Nebraska, 433pp.

Liang, Y., J.D. Van Nostrand, Y. Deng, Z. He, L. Wu, X. Zhang, G. Li, and J. Zhou. 2011. Functional gene diversity of soil microbial communities from five oil-contaminated fields in China. ISME J. 5(3): 403–416.

Lin, J., D. Pan, S.J. Davis, Q. Zhang, K. He, C. Wang, D.G. Streets, D.J. Wuebbles, and D. Guan. 2014. China's international trade and air pollution in the United States. Proc. Natl. Acad. Sci.: 201312860.

Lind, O.C., P. Stegnar, B. Tolongutov, B.O. Rosseland, G. Strømman, B. Uralbekov, A. Usubalieva, A. Solomatina, J.P. Gwynn, E. Lespukh, and B. Salbu. 2016. Environmental impact assessment of radionuclide and metal contamination at the former U site at Kadji Sai, Kyrgyzstan. J. Environ. Radioact. 123: 37–49.

Lloyd, J., and J.A. Taylor. 1994. On the Temperature Dependence of Soil Respiration. Funct. Ecol. 8(3): 315–323.

Lohila, A., T. Laurila, J.-P. Tuovinen, M. Aurela, J. Hatakka, T. Thum, M. Pihlatie, J. Rinne, and T. Vesala. 2007. Micrometeorological Measurements of Methane and Carbon Dioxide Fluxes at a Municipal Landfill. Env. Sci Technol 41(8): 2717–2722.

Lundegard, P.D., and P.C. Johnson. 2006. Source Zone Natural Attenuation at Petroleum Hydrocarbon Spill Sites—II: Application to a Former Oil Field. Ground Water Monit. Remediat. 26(4): 93–106.

Lundegard, P.D., P.C. Johnson, and P. Dahlen. 2008. Oxygen Transport From the Atmosphere to Soil Gas Beneath a Slab-on-Grade Foundation Overlying Petroleum-Impacted Soil. Environ. Sci. Technol. 42(15): 5534–5540.

Lundegard, P.D., R.E. Sweeney, and G.T. Ririe. 2000. Soil Gas Methane at Petroleum Contaminated Sites: Forensic Determination of Origin and Source. Environ. Forensics 1(1): 3–10.

Luo, H., P. Dahlen, P.C. Johnson, T. Peargin, and T. Creamer. 2009. Spatial Variability of Soil-Gas Concentrations near and beneath a Building Overlying Shallow Petroleum Hydrocarbon–Impacted Soils. Ground Water Monit. Remediat. 29(1): 81–91.

Luo, Y., and X. Zhou. 2006. Chapter 2 - Importance and roles of soil respiration. p. 17–32. In Luo, Y., Zhou, X. (eds.), Soil Respiration and the Environment. Academic Press, Burlington.

Luo, Y., and X. Zhou. 2006. Chapter 6 - Temporal and spatial variations in soil respiration. p. 107–131. In Luo, Y., Zhou, X. (eds.), Soil Respiration and the Environment. Academic Press, Burlington.

Luton, P.E., J.M. Wayne, R.J. Sharp, and P.W. Riley. 2002. The mcrA gene as an alternative to 16S rRNA in the phylogenetic analysis of methanogen populations in landfill. Microbiology 148: 3521–3530.

Luz, A.P., V.H. Pellizari, L.G. Whyte, and C.W. Greer. 2004. A survey of indigenous microbial hydrocarbon degradation genes in soils from Antarctica and Brazil. Can. J. Microbiol. 50(5): 323–336.

Ma, J., C.W. Nossa, Z. Xiu, W.G. Rixey, and P.J.J. Alvarez. 2016. Adaptive microbial population shifts in response to a continuous ethanol blend release increases biodegradation potential. Environ. Pollut. 178: 419–425.

Mahieu, K., A. De Visscher, P.A. Vanrolleghem, and O. Van Cleemput. 2008. Modelling of stable isotope fractionation by methane oxidation and diffusion in landfill cover soils. Waste Manage. 28:1535–1542.

Maljanen, M., J. Hytönen, and P.J. Martikainen. 2001. Fluxes of N2O, CH4 and CO2 on afforested boreal agricultural soils. Plant Soil 231(1): 113–121.

Mancini, S.A., A.C. Ulrich, G. Lacrampe-Couloume, B. Sleep, E.A. Edwards, and B.S. Lollar. 2003. Carbon and Hydrogen Isotopic Fractionation during Anaerobic Biodegradation of Benzene. Appl. Environ. Microbiol. 69(1): 191–198.

Martin, J.G., Bolstad, P.V., and J.M. Norman. 2004. A carbon dioxide flux generator for testing infrared gas analyzer-based soil respiration systems. Soil Sci. Soc. Am. J. 68, 514–518.

Mason E A and A.P. Malinauskas. 1986. Gas transport in porous media. The Dusty-Gas Model. Elsevier, Amsterdam.

Mason, E.A., and A.P. Malinauskas. 1983. Gas transport in porous media : the dusty-gas model / E.A. Mason and A.P. Malinauskas. Elsevier Scientific Pub. Co, Amsterdam ; New York.

Mayer, K.U., E.O. Frind, and D.W. Blowes. 2002. Multicomponent reactive transport modeling in variably saturated porous media using a generalized formulation for kinetically controlled reactions. Water Resour. Res. 38:1174–1195. doi:10.1029/2001WR000862.

Mayer, K.U., S.G. Benner, and D.W. Blowes. 2006. Process-based reactive transport modeling of a permeable reactive barrier for the treatment of mine drainage. J. Contam. Hydrol. 85(3–4): 195–211.

McClintock, N. 2012. Assessing soil lead contamination at multiple scales in Oakland, California: Implications for urban agriculture and environmental justice. Appl. Geogr. 35(1–2): 460–476.

McCulley, R.L., S.R. Archer, T.W. Boutton, F.M. Hons, and D.A. Zuberer. 2004. Soil respiration and nutrient cycling in wooded communities developing in grassland. Ecology 85(10): 2804–2817.

Meckenstock, R.U., B. Morasch, C. Griebler, and H.H. Richnow. 2004. Stable isotope fractionation analysis as a tool to monitor biodegradation in contaminated acquifers. J. Contam. Hydrol. 75(3–4): 215–255.

Mello, W.Z. de, and M.E.Hines. 1994. Application of static and dynamic enclosures for determining dimethyl sulfide and carbonyl sulfide exchange in Sphagnum peatlands: Implications for the magnitude and direction of flux. J. Geophys. Res. 99, 601– 607.

Mielnick, P.C., and W.A. Dugas. 2000. Soil CO2 flux in a tallgrass prairie. Soil Biol. Biochem. 32(2): 221–228.

Millington, R. J. 1959. Gas diffusion in porous media. Science. 130:100–102

Millington, R., and J. Quirk. 1961. Permeability of porous solids. Trans. Faraday Soc. 57:1200–1207.

Millington, R.J., and J.P. Quirk. 1961. Permeability of porous solids. Trans. Faraday Soc. 57(0): 1200–1207.

Moldrup, P., T. Olesen, P. Schjønning, T. Yamaguchi, and D.E. Rolston. 2000. Predicting the Gas Diffusion Coefficient in Undisturbed Soil from Soil Water Characteristics. Soil Sci. Soc. Am. J. 64(1): 94.

Molins, S., and K.U. Mayer. 2007. Coupling between geochemical reactions and multicomponent gas and solute transport in unsaturated media: A reactive transport modeling study. Water Resour. Res. 46. W05435. doi:10.1029/2006WR005206.

Molins, S., K.U. Mayer, R.T. Amos, and B.A. Bekins. 2010. Vadose zone attenuation of organic compounds at a crude oil spill site - Interactions between biogeochemical reactions and multicomponent gas transport. J. Contam. Hydrol. 112:15–29.

Molins, S., K.U. Mayer, R.T. Amos, and B.A. Bekins. 2010. Vadose zone attenuation of organic compounds at a crude oil spill site — Interactions between biogeochemical reactions and multicomponent gas transport. J. Contam. Hydrol. 112(1–4): 15–29.

Molson, J.W., J.F. Barker, E.O. Frind, and M. Schirmer. 2002. Modeling the impact of ethanol on the persistence of benzene in gasoline-contaminatedgroundwater. Water Resour. Res. 38(1): 1006.

Molson, J.W., O. Fala, M. Aubertin, and B. Bussière. 2005. Numerical simulations of pyrite oxidation and acid mine drainage in unsaturated waste rock piles. J. Contam. Hydrol. 78(4): 343–371.

Morris, B.E.L., R. Henneberger, H. Huber, and C. Moissl-Eichinger. 2016. Microbial syntrophy: interaction for the common good. FEMS Microbiol. Rev. 37(3): 384–406.

Mosher, B.W., P.M. Czepiel, R.C. Harriss, J.H. Shorter, C.E. Kolb, J.B. McManus, E. Allwine, and B.K. Lamb. 1999. Methane Emissions at Nine Landfill Sites in the Northeastern United States. Env. Sci Technol 33(12): 2088–2094.

Mulligan, C.N. and R.N. Yong. 2004. Natural attenuation of contaminated soils. Environ. Int. 30:587–601. doi: 10.1016/j.envint.2006.11.001.

Mulligan, C.N., and R.N. Yong. 2004. Natural attenuation of contaminated soils. Environ. Int. 30(4): 587–601.

Murphy, E.M., T.R. Ginn, A. Chilakapati, C.T. Resch, J.L. Phillips, T.W. Wietsma, and C.M. Spadoni. 1997. The Influence of Physical Heterogeneity on Microbial Degradation and Distribution in Porous Media. Water Resour. Res. 33: 1087–1106.

Nadim, F., G.E. Hoag, S. Liu, R.J. Carley, and P. Zack. 2000. Detection and remediation of soil and aquifer systems contaminated with petroleum products: an overview. J. Pet. Sci. Eng. 26(1–4): 169–178.

Nedwell, D.B., T.M. Embley, and K.J. Purdy. Sulphate reduction, methanogenesis and phylogenetics of the sulphate reducing bacterial communities along an estuarine gradient. Aquat. Microb. Ecol. 37(3): 209–217.

Nelson, D.K., T.M. LaPara, and P.J. Novak. 2010. Effects of Ethanol-Based Fuel Contamination: Microbial Community Changes, Production of Regulated Compounds, and Methane Generation. Environ. Sci. Technol. 44(12): 4525–4530.

Nelson, G.C., E. Bennett, A. Berhe, K. Cassman, R. DeFries, T. Dietz, A. Dobermann, A. Dobson, A. Janetos, M. Levy, D. Marco, N. Nakicenovic, B. O'Neill, R. Norgaard, G. Petschel-Held, D. Ojima, P. Pingali, R. Watson, and M. Zurek. 2006. Anthropogenic Drivers of Ecosystem Change: an Overview. Ecol. Soc. 11(2).

Ng, G.-H., B.A. Bekins, I.M. Cozzarelli, M.J. Baedecker, P.C. Bennett, and R.T. Amos. A Mass Balance Approach to Investigating Geochemical Controls on Secondary Water Quality Impacts at a Crude Oil Spill Site near Bemidji, MN. J. Contam. Hydrol.Available at http://www.sciencedirect.com/science/article/pii/S0169772214000618 (verified 29 May 2014).

Nielsen, D.M. 2005. Practical Handbook of Environmental Site Characterization and Ground-Water Monitoring, Second Edition. CRC Press.

Niemann, H., T. Lösekann, D. de Beer, M. Elvert, T. Nadalig, K. Knittel, R. Amann, E.J. Sauter, M. Schlüter, M. Klages, J.P. Foucher, and A. Boetius. 2006. Novel microbial communities of the Haakon Mosby mud volcano and their role as a methane sink. Nature 443(7113): 854–858.

NOAA climate normals. Available online at http://cdo.ncdc.noaa.gov/climatenormals/clim20/mn/210646.pdf (verified 20 Oct. 2011).

Nogales, B., E.R.B. Moore, W.-R. Abraham, and K.N. Timmis. 1999. Identification of the metabolically active members of a bacterial community in a polychlorinated biphenyl-polluted moorland soil. Environ. Microbiol. 1(3): 199–212.

Norman, J.M., C.J. Kucharik, S.T. Gower, D.D. Baldocchi, P.M. Crill, M. Rayment, K. Savage, and R.G. Striegl. 1997. A comparison of six methods for measuring soil-surface carbon dioxide fluxes. J. Geophys. Res. 102(D24): 28771–28,777.

Olsson, I.U. 1970. The use of oxalic acid as a standard. p. 17. In I.U. Olsson (ed.) Radiocarbon variations and absolute chronology. Nobel Symposium, 12th Proc., John Wiley & Sons, New York.

Ostendorf, D.W., and D.H. Kampbell. 1991. Biodegradation of hydrocarbon vapors in the unsaturated zone. Water Resour. Res. 27:453–462.

Owsianiak, M., Ł. Chrzanowski, A. Szulc, J. Staniewski, A. Olszanowski, A.K. Olejnik-Schmidt, and H.J. Heipieper. 2009. Biodegradation of diesel/biodiesel blends by a consortium of hydrocarbon degraders: Effect of the type of blend and the addition of biosurfactants. Bioresour. Technol. 100(3): 1497–1500.

Pal, A., K.Y.-H. Gin, A.Y.-C. Lin, and M. Reinhard. 2010. Impacts of emerging organic contaminants on freshwater resources: Review of recent occurrences, sources, fate and effects. Sci. Total Environ. 408(24): 6062–6069.

Parameswaran, P., C.I. Torres, H.-S. Lee, R. Krajmalnik-Brown, and B.E. Rittmann. 2009. Syntrophic interactions among anode respiring bacteria (ARB) and Non-ARB in a biofilm anode: electron balances. Biotechnol. Bioeng. 103(3): 513–526.

Parkin, T.B., and T.C. Kaspar. 2004. Temporal Variability of Soil Carbon Dioxide Flux. Soil Sci. Soc. Am. J. 68(4): 1234.

Pérez-Pantoja, D., R. Donoso, L. Agulló, M. Córdova, M. Seeger, D.H. Pieper, and B. González. 2012. Genomic analysis of the potential for aromatic compounds biodegradation in Burkholderiales. Environ. Microbiol. 14(5): 1091–1117.

Peters, K.E., C.C. Walters, and J.M. Moldowan. 2005. The Biomarker Guide: Biomarkers and isotopes in the environment and human history. Cambridge University Press.

Peters, K.E., C.C. Walters, and J.M. Moldowan. 2007. The Biomarker Guide: Volume 2. Biomarkers and Isotopes in Petroleum Systems and Earth History. 2nd ed. Cambridge University Press.

Pinnacle Engineering, Inc., 2004. Site Investigation Report for DM&E Railroad Release, Balaton, Minnesota. Maple Grove, Minnesota: Pinnacle Engineering, Inc.

Pinnacle Engineering, Inc., 2007. Summary Report Initial Investigation for DM&E Railroad Ethanol Release, Cambria, Minnesota. Maple Grove, Minnesota: Pinnacle Engineering, Inc.

Plugge, C.M., J.B. van Lier, and A.J.M. Stams. 2010. Syntrophic Communities in Methane Formation from High Strength Wastewaters. p. 59–77. In Insam, H., Franke-Whittle, I., Goberna, M. (eds.), Microbes at Work. Springer Berlin Heidelberg.

Poling, B.E., Thomson, G.H., Friend, D.G., Rowley, R.L., and W.V. Wilding. 2007. Physical and Chemical Data, p. 2-1 – 2-517, In Green, D. W. and R.H. Perry. Perry's Chemical Engineers' Handbook. 8th ed. McGraw-Hill Professional Publishing, Blacklick, OH.

Powers, S.E., C.S. Hunt, S.E. Heermann, H.X. Corseuil, D. Rice, and P.J.J. Alvarez. 2001. The Transport and Fate of Ethanol and BTEX in Groundwater Contaminated by Gasohol. Crit. Rev. Environ. Sci. Technol. 31(1): 79–123.

Powers, S.E., C.S. Hunt, S.E. Heermann, H.X. Corseuil, D. Rice, and P.J.J. Alvarez. 2001. The Transport and Fate of Ethanol and BTEX in Groundwater Contaminated by Gasohol. Crit. Rev. Environ. Sci. Technol. 31(1): 79–126.

Pruesse, E., C. Quast, K. Knittel, B.M. Fuchs, W. Ludwig, J. Peplies, and F.O. Glockner. 2007. SILVA: a comprehensive online resource for quality checked and aligned ribosomal RNA sequence data compatible with ARB. Nucleic Acids Res. 35(21): 7188–7196.

Qi, Y., M. Xu, and J. Wu. 2002. Temperature sensitivity of soil respiration and its effects on ecosystem carbon budget: nonlinearity begets surprises. Ecol. Model. 153(1–2): 131–142.

R Development Core Team (2013). R: A language and environment for statistical computing. R Foundation for Statistical Computing, Vienna, Austria. ISBN 3-900051-07-0, URL http://www.R-project.org.

Raich, J.W., and W.H. Schlesinger. 1992. The global carbon dioxide flux in soil respiration and its relationship to vegetation and climate. Tellus B 44(2): 81–99.

Reed, M.S., M. Buenemann, J. Atlhopheng, M. Akhtar-Schuster, F. Bachmann, G. Bastin, H. Bigas, R. Chanda, A.J. Dougill, W. Essahli, A.C. Evely, L. Fleskens, N. Geeson, J.H. Glass, R. Hessel, J. Holden, A. a. R. Ioris, B. Kruger, H.P. Liniger, W. Mphinyane, D. Nainggolan, J. Perkins, C.M. Raymond, C.J. Ritsema, G. Schwilch, R. Sebego, M. Seely, L.C. Stringer, R. Thomas, S. Twomlow, and S. Verzandvoort. 2011. Cross-scale monitoring and assessment of land degradation and sustainable land management: A methodological framework for knowledge management. Land Degrad. Dev. 22(2): 261–271.

Reiners, W.A. 1968. Carbon Dioxide Evolution from the Floor of Three Minnesota Forests. Ecology 49(3): 471–486.

Revesz, K., T.B. Coplen, M.J. Baedecker, and P.D. Glynn. 1995. Methane Production and Consumption Monitored by Stable H and C Isotope Ratios at a Crude Oil Spill Site, Bemidji, Minnesota. Appl. Geochem. 10: 505–516.

Revesz, K., T.B. Coplen, M.J. Baedecker, P.D. Glynn, and M. Hult. 1995. Methane production and consumption monitored by stable H and C isotope ratios at a crude oil spill site, Bemidji, Minnesota. Appl. Geochem.10:505–516.

Richnow, H.H., E. Annweiler, W. Michaelis, and R.U. Meckenstock. 2006. Microbial in situ degradation of aromatic hydrocarbons in a contaminated aquifer monitored by carbon isotope fractionation. J. Contam. Hydrol. 65:101–120.

Rittmann, B.E. 2004. Definition, Objectives, and Evaluation of Natural Attenuation. Biodegradation. 15:349–357.

Rivett, M.O., G.P. Wealthall, R.A. Dearden, and T.A. McAlary. 2011. Review of unsaturated-zone transport and attenuation of volatile organic compound (VOC) plumes leached from shallow source zones. J. Contam. Hydrol. 123:130–156.

Rochette, P., and N.S. Eriksen-Hamel. 2008. Chamber Measurements of Soil Nitrous Oxide Flux: Are Absolute Values Reliable? Soil Sci. Soc. Am. J. 72(2): 331.

Röling, W.F.M. 2007. Do microbial numbers count? Quantifying the regulation of biogeochemical fluxes by population size and cellular activity. FEMS Microbiol. Ecol. 62: 202–210.

Roslev P., N. Iversen, and K. Henricksen. 1997. Oxidation and assimilation of atmospheric methane by soil methane oxidizers. Appl. Environ. Microbiol. 63:874–880.

Rotthauwe, J.H., K.P. Witzel, and W. Liesack. 1997. The ammonia monooxygenase structural gene amoA as a functional marker: molecular fine-scale analysis of natural ammonia-oxidizing populations. Appl. Environ. Microbiol. 63: 4704–4712.

Samanta, S.K., O.V. Singh, and R.K. Jain. 2002. Polycyclic aromatic hydrocarbons: environmental pollution and bioremediation. Trends Biotechnol. 20(6): 243–248.

Santoni, G.W., B.H. Lee, J.P. Goodrich, R.K. Varner, P.M. Crill, J.B. McManus, D.D. Nelson, M.S. Zahniser, and S.C. Wofsy. 2012. Mass fluxes and isofluxes of methane (CH4) at a New Hampshire fen measured by a continuous wave quantum cascade laser spectrometer. J. Geophys. Res. 117(D10): D10301.

Savage, K.E., and E.A. Davidson. 2006. A comparison of manual and automated systems for soil CO2 flux measurements: trade-offs between spatial and temporal resolution. J. Exp. Bot. 54(384): 891–899.

Scheffer, M., S.R. Carpenter, T.M. Lenton, J. Bascompte, W. Brock, V. Dakos, J. van de Koppel, I.A. van de Leemput, S.A. Levin, E.H. van Nes, M. Pascual, and J. Vandermeer. 2012. Anticipating Critical Transitions. Science 338(6105): 344–348.

Schoefs, O., M. Perrier, and R. Samson. 2004. Estimation of contaminant depletion in unsaturated soils using a reduced-order biodegradation model and carbon dioxide measurement. Appl. Microbiol. Biotechnol. 64(1): 53–61.

Schrier-Uijl, A., A. Veraart, P. Leffelaar, F. Berendse, and E. Veenendaal. 2011. Release of CO₂ and CH₄ from lakes and drainage ditches in temperate wetlands. Biogeochemistry 102(1): 265–279.

Schwinning, S., and O.E. Sala. 2004. Hierarchy of responses to resource pulses in arid and semi-arid ecosystems. Oecologia 141(2): 211–220.

Segarra, K.E.A., V. Samarkin, E. King, C. Meile, and S.B. Joye. 2013. Seasonal variations of methane fluxes from an unvegetated tidal freshwater mudflat (Hammersmith Creek, GA). Biogeochemistry 115(1-3): 349–361.

Semple, K.T., N.M. Dew, K.J. Doick, and A.H. Rhodes. 2006. Can microbial mineralization be used to estimate microbial availability of organic contaminants in soil? Environ. Pollut. Barking Essex 1987 140(1): 164–172.

Sheik, C.S., W.H. Beasley, M.S. Elshahed, X. Zhou, Y. Luo, and L.R. Krumholz. 2011. Effect of warming and drought on grassland microbial communities. ISME J. 5(10): 1692–1700.

Sihota, N.J., and K.U. Mayer. 2012. Characterizing Vadose Zone Hydrocarbon Biodegradation Using Carbon Dioxide Effluxes, Isotopes, and Reactive Transport Modeling. Vadose Zone J. 11(4): 0.

Sihota, N.J., K.U. Mayer, M.A. Toso, and J.F. Atwater. 2013. Methane emissions and contaminant degradation rates at sites affected by accidental releases of denatured fuel-grade ethanol. J. Contam. Hydrol. 151: 1–15.

Sihota, N.J., K.U. Mayer, M.A. Toso, and J.F. Atwater. 2016. Methane emissions and contaminant degradation rates at sites affected by accidental releases of denatured fuel-grade ethanol. J. Contam. Hydrol. 151: 1–15.

Sihota, N.J., O. Singurindy, and K.U. Mayer. 2011. CO2-efflux measurements for evaluating source zone natural attenuation rates in a petroleum hydrocarbon contaminated aquifer. Environ. Sci. Technol. 45: 482–488. doi:10.1021/es1032585.

Smith, S.E., and M. F. Hult. 1996. Hydrogeologic data collected from a crude-oil spill site near Bemidji, Minnesota, 1983-91. U.S. Geological Survey Open-File Report 93-496.

Soga, K, J W E Page, and T H Illangasekare. "A Review of NAPL Source Zone Remediation Efficiency and the Mass Flux Approach." Journal of Hazardous Materials 110, no. 1–3 (July 5, 2004): 13–27. doi:10.1016/j.jhazmat.2004.02.034.

Soil Survey Staff, Natural Resources Conservation Service, United States Department of Agriculture. Web Soil Survey. Available online at http://websoilsurvey.nrcs.usda.gov/. Accessed 07/04/14.

Sondermann, W. D. and B. Knorpp. 2004. Legal Aspects of Natural Attenuation in Germany. Biodegradation. 15:467–476.

Spaans, E.J.A., and J.M. Baker. 1995. Examining the use of time domain reflectometry for measuring liquid water content in frozen soil. Water Resour. Res. 31(12): 2917–2925.

Spalding, R.F., M.A. Toso, M.E. Exner, G. Hattan, T.M. Higgins, A.C. Sekely, and S.D. Jensen. 2011. Long-Term Groundwater Monitoring Results at Large, Sudden Denatured Ethanol Releases. Ground Water Monit. Remediat. 31(3): 69–81.

Stackebrandt, E., C.S. Cummins, and J.L. Johnson. 2006. Family Propionibacteriaceae: The Genus Propionibacterium. p. 400–418. In Dr, M.D.P., Falkow, S., Rosenberg, E., Schleifer, K.-H., Stackebrandt, E. (eds.), The Prokaryotes. Springer New York.

Stoffel, J.L., S.T. Gower, J.A. Forrester, and D.J. Mladenoff. 2010. Effects of winter selective tree harvest on soil microclimate and surface CO2 flux of a northern hardwood forest. For. Ecol. Manag. 259(3): 257–265.

Suchomel, K.H., D.K. Kreamer, and A. Long. 1990. Production and transport of carbon-dioxide in a contaminated vadose zone - a stable and radioactive carbon isotope study. Environ. Sci. Technol. 24:1824–1831.

Sulman, B.N., A.R. Desai, B.D. Cook, N. Saliendra, and D.S. Mackay. 2009. Contrasting carbon dioxide fluxes between a drying shrub wetland in Northern Wisconsin, USA, and nearby forests. Biogeosciences 6(6): 1115–1126.

Suseela, V., R.T. Conant, M.D. Wallenstein, and J.S. Dukes. 2012. Effects of soil moisture on the temperature sensitivity of heterotrophic respiration vary seasonally in an old-field climate change experiment. Glob. Change Biol. 18(1): 336–348.

Suseela, V., R.T. Conant, M.D. Wallenstein, and J.S. Dukes. 2012. Effects of soil moisture on the temperature sensitivity of heterotrophic respiration vary seasonally in an old-field climate change experiment. Glob. Change Biol. 18(1): 336–348.Aelion, C.M., B.C. Kirtland, and P.A. Stone. 1997. Radiocarbon assessment of aerobic petroleum

bioremediation in the vadose zone and groundwater at an AS/SVE site. Environ. Sci. Technol. 31:3363–3370.

Szalay, K.Z., and P. Csermely. 2016. Perturbation Centrality and Turbine: A Novel Centrality Measure Obtained Using a Versatile Network Dynamics Tool. PLoS ONE 8(10): e78059.

Teske, A., E. Alm, J.M. Regan, S. Toze, B.E. Rittmann, and D.A. Stahl. 1994. Evolutionary relationships among ammonia- and nitrite-oxidizing bacteria. J. Bacteriol. 176(21): 6623–6630.

Thornton, S.F., S.H. Bottrell, K.H. Spence, R. Pickup, M.J. Spence, N. Shah, H.E.H. Mallinson, and H.H. Richnow. 2011. Assessment of MTBE biodegradation in contaminated groundwater using 13C and 14C analysis: Field and laboratory microcosm studies. Appl. Geochem. 26(5): 828–837.

Tipping, E., E.J. Smith, C.L. Bryant, and J.K. Adamson. 2007. The organic carbon dynamics of a moorland catchment in N. W. England. Biogeochemistry 84(2): 171–189.

Tokida, T., M. Mizoguchi, T. Miyazaki, A. Kagemoto, O. Nagata, and R. Hatano. 2007. Episodic release of methane bubbles from peatland during spring thaw. Chemosphere 70(2): 165–171.

Trumbore, S. 2000. Age of soil organic matter and soil respiration: radiocarbon constraints on belowground C dynamics. Ecol. Appl. 10:399–411.

Trumbore, S.E., J.L. Bubier, J.W. Harden, and P.M. Crill. 1999. Carbon cycling in boreal wetlands: A comparison of three approaches. J. Geophys. Res. Atmospheres 104(D22): 27673–27682.

United States Environmental Protection Agency (USEPA). 2012. Renewable Fuels: Regulations and Standards. Available at

http://www.epa.gov/otaq/fuels/renewablefuels/regulations.htm Accessed October 16, 2012.

Urich, T., A. Lanzén, J. Qi, D.H. Huson, C. Schleper, and S.C. Schuster. 2008. Simultaneous Assessment of Soil Microbial Community Structure and Function through Analysis of the Meta-Transcriptome. PLoS ONE 3(6): e2527.

Urmann, K., G. Gonzalez-Gil, M.H. Schroth, M. Hofer, and J. Zeyer. 2005. New field method: gas push-pull test for the in-situ quantification of microbial activities in the vadose zone. Environ. Sci. Technol. 39(1): 304–310.

Van Breukelen, B.M., and H. Prommer. 2008. Beyond the Rayleigh equation: Reactive transport modeling of isotope fractionation effects to improve quantification of biodegradation. Environ. Sci. Technol. 42:2457–2466.

Wagner, M., A.J. Roger, J.L. Flax, G.A. Brusseau, and D.A. Stahl. 1998. Phylogeny of Dissimilatory Sulfite Reductases Supports an Early Origin of Sulfate Respiration. J. Bacteriol. 180: 2975–2982.

Wang, S.-Y., E.B. Sudduth, M.D. Wallenstein, J.P. Wright, and E.S. Bernhardt. 2011. Watershed Urbanization Alters the Composition and Function of Stream Bacterial Communities. PLoS ONE 6(8).

Webb, S.W., and K. Pruess. 2003. The Use of Fick's Law for Modeling Trace Gas Diffusion in Porous Media. Transp. Porous Media 51(3): 327–341.

Weiss, J.V., and I.M. Cozzarelli. 2008. Biodegradation in contaminated aquifers: Incorporating microbial/molecular methods. Ground Water 46: 305–322.

Whalen, S. C., W. S. Reeburgh, and K. A. Sandbeck. 1990. Rapid Methane Oxidation in a Landfill Cover Soil. Appl. Environ. Microbiol. 56:3405–341.

Whiticar, M.J., and E. Faber. 1986. Methane oxidation in sediment and water column environments - isotope evidence. Org. Geochem.10:759–768.

Widén, B., and A. Lindroth. 2006. A calibration system for soil carbon dioxide-efflux measurement chambers. Soil Sci. Soc. Am. J. 67, 327–334.

Wilke, C., and C. Lee. 1955. Estimation of Diffusion Coefficients for Gases and Vapors. Ind. Eng. Chem. 47(6): 1253–1257.

Wilson, R.D., S.F. Thornton, and D.M. Mackay. 2004. Challenges in Monitoring the Natural Attenuation of Spatially Variable Plumes. Biodegradation 15(6): 359–369.

Wu, M.L., M.C.F. van Teeseling, M.J.R. Willems, E.G. van Donselaar, A. Klingl, R. Rachel, W.J.C. Geerts, M.S.M. Jetten, M. Strous, and L. van Niftrik. 2012. Ultrastructure of the Denitrifying Methanotroph "Candidatus Methylomirabilis oxyfera," a Novel Polygon-Shaped Bacterium. J. Bacteriol. 194(2): 284–291.

Xu, L., M.D. Furtaw, R.A. Madsen, R.L. Garcia, D.J. Anderson, and D.K. McDermitt. 2006. On maintaining pressure equilibrium between a soil CO2 flux chamber and the ambient air. J. Geophys. Res. 111(D8): D08S10.

Yoonm, P., and G. Thodos. 1970. Viscosity of nonpolar gaseous mixtures at normal pressures. AIChE J. 16:300–304. doi: 10.1002/aic.690160225.

Appendix 1: Supporting information for chapter 2

Vadose zone carbon balance at the Bemidji site

Molins et al. (2010) conducted a multicomponent reactive transport study to integrate available data on vadose zone natural attenuation at the Bemidji site. The simulations included water flow through the unsaturated zone, solute and gas transport, and the main pathways for crude oil degradation coupled with aerobic respiration, Fe and Mn reduction, and methanogenesis. The re-oxidation of CH_4 in the vadose zone and major ion chemistry including hydrolysis and dissolution-precipitation reactions were also included. The simulations assumed that net uptake of carbon by biomass is minimal and that biomass is effectively at a steady state. For details on the simulation approach and results, see Molins et al., 2010.

Table A1.1: Simulated carbon balance along the North Pool Transect after T = 28 years (Analysis of mass balance data from Molins et al. (2010), calcite dissolution and speciation of aqueous carbonate species at equilibrium, biomass assumed at steady state.

	C flux/rate [moles d^{-1} m^{-1}]	**C flux/rate (%)**
Biodegradation	22.3	99.8
Calcite dissolution	0.033	0.2
Total source	**22.33**	
Recharge to saturated zone	0.25	1.1
Change in storage	0.13	0.6
Gas efflux to atmosphere	**21.96**	**98.3**
Total sink	**22.33**	

An analysis of the mass balance results obtained from the simulation (Table S1) reveals that under conditions present in 2007 almost all carbon mineralized by biodegradation processes reports as a gaseous efflux in form of CO_2 to the ground surface (>98%). The simulations indicate that only a small amount of carbon is added from calcite dissolution in response to acid generation associated with the biodegradation reactions, while approximately 1% of carbon is lost to the saturated zone with recharging groundwater.

Dynamic closed chamber CO_2 efflux measurement method

CO_2 effluxes were measured by way of a commercially available DCC system (LI-COR Inc., Lincoln, NE), using either a survey chamber (LI 8100-103) or a long-term chamber (LI 8100-104). In principle, the CO_2 efflux is measured in the same manner for both chambers. Survey chambers have the advantage that measurements can be taken at multiple spatial locations in a comparably short time frame. Long-term chambers (continuous measurements) are able to provide time-series data of CO_2-effluxes at selected locations, accounting for the effect of environmental parameters over time (e.g.: alteration of soil moisture, barometric pressure, temperature - all of which exert controls on diffusive gas efflux). The chambers are vented to eliminate pressure effects, have a fixed headspace, and are opened and closed under automation. The chambers are placed on soil collars, which are inserted into the ground to ensure an adequate seal with respect to the above-ground atmosphere; collars are inserted at least 24 hours prior to initial measurement to allow soil gas transport to re-stabilize.

When operating, the chamber is connected to an infra-red gas analyzer (IRGA) contained within an analyzer control unit (ACU). During a measurement, air is circulated between the chamber headspace and the IRGA at an operator-specified flow rate (upon consultation with the manufacturer, a flow rate of 1.5L min^{-1} was selected). The IRGA measures the concentration of CO_2 within the headspace at a rate of one measurement per second. The system is dedicated to measure CO_2 effluxes, O_2 influxes were not quantified. However, gas samples were collected from the sealed collars to test whether CH_4 effluxes were occurring. This was accomplished by capping the collar and removing a sample by way of a syringe inserted into a septum secured into the cap. Approximately 5 minutes were allowed to elapse prior to sample collection. The

samples were analyzed using a Varian CP-4900 dual channel gas chromatograph, equipped with TCD detectors, a Molsieve 5A PLOT column to separate Ar, O_2, and N_2 and a PoraPLOT U column to separate CH_4 and CO_2.

Measurement of the CO_2 efflux within the chamber is based on the rate of accumulation of CO_2. In order to ensure complete mixing within the chamber headspace, the first 20 seconds of data collected after the chamber has closed are discarded (discard time selection for this study was guided by discussion with the manufacturer and upon initial inspection of data). Measurement periods were limited to 1.5 minutes in order to minimize the changes in chamber concentration, which may lead to altered soil gas concentration gradients (Healy et al., 1996). Bench corrections for temperature, pressure and relative humidity are also included when calculating the CO_2 efflux. In addition a correction for the increase in CO_2 concentration is employed, enabling a calculation of the initial rate of change within the headspace.

Data was post-processed using the manufacturer-supplied software. CO_2 efflux is calculated by determining the rate of change of CO_2 in the chamber headspace using a linear or exponential regression to fit the data; both regression lines are considered and the best fit is selected based on the R^2 value closest to 1.

The CO_2 efflux is calculated from measured data using the following equation (LI-COR, 2007):

$$F_c = \frac{10VP_0\left(1 - \frac{W_0}{1000}\right)}{RS(T_0 + 273.15)} \frac{\partial C'}{\partial t}$$

where F_C is the soil CO_2 efflux rate (μmol m^{-2} s^{-1}), V is volume (cm^3), P_0 is the initial pressure (kPa), W_0 is the initial water vapor mole fraction (mmol mol^{-1}), R is the gas constant (8.314 J K^{-1}

mol^{-1}), S is soil surface area (cm^2), T_0 is initial air temperature (°C), and $\partial C'/\partial t$ is the initial rate of change in water-corrected CO_2 mole fraction (μmol m^{-2} s^{-1}).

Statistical analysis of accuracy and sensitivity of CO_2 efflux method

A statistical analysis was performed to evaluate the sensitivity of the determination of CSR to local variations of TSR in the 'affected' region and NSR in the background locations ('unaffected' region). A two sample t test was used to determine whether significant differences exist between the upgradient wells (310, 603, and 604) and downgradient wells (534, 9103, 533, 9109, 532, 518, 531 and 530) in the 'unaffected' region. The difference between these two groups was insignificant (difference = 0.023; P = 0.95) indicating that it is reasonable to combine upgradient and downgradient measurements to represent the region that is 'unaffected' by oil biodegradation.

Table A1.2. Evaluation of accuracy of the DCC method for estimation of contaminant mineralization rates in the source zone; also evaluated is the sensitivity of the accuracy to the magnitude of TSR in the 'affected' region (SEM = standard error on the mean value).

	Two sample t test				
	Decrease in TSR	**Measured**	**10%**	**20%**	**30%**
Affected (TSR)	**Average (TSR)**	5.89	5.29	4.71	4.12
	Std Dev	0.71	0.64	0.57	0.50
	SEM	0.30	0.26	0.23	0.20
Unaffected (NSR)	**Average (NSR)**	3.29	3.29	3.29	3.29
	Std Dev	0.51	0.51	0.51	0.51
	SEM	0.15	0.15	0.15	0.15
CSR = TSR-NSR	**Average (CSR)**	2.59	2.00	1.41	0.83
	Percent difference F = CSR/NSR [%]	78.7	60.6	42.8	25.1
	95% Confidence interval on CSR	1.96 to 3.23	1.40 to 2.61	0.84 to 1.99	0.28 to 1.37
	Accuracy of CSR [%]	+/- 24.4	+/- 30.5	+/- 41.1	+/- 65.1
	Significant at P = 0.05?	Y	Y	Y	Y
	P Value	P = <0.001	P = <0.001	P = <0.001	P = 0.006

Two sample t-tests were then conducted for the data set by determining whether significant differences exist between the averages of NSR ('unaffected' region) and TSR ('affected' region) (**Table A1.2**). The 95% confidence interval for CSR and the accuracy of CSR relative to its average value (for 95% confidence) were also determined. **Table A1.2** demonstrates that the differences between TSR and NSR are statistically significant. The analysis shows that the accuracy of CSR for the actual data set is +/- 24% for a 95% confidence interval, with CSR being about 79% of NSR.

In addition, a sensitivity analysis was conducted to estimate the magnitude of CSR in relation to NSR that is required to positively distinguish CSR from natural variations in the background effluxes. This was accomplished by uniformly decreasing all individual measurement values for TSR in the 'affected' region in 10% increments, while keeping NSR effluxes in the 'unaffected' region the same. The analysis for lower CSR values indicates that for

sites with similar conditions and efflux variability as those found at the Bemidji site, it should be possible to identify hydrocarbon source zones for CSR rates that are significantly lower than present in the measured data (down to appr. 25% of NSR; column for 30% decrease in TSR, Table S2). Although differences between TSR and NSR are still statistically significant - allowing a delineation of the source zone - the accuracy of the degradation rate estimate decreases substantially for smaller CSR-values (**Table A1.2**).

Continuous chamber measurements

Selected locations were further evaluated using continuous chamber measurements to determine temporal variability of the effluxes over time periods reaching from 2-8 hours. Sites selected for continuous measurements include locations near which the highest soil CO_2 effluxes were noted during survey sampling (next to wells 9017 (**Figure A1.1**) and 601 (**Figures A1.2 and A1.3**)). Continuous measurements were also obtained near well 310 (background, **Figure A1.4**) and wells 534 and 530 (downgradient of source zone, **Figures A1.5 and A1.6** respectively).

In addition, hourly measurements of barometric pressure, precipitation, and air temperature were obtained from the USGS (recorded at background well 310) measured with a Setra CS100 Barometric Pressure Sensor, model 278; Met One 12" AC Heated Rain Gage, model 385; and Campbell Scientific Temperature Sensor, model 107-L, respectively.

Atmospheric pressure, air temperature and precipitation data were analyzed in conjunction with measured CO_2 efflux rates. Only rainfall had a pronounced effect on CO_2 effluxes, as was observed at well 601 in response to an intense precipitation event (see Figure S3). The rainfall event temporarily inhibited surficial CO_2 efflux, consistent with findings of Jassal et al. (2005) and Kabwe et al. (2005), who demonstrated that decreased surficial CO_2 effluxes correlate with increased soil moisture following precipitation events. A significant

correlation between pressure and temperature data and the CO_2 effluxes could not be determined over the measurement intervals (data not shown).

Overall the results from the continuous measurements confirm the observations from the survey measurements and demonstrate that differences in CO_2 effluxes between 'affected' (**Figures A1.1 - A1.3**) and 'unaffected' (**Figures A1.4 - A1.6**) locations are consistent and significant over the time interval of observation.

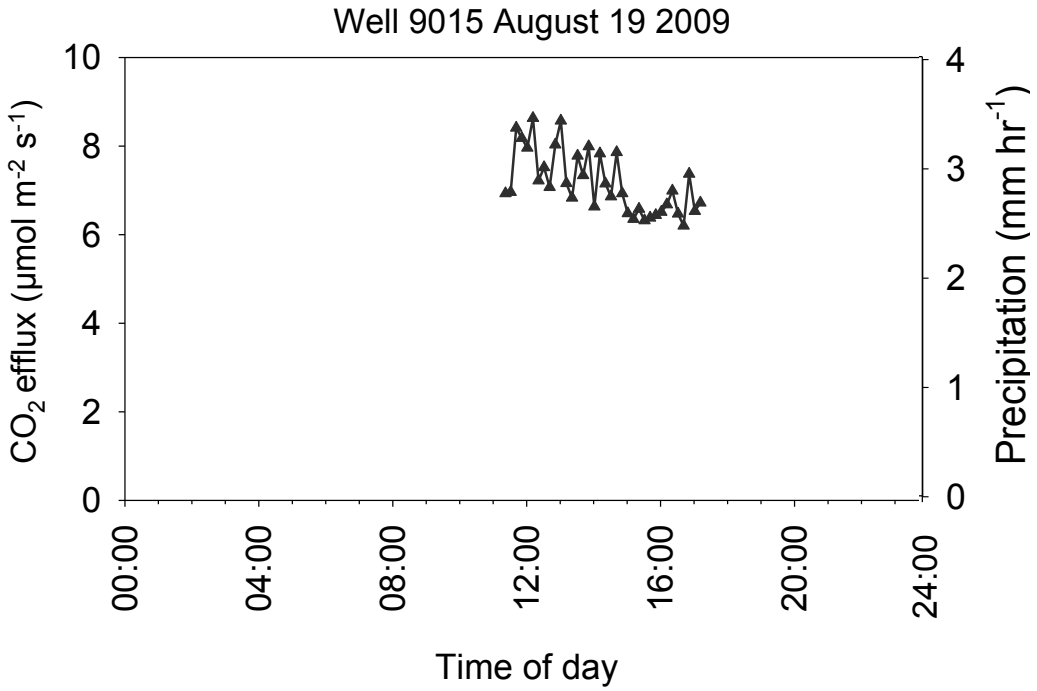

Figure A1.1. Observed CO2 efflux and precipitation near well 9017, August 19, 2009

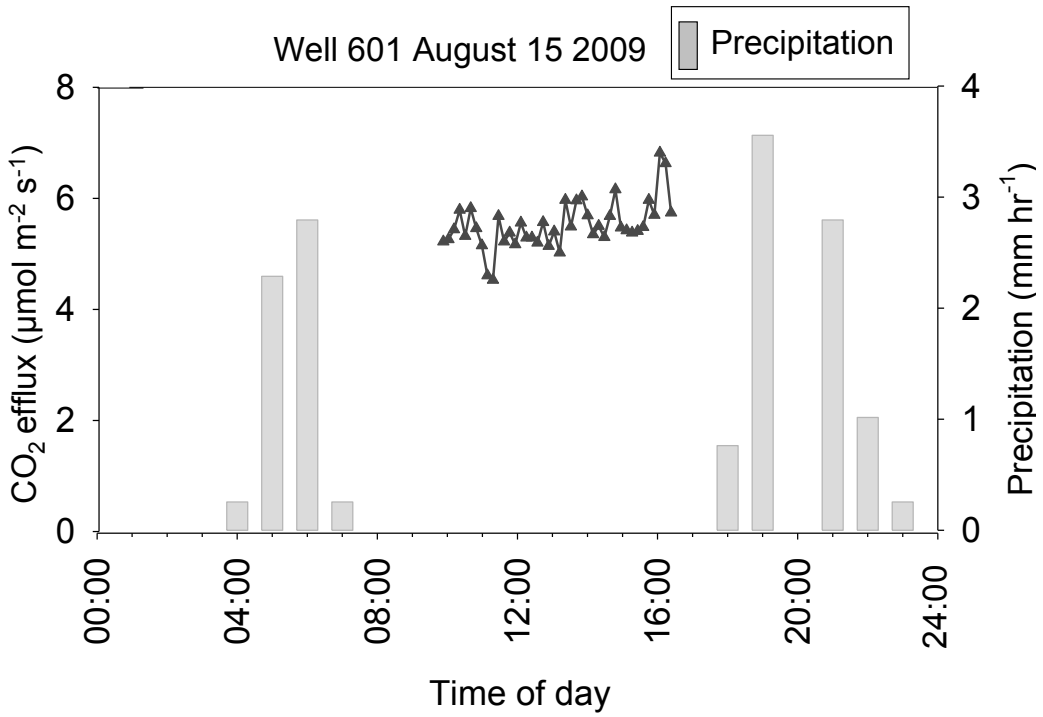

Figure A1.2. Observed CO2 efflux and precipitation near well 601, August 15, 2009

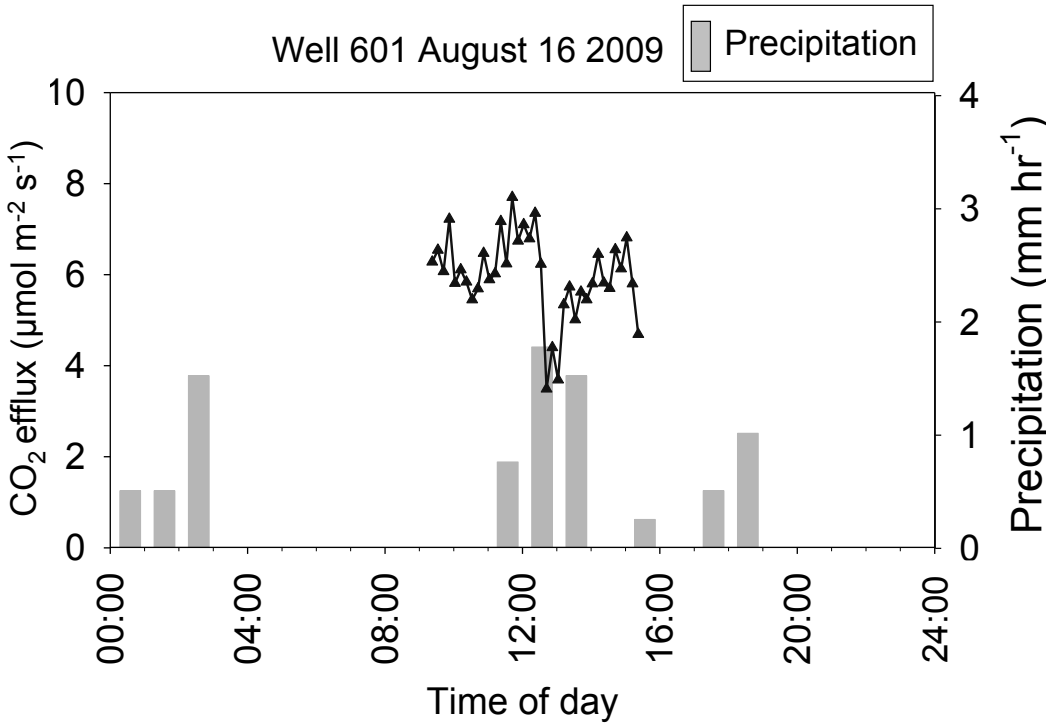

Figure A1.3. Observed CO2 efflux and precipitation near well 601, August 16, 2009

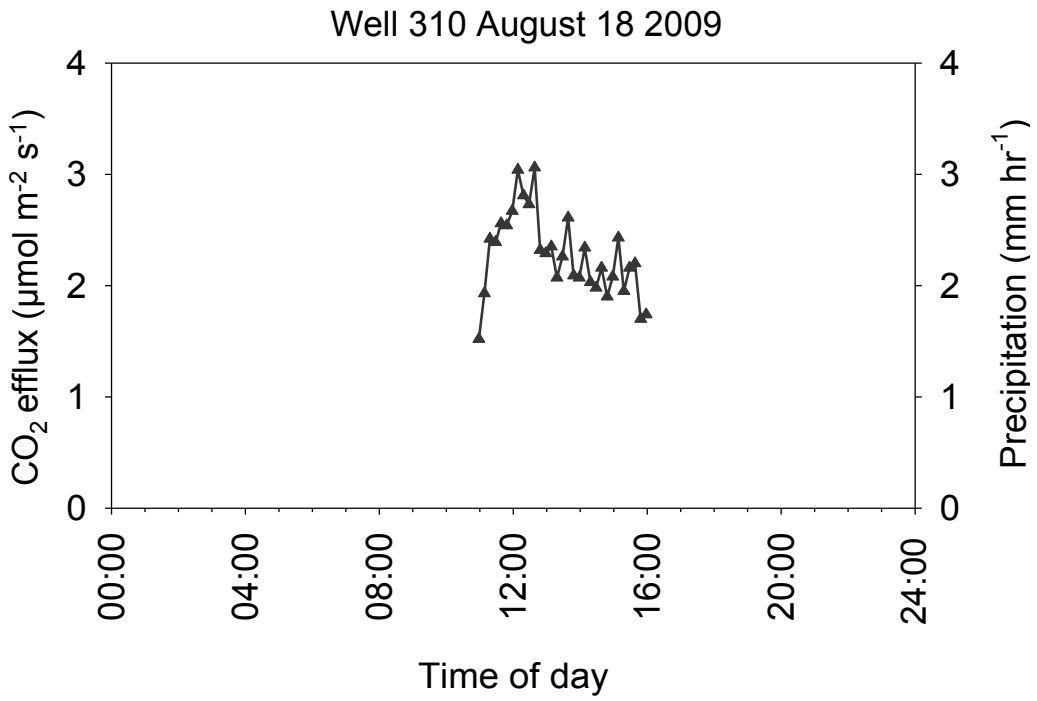

Figure A1.4. Observed CO2 efflux and precipitation near well 310, August 18, 2009

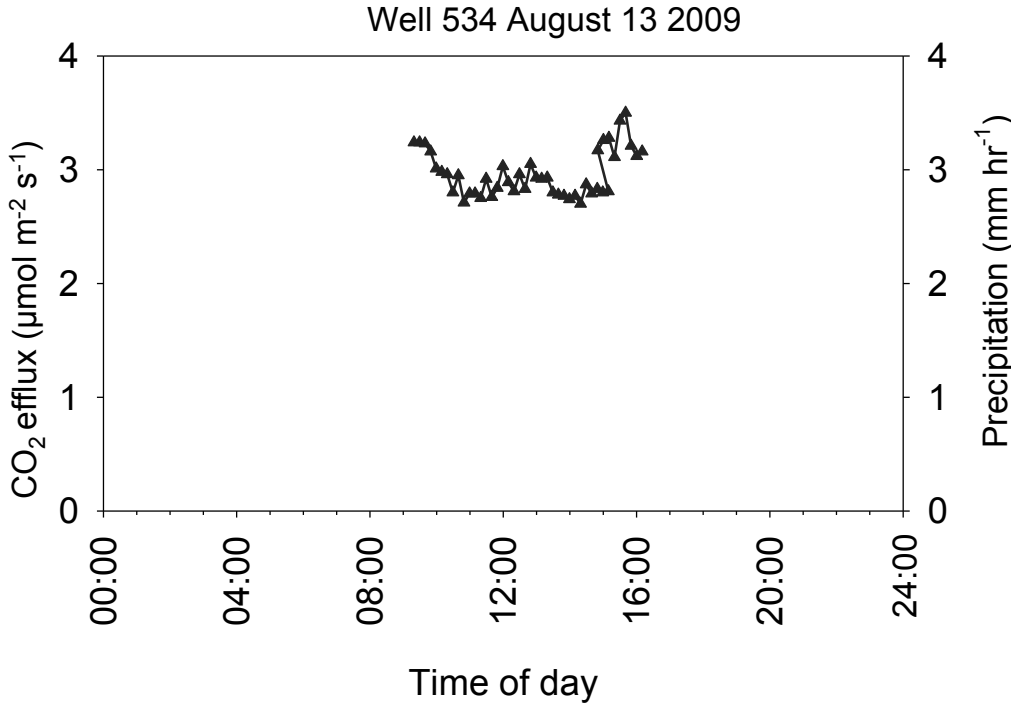

Figure A1.5. Observed CO2 efflux and precipitation near well 534, August 13, 2009

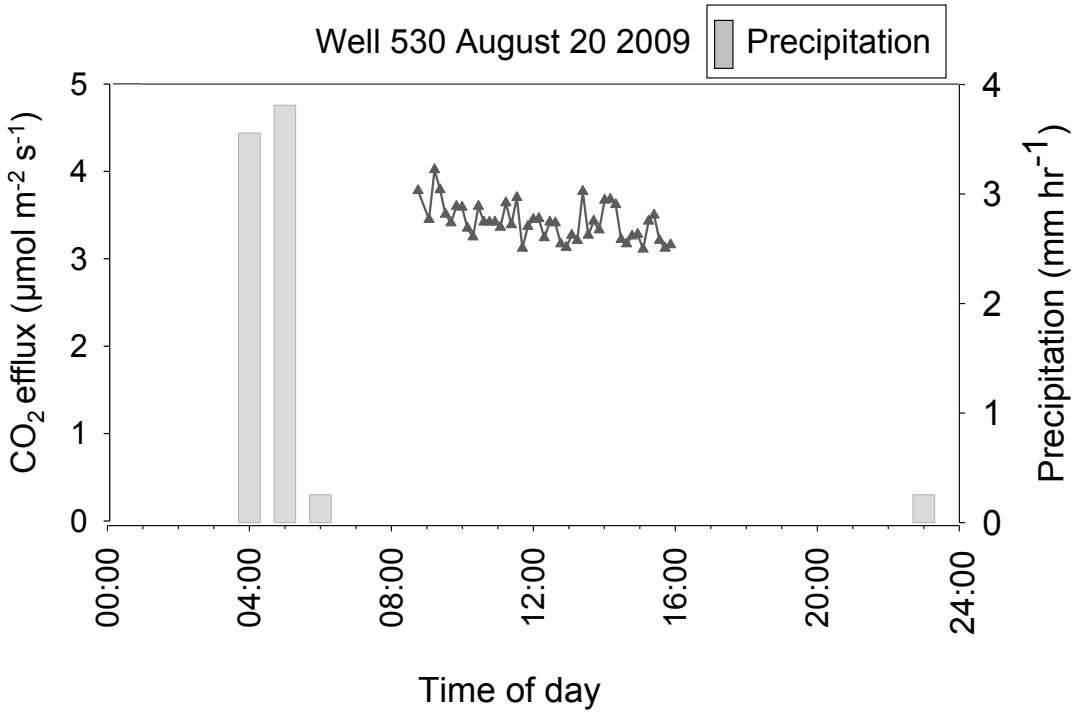

Figure A1.6. Observed CO_2 efflux and precipitation near well 530, August 20, 2009

Table A1.3. Comparison of natural soil respiration (NSR) rates reported in the literature with background CO_2-efflux measurements obtained in present study

Location	Natural soil respiration (NSR) (μmol m^{-2} s^{-1})	Reference
Natural environments		
Pasture	2.7	Bolstad and Vose (2005)
Grassland	2.5 and 2.1	Grahammer et al. (1991)
Grasslands	1.4	McCulley et al. (2004)
Forest, sandy soils	1 – 1.5	Borken et al. (2002)
Natural sites in Minnesota		
Oak-mixed:	2.5	Millington and Quirk, (1961)
Ash-mixed	2.2	
Cypress family, birch and swamp	2.3	
Bemidji site	2.9 - 3.3	Present study

.

Calculations of CO_2 effluxes based on the gradient method

The gradient method was used to calculate CO_2 effluxes due to contaminant-related soil respiration at the Bemidji crude oil spill site. The Millington and Quirk model (Millington and Quirk, 1961) was used to estimate effective diffusion coefficients. Calculations are summarized in Table S4. In order to evaluate the effect of different diffusion models, calculations were also conducted with the model by for undisturbed soils; however, differences between the Millington and Quirk model (Millington and Quirk, 1961) and the model by Moldrup et al. (2000) were minimal for the soil gas saturations under investigation (<8%). To evaluate the effects of parameter uncertainty on the calculation of CO_2 efflux, gas saturations and porosity were varied independently. A 10% decrease in the gas saturation results in approximately a 30% decrease in calculated efflux, while an increase of the same magnitude results in a 37% increase in calculated CO_2-efflux. A 10% variation in porosity results in a 13% change in calculated efflux. These results are expected given that the gas saturation is raised to a higher power (10/3) than the porosity (4/3) in the Millington and Quirk formulation employed in this study.

Table A1.4. CO_2 efflux calculations for wells 301 and 9017 using equations 1 and 2 in associated paper.

Vadose Zone Well	**301**	**9016**		**Comment**
Gas saturation	0.65	0.6	0.8	from Dillard et al. (1997)
Porosity [-]	0.38			from Dillard et al. (1997)
Gas filled porosity [-]	0.25	0.24	0.3	
D_0 [m^2 s^{-1}]	1.64×10^{-5}			from Luo and Zhou (2006)
D_{eff} [m^2 s^{-1}]	1.07×10^{-6}	8.22×10^{-7}	2.15×10^{-6}	based on Millington and Quirk (1961)
CO_2 [%]	3.39	4.21		field measurement
CO_2 fraction	0.03	0.04		
CO_2 [mol L^{-1}]	1.39×10^{-3}	1.72×10^{-3}		based on ideal gas law
CO_2 [mol m^{-3}]	1.39	1.72		
Δz [m]	0.5	1.5		depth below ground surface
Gradient [mol m^{-4}]	2.77	1.15		
Calculated CO_2 efflux [μmol m^{-2} s^{-1}]	**2.98**	**0.94**	**2.46**	

Observed Vadose Zone CH_4 and O_2 Concentrations

In addition to CO_2 (see Figure 3), O_2, CH_4, Ar and N_2 were also analyzed along the North Pool Transect. Figures S7 and S8 depict CH_4 and O_2 data demonstrating that CH_4 oxidation occurs at the Bemidji site. As a result, CH_4 is not reaching the ground surface and carbon efflux to the atmosphere is dominated by CO_2 efflux.

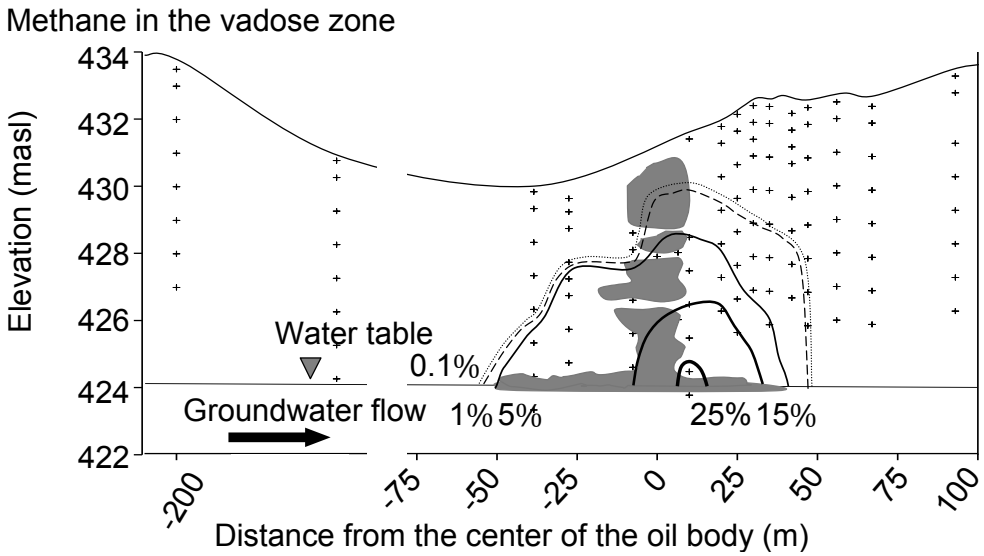

Figure A1.7. Observed vadose zone CH_4 concentration contours along the North Pool Transect.

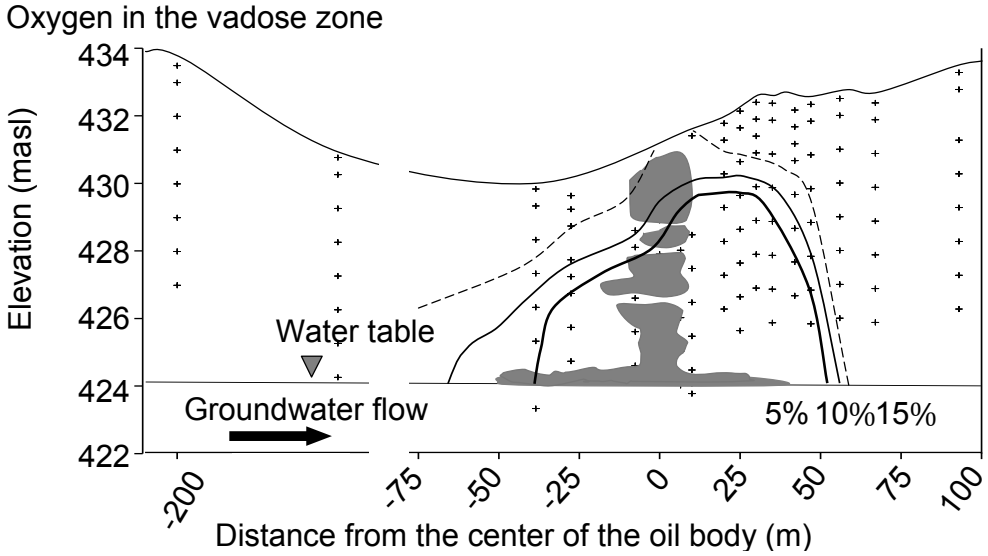

Figure A1.8. Observed vadose zone O2-concentration contours along the North Pool Transect.

Appendix 2: Supporting information for chapter 3

Table A2.1. Definition of abbreviations and acronyms.

Acronym	Definition
BGC	Background correction
CSR	Contaminant-related soil respiration. Defined here as contaminant mineralization (Sihota et al., 2011)
F_{CSR}	Fraction of CSR
F_{NSR}	Fraction of NSR
J_{CSR}^{CGM}	CSR flux calculated using concentration gradient method and Fick's law
J_{CSR}^{BGC}	CSR flux calculated using the background correction approach (Sihota et al., 2011)
J_{CSR}^{14C}	CSR flux calculated using the 14C content measured in soil CO_2
LNAPL	light non-aqueous phase liquids
mbgs	Meters below ground surface
NA	Natural attenuation
NSR	Natural soil respiration. Defined as the CO_2 generated from plant roots and microbes present in the surficial soil zone (Sihota et al., 2011).
PHC	Petroleum hydrocarbon compounds
pMC	Percent modern carbon
Sg	Soil gas saturation
SZNA	Source zone natural attenuation, i.e. attenuation processes taking place in regions of the vadose zone and capillary fringe that contain LNAPL

Stable isotopic analysis

To obtain the appropriate sample mass for analysis on the Thermo Finnigan DeltaPlusXL, samples were extracted from 100 cc glass vials using either a 500 µL or 1mL gas tight syringe (Hamilton) depending on the CO_2 partial pressure in the vial. The sample was then injected to a helium flushed exotainer. Analysis was performed on the gas bench using a Thermo Finnigan DeltaPlusXL equipped with an auto sampler and operating in continuous flow. Following Coplen (1994) the instrument was calibrated using carbonate standards acidified with 99% purity H_2PO_4 in helium-flushed exotainers, with headspace gas measured in a helium flow. Analyses were corrected for fractionation using repeat analyses of UBC internal carbonate standards BN 13, BN 83-2, H6M, which have been calibrated against NBS international standards NBS 18 & 19. Results for $\delta^{13}C_{VPDB}$ is corrected to VPBD (1.1237 X 10^{-2} (Kendall and Caldwell, 1998)) based on an average of multiple analyses of internal NBS standards18 & 19.

Radioisotopic analysis

CO_2 for radioisotope (^{14}C) analysis was isolated to flame-sealed glass ampoules from the 100 cc glass sample vial using a custom built vacuum line. Ampoules were fashioned in the lab at UBC and baked at 525º C for 1.5 hours to remove any traces of organic material. To transfer the sample, the tip of a 20 gauge needle connected to the vacuum line was inserted into the silicon-covered butyl septa; a vacuum of 10^{-3} mbar was then generated in the line. Sample gas was introduced to the line by sealing a portion of the line under vacuum and passing the needle through the silicon-covered butyl stopper. CO_2 was isolated by passing the gas first over an ethanol-dry ice slush (to remove water vapour) and then concentrating the CO_2 in a glass ampoule using a liquid nitrogen cold finger. After samples had been frozen for five minutes the line was again opened to vacuum to pump off other gasses. Glass ampoules were then sealed under vacuum using a butane torch.

Analyses were completed by accelerated mass spectrometry at the National Ocean Sciences Accelerator Mass Spectrometry Facility (NOSAMS) at Woods Hole Oceanographic Institution (WHOI) or the Australian National University in Canberra.

Table A2.2 Diffusion Coefficients Used in Reactive Transport Modeling at Well 9017.

Binary Gas Pair	**Diffusion Coefficient**
	[m^2s^{-1}] x 10^{-5}
O_2-$^{12}CH_4$	2.263
O_2-$^{13}CH_4$	2.219
O_2-$^{12}C^{16}O_2$	1.635
O_2-$^{13}C^{16}O_2$	1.628
O_2-$^{14}C^{16}O_2$	1.622
O_2-Ar	1.928
O_2-N_2	2.083
$^{12}CH_4$-$^{13}CH_4$	1.680
$^{12}CH_4$-$^{12}C^{16}O_2$	1.701
$^{12}CH_4$-$^{13}C^{16}O_2$	1.683
$^{12}CH_4$-$^{14}C^{16}O_2$	1.705
$^{12}CH_4$-Ar	1.705
$^{12}CH_4$-N_2	1.705
$^{13}CH_4$-$^{12}C^{16}O_2$	1.667
$^{13}CH_4$-$^{13}C^{16}O_2$	1.700
$^{13}CH_4$-$^{14}C^{16}O_2$	1.696
$^{13}CH_4$-Ar	1.669
$^{13}CH_4$-N_2	1.673

Binary Gas Pair	Diffusion Coefficient
$^{12}C^{16}O_2$-$^{13}C^{16}O_2$	1.696
$^{12}C^{16}O_2$-$^{14}C^{16}O_2$	1.688
$^{12}C^{16}O_2$-Ar	1.705
$^{12}C^{16}O_2$-N_2	1.705
$^{13}C^{16}O_2$-$^{14}C^{16}O_2$	1.705
$^{13}C^{16}O_2$-Ar	1.688
$^{13}C^{16}O_2$-N_2	1.697
$^{14}C^{16}O_2$-Ar	1.699
$^{14}C^{16}O_2$-N_2	1.690
Ar-N_2	1.954
O_2	2.040
$^{12}CH_4$	1.090
$^{13}CH_4$	1.864
$^{12}C^{16}O_2$	1.090
$^{13}C^{16}O_2$	1.907
$^{14}C^{16}O_2$	1.914
Ar	2.220
N_2	1.750

Atomic masses were defined following Berglund and Wieser (2011).

Table 3.3. Reference gas viscosities used in reactive transport modeling at well 9017.

Species	Viscosity, η^o [Pa s] x 10^{-5}
O_2	1.33
$^{12}CH_4$	1.04
$^{13}CH_4$	1.08
$^{12}C^{16}O_2$	1.49
$^{13}C^{16}O_2$	1.51
$^{14}C^{16}O_2$	1.53
Ar	2.18
N_2	1.70

Atomic masses were defined following Berglund and Wieser (2011).

Appendix 3: Supporting information for chapter 4

Table A3.1. Cross-reference names between sites in this paper and sites found on the Bemidji Site website (http://mn.water.usgs.gov/projects/bemidji/p/list.html) and x- and y- coordinates in UTMa, land surface elevationb, and water table elevationb for each site.

Name in paper	Bemidji Site Name	X-Coordinate UTM, m	Y-Coordinate UTM, m	Land Surface Elevation, m	Water Table Elevation, m[c]
Site 1a	WT0901	342606.36	5270950.65	433.328	424.66
Site 1b	WT1001	342699.55	5271080.63	431.762	424.26
Site 2	WT1002	342745.02	5271050.30	430.339	424.26
Site 3	WT1003	342753.52	5271042.74	430.146	424.26
Site 4	WT1101 WT1004	342761.56	5271034.77	430.027	424.26
Site 5	WT0903	342811.76	5271048.85	432.963	424.14

[a] NAD83 UTM Zone 15N
[b] NAVD88
[c] June, 2011

Table A3.2. Elevations and microbial concentrations of samples taken from each site.

		Microbial concentration, copies/g				
	Elevation, m	Methano-trophs	Ammonia oxidizers	Iron reducers	Sulfate reducers	Methano-gens
Site 1b	429.927	*BD*	*BD*	*BD*	*BD*	*BD*
	427.997	*BD*	*BD*	1.24E+03	*BD*	*BD*
	426.123	*BD*	*BD*	2.78E+03	*BD*	*BD*
	424.283	*BD*	*BD*	5.86E+03	*BD*	*BD*
	424.083	*BD*	*BD*	1.12E+03	*BD*	*BD*
Site 2	428.337	*BD*	*BD*	4.10E+03	*BD*	*BD*
	427.118	1.55E+06	9.93E+02	7.30E+06	6.29E+04	2.33E+05
	425.949	3.51E+04	*BD*	3.61E+04	8.33E+02	2.62E+05
	424.680	3.74E+04	*BD*	2.42E+06	2.36E+04	5.06E+05
	423.930	2.85E+04	*BD*	1.27E+05	1.83E+03	1.36E+06
Site 3	428.297	*BD*	9.86E+02	4.55E+06	3.59E+06	*BD*
	426.730	9.16E+06	1.83E+04	2.64E+07	4.67E+06	2.07E+06
	425.909	6.76E+05	5.45E+02	8.78E+05	5.13E+04	1.90E+07
	424.640	4.51E+04	5.52E+01	5.52E+05	1.47E+04	4.02E+05
	423.940	1.36E+06	2.74E+02	4.52E+06	1.22E+05	3.22E+07
Site 4	428.369	2.37E+03	*BD*	3.98E+06	1.99E+07	*BD*
	427.860	2.61E+03	*BD*	1.85E+07	1.65E+04	*BD*
	427.685	1.15E+06	1.10E+03	1.61E+07	8.57E+04	4.28E+04
	425.992	2.76E+03	*BD*	1.22E+06	6.33E+03	4.07E+06
	424.603	2.46E+04	*BD*	7.47E+05	1.18E+04	1.98E+06
	423.803	3.12E+04	*BD*	2.40E+05	6.76E+03	3.49E+06
Site 5	423.712	1.95E+03	2.06E+02	3.69E+04	1.95E+03	1.23E+05
	424.417	4.34E+02	*BD*	8.39E+04	3.21E+03	1.74E+05

BD indicates values below detection limits.

Appendix 4: Supporting information for chapter 5

Table A4.1. Seasonality in the extent of SZNA processes. *normalized to the extent of the oil body (2,790 m2)

Sampling date	**Total Flux** [μmol m^{-2} s^{-1}]	**Avg. flux** [μmol m^{-2} s^{-1}]	**Apparent extent of affected area** [% of oil body]	**SZNA rate*** [μmol s^{-1}]
2011-06-16	7018.5	2.4	104.8	2.5
2011-10-27	1919.3	1.6	44.0	0.7
2011-11-21	1853.0	1.6	41.3	0.7
2011-12-20	1974.7	1.5	46.6	0.7
2012-05-14	2253.4	1.5	53.7	0.8

Table A4.2. Summary of soil parameters used in model simulation.

Parameter	**Background aquifer**	**Low K layer**	**Ice layer**	**Units**	**Reference**
Hydraulic conductivity	5.0×10^{-5}	5.0×10^{-9}	1.3×10^{-9}	[m s^{-1}]	Molins and Mayer (2007)
Van Genuchten Parameters alpha n exponent	 9.34 2.5 1	 9.34 2.5 0.5	 9.34 2.5 0.5	 [m^{-1}] [-] [-]	Dillard et al. (1997)
Residual Saturation	0.05	0.30	0.30	[m^3 H_2O m^{-3} void]	Dillard et al. (1997)
Porosity	0.38	0.38	0.1	[m^3 void m^{-3} porous medium]	Dillard et al. (1997)
Dispersivity	0.1	0.1	0.1	[m]	Molins and Mayer (2007)

Table A4.3. Reaction stoichiometries and rate constants used in model simulation. K_i^I: inhibition constant for species i; K_i^S: half-saturation constant; for species i; k_i: rate constant for species i. Reaction parameters' were selected based on Molins et al. (2010) and Sihota and Mayer (2012). All additional parameters are provided in (Sihota and Mayer, 2012).

Process	**Stoichiometry** **Rate Expression (R)**	**Rate, Monod, and Inhibition Constants**	**Units**
Soil respiration **(NSR)**	$CH_2O + O_2 \rightarrow CO_2 + H_2O$ $R = -k_{CH_2O}$	*Scenario 1:* Fast Carbon: k_{CH2O} = 6.9 x 10^{-9} Slow Carbon: k_{CH2O} = 2.6 x 10^{-9}	[mol $dm^{-3}s^{-1}$] [mol dm^{-3}-s^{-1}]
Aerobic oxidation **(CSR)**	$C_7H_{16} + 11O_2 \rightarrow 7CO_2 + 8H_2O \;\; R = -k_{C_7H_{16},ae}\left(\frac{C_{O_2}}{K^S_{O_2} + C_{O_2}}\right)$	*Scenario 1:* $k_{C7H16,\,ae}$ = 1.9 x 10^{-10} *Scenarios 2-3:* $k_{C7H16,\,ae}$ = 1.4 x 10^{-10} K^S_{O2} = 1.0 x 10^{-5}	[mol dm^{-3} s^{-1}] [mol dm^{-3} s^{-1}] [mol L-H_2O^{-1}]
Methane oxidation **(CSR)**	$CH_4 + 1.515O_2 \rightarrow 0.515CO_2 + 1.515H_2O + 0.485CH_2O(biomass)$ $R = -k_{CH_4}\left(\frac{C_{CH_4}}{K^S_{CH_4} + C_{CH_4}}\right)\left(\frac{C_{O_2}}{K^S_{O_2} + C_{O_2}}\right)$	*Scenario 1:* k_{CH4} = 9.8 x 10^{-7} *Scenario 1:* k_{CH4} = 4.9 x 10^{-7} K^S_{12CH4} = 1.0 x 10^{-5} K^S_{13CH4} = 8.1 x 10^{-8} K^S_{O2} = 3.1 x 10^{-6}	[mol L-H_2O^{-1} s^{-1}] [mol L-H_2O^{-1} s^{-1}] [mol L-H_2O^{-1}] [mol L-H_2O^{-1}] [mol L-H_2O^{-1}]
Anaerobic oxidation **(CSR)**	$C_7H_{16} + 3H_2O \rightarrow 1.5CO_2 + 5.5CH_4 \;\; R = k_{C_7H_{16},an}\left(\frac{K^I_{O_2}}{K^I_{O_2} + C_{O_2}}\right)$	*Scenario 1:* $k_{C7H16,\,an}$ = 1.7 x 10^{-10} *Scenarios 2-3:* $k_{C7H16,\,an}$ = 1.3 x 10^{-10} K^I_{O2}=1.0 x 10^{-6}	[mol dm^{-3} s^{-1}] [mol dm^{-3} s^{-1}] [mol L-H_2O^{-1}]

Appendix 5: Supporting information for chapter 6

Description of statistical analyses

Statistical analyses of site metadata was conducted using R statistical software (R core team 2013). To evaluate the appropriate statistical tests to conduct, site metadata were first visually assessed for normality (through inspection of histograms), and then tested using the Shapiro-Wilk normality test. Results showed data to deviate from a normal distribution; data transformations did not result in normal distributions. Consequently, to examine the relationships between the metadata, surficial CO_2 fluxes, and SZNA rate estimates, Spearman's Sign Rank correlations (which provides a measure of the relationship strength between two variables' by assessing how well an arbitrary monotonic function can describe the relationship without assumptions about the frequency distribution of either variable (Hauke and Kossowski, 2011)) were used.

Table A5.1. Results of CO_2 flux measurements and calculated SZNA rates (μmol m^{-2} s^{-1}). P values are provided in brackets. *

Dataset	**HR-BGC**		**MR-RCC**		
Correction method	**Total**	**SZNA (BGC)**	**Total**	**SZNA (RCC)**	**SZNA (BGC)**
Source Zone Thickness	0.6* (<0.0001)	0.5* (<0.0001)	0.6* (0.0003)	0.5* (0.05)	0.3 (0.1)
Source Zone above water table	0.4* (0.0001)	0.4* (0.002)	0.6* (0.0007)	0.4 (0.1)	0.4 (0.06)
LNAPL Persistence	0.5* (<0.0001)	0.3* (0.03)	0.5* (0.008)	0.6* (0.02)	0.4 (0.05)
Toluene Mole Fraction	0.6* (<0.0001)	0.5* (<0.0001)	0.6* (0.0003)	0.5 (0.1)	0.4 (0.06)
Naphthalene Mole Fraction	0.6* (<0.0001)	0.6* (<0.0001)	0.6* (0.0008)	0.3 (0.3)	0.3 (0.28)
Benzene Mole Fraction	0.5* (<0.0001)	0.4* (0.0004)	0.6* (0.0002)	0.6* (0.02)	0.4 (0.06)
LIF Intensity	0.5* (<0.0001)	0.2 (0.2)	0.5* (0.006)	0.1 (0.78)	0.2 (0.3)

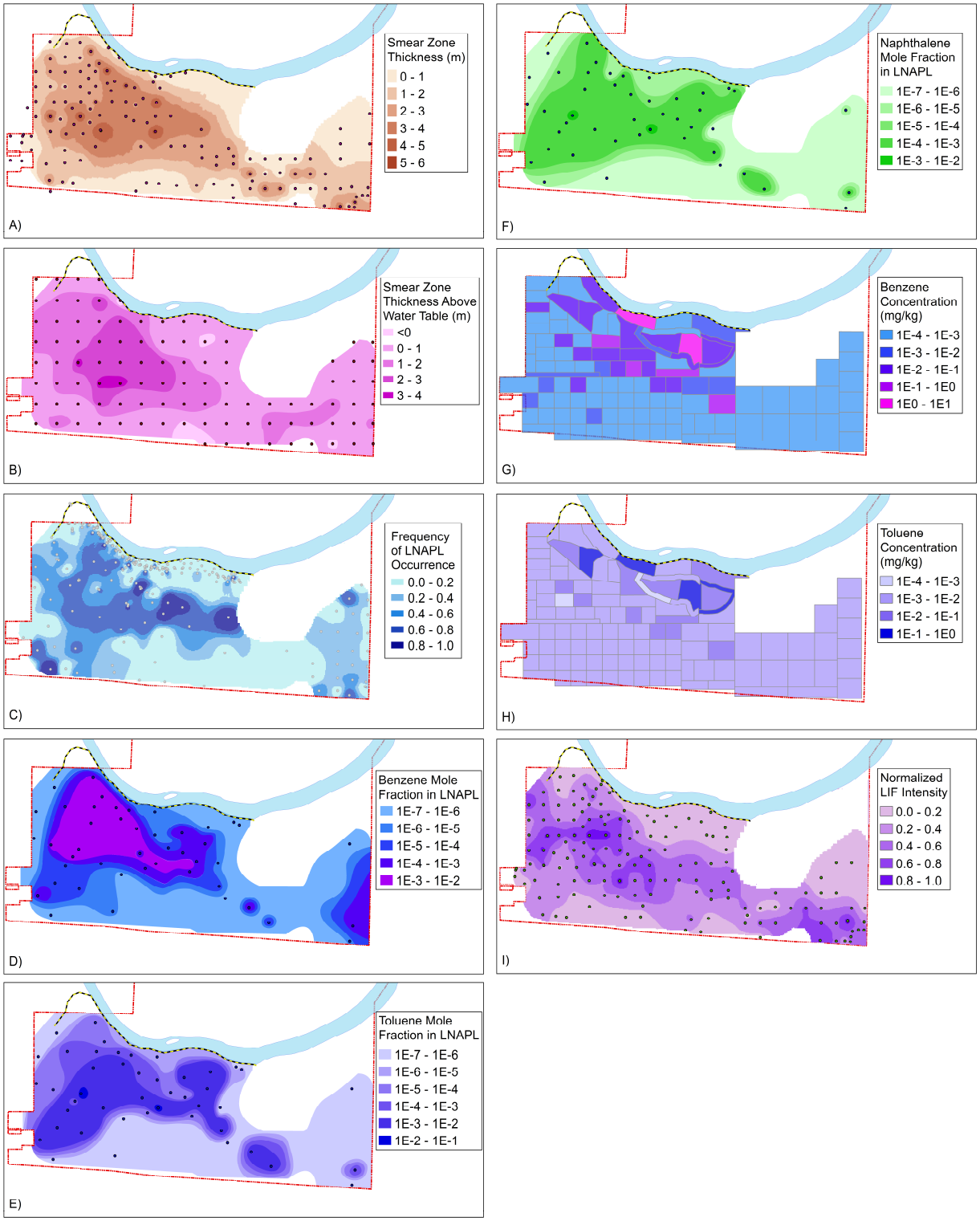

Figure A5.1. Distribution of parameter values used in correlation analyses.

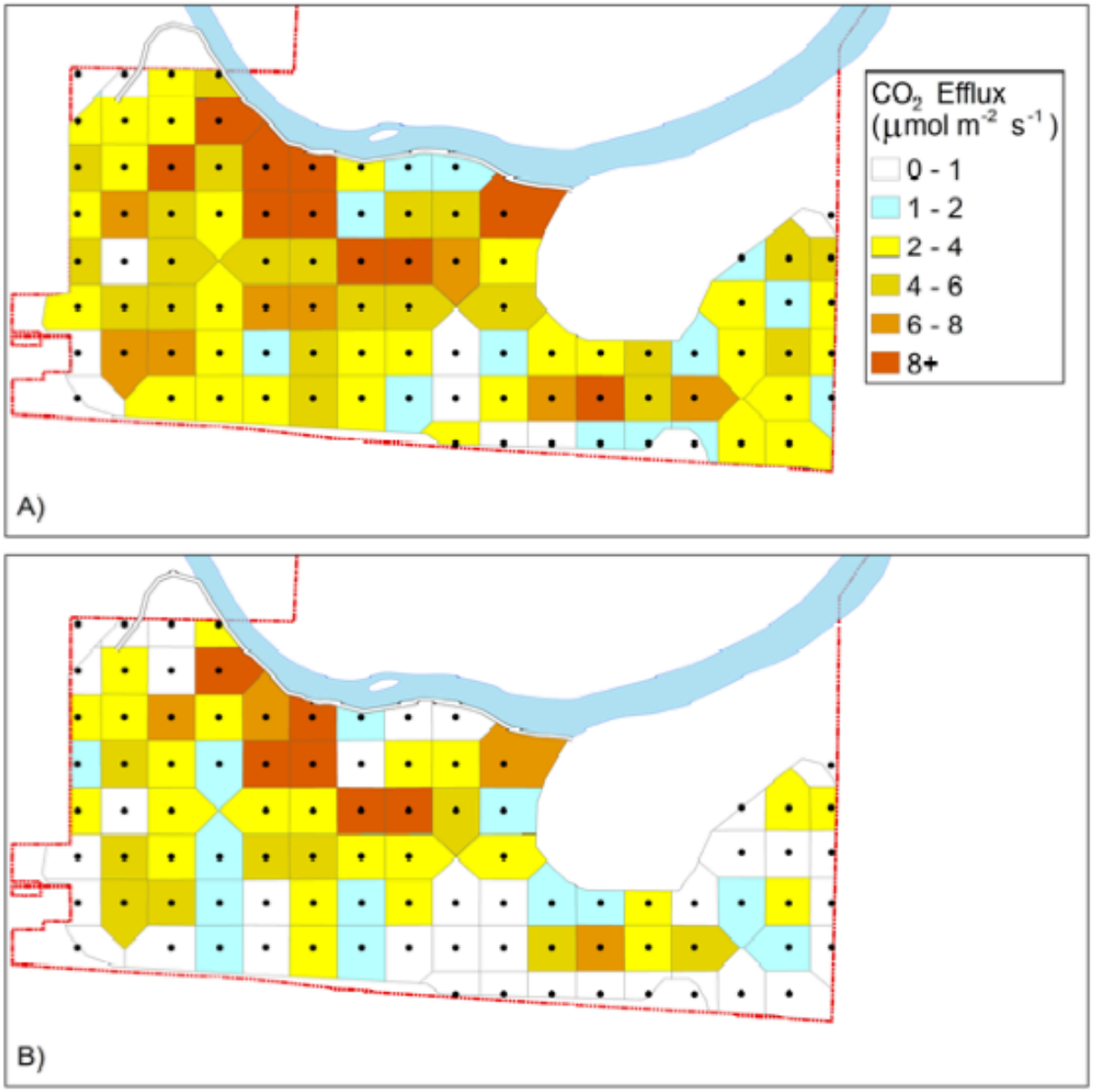

Figure A5.2. Areas used in point-based SZNA mass loss calculations for the HR-BGC dataset (BGC method). Panels A and B show gridded areas for the complete and BGC data, respectively.

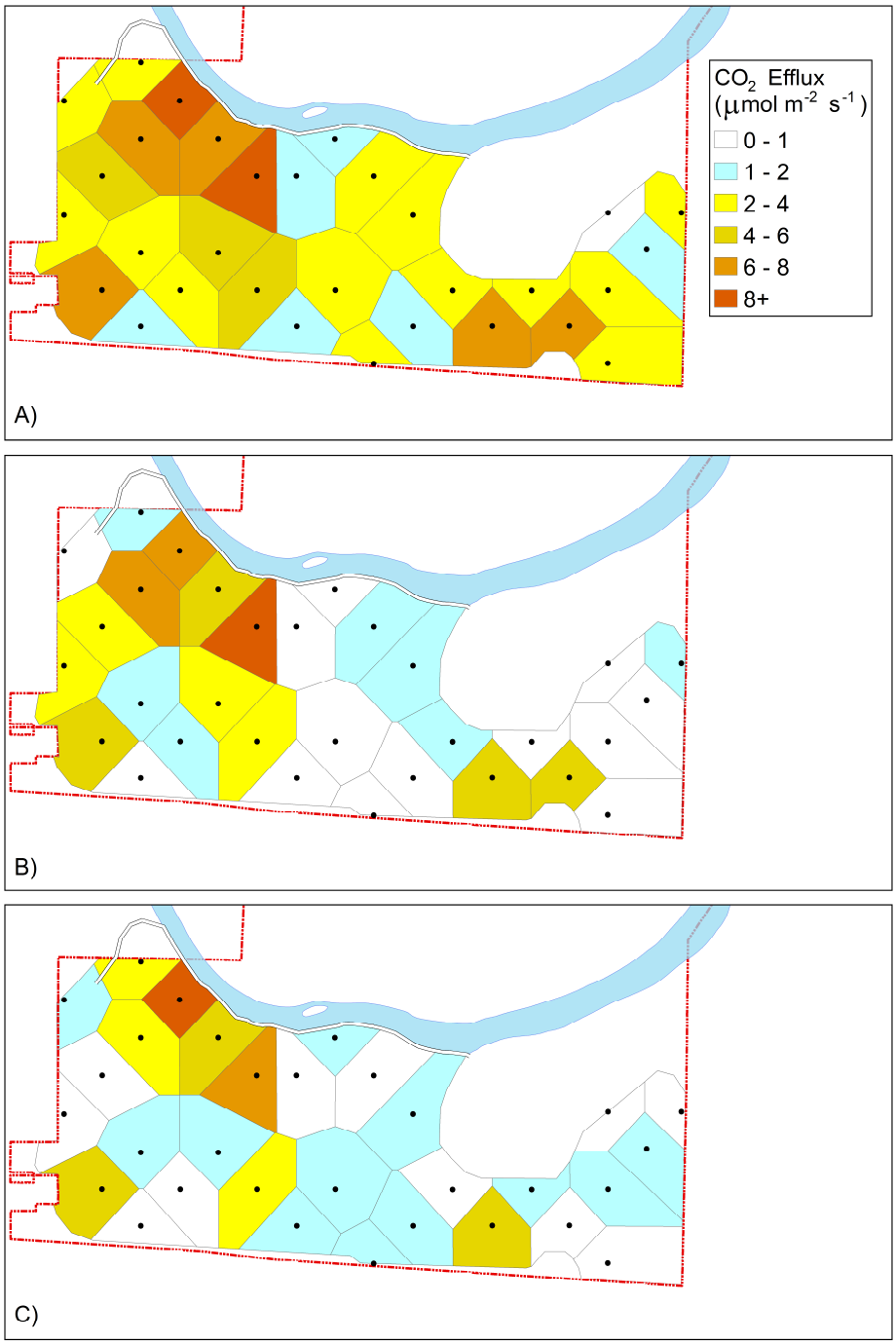

Figure A5.3. Areas used in point-based SZNA mass loss calculations for the MR-RCC dataset. Panels A, B and C show gridded areas for the complete, BGC, and RCC data, respectively.

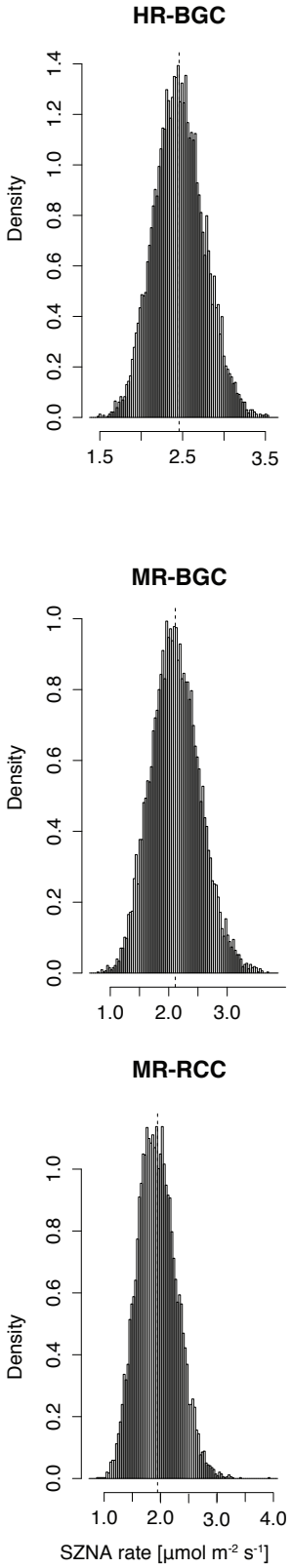

Figure A5.4. Probability density of average SZNA rate over 10,000 iterations for the HR-BGC, MR-BGC, and MR-RCC.

Appendix 6: Supporting information for chapter 7

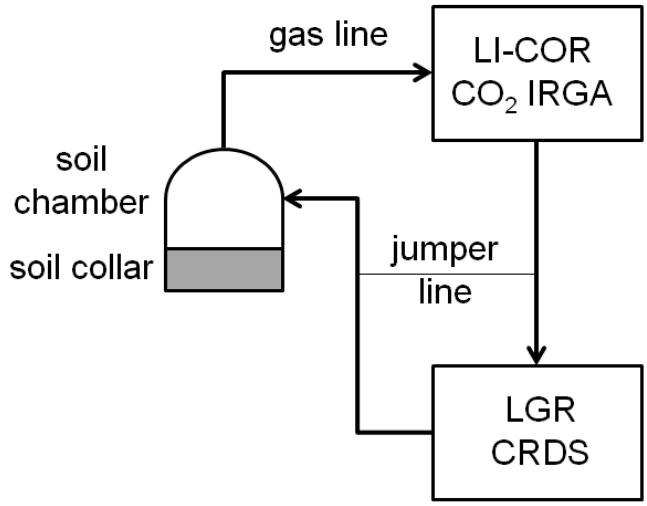

Figure A6.1. Conceptual diagram of instrumentation used for real time measurement of CO_2 and CH_4 effluxes.

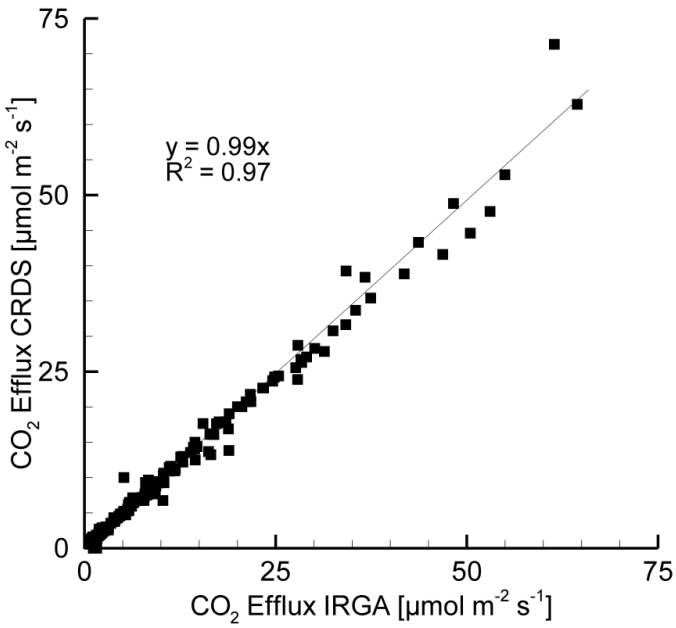

Figure A6.2. Comparison of CO_2 effluxes calculated using the IRGA and CRDS instruments under laboratory conditions.

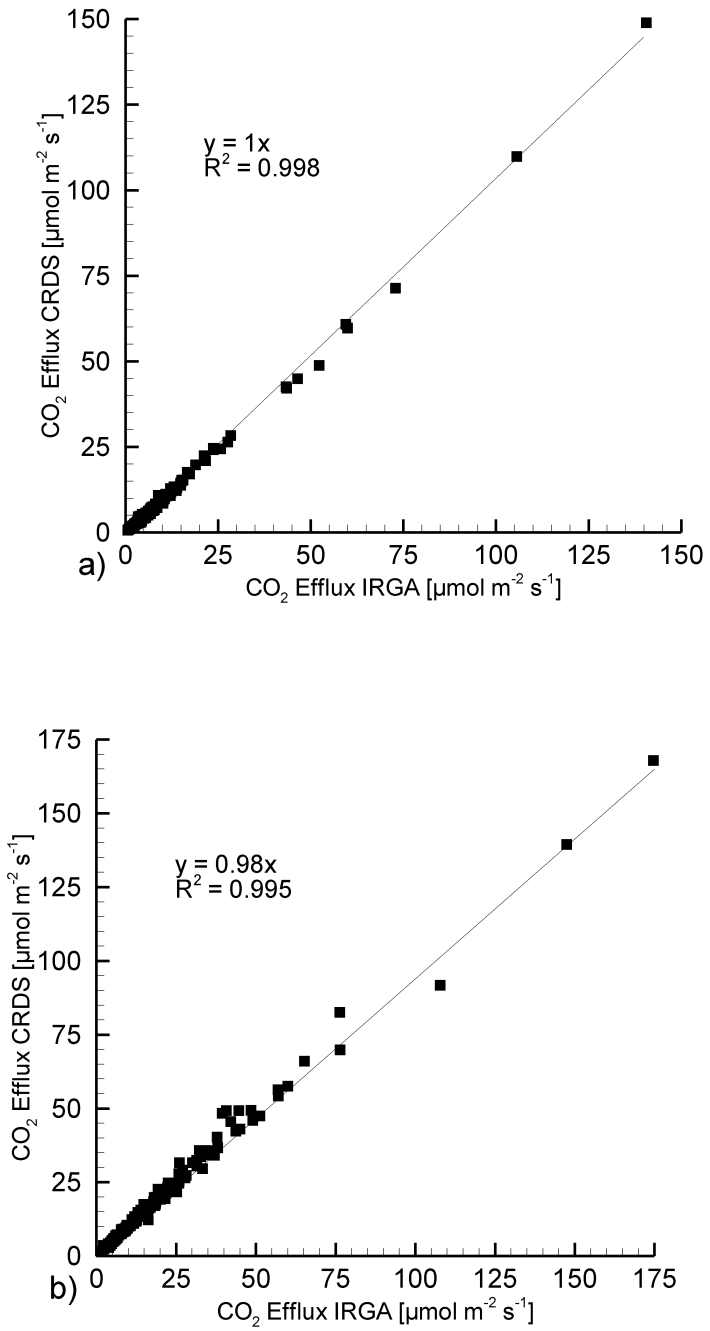

Figure A6.3. Comparison of CO_2 effluxes calculated for the IRGA and CRDS instruments under field conditions. a) Balaton site. b) Cambria site.

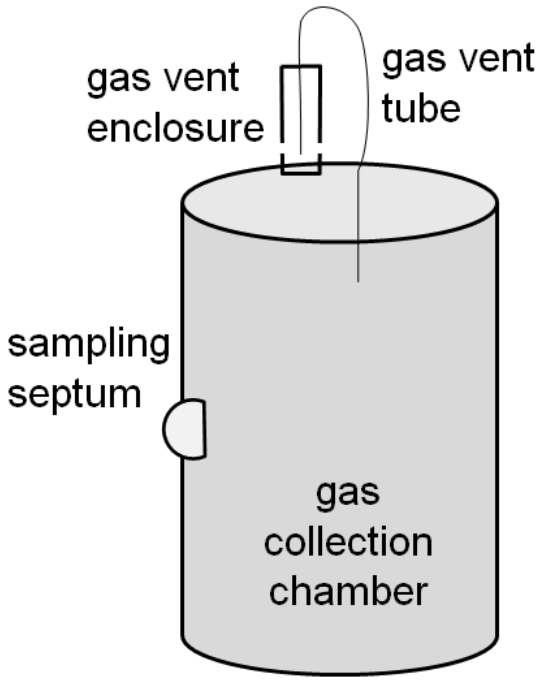

Figure A6.4. Conceptual diagram of custom-designed gas collection chamber, used to evaluate the potential for accumulation of CH_4 and CO_2 in confined spaces.

Appendix 7: Supporting information for chapter 8

Supplementary Results

Field site description: Following removal of ponded product (no soil excavation occurred), ~ 4.9 x 10^4 L of DFE remained, with the majority pooling in a local depression to the west of the rail line (**Figure A7.1**). Ethanol concentrations in groundwater at the SS have remained elevated since the spill occurred, with acetate formation measured within ~ 6 months of release, and dissolved CH_4 measured within ~ 1 year (Spalding et al., 2011). Soils surrounding the SS are comprised of silty sand and loam. Following spring rainfall, ponded conditions occur. During drier periods, the water table is ~ 1 m below ground surface (bgs). These seasonal changes have the potential to change soil redox conditions with resulting feedback on microbial mediated DFE transformation processes.

Community diversity and composition: Differences in microbial community structure among and between RS and SS samples were determined by calculating alpha and beta diversity using rRNA sequences from the SS and rDNA sequences obtained from both RS and SS. *Alpha* diversity was relatively consistent between the RS and SS (Table A7.1), while beta diversity was lower in the RS (Table A7.1). Within the SS, alpha diversity decreased in the rRNA dataset suggesting a change in the active community associated with EtOH exposure. To further evaluate within-site differences in RS and SS, samples *collected from discrete depths at each site* were grouped using Wards agglomerative hierarchical clustering algorithm. At the RS, the topsoil group manifested ~40 % greater alpha diversity than the subsurface group, consistent with typical soil profiles (Urich et al., 2008) (Table A7.1, Figure A7.1). Within the SS, alpha diversity in the rRNA dataset decreased compared to the rDNA dataset for the VZ (17%) and SZ (39%), but increased for the CZ (61%), consistent with rarefaction curves (**Figure A7.1**).

Co-variation in rDNA and rRNA diversity was evaluated through comparison of diversity between discrete samples at the SS. Results show diversity in the rRNA and rDNA datasets correlated well, aside from the 60 cm sample (peak EtOH depth). If the sample at 60 cm is excluded, the correlation between the DNA and rRNA datasets is relatively strong ($r^2 = 0.8$, $p < 0.01$). Deviations from the mean rho were apparent in the samples collected from the 30, 60 and 70 cm depths (with tau values of 0.16, 0.16, and 0.22, respectively). To evaluate differences in community composition between RS and SS samples and activity within SS samples, taxonomic distribution and abundance within the rDNA and rRNA datasets were examined (**Figure A7.4**) and dominant taxa were identified as those representing ≥ 10% of the total community within the VZ, CZ, or SZ.

Community composition and trait-based mapping of active taxonomic groups: To better resolve the differential contributions of rare, intermediate and abundant taxa to community structure and function within the SS we initially compared microbial groups representing > 0.5% of the community in any given sample at the rDNA and rRNA datasets, respectively *(*Figure 8.*3,* Figure A7.*3)***.** The rDNA dataset was dominated by OTUs affiliated with Actinobacteria, Acidobacteria and Chloroflexi in the VZ, Clostridia, Bacilli and Methanobacteria in the CZ, and Methanobacteria and Clostridia in the SZ, suggesting a transition from aerobic to anaerobic metabolism in the soil profile. Within the rRNA dataset, the active community was dominated by OTUs affiliated with Alpha- and Deltaproteobacteria in the VZ, Methanomicrobia, Methanobacteria, and Bacilli in the CZ, and Deltaproteobacteria, Methanobacteria and Bacteriodetes in the SZ, consistent with observed redox transitions.

Network analyses: Networks were constructed using the following criteria: OTU correlation strengths r^2 >0.8, P > 0.8 and presence of the OTU in at least 3 samples. The rDNA network at the RS contained 2,093 nodes and 58,625 edges, an average degree of 28, an average path length of 6.9, an average clustering coefficient of 0.86 and a modularity of 0.8 (132 modules). The rDNA network at the SS contained 3,167 nodes and 4,845 edges, had an average degree of 74.3, an average path length of 5.2, an average clustering coefficient of 0.67 and a modularity of 0.6 (99 modules). The rRNA network at the SS contained 1,659 nodes and 4,846 edges, had an average degree of 30.95, an average path length of 8.3, an average clustering coefficient of 0.64 and a modularity of 0.7 (151 modules). The rRNA:rDNA network contained 1,698 nodes and 44,690 edges, had an average degree of 26.3, an average path length of 3.3, an average clustering coefficient of 0.89, and a modularity of 0.9 (150 modules). A more detailed description of the properties of each network is provided in **Table A7.2**; results of modularity analyses conduced on the rRNA:rDNA network are provided in **Table A7.4.**

Table A7.1. Depth distribution of Fisher diversity at the background and source zone locations.

Location	Index	Depth [cm bgs]	RS-rDNA	SS-rDNA	SS-rRNA
among sites	Simpson	-	0.98	0.97	0.97
	Fisher	-	291	749	1028
between samples	Fisher	10	1035	2834	1905
		20	-	1603	2039
		30	1438	2521	2091
		40	1258	1601	1028
		50	656	576	251
		60	291	792	2444
		70	457	673	581
		80	507	811	411
		90	-	749	508
		100	444	883	570
		110	-	374	-

Table A7.2. Metabolism represented in the intermediate and abundant community members at the SS using (16S rDNA frequency) : (16S DNA frequency), as represented in Figure 8.3.

Taxa	**Metabolism**	**Reference**
Burkholderiales	aromatic catabolism	(Pérez-Pantoja et al., 2012)
Bacillales	facilitative aerobes	(Chang et al., 2008b)
Rhizobiales	CH_4 oxidation	(Andreote et al., 2009)
Methylococcales	methane oxidation	(Niemann et al., 2006)
Nitrospirales	NO_3^- oxidation	(Teske et al., 1994)
Desulfuromonadales	Fe (III) reduction; FVA oxidation	(Holmes et al., 2002)
Desulfobacterales	SO_4^{2-} reduction; FVA oxidation	(Nedwell et al.,)
Syntrophobacterales	SO_4^{2-} reduction; FVA oxidation	(Kirk et al., 2012)
Clostridiales	H_2 production, EtOH, VFA oxidation	(Plugge et al., 2010)
Propionibacteriales	VFA formation	(Stackebrandt et al., 2006)
Methanobacteriales	CH_3COO^-; ltd. substrate	(Bonin and Boone, 2006)
Methanosarcinales	CH_3COO^-; wide substrate	(Kendall and Boone, 2006)
Methanomicrobiales	H_2 metabolism	(Garcia et al., 2006)

Table A7.3. Network Properties.

Parameter	RS rDNA	Random 1	SS rDNA	Random 2	SS rRNA	Random 3	SS rDNA:DNA	Random 4
Number of Nodes	2,093	2,093	3,167	3,167	1,659	1,659	1,698	1,698
% VZ OTUs		-	58	-	48	-	55	-
% CZ OTUs		-	15	-	22	-	15	-
% SZ OTUs		-	27	-	31	-	30	-
% rare OTUs represented	6.2*	-	80	-	63	-	69	-
% intermediate OTUs represented	1.3*	-	18	-	25	-	28	-
% abundant OTUs represented	0.2*	-	2	-	4	-	4	-
Number of Edges	58,625	109,689	235,308		4,846	119,878	44,690	
Average Degree	28.01	52.408	74.3	78.94	30.95	41.3	26.32	42.32
Network Diameter	24	3	18	3	24	3	15	3
Graph Density	0.027	0.05	0.047	0.05	0.037	0.05	0.031	0.05
Modularity (# of modules)	0.804	0.081 (10)	0.553 (99)	0.067 (9)	0.66 (151)	0.094 (9)	0.881 (150)	0.093 (9)
Connected Components	214	1	92	1	135	1	144	1
Avg. Clustering Coefficient	0.864	0.05	0.674	0.05	0.638	0.05	0.891	0.05
Eigenvector Centrality (sum change)	0.189	0.003	0.211	0.0026	0.16	0.005	0.357	0.0043
Avg. Path Length	6.876	1.955	5.16	1.95	8.216	1.97	3.283	1.964

Table A7.4. Comparison of modularity attributes for the SS rRNA:rDNA network.

Modularity ID	**131**	**64**	**130**	**117**	**67**	**73**	**26**	**58**	**56**	**50**	**37**	**122**
VZ	50	206	107	86	66	171	1	0	0	0	0	0
CZ	0	4	1	0	2	26	45	14	1	0	0	1
SZ	0	0	0	1	1	0	0	34	64	109	43	151
VZ (%)	100	98	99	99	96	87	2	0	0	0	0	0
CZ(%)	0	2	1	0	3	13	98	29	2	0	0	1
SZ(%)	0	0	0	1	1	0	0	71	98	100	100	99
% network (1698 nodes)	2.94	12.37	6.36	5.12	4.06	11.60	2.71	2.83	3.83	6.42	2.53	8.95

Table A7.4. Comparison of modularity attributes for the SS rRNA:rDNA network.

Modularity ID	**131**	**64**	**130**	**117**	**67**	**73**	**26**	**58**	**56**	**50**	**37**	**122**
Eigenvector Centrality	0.02	0.16	0.41	0.16	0.07	0.01	0.02	0	0.06	0.43	0.02	0.85
In-Degree	24.5	33.88	53.5	43	34	14.02	22.5	4.83	32	54	21	56.65
Out-Degree	24.5	33.6	53.5	43	34	14.32	22.5	4.69	32	54	21	56.72
Degree	49	67.48	107	86	68	28.34	45	9.52	64	108	42	113.38
Eccentricity	1	10.34	1	1	1	10.57	1	7.38	1	1	1	6.76
Closeness Centrality	1	3.34	1	1	1	4.12	1	3.88	1	1	1	2.02

Modularity ID	131	64	130	117	67	73	26	58	56	50	37	122
Betweenness Centrality	0	656.93	0	0	0	636.41	0	254.1	0	0	0	130.79
Authority	5.49E-04	7.53E-04	1.19E-03	9.56E-04	7.58E-04	3.23E-04	5.06E-04	1.16E-04	7.14E-04	1.20E-03	4.73E-04	1.26E-03
Hub	5.49E-04	7.53E-04	1.19E-03	9.56E-04	7.58E-04	3.23E-04	5.06E-04	1.16E-04	7.14E-04	1.20E-03	4.73E-04	1.26E-03
PageRank	6.12E-04	6.41E-04	6.12E-04	6.12E-04	6.12E-04	5.94E-04	6.12E-04	5.73E-04	6.12E-04	6.12E-04	6.12E-04	6.34E-04
Clustering Coefficient	1	0.76	1	1	1	0.67	1	0.6	1	1	1	0.93
Number of triangles	1176	2362	5671	3655	2278	406	990	46.3	2016	5778	861	6800.6
Activity Ratio	1.46	3.64	2.45	2.54	3.73	5.31	2.63	7.73	3.36	3.26	4.3	5.86
% rare OTUs	1.96	7.24	5.5	4.41	3.54	5.72	1.53	0.93	3.21	5.07	2.18	5.01
% intermediate OTUs	0.71	3.92	0.38	0.33	0.22	4.79	0.87	1.2	0.33	0.76	0.11	2.94
% abundant OTUs	97.33	88.83	94.12	95.26	96.24	89.49	97.6	97.88	96.46	94.17	97.71	92.05

Supplementary figures

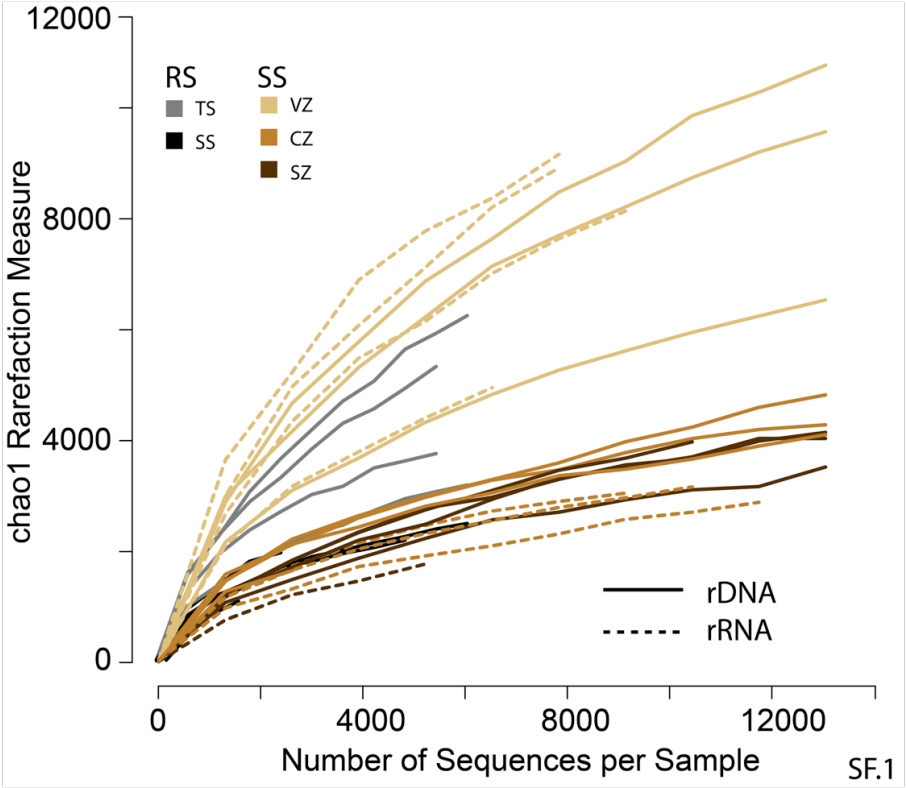

Figure A7.1. Rarefaction curves for 16S rDNA and 16S rDNA OTUs defined in the pyrosequence dataset for the RS and SS.

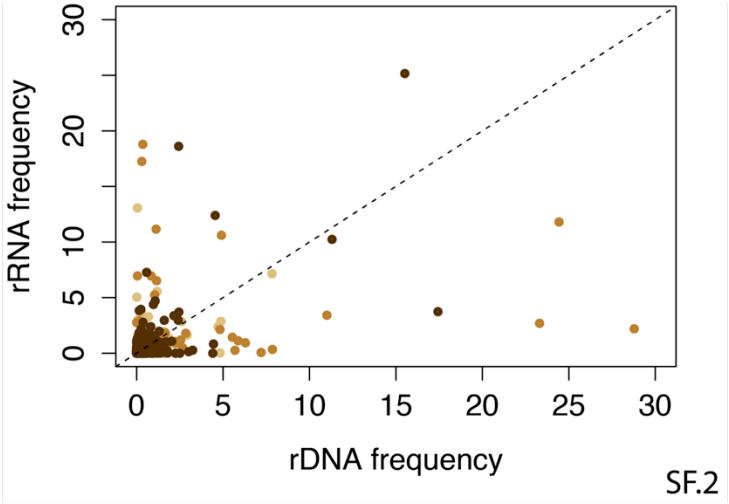

Figure A7.2. Relationships between frequencies of 16S rRNA and 16S rDNA OTUs defined in the pyrosequence dataset at the SS. The points are paired 16S rRNA and rDNA frequencies for each OTUs. Colors represent OTUs in the VZ, CF, and SZ clusters, respectively. The dotted line is the 1:1 line.

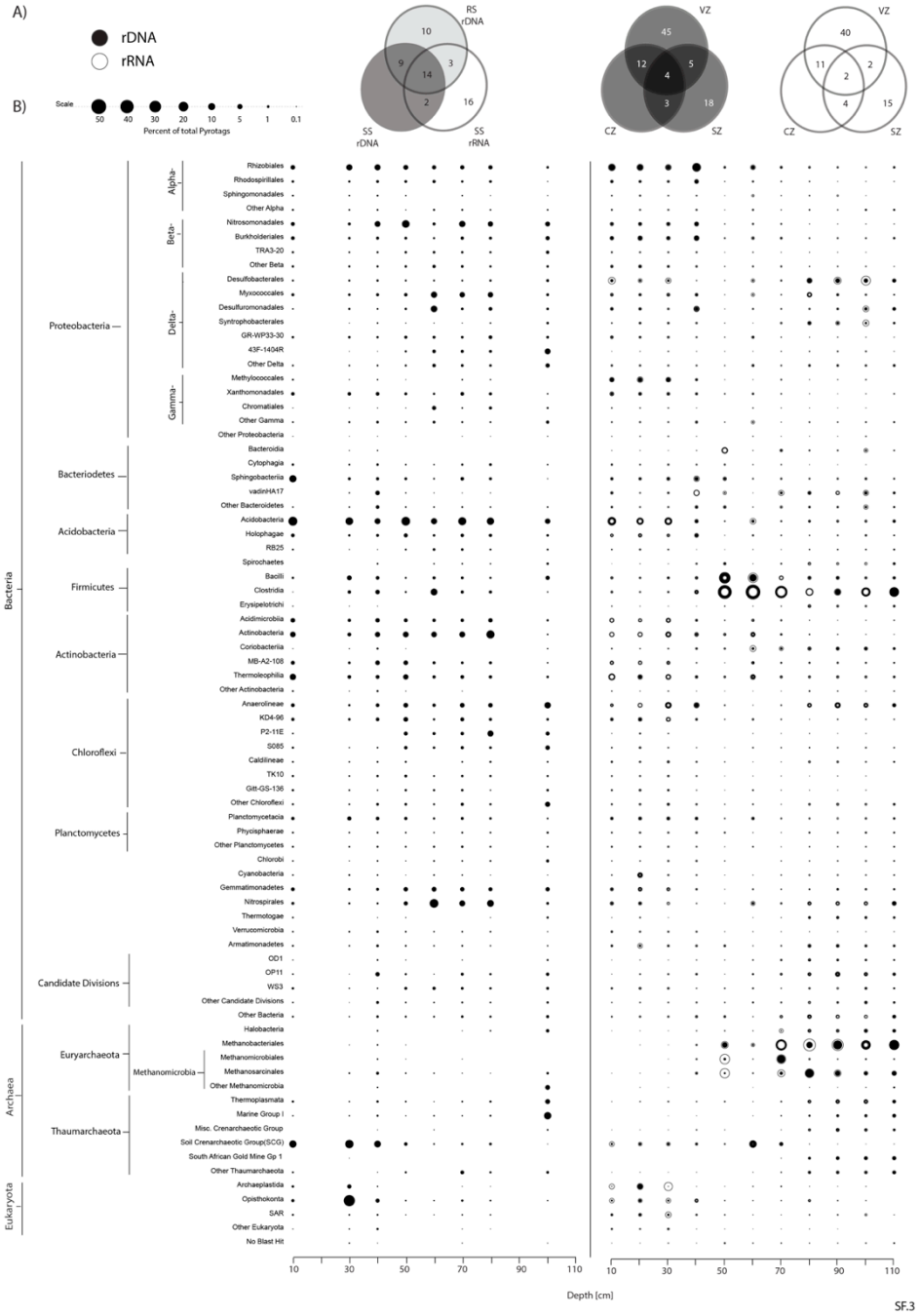

Figure A7.3. Distribution and activity of microbial community composition at the RS and SS. A) Comparison of percentage of shared OTUs. B) Abundant and active community groupings at the RS (left-hand side) and SS (right-hand side).

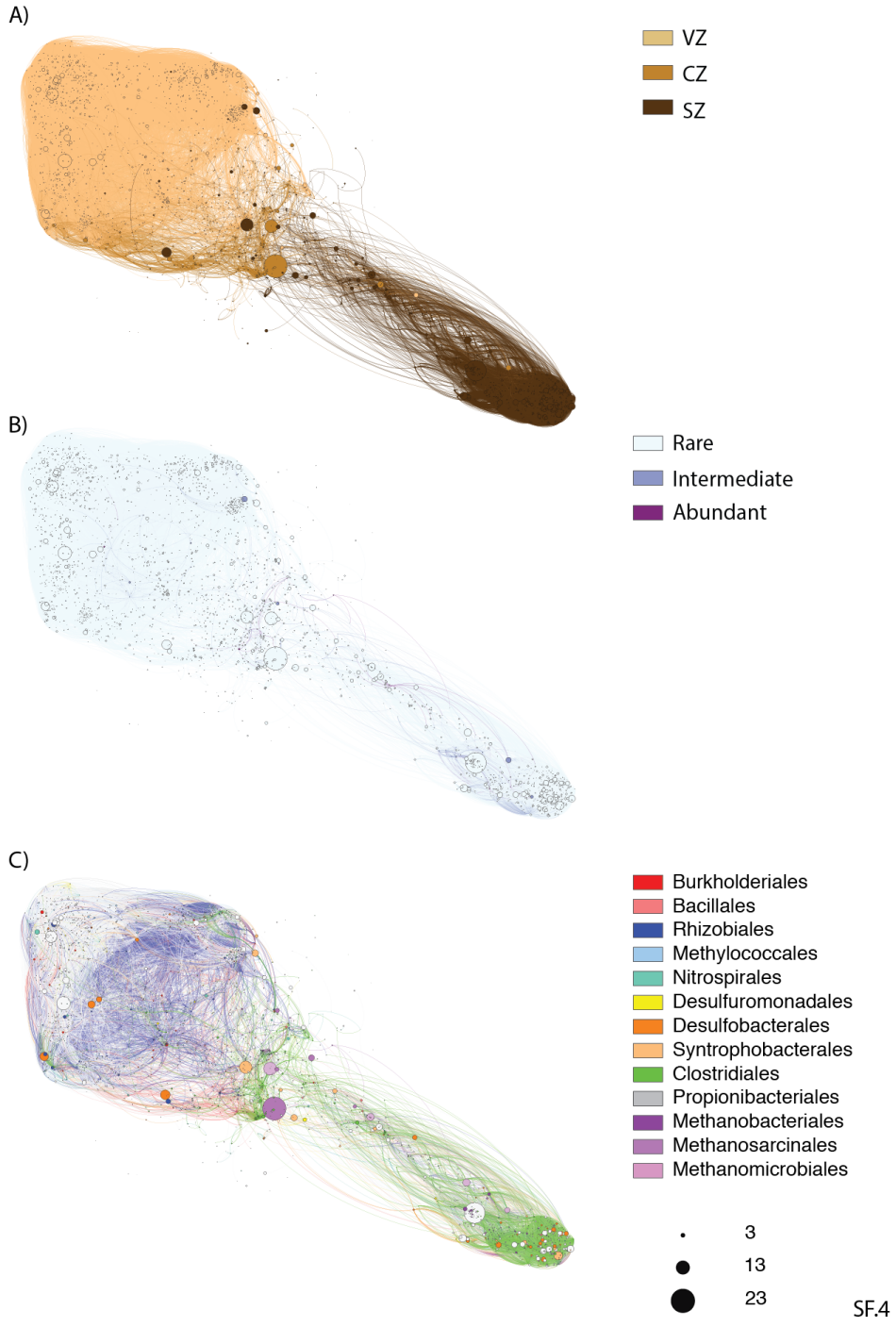

Figure A7.4. Network of communities identified based on interactions between OTUs identified in the rDNA dataset at the SS. Distribution of OTUs within A) soil zones, B) microbial community categories, and C) phylogenetic mappings. Nodes are sized to rRNA:rDNA ratio with non-active OTUs assigned a size of 1.

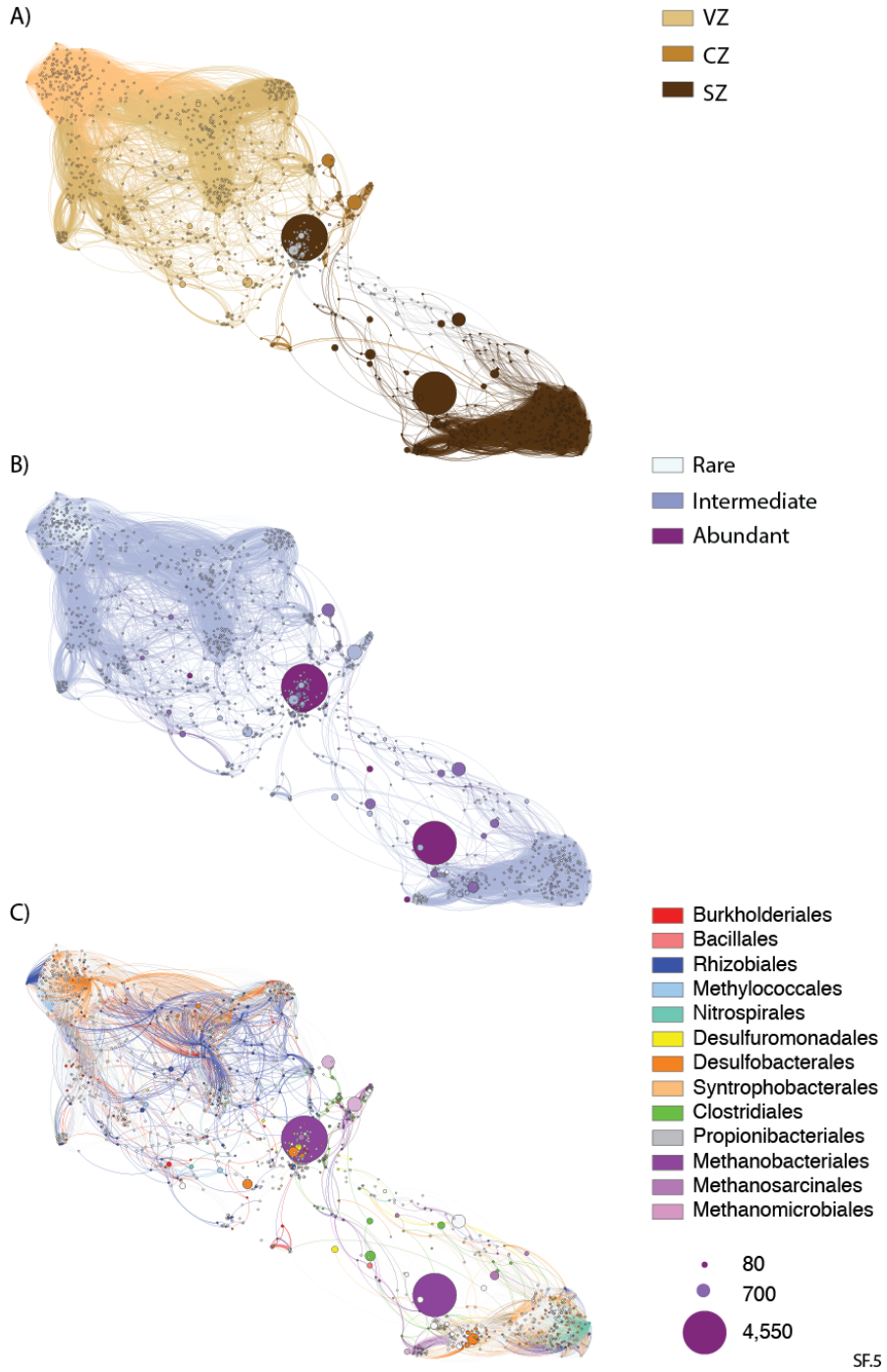

Figure A7.5. Network of communities identified based on interactions between OTUs identified in the rRNA dataset at the SS. Distribution of OTUs within A) soil zones, B) microbial community categories, and C) phylogenetic mappings. Nodes are sized to rRNA counts.